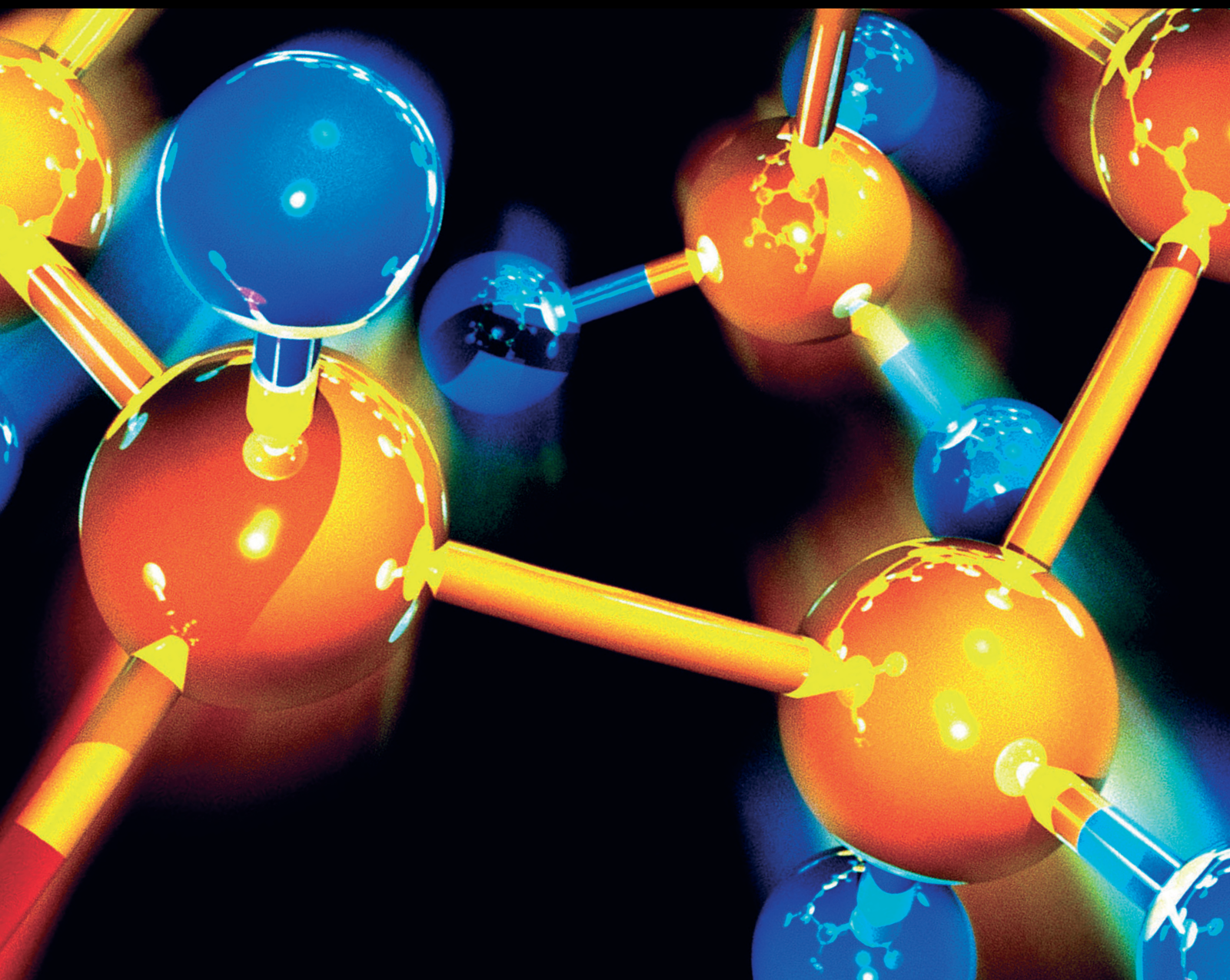# Use of Agro or Clay Based Polymer Nano-composites for Wastewater Treatment

Lead Guest Editor: Rabia Rehman
Guest Editors: Fadi Alakhras and Mehdi Vosoughi

Use of Agro or Clay Based Polymer Nano-composites for Wastewater Treatment

Use of Agro or Clay Based Polymer Nano-composites for Wastewater Treatment

Lead Guest Editor: Rabia Rehman
Guest Editors: Fadi Alakhras and Mehdi Vosoughi

Chief Editor

Kaustubha Mohanty, India

Associate Editors

Mohammad Al-Ghouti, Qatar
Tingyue Gu, USA
Teodorico C. Ramalho, Brazil
Artur M. S. Silva, Portugal

Academic Editors

Jinwei Duan , China
Luqman C. Abdullah, Malaysia
Dr Abhilash, India
Amitava Adhikary, USA
Amitava Adhikary, USA
Mozhgan Afshari, Iran
Daryoush Afzali, Iran
Mahmood Ahmed, Pakistan
Islam Al-Akraa, Egypt
Juan D. Alché, Spain
Gomaa A. M. Ali, Egypt
Mohd Sajid Ali, Saudi Arabia
Shafaqat Ali, Pakistan
Patricia E. Allegretti, Argentina
Marco Anni, Italy
Alessandro Arcovito, Italy
Hassan Arida, Saudi Arabia
Umair Ashraf, Pakistan
Narcis Avarvari, France
Davut Avci, Turkey
Chandra Azad, USA
Mohamed Azaroual, France
Rasha Azzam, Egypt
Hassan Azzazy, Egypt
Renal Backov, France
Suresh Kannan Balasingam, Republic of Korea
Sukanta Bar, USA
Florent Barbault, France
Maurizio Barbieri, Italy
James Barker, United Kingdom
Salvatore Barreca, Italy
Jorge Barros-Velázquez, Spain
THANGAGIRI Baskaran, India
Haci Baykara, Ecuador
Michele Benedetti, Italy
Laurent Billon, France

Marek Biziuk, Poland
Jean-Luc Blin, France
Tomislav Bolanca, Croatia
Ankur Bordoloi, India
Cato Brede, Norway
Leonid Breydo, USA
Wybren J. Buma, The Netherlands
J. O. Caceres, Spain
Patrizia Calaminici, Mexico
Claudio Cameselle, Spain
Joaquin Campos, Spain
Dapeng Cao, China
Domenica Capasso, Italy
Stefano Caporali, Italy
Zenilda Cardeal, Brazil
Angela Cardinali, Italy
Stefano Carli, Italy
Maria F. Carvalho, Portugal
Susana Casal, Portugal
David E. Chavez, USA
Riccardo Chelli, Italy
Zhongfang Chen, Puerto Rico
Vladislav Chrastny, Czech Republic
Roberto Comparelli, Italy
Filomena Conforti, Italy
Luca Conti, Italy
Christophe Coquelet, France
Filomena Corbo, Italy
Jose Corchado, Spain
Maria N. D.S. Cordeiro, Portugal
Claudia Crestini, Italy
Gerald Culioli, France
Nguyen Duc Cuong, Vietnam
Stefano D'Errico, Italy
Matthias D'hooghe, Belgium
Samuel B. Dampare, Ghana
Umashankar Das, Canada
Victor David, Romania
Annalisa De Girolamo, Italy
Antonio De Lucas-Consuegra, Spain
Marcone A. L. De Oliveira, Brazil
Paula G. De Pinho, Portugal
Damião De Sousa, Brazil
Francisco Javier Deive, Spain
Tianlong Deng, China

Fatih Deniz (iD), Turkey
Claudio Di Iaconi, Italy
Irene Dini (iD), Italy
Daniele Dondi, Italy
Yingchao Dong (iD), China
Dennis Douroumis (iD), United Kingdom
John Drexler, USA
Qizhen Du, China
Yuanyuan Duan (iD), China
Philippe Dugourd, France
Frederic Dumur (iD), France
Grégory Durand (iD), France
Mehmet E. Duru, Turkey
Takayuki Ebata (iD), Japan
Arturo Espinosa Ferao (iD), Spain
Valdemar Esteves (iD), Portugal
Cristina Femoni (iD), Italy
Gang Feng, China
Dieter Fenske, Germany
Jorge F. Fernandez-Sanchez (iD), Spain
Alberto Figoli (iD), Italy
Elena Forte, Italy
Sylvain Franger (iD), France
Emiliano Fratini (iD), Italy
Franco Frau (iD), Italy
Bartolo Gabriele (iD), Italy
Guillaume Galliero (iD), France
Andrea Gambaro (iD), Italy
Vijay Kumar Garlapati, India
James W. Gauld (iD), Canada
Barbara Gawdzik (iD), Poland
Pier Luigi Gentili (iD), Italy
Beatrice Giannetta (iD), Italy
Dimosthenis L. Giokas (iD), Greece
Alejandro Giorgetti (iD), Italy
Alexandre Giuliani (iD), France
Elena Gomez (iD), Spain
Yves Grohens, France
Katharina Grupp, Germany
Luis F. Guido (iD), Portugal
Maolin Guo, USA
Wenshan Guo (iD), Australia
Leena Gupta (iD), India
Muhammad J. Habib, USA
Jae Ryang Hahn, Republic of Korea

Christopher G. Hamaker (iD), USA
Ashanul Haque (iD), Saudi Arabia
Yusuke Hara, Japan
Naoki Haraguchi, Japan
Serkos A. Haroutounian (iD), Greece
Rudi Hendra (iD), Indonesia
Javier Hernandez-Borges (iD), Spain
Miguel Herrero, Spain
Mark Hoffmann (iD), USA
Hanmin Huang, China
Doina Humelnicu (iD), Romania
Charlotte Hurel, France
Nenad Ignjatović (iD), Serbia
Ales Imramovsky (iD), Czech Republic
Muhammad Jahangir, Pakistan
Philippe Jeandet (iD), France
Sipak Joyasawal, USA
Sławomir M. Kaczmarek, Poland
Ewa Kaczorek, Poland
Mostafa Khajeh, Iran
Srećko I. Kirin (iD), Croatia
Anton Kokalj (iD), Slovenia
Sevgi Kolaylı (iD), Turkey
Takeshi Kondo (iD), Japan
Christos Kordulis, Greece
Ioannis D. Kostas (iD), Greece
Yiannis Kourkoutas (iD), Greece
Henryk Kozlowski, Poland
Yoshihiro Kudo (iD), Japan
Avvaru Praveen Kumar (iD), Ethiopia
Dhanaji Lade, USA
Isabel Lara (iD), Spain
Jolanta N. Latosinska (iD), Poland
João Paulo Leal (iD), Portugal
Woojin Lee, Kazakhstan
Yuan-Pern Lee (iD), Taiwan
Matthias Lein (iD), New Zealand
Huabing Li, China
Jinan Li (iD), USA
Kokhwa Lim (iD), Singapore
Teik-Cheng Lim (iD), Singapore
Jianqiang Liu (iD), China
Xi Liu (iD), China
Xinyong Liu (iD), China
Zhong-Wen Liu (iD), China

Eulogio J. Llorent-Martínez (iD), Spain
Pasquale Longo (iD), Italy
Pablo Lorenzo-Luis (iD), Spain
Zhang-Hui Lu, China
Devanand Luthria, USA
Konstantin V. Luzyanin (iD), United Kingdom
Basavarajaiah S M, India
Mari Maeda-Yamamoto (iD), Japan
Isabel Mafra (iD), Portugal
Dimitris P. Makris (iD), Greece
Pedro M. Mancini, Argentina
Marcelino Maneiro (iD), Spain
Giuseppe F. Mangiatordi (iD), Italy
Casimiro Mantell (iD), Spain
Carlos A Martínez-Huitle (iD), Brazil
José M. G. Martinho (iD), Portugal
Andrea Mastinu (iD), Italy
Cesar Mateo (iD), Spain
Georgios Matthaiolampakis, USA
Mehrab Mehrvar, Canada
Saurabh Mehta (iD), India
Oinam Romesh Meitei (iD), USA
Saima Q. Memon (iD), Pakistan
Morena Miciaccia, Italy
Maurice Millet (iD), France
Angelo Minucci, Italy
Liviu Mitu (iD), Romania
Hideto Miyabe (iD), Japan
Ahmad Mohammad Alakraa (iD), Egypt
Kaustubha Mohanty, India
Subrata Mondal (iD), India
José Morillo, Spain
Giovanni Morrone (iD), Italy
Ahmed Mourran, Germany
Nagaraju Mupparapu (iD), USA
Markus Muschen, USA
Benjamin Mwashote (iD), USA
Mallikarjuna N. Nadagouda (iD), USA
Lutfun Nahar (iD), United Kingdom
Kamala Kanta Nanda (iD), Peru
Senthilkumar Nangan, Thailand
Mu. Naushad (iD), Saudi Arabia
Gabriel Navarrete-Vazquez (iD), Mexico
Jean-Marie Nedelec (iD), France
Sridhar Goud Nerella (iD), USA

Nagatoshi Nishiwaki (iD), Japan
Tzortzis Nomikos (iD), Greece
Beatriz P. P. Oliveira (iD), Portugal
Leonardo Palmisano (iD), Italy
Mohamed Afzal Pasha (iD), India
Dario Pasini (iD), Italy
Angela Patti (iD), Italy
Massimiliano F. Peana (iD), Italy
Andrea Penoni (iD), Italy
Franc Perdih (iD), Slovenia
Jose A. Pereira (iD), Portugal
Pedro Avila Pérez (iD), Mexico
Maria Grazia Perrone (iD), Italy
Silvia Persichilli (iD), Italy
Thijs A. Peters (iD), Norway
Christophe Petit (iD), France
Marinos Pitsikalis (iD), Greece
Rita Rosa Plá, Argentina
Fabio Polticelli (iD), Italy
Josefina Pons, Spain
V. Prakash Reddy (iD), USA
Thathan Premkumar, Republic of Korea
Maciej Przybyłek (iD), Poland
María Quesada-Moreno (iD), Germany
Maurizio Quinto (iD), Italy
Franck Rabilloud (iD), France
C.R. Raj, India
Sanchayita Rajkhowa (iD), India
Manzoor Rather (iD), India
Enrico Ravera (iD), Italy
Julia Revuelta (iD), Spain
Muhammad Rizwan (iD), Pakistan
Manfredi Rizzo (iD), Italy
Maria P. Robalo (iD), Portugal
Maria Roca (iD), Spain
Nicolas Roche (iD), France
Samuel Rokhum (iD), India
Roberto Romeo (iD), Italy
Antonio M. Romerosa-Nievas (iD), Spain
Arpita Roy (iD), India
Eloy S. Sanz P rez (iD), Spain
Nagaraju Sakkani (iD), USA
Diego Sampedro (iD), Spain
Shengmin Sang (iD), USA

Vikram Sarpe, USA
Adrian Saura-Sanmartin, Spain
Stéphanie Sayen, France
Ewa Schab-Balcerzak, Poland
Hartwig Schulz, Germany
Gulaim A. Seisenbaeva, Sweden
Serkan Selli, Turkey
Murat Senturk, Turkey
Beatrice Severino, Italy
Sunil Shah Shah, USA
Ashutosh Sharma, USA
Hideaki Shirota, Japan
Cláudia G. Silva, Portugal
Ajaya Kumar Singh, India
Vijay Siripuram, USA
Ponnurengam Malliappan Sivakumar, Japan
Tomás Sobrino, Spain
Raquel G. Soengas, Spain
Yujiang Song, China
Olivier Soppera, France
Radhey Srivastava, USA
Vivek Srivastava, India
Theocharis C. Stamatatos, Greece
Athanassios Stavrakoudis, Greece
Darren Sun, Singapore
Arun Suneja, USA
Kamal Swami, USA
B.E. Kumara Swamy, India
Elad Tako, USA
Shoufeng Tang, China
Zhenwei Tang, China
Vijai Kumar Reddy Tangadanchu, USA
Franco Tassi, Italy
Alexander Tatarinov, Russia
Lorena Tavano, Italy
Tullia Tedeschi, Italy
Vinod Kumar Tiwari, India
Augusto C. Tome, Portugal
Fernanda Tonelli, Brazil
Naoki Toyooka, Japan
Andrea Trabocchi, Italy
Philippe Trens, France
Ekaterina Tsipis, Russia
Esteban P. Urriolabeitia, Spain

Toyonobu Usuki, Japan
Giuseppe Valacchi, Italy
Ganga Reddy Velma, USA
Marco Viccaro, Italy
Jaime Villaverde, Spain
Marc Visseaux, France
Balaga Viswanadham, India
Alessandro Volonterio, Italy
Zoran Vujcic, Serbia
Chun-Hua Wang, China
Leiming Wang, China
Carmen Wängler, Germany
Wieslaw Wiczkowski, Poland
Bryan M. Wong, USA
Frank Wuest, Canada
Yang Xu, USA
Dharmendra Kumar Yadav, Republic of Korea
Maria C. Yebra-Biurrun, Spain
Dr Nagesh G Yernale, India
Tomokazu Yoshimura, Japan
Maryam Yousaf, China
Sedat Yurdakal, Turkey
Shin-ichi Yusa, Japan
Claudio Zaccone, Italy
Ronen Zangi, Spain
John CG Zhao, USA
Zhen Zhao, China
Antonio Zizzi, Italy
Mire Zloh, United Kingdom
Grigoris Zoidis, Greece
Deniz ŞAHİN, Turkey

Contents

Review Article

Review of Clay-Based Nanocomposites as Adsorbents for the Removal of Heavy Metals

Ismael Kithinji Kinoti,[1] **Esther Muthoni Karanja,**[1] **Esther Wanja Nthiga,**[2]
Cyprian Muturia M'thiruaine,[1] **and Joseph Mwiti Marangu** [1]

[1]*Physical Sciences, Meru University of Science and Technology, Meru, Kenya*
[2]*Department of Chemistry, Dedan Kimathi University of Technology, Nyeri, Kenya*

Correspondence should be addressed to Joseph Mwiti Marangu; jmarangu2011@gmail.com

Due to rapid industrialization, urbanization, and surge in modern human activities, water contamination is a major threat to humanity globally. Contaminants ranging from organic compounds, dyes, to inorganic heavy metals have been of major concern in recent years. This necessitates the development of affordable water remediation technologies to improve water quality. There is a growing interest in nanotechnology recently because of its application in eco-friendly, cost-effective, and durable material production. This study presents a review of recent nanocomposite technologies based on clay, applied in the removal of heavy metals from wastewater, and highlights the shortcomings of existing methods. Recently published reports, articles, and papers on clay-based nanocomposites for the removal of heavy metals have been reviewed. Currently, the most common methods utilized in the removal of heavy metals are reverse osmosis, electrodialysis, ion exchange, and activated carbon. These methods, however, suffer major shortcomings such as inefficiency when trace amounts of contaminant are involved, uneconomical costs of operation and maintenance, and production of contaminated sludge. The abundance of clay on the Earth's surface and the ease of modification to improve adsorption capabilities have made it a viable candidate for the synthesis of nanocomposites. Organoclay nanocomposites such as polyacrylamide-bentonite, polyaniline-montmorillonite, and β-cyclodextrin-bentonite have been synthesized for the selective removal of various heavy metals such as Cu^{2+}, Co^{2+}, among others. Bacterial clay nanocomposites such as *E. coli* kaolinite nanocomposites have also been successfully synthesized and applied in the removal of heavy metals. Low-cost nanocomposites of clay using biopolymers like chitosan and cellulose are especially in demand due to the cumulative abundance of these materials in the environment. A comparative analysis of different synthetic processes to efficiently remove heavy metal contaminants with clay-based nanocomposite adsorbents is made.

1. Introduction

Water is considered as the most essential source of life with its usage ranging from domestic consumption to industrial applications in cooling machinery and manufacturing. Globally, water makes up 71% of the Earth's surface, with a major part of it (95.5%) in the oceans [1]. In a publication by FAO-AQUASTAT, [2] it is estimated that by 2050, food and water will need to be provided to about 9-10 billion people, owing to a growing global population. The North American and European industries alone use about 50% of all water [3]. This is in comparison to 4 to 12% in developing countries. World Health Organization [4] outlines that about 785 million people do not have access to clean and safe water. About 37% of these people live in Sub-Saharan Africa. The same report outlines that 1 in 3 people worldwide does not have access to safe and clean drinking water, a state much more worsened when referencing children. More than 500,000 children die annually due to poor sanitation and unsafe or contaminated water [5]. Industrialization, modern agriculture, and other effects of human activities are the major sources of water contaminants (Philippines, [6]).

Wastewater, generally classified as domestic, industrial, or stormwater, has been defined as the used or polluted form

of water due to human activities or rainwater runoff [7]. The EPA [8] estimates that 23,000–75,000 sanitary sewers overflow each year, contaminating adjacent water sources. In addition to this, about 80% of global wastewater finds its way back to the ecosystem without undergoing any form of treatment [9]. This translates that close to 1.8 billion people globally utilize contaminated water sources. In Kenya, approximately 32% of the total population consumes water from water sources prone to contamination [10]. Industrial wastewater has been defined as the effluent resulting from substances suspended or dissolved in water after it has undergone a manufacturing process or cleaning activities involved in that process [11]. Very high volumes ranging from 3 to 10 billion gallons of sewerage effluents are released annually from treatment plants [12]. Industrial sewerage is estimated to account for approximately 22% of global water use, according to FAO-AQUASTAT [2]. In addition, approximately 80% of global municipal and industrial wastewater end up polluting the environment in untreated forms. Globally, public wastewater treatment facilities process more than 8 million tons of dry sludge annually, which consumes about a third of electricity use [13]. Lower middle-income countries are reported to treat only about 28% of their wastewater, which means that in most countries in Africa, about 72% of the sewerage effluents produced end up contaminating the environment, endangering human lives [10].

Wastewater effluents from factories are common heavy metal contaminants to the environment, especially if the effluents are not properly treated prior to disposal [14]. Heavy metals have been defined as metallic elements whose density is considerably higher than that of water and, in relatively low concentrations, exhibit toxicity or poisonous effects [15]. Some of these metals include lead (Pb), mercury (Hg), arsenic (As), thallium (Tl), and cadmium (Cd). Some heavy metals like gold exist naturally on Earth's crust and are often exploited for various applications. Others like manganese, iron, among others, play an important role in biochemical processes within the body, while they are present in trace amounts [16]. Bioaccumulation of heavy metals in the human body is what causes adverse effects as affecting the nervous system, kidneys, among others [17]. Heavy metals eventually find their way to human bodies as a result of anthropogenic activities like industrial waste release, mining activities, use of contaminated water for irrigation, among others. Most heavy metals exist as compounded salts in ores as sulfides or oxides. Copper, gold, and manganese are known to exist naturally as oxides. Silver, lead, and iron exist naturally as sulfides. When mined, these ores are blasted and heavy metals are released into the open environment, consequently finding their way into water bodies, air, and soil as effluents. In industries, paints, pesticides, herbicides, and cosmetics are common carriers of heavy metals that are exposed to the environment through erosion or runoff [16].

Heavy metals have diverse effects when they bioaccumulate in human bodies. Arsenic, in an inorganic state, occurs as arsenate and arsenite. Major sources of this metal include microelectronic industries and smelting zones.

Other sources include paints, wood preservatives, and pesticides [18]. Arsenic bioaccumulates in nails, hair, and the skin when it gets into the body. In some instances, it is transported through the bloodstream to accumulate in the heart, liver, neural tissues, and kidney [16]. The mechanism of the biological toxicity of arsenic is not clear. It is however reported that it generates free radicals like the peroxyl *radical* ($ROO^.$), dimethyl *arsenic radical* ($(CH_3)_2As\cdot$), *superoxide* ($O_2\cdot$), *nitric oxide* (NO•), *singlet oxygen* ($^1O_2$), among others [19]. Lead is one of the flagged heavy metals for acute environmental poisoning today [20]. Major sources of lead are linked to cigarettes, and domestic and industrial sources. Storage batteries, gasoline, paints, and some plumbing pipes have been documented as some major sources of lead contamination [17]. Once it finds its way to human bodies, lead can induce carcinogenic processes that have been reported to cause DNA damage and interfere with the DNA repair processes through the generation of reactive oxygen species [20]. Cadmium is widely distributed on the Earth's surface and is estimated to have an average concentration of about 0.1 mg/kg [21]. Applications of this metal include the production of batteries, alloys, and pigments [22]. Due to strict environmental regulations, cadmium uptake has been on the decrease especially in developed countries. In the United States, the daily uptake of cadmium has been reported to be about 0.4 ug/kg, which is less than half of the U.S. EPA oral reference dose (US, [8]). Exposure to cadmium occurs through occupational exposure like working in cadmium-contaminated industries, smoking cigarettes, or eating contaminated food. In some foods, cadmium is found in trace amounts like in leafy vegetables, liver and kidney, dried seaweed, among others [21]. Exposure is determined through blood samples or urine analysis, with cigarette smokers estimated to have the highest cadmium levels in both samples [23]. Symptoms associated with cadmium exposure include nausea, abdominal pain, muscle cramps, burning sensation, shock, and in severe cases, loss of consciousness within 15 to 30 minutes [21].

In this regard, different methods have been employed in the remediation of heavy metals from wastewater. Clay-based nanocomposites have recently gained much attention in the removal of heavy metals due to their increased surface area and modifiable structures for selective contaminant removal [24]. The removal of various heavy metals, by various clay-based nanocomposites, is discussed in this review.

2. Wastewater

2.1. Components of Wastewater. Wastewater is made up of major components that are related to the treatment processes employable on the sewage [25]. Some of these components include biochemical oxygen demand (BOD), total suspended solids (TSSs), pathogens, nutrients, and other emergent contaminants [25]. BOD is described as the amount of oxygen required or demanded by organic compounds in wastewater to break down into simple and stable compounds. A high BOD dictates that wastewater

microbes would compete for oxygen with marine life if such effluent is released to water bodies. It is of importance to reduce BOD before the wastewater is released into water bodies. The EPA standard concentration for BOD is 50 mg/L [26]. However, different countries have their respective allowable standard values of BOD for wastewater. Unpolluted water typically has a BOD concentration of approximately 1 mg/L [27]. Household wastewater is typically in the range of 200 mg/L for BOD [25]. This means that, under standard procedures, it would take approximately 200 mg of dissolved oxygen to break down its organic matter in approximately 5 days. Values in the range of 200–600 mg/L have the water considered polluted and must be processed before releasing to the environment [27]. According to Bezsenyi et al. [28], the effect of hydrogen peroxide on the values of BOD measured during ionizing radiation treatment of wastewater can be erroneously overestimated in the presence of high concentrations of hydrogen peroxide. In a study conducted by Skoczko et al. [29] investigating the influence of seasonal changes on various wastewater factors, it was reported that the values of BOD removal efficiency showed no significant difference over the seasons. However, the removal efficiency increased slightly from winter to summer due to the positive change in temperature. Nezhadheydari et al. [30] investigated the effect of magnetic nanoparticle concentrations on aquaculture wastewater treatment. The study reported that the effect of the nanoparticles on BOD was only significant at high concentrations. Pavithra and Shanthakumar [31] reported BOD removal of 62.7% and 57.27% when using silica and iron nanoparticles, respectively, from aquaculture wastewater. Gharloghi et al. [32] estimated that iron oxide nanoparticles could reduce BOD by approximately 25% when applied to municipal wastewater.

TSS is the number of solids of a specific size (more than 2 microns) dispersed in the wastewater in suspension. It is the specific measurement of the total suspended mass of solid material in wastewater, whether organic or inorganic. Any particles less than 2 microns in size are considered dissolved solids [33]. In the environment, they are capable of clogging fish gills, smothering fish eggs, and decreasing light dispersion in water bodies. They can be organic, such as fecal matter, or inorganic, such as silt or clay. A high value of TSS indicates a high biological oxygen demand, meaning that a high percentage of solids is organic matter [25]. Often, turbidity measurements are an estimate, and not an exact value, of TSS. Turbidity is the optical determination of the clarity of water, that is affected by both the dissolved matter and the suspended particles in a water column [8]. Turbidity values indicate the change in TSS concertation of wastewater without giving exact measurements [34]. In most cases, TSS values below 20 mg/L will show low turbidity levels of about 5 NTU, which is visually clear. TSS levels over 40 mg/L shows cloudiness, which in comparison to estimated turbidity levels show a value of about 55 NTU [35]. Raw wastewater will often have TSS in the range of 155–330 mg/L, whereby 250 mg/L is considered a typical wastewater TSS concentration. After the primary treatment stage, this value is expected to fall below 65 mg/L and below 25 mg/L after the advanced secondary treatment system [36]. TSS-contaminated wastewater increases the TSS value of waterbodies it may be dumped into. When this happens, the rise in TSS value can contribute to a rise in water temperature and consequently decrease in dissolved oxygen (DO) [34]. This happens when radiant heat from the sunlight is absorbed by suspended matter that heats the water molecules by conduction. Warmer waters release oxygen easier than colder waters; therefore, this process lowers the levels of DO [37]. In addition, high TSS levels can induce water stratification, whereby water layers themselves by temperature zones in such a way that the colder layers (bottom) do not intermix with warmer layers (top). Since respiration and decomposition occur in the lower layers, the lack of intermiscibility would cause a state of hypoxia when gradually decreasing oxygen levels to make it challenging for organisms to survive [33]. In a study conducted by Amerian et al. [38], studying the effect of TSS, among other factors, on peracetic acid (PAA) decomposition, it was reported that PAA demand increased for both primary and secondary effluents with increase in concentration of TSS. The higher demand for PAA in primary effluent was attributed to a higher concentration of suspended organic matter. The observed decay rate was 0.014 L/mg·min and 0.0039 L/mg·min in primary and secondary effluents, respectively, for every 10 mg/L increase in TSS concentration. The higher decay rate in primary effluent was also attributed to a higher concentration of organic matter in primary effluent. In a similar study by, PAA rate of decay was observed to increase by a factor of five as the concentration of TSS increased gradually from 40 to 160 mg/L.

2.2. Characteristics of Wastewater and Effluent Quality Parameters.

Wastewater is characterized into three major groups, namely physical, chemical, and biological characteristics [39]. The physical characteristics include the color, turbidity, temperature, odor, and total solids in the wastewater. Sewer water is often brown and yellow when fresh, and turns to dark color in time, as the organic matter begins to decay [40]. It is a common characteristic of sewer effluents to have a strong pungent odor. Temperatures are always higher than normal due to biological activities that occur in the sewer water. Additionally, the turbidity of sewerage is high due to a high percentage of suspended solids [41].

Chemical characteristics include nitrogen, chemical oxygen demand (COD), alkalinity, pH, total organic carbon (TOC), chlorides, heavy metals, phosphorus, among others [42]. COD defines the organic matter in wastewater by determining the amount of oxygen required to oxidize them. It is the quantity of oxygen that must be in the water to oxidize the embedded chemical organic pollutants. High levels of COD could indicate an imminent decrease in dissolved oxygen, which can negatively impact marine life and balance [43]. The TOC describes the amount of carbon embedded in the organic materials in the wastewater. This parameter is usually investigated as an ongoing assessment of the change or lack of change of the organic content in the wastewater [44]. Whitehead argued that TOC on its own does not give satisfactory data regarding the organic content

in wastewater as compounds containing carbon can exist in different forms. Phosphorus can exist both organically and inorganically in wastewater. Nitrogen is often found in organic forms in wastewater.

The biological characteristics include bacteria, fungi, algae, viruses, and protozoa [41]. In the sewage, both intestinal and sewage bacteria are found. Pathogenic and nonpathogenic intestinal bacteria such as fecal coliform, *Salmonella, Vibrio cholera,* among others, find their way to sewers through human stool. Anaerobic and aerobic sewage bacteria exist naturally in sewer systems, playing a key role in breaking down organic matter. *Pepto coccus, Bifidobacterium, Nocardia, Achromobactin,* among others, are some of the common real sewage bacteria. Algae and fungi in sewerage effluents play an important role in trickling filters during sewage treatment [41].

2.3. Wastewater Treatment. Edwards [11] classified wastewater treatment methods into physical/chemical, thermal, and biological classes. As the class names dictate, physical/chemical methods employ the physical or chemical properties of the wastewater constituents to effect ample change in the composition. Thermal methods involve the use of heat that decomposes pollutants, while biological methods involve the use of microorganisms in the removal of undesirable wastes. In wastewater treatment, however, three major steps, namely primary, secondary, and tertiary, are undertaken to ensure clean and safe water [45].

Primary treatment, also known as a preliminary treatment, involves the removal of grit and screenings from the wastewater, often by the use of physical methods [46]. Primary sanitation technology reduces suspended solids through the removal of scum and suspended solids through surface screening and gravity settling. Bar screens are used for the screening step and gravity settling makes use of grit chambers to remove the settled grit [47]. Secondary treatment is usually standardized to remove dissolved organic matter that is not caught by the primary treatment stage and suspended solids [7]. Biological processes play a key role in waste removal at this stage, as microorganisms metabolize organic matter to energy, water, and carbon dioxide. The methods employed at this stage are trickling filters, oxidation ponds, and activated sludge processes [45]. Recently, a rotating biocontacter has been used [7]. Activated sludge process, being the most common method in developing countries, has been reported to remove approximately 80% BOD and 78.28% COD in attached and suspended growth reactors [48]. Tertiary processes are usually employed in cases where the quality of the remediated water is of utmost importance. Therefore, tertiary methods polish secondary effluents to reduce unsafe concentrations of dissolved chemicals such as heavy metals, phosphates, and nitrates [45]. Granular media filters and micro-strainers are used to remove BOD and any suspended solids from secondary effluents in a process known as effluent polishing [49, 50]. These steps are summarized in Figure 1. Percentage removal efficiencies of different pollutants at different stages are summarized in Table 1 [53].

In developing countries, the primary and the secondary treatment stages are the most common in the municipal wastewater process. This is due to the high maintenance costs involved in setting up modern tertiary treatment facilities, which often leave their application to private companies. The existing methods applied in the primary and secondary stages such as the activated sludge process do not particularly address the removal of heavy metals. This means that most wastewater effluents from the primary and secondary treatment contain heavy metal concentrations dangerous to the environment, animals, and humans alike. Sustainable and affordable technologies such as clay-based nanocomposites are being looked into to address this problem, especially in developing countries whereby modern tertiary wastewater remediation methods are expensive to set up and maintain.

3. Techniques of Heavy Metal Decontamination

3.1. Metal Precipitation. Metal precipitation methods remove metals from wastewater by converting the metal ion from the dissolved state to a solid state that is precipitated. These methods employ chemical additives or make use of microbiological processes. The most important parameter in these methods is that the concentration of the metal ion has to be high in complex liquid states. Metal precipitation techniques do not achieve complete metal ion removal, and often multiple techniques are employed in addition to removing the metal ions [54].

3.1.1. Chemical Precipitation. Chemical precipitation works under the metal ion saturation principle. When a solution becomes saturated with metal ions and the solubility product (Ksp) of the system is exceeded, the metal ion is precipitated [55]. Ksp is the product at equilibrium between a solid and its ions in the solution. The stages followed by a precipitation process include the nucleation stage, nucleus growth, and then the crystallization or aggregation stage [54]. Factors that affect the quality of the precipitation process include the concentration of the metal ions of interest, their type, the conditions of the reaction like pH, the type of precipitant used, and most importantly, the availability of precipitation inhibitors [56].

Hydroxide precipitation employs alteration in pH using calcium hydroxide or sodium hydroxide as the precipitation agent. Different metals have optimal pH values for the optimum hydroxide precipitation to occur, mainly in the range of 7.5 to 11. The main challenge for this method is that most metallic hydroxides exhibit amphoteric behavior, which imposes a different challenge on precipitated metals to solubilize back into the solution [56]. In addition to this limitation, this method is prone to problematic sludge that needs further processing. Wang and Chen [57] proposed a method to sequentially precipitate heavy metals (Fe, Cu, and Zn) and treat the sludge concurrently by modifying the hydroxide precipitation with sulfide precipitation and oxidation treatment. In this manner, they achieved 99.8% Fe removal, 94% Cu removal, and 96.1% Zn removal and an
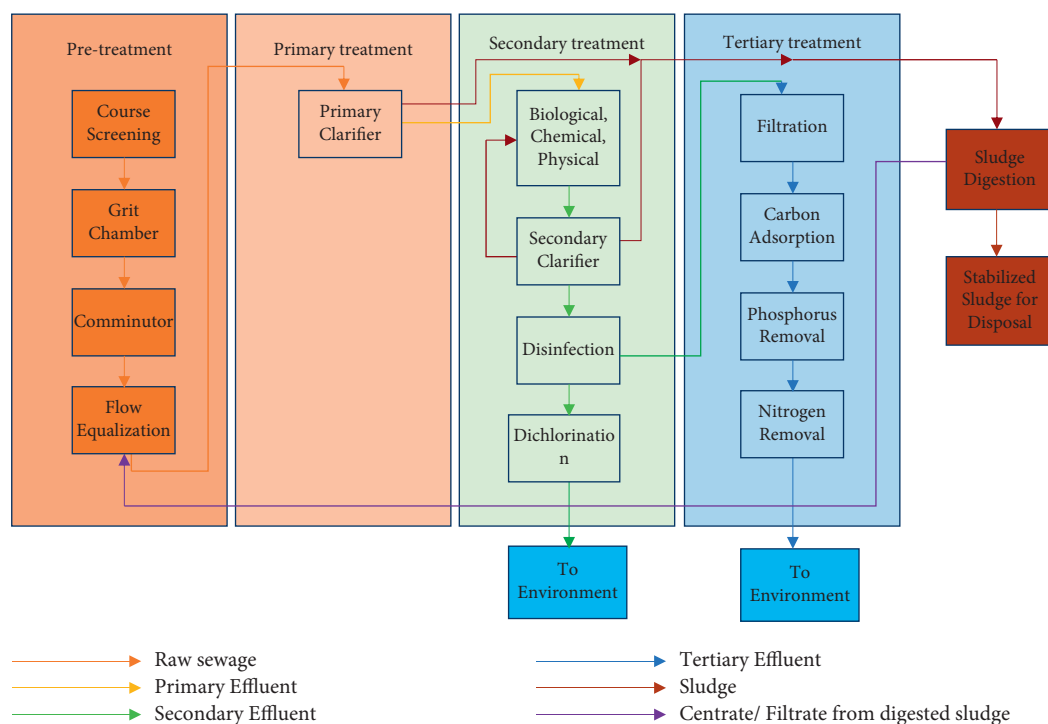
FIGURE 1: Summary of wastewater treatment steps.

TABLE 1: Percentage removal of pollutants at different stages.

| Stage	Method	% Removal					References
		COD/BOD	TSS	Pathogens	Nitrogen	Phosphorus	
Primary	Sedimentation	45%	70%	—	0–35%	0–35%	[46]
	Fine screen	45%	—	—	—	—	
Secondary	Primary clarifier	30.59%	50.61%	—	—	—	[51, 52]
	Aeration tanks	73%	80%	75%	60%	50%	
	Activated sludge	91.28%	86.76%	50–80%	>70%	>70%	
Tertiary	Activated carbon	85%	52%	95%	50%	60%	[52]
	Ion exchange	70–95%	35–85%	>80%	35–80%	35–80%	
	Disinfection	—	—	98%	—	—	

increasing need for sludge disposal. In a study by Li et al. [58], hydroxide precipitation method was used in the recovery of Zn ions achieving 70–80% removal, in a combined Fenton process.

Sulfide precipitation provides less soluble metal precipitates and offers potential for selectivity in heavy metal removal. This method is however used sparingly, due to difficulties in controlling sulfide dosage and dangers of toxicity in the case of excess sulfide. This form of precipitation can be achieved by the use of solid iron sulfide or calcium sulfide, aqueous ammonium sulfide, sodium sulfide or sodium hydrogen sulfide, or gaseous hydrogen sulfide [59]. Zainuddin et al. [60] studied the comparative adsorption of Ni, Cu, and Zn by hydroxide and sulfide precipitation and reported more efficient removal by sulfide. A 95.32% Ni removal was achieved using sulfide precipitation compared to 76.66% hydroxide precipitation removal. In another study, Li et al. [58] removed Ti ions to trace levels through combining Fenton process and sulfide precipitation. The Fenton process achieved an excess of 95% Ti ion removal, and the sulfide precipitation made the method further effective to bring the ion concentration to trace levels in industrial wastewater.

3.1.2. Biological Precipitation. Metal ions can be precipitated as a consequence of the metabolism of microorganisms either directly or indirectly when they produce metabolites that react with the metal ions to precipitate them. Biological precipitation has been reported to offer better selectivity in metal ion removal compared to chemical precipitation. For example, the metal precipitation of engineered systems is optimized according to the rate of biological sulfide production, the precipitation of metal sulfides, and the quality of the metal precipitate product. In addition, it is low cost, applicable in low-metal concentration leachates, and it provides better settling. It is however more complex to operate compared to the chemical precipitation method [61].

Sulfate reduction by bacteria is a common method applied in heavy metal precipitation in this genre. A carbon source such as acetate, hydrogen, or sulfate is utilized to produce a sulfide under anaerobic conditions, which reacts with a metal ion to form a precipitable metal sulfide [62]. This method has been applied in metal recovery from an acid mine drainage system [63]. The [54] mechanism is illustrated in the following equations:
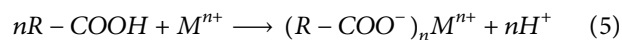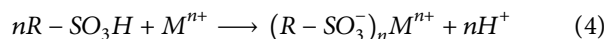
$$e^- \text{ donor} + SO_4^{2-} \longrightarrow S^{2-} + HCO_3^- \qquad (1)$$

$$S^{2-} + Me^{2+} \longrightarrow MeS_\downarrow + H^+ \qquad (2)$$
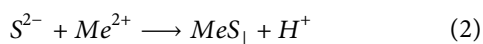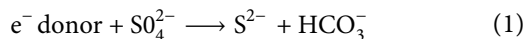
where e^- is an electron, Me^{2+} is a metal ion, and $MeS_\downarrow$ is the precipitated metal sulfide. In (1), sulfate-reducing bacteria act on the electron donor species, such as acetate, in a process to reduce the sulfate ions to sulfide ions. Organic compounds acting as electron donors are reduced to carbonates. In (2), the sulfide ion reacts chemically with dissolved heavy metal ions to produce precipitable metal sulfides that can be removed from the wastewater [62]. The process in (2) lowers the pH of the reaction medium due to the generation of high concentration of hydrogen ions. The acidity is neutralized through biogenic alkalinity resulting from equation (1). This is illustrated in equation (3) [64].

$$HCO_3^- + H^+ \longrightarrow CO_2(g) + H_2O \qquad (3)$$
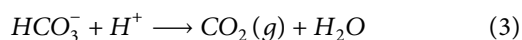
Another approach used in metal ion removal in biological precipitation is bioreductive precipitation, whereby the microorganisms utilize the metal ions in microbial metabolism. In this manner, metal-reducing bacteria take part in reducing the dissolved metal ions to precipitate. For example, uranium-reducing bacteria have been used in bioreducing uranium (VI) to uranium (IV) [65]. Some of these bacteria include denitrifiers, thermophilic bacteria, hyper thermophilic archaea, acid-tolerant bacteria, fermentative bacteria, and myxobacteria [64]. Some microorganisms are able to produce energy through bioreduction mechanisms by utilizing the metal as an alternative electron acceptor, while others reduce heavy metal cometabolically, in which case energy is not generated [66]. Growth of *Desulfotomaculum, Shewanella,* and *Geobacter* has been documented to increase with reduction of U6+ U4+, whereas *Desulfovibrio* shows cometabolic reduction when reducing U^{6+} [67]. Zhou et al. [68] used a hydrogen-based membrane in the removal of U^{6+} using a culture of *Desulfovibrio vulgaris* in which a sole electron acceptor of U^{6+} was fed. It was observed that the reactor performance increased to about 98% and then an almost complete reduction of U^{6+} occurred. Nanocrystalline UO_2 and U aggregates and precipitates were observed; authors associated them with vegetative cells.

3.2. Ion Exchange.

This method is used mainly due to its major advantages in high efficiency and fast kinetics of heavy metal removal [69]. Ion exchange resins, which can either be natural or synthetic, are employed in this method. Synthetic resins are preferable due to their high efficiency [70]. The following equations show an illustration of ion exchange resin with the sulfonic acid group and a carboxylic acid group:

$$nR - SO_3H + M^{n+} \longrightarrow (R - SO_3^-)_n M^{n+} + nH^+ \qquad (4)$$

$$nR - COOH + M^{n+} \longrightarrow (R - COO^-)_n M^{n+} + nH^+ \qquad (5)$$

In (3), the exchange resin based on sulfonic acid group can remove metal ion by exchanging the hydrogen ion on the sulfonic group. In equation (4), the exchange resin is based on carboxylic acid. In a scenario similar to equation (3), the hydrogen ion on the carboxylic group is exchangeable for the metal ion.

Alyuz and Veli [70] studied the kinetics of the removal of nickel and zinc, based on ionic exchange resins, and found that ion exchange was highly dependent on pH, temperature, contact time, and initial temperature of the solution, whereby the major removal was acquired in the pH range of 4–6 for zinc and nickel ions. Abo-Farha et al. [71] observed similar results with cerium, iron, and lead ions and concluded that the adsorption sequence was $Ce^{4+} > Fe^{3+} > Pb^{2+}$.

3.3. Adsorption.

The adsorption process is considered a thermal process that can occur physically or chemically. The adsorbate must adsorb to the pores of the adsorbent to be separated from the matrix through physical (physisorption) or chemical (chemisorption) processes [72]. During physisorption, van der Waals forces are the major players in the separation, while in chemisorption, separation relies on chemical interaction between the adsorbent and the adsorbate. Adsorbents fall under the following three classifications based on pore size: 2–5 nm pore sizes make up micropores, 5–50 nm make up mesopores, and 50–100 nm make up macropores [72]. This method of water purification is considered highly effective and economic since in many instances it results in highly purified effluents, in addition to being flexible in terms of design and operation [69].

Activated carbon is a commonly used adsorbent because of its high porosity; non-polarity; and made from carbon-rich materials of mineral, plant, or animal origin. The activation process can either be physical or chemical depending on the raw material and required texture. Physical activation mainly involves carbonizing the starting materials to about 450°C and then heating in carbon dioxide, air, or steam at temperatures of about 900°C at low pressures [72]. The porosity of activated charcoal can be as high as 2000 g/m³, making it very useful for the removal of inorganic, organic, and biological waste in water [73]. However, its nonpolarity makes it a poor remover of heavy metals. To remove heavy metals from water, activated charcoal has to be modified chemically by the use of chelating groups [74]. Activated charcoal comes in either granular activated charcoal form or powdered activated charcoal form.

Carbon nanotubes (CNT) are carbon-based tubular structures entirely made up of hexagonally arranged hybrid carbon atoms [75]. They can be single-walled if made up of a singular sheet of graphene or multi-walled if multiple layers of graphene make up the structure [76]. CNTs attract attention as adsorbents as a result of their inert surfaces and

high specific surface areas, making them excellent physical adsorbers. They have been of great interest due to well-defined and uniform atomic structure compared to activated carbons [75]. Alijani and Shariatinia [77] fabricated a single-walled CNT-based nanocomposite for the removal of mercury from wastewater and achieved 99.56% adsorption in about 7 minutes. Single-walled CNT alone was reported to achieve about 45.39% adsorption of mercury.

A summary of the removal efficiency and operational cost estimates of some of the methods discussed is summarized in Table 2 [84].

4. Adsorbents

According to Pandit et al. [85], adsorbents can be defined as solid materials that can remove or separate contaminants from liquids or gases to avoid environmental harm. The separation of contaminants is usually based on their selective binding, or adsorption, on the surface of the adsorbent. This selectivity can be kinetic and/or thermodynamic, based on the specific interaction between the adsorbent's surface and the contaminants. In this manner, there's an underlying complex interaction among these three components, namely the adsorbent, adsorbate, and wastewater [86]. The relationship is illustrated in Figure 2 [86].

In the ternary system illustrated in Figure 2, the main interaction that controls the entire adsorption system is between the adsorbate and the adsorbent. Other factors, however, come into play to affect this interaction, that is the affinity between the solution and the adsorbate, solution and the adsorbent, and the contaminants. Owing to low solubility, hydrophobic compounds in aqueous solutions are observed to get attracted to the surface of the adsorbent. Therefore, the adsorption capacity is considerably dependent on the forces that arise from the interaction of these three components [86]. Since the adsorption is by principle a surface phenomenon, any solid needs to be porous and possess a large surface area, to be considered an adsorbent. In addition, other considerations are based on: ready availability and low cost, great physical strength especially in solutions, good mechanical properties, ability to regenerate, and long life [87].

In order to ensure efficient contact between the adsorbent and the wastewater, different systems have been proposed and applied both at the industrial and laboratory level. Some of these methods include mobile mat filters, pulsed beds, fluidized beds, fixed bed-type processes, and batch methods. Depending on the application, the most common systems are fixed bed and batch-type processes. When a continuous system for contact is necessary, like in an industrial scale, the fixed bed-type contact system (reactor and columns) is applicable, while for laboratory-level experimentation, batch processes are usually applicable [88]. The batch processes are necessitated at laboratory scale due to their efficiency at small volumes of wastewater, ease of use, and simplicity.

In fixed bed reactors, adsorption is heavily dependent on the concentration of the adsorbate in the wastewater. The contaminated solution (wastewater) is always in contact with the adsorbate, which with continuous adsorption of the solute ensures continuous dynamism in the concentration of the adsorbate in the solution. This system offers great mass and heat transfer and greater residence times than any other batch reactor on the industrial scale [88]. Mat filters are often implemented as depth filters with the ability to separate contaminants from the liquid phase through sieving, interception, and adsorption [89]. They are referred to as depth filters because they not only filter on the surface but also in the interior pores through adsorption [90]. Due to the intimate contact, they introduce between the adsorbate and adsorbent in the liquid phase, they are most applicable when the influent contains high particulate matter [91]. Yigzaw et al. [90] and Shukla and Kandula [91] have utilized mat filters in biological sciences for antibody purification and recovery. For application in wastewater treatment, nanofibers have been used in mat filter fabrication to adsorb various heavy metals such as Cu^{2+} and Pb^{2+} [92].

In pulsed bed adsorption, the feed flows from the underside of the adsorbent material upwards. When the adsorbent is spent, it is removed from the bottom and refilled from the top (i.e., opposite the flow of the feed) to ensure a constant column height to maintain efficiency [93]. Pulsed bed adsorption is most preferable when the adsorbent and the feed are of a high relative performance rate. Fluidized beds are incorporated when high heat and mass transfer applications are required. Most sets incorporate adsorption and desorption sections to improve the efficiency of the process. During adsorption, a solid adsorbent is fluidized by the upward movement of the mobile phase influent, causing a downward "flow" of the adsorbent as a fluid. This increases contact between the phases and thus high adsorption is possible in this setup. The fluidized adsorbent falls to a lower desorption bed whereby desorption occurs through heat exchange and the adsorbent can be gased to the top of the column for cycling [94].

In an effort to control the liquid-phase adsorption performance in a solid material, a number of factors affect the adsorption process. Some of these factors include ([95] (1)) the nature and origin of the adsorbent solid. This includes the physical considerations such as the specific surface area, the particle size, and porosity; chemical considerations including the functional groups of the solid, surface charge, and pH when the solid has no charge; and mechanical properties. (2) Conditions necessary for the activation of the solid. These include considerations such as chemical or physical treatment to activate the material and the effects of the variables of the process applicable in the contacting system. These variables include the initial concentration of the pollutants, contact time, stirring rate, and solid dosage. (3) The mechanism of removal of the pollutants. This includes the conditions of the solution such as the temperature, pH, presence of impurities, among others.

Adsorbents have been classified to five categories according to Crini et al. [86]. This classification is based on the applications of the adsorbent in both the industrial setting and the applicability in laboratory practice. Natural materials are adsorbents that include wood, bauxite, sawdust, and fuller's earth. Treated natural materials are another classification that

TABLE 2: Removal efficiency and removal cost estimate of various methods.

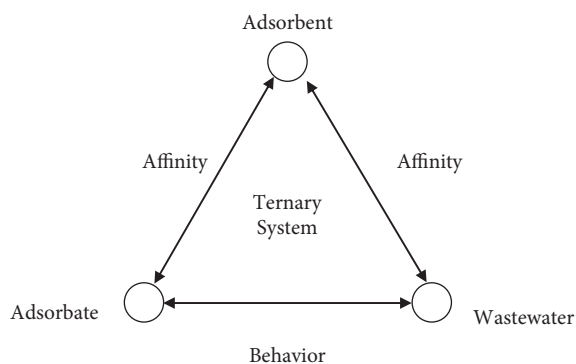| Method	Operational cost estimate per year (USD)	Removal efficiency		References
		Contaminant	Removal capacity (mg/g or%)	
Reverse osmosis	~17 million	Cu^{2+}	98%	[78]
		Cd^{2+}	99%	
		Pb^{2+}	99%	[79]
		Zn^{2+}	97%	
Nanofiltration	~17 million	Cu^{2+}	>90%	[80]
		As^{3+}	48%	
Ion exchange	3 million	Hg^{2+}	99.9%	[81]
		Ni^{2+}	99.9%	
Electrodialysis	150, 000	Fe^{2+}	>66%	[82]
		Ag^+	99%	
Granular activated carbon	74–209 million	Pb^{2+}	16.2 mg/g	[83]
		Cr^{3+}	638 mg/g	

FIGURE 2: Relationships of a three-component adsorption system.

include activated carbons, silica gel, or alumina. Manufactured materials such as zeolites, resins, and aluminosilicates are also among the adsorbent classification. Another type is the industrial by-products and solid agricultural wastes such as red mud and fly ash. The last type is the biosorbents that include fungi, chitosan, cellulose, among others.

4.1. Low-Cost Adsorbents. Agricultural wastes and biosorbents are termed low-cost adsorbents due to their abundant nature and they inexpensive and potential to act as complexing materials [95]. Chitosan occurs naturally in large amounts and is a low-cost sustainable adsorbent for waste water remediation [96]. It has been reported to bind effectively with small ionic diameter metal ions such as Cu (II) ions. To effectively remove larger ions, chitosan has been modified to improve its structural properties [96]. Hosseinzadeh and Ramin [97] used a magnetic chitosan/graphene oxide nanocomposite to remove copper ions from wastewater and reported a maximum adsorption capacity of approximately 217.4 mg/g.

Cellulose is one of the most abundant biopolymers that are biodegradable, insoluble in most solvents, and nonmeltable [98]. The most common commercial sources of this abundant material are wood and cotton but it is extractable from other credible sources. Cellulose exhibits low

adsorption in an unmodified state and to be utilized for heavy metal adsorption as a low-cost adsorbent, it often requires modification [98]. Dridi-Dhaouadi et al. [99] investigated the adsorption of lead (II) ion and yellow 44 dye by unmodified cellulose isolated from *Posidonia oceanica* and observed that the cellulose had higher adsorption for lead than for dye. Wu et al. [100] also investigated the adsorption of lead (II) ions on cellulose and reported optimum removal at a pH of 6 with a maximum adsorption capacity of 10.78 m²/g. The authors also reported that modification of the cellulose with thiol groups increased metal adsorption.

5. Clay

5.1. Structure and Properties. aClay essentially refers to soil particles of the size less than 5 μm or rock made up of clay minerals. Clay exhibits high plasticity when wet, and is considered coherent when dry [101]. In soil, it ensures proper porosity; good water retention; and acts as a reservoir for nitrogen, calcium oxide, and potassium oxide minerals [102]. Clay minerals are produced majorly through weathering, hydrothermal alteration, and diagenesis processes [102]. Clay minerals are structured to magnesia or alumina octahedral sheets and silica tetrahedral sheets (Figure 3). According to the arrangement of these sheets, clay minerals are classified into four main groups namely kaolinite, chlorite, illite, and smectite [103] and are shown in Figure 3 [104].

In kaolinite, the structure arrangement between the octahedral and tetrahedral sheets is in a ratio 1:1 and consists of kaolinite, halloysite, dickite, and anauxite. The charges between the two layers are usually balanced, and thus the clay does not swell. The chlorite group includes an extra brucite layer alternating with tetrahedral-octahedral-tetrahedral layers [105]. The illite and smectite form tetrahedral-octahedral-tetrahedral layers (i.e., 2:1 ratio) joined to each other by hydrogen bonding and electrostatic forces [103]. The smectite group, consisting of bentonite and montmorillonite (MMT), exhibits a higher swelling capacity than illite. For application in heavy metal removal, the clay
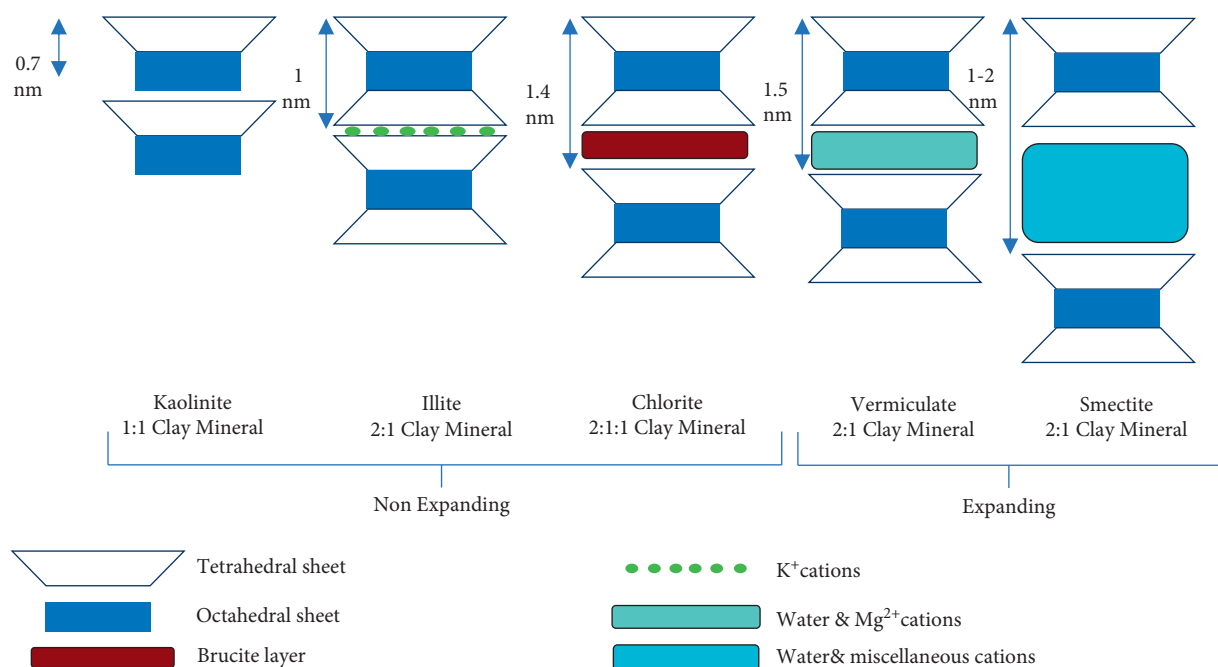
FIGURE 3: Classes of clays according to structural arrangement (Ghadiri et al., 2015).

mineral needs to have a high cation exchange capacity (CEC) and a specific surface area. CEC is a characteristic quality of soil to hold positively charged ions [106]. Karpiński and Szkodo [105] reported that the smectite group has a higher CEC (80–150 meq/100 g) and a specific surface area (800 m^2/g) compared to illite (10–40 meq/100 g, 15 m^2/g). Kaolinite was reported to have the lowest CEC.

Clay on its own has been applied in heavy metal removal by various researchers. Kaolinite in raw and modified forms has been used in the removal of chromium (VI) ions, and adsorption has been reported to be highly sensitive to the pH of the solution, with increasing adsorption from pH 1 to 7 [107]. Montmorillonite clay has also been used in the removal of lead (II) ions in its raw form and maximum adsorption is reported to be about 28 mg/g [108]. In modified form, montmorillonite was reported to increase metal ion adsorption to 131.579 mg/g owing to an increase in active sites with modification by acetic acid [109]. Bentonite has been applied in the removal of various heavy metal ions including copper (II), cobalt (II), nickel (II), and lead (II). The highest adsorption capacity of lead (II) by unmodified bentonite is 59.7 mg/g and in modified form is 123.3 mg/g [24]. Al-Jlil [110] reported that the maximum removal of chromium (III) by raw bentonite was 13.79 mg/g and in a modified state of 4-*aminoantipyrine*, the adsorption capacity was 38.8 mg/g.

5.2. Types of Nano-Clay-Based Adsorbents. Clay is employed as a nano adsorbent in several adsorption procedures due to its unique characteristics and high removal effectiveness [111]. Nanoclays are a potential property enhancer that has been discovered to be super effective in the purification of water. A large number of researchers have investigated the use of clay minerals as adsorbent materials for the adsorption of different hazardous substances such as heavy metals, coloring

agents, antibiotics, biocide substances, and other organic chemicals. Nano adsorbents are made up of nanoparticles with a large specific surface area and connected sorption sites. The sorbent exhibits better adsorption for organic chemicals due to the short intra-particle dispersal distance and adjustable pore size and surface chemistry.

5.2.1. 1D Clay Nano Rods. Attapulgite (APT) is a one-dimensional (1D) clay that is natural with a structure comparable to carbon nanorods. Awasthi et al. [112] suggest that the APT is made up of 2 : 1 phyllosilicate ribbons, with interspaces between them measuring around 0.4 nm × 0.6 nm. Natural APT has a good adsorption capacity for dyes and heavy metals, thanks to these zeolite-like nano channels. Because of the hydrogen bonds and Van der Waals force, natural APT exists as mass aggregated crystal bundles that inhibit dye macromolecules from reaching efficient interaction with sites that are active sorption. The fabrication of 1D APT nanorods by shattering bulk bundles has sparked a lot of curiosity lately. The permanent inherent negatively charged electrode and specifically large surface area of disintegrating 1D APT nanorods enabled the development of adsorbents that were 1D APT based.

They can develop hybrids with materials that are 2D layered depending on different 1D morphology of APT nanorods to acquire the highly customizable framework for making full use of the properties of nanorods and nanosheets. Clay/APT nanocomposites were made by mixing 1D APT with 2D bentonite nanosheets using homogenization of a high-pressure. When APT was added, the rate of hydration of bentonite and salt resistance improved, resulting in a higher dosage of MB adsorbent in the presence of sodium chloride. [113] developed a ceramic-supported composite film of attapulgite/graphene oxide (GOA) with 1D APT

inserted into 2D lamellar GO sheets, allowing high-flux water transport through nano channels. The prepared GOA showed about 100% disapproval efficacy against Ni^{2+}, Cd^{2+}, Pb^{2+}, and Cu^{2+}. This was due to the size exception effect, that was based on nanotube correlation between the GO layers formed by 6 APT nanorods.

5.2.2. 2D Clay Nanosheets.

Clay minerals are mostly made up of 2D nanosheet units, which are made up of a set of neatly stacked layers [114]. Strong interactions such as hydrogen bonding combine neighboring 2D nanosheet units, while Van der Waals weak forces combine adjacent 2D nanosheet units. Such clays have strong adsorption capability due to the unique interlayer space, that has been extensively used in the pollutant removal from wastewater. However, because the various sites of adsorption on the interior surface have not yet been fully explored, the effectiveness of lamellar clay as an adsorbent is diminishing when used immediately. Exfoliated 2D clay nanosheets were able to totally release active adsorption sites and considerably increase the surface area, both of which are beneficial to improving adsorption performance. Because of its good hydration swelling property, montmorillonite clay can be easily exfoliated into 2D nanosheets. The fabrication of a range of sophisticated functional nanocomposites using 2D MMT nanosheets (MMTNS) with completely visible sites that are active following exfoliation has further pushed the use of MMT as adsorbents. According to El Kassimi et al. [114], the hydrogel phase with three-dimensional macroscopic nanostructures is particularly helpful for simple solid-liquid separation succeeding in removing contaminants from liquids, among the many MMTNS-based adsorbent materials. Also, the hydrogel's ion diffusion velocity is comparable to that of water, resulting in faster adsorption kinetics. As a result, hydrogels are becoming an interesting topic in search of adsorbents that are novel and can effectively remove pollutants from water.

El Haouti et al. [115] created a new self-assembled gel for the removal of MB under the influence of H_2O_2 under visible light. The Fe-CS/MMTNS gel with iron demonstrated outstanding reuse and maintaining quality MB removal efficiency attributed to the synergistic impact of reaction of Fenton and adsorption degradation. Due to the complex formation between iron and chitosan, the Fe-CS/MMTNS is stable and operates well across a wide pH range attributed to the prevalence of hydroxyls on the surface of MMTNS (CS).

5.2.3. Clay-Supported Nanoparticles as Composites.

Nanoparticles (NPs) are a form of adsorbent that uses nanoscale effect, extremely high surface area, and reactivity to remove contaminants from water. NPs are tiny atomic clusters that are less than 100 nanometers in size. Although NPs have a larger capacity of adsorption than micron-sized counterparts because of their nano size-particle distribution, NPs are more afflicted to clustering in water because of their increased energy of the surface, which reduces effective sorption. As a result, the main hurdles in the use of nano adsorbents are ensuring NP disposability after adsorption in

liquid/solid dissociation and water. Masoudi et al. [116] developed nanoscale Fe_2O_3-treated halloysite nanotube (HNT) adsorbents for treating excess phosphate in water and preventing eutrophication. The surface charge density of treated iron oxide was observed to boost the capacity of adsorption of the nano adsorbent toward phosphate. To remove dyes, Rafati et al. [117] used a carboxymethylcellulose-bentonite (LCB) composite loaded with lanthanum (La). By crosslinking clay and polymer, the addition of La^{3+} strengthened the framework. In the field of geo-engineering, Phoslock®, a type of lanthanum (La)-modified bentonite clay, has been utilized to regulate oxyanions in waste streams and sediments.

5.2.4. 1D Clay Nanotubes.

Halloysite nanotubes (HNTs) represent one-dimensional tubular clay. Such naturally present nano-minerals are gaining favor as low-cost options to produced nanotube substances like carbon nanotubes, thanks to the exceptional properties of a 1D tubular structure. Shapira and Zucker [118] created an Ag_3PO_4-HNT adsorbent for the treatment of polluted water. The adsorbent produced was capable of adsorbing soluble dyes and medicinal compounds on HNT, which were subsequently photocatalyzed by Ag_3PO_4 and destroyed in visible light. Zhang et al. [111] created a redox-participating HNT-CeOx($x = 1.5$–2.0) nanohybrid. Electrostatic interaction uniformly coated CeO_2 nanoparticles on the HNT substrate, greatly increasing the adsorption capacity of As (III) (209 mg/g) compared to unsupported CeO_2 nanoparticles (62 mg/g).

5.3. Clay-Based Nanocomposites as Adsorbents.

Nanocomposites have been reported to possess high porosity and immense surface area making them excellent candidates for heavy metal removal [24]. The most important properties for good adsorption (porosity, active surface area, CEC, pore volume among others) are enhanced by one or more components of the nanocomposite [24]. Clay polymer-based nanocomposite adsorbents such as cellulose-montmorillonite [119], polyaniline-montmorillonite [120], poly (acrylic acid)/organo-montmorillonite [121], and β-cyclodextrin based bentonite [122] have been reported.

Irani et al. [123] synthesized an organomontmorillonite hydrogel nanocomposite for the removal of lead (II) ions and reported a maximum removal capacity of 430 mg/g. Other researchers have also reported lead (II) ion removal by use of clay-based nanocomposites [124, 125]. On the chitosan-clay nanocomposite, the maximum adsorption of cadmium (II) ions was reported to be approximately 72.31 mg/g by Tirtom et al. [126]. The maximum adsorption of chromium (III) ions was reported to be about 0.25 mg/g on a similar chitosan-clay nanocomposite [127].

Copper (II) ion removal has previously been investigated by the use of various nanocomposites [125, 128–130] and the maximum adsorption reported to be about 106.2 mg/g when polyacrylamide-bentonite (PAA-B) nanocomposite modified with humic acid-immobilized-amine [128]. In a different study, the adsorption capacity was observed to increase from 11 mg/g to 20 mg/g in PAA-B when the pH of the solution was reduced from 6.2 to 5 [131].

Removal of nickel (II) ion has also been studied and reported by various researchers [126, 132–134]. Tirtom et al. utilized an epichlorohydrin crosslinker in chitosan-clay nanocomposite in a study to comparatively adsorb nickel (II) and cadmium (II) ions. According to the Langmuir isotherm, Ni^{2+} removal was reported to be 32.36 mg/g and 72.31 mg/g for Cd^{2+}. Zhang and Wang [134] used a low-cost lignocellulose/montmorillonite nanocomposite to adsorb nickel (II) ions from synthetic wastewater. At a solution temperature of 70°C and a pH of 6.8, the ion's adsorption was reported to reach 94.86 mg/g. García-Padilla et al. [132] reported high nickel (II) adsorption (97.1%) at a pH of 4.5 using starch/sodium montmorillonite nanocomposite.

Other reports are summarized in Table 3.

6. Adsorption Studies

6.1. Factors Affecting Adsorption. For a fixed amount of the adsorbent, an optimum concentration of the ion to be removed is required. When the initial ion concentration is low, adsorption tends to be slow. Increasing the initial ion concentration increases the adsorption rate, up to a certain point, beyond which removal decreases. This is attributed to the flooding of metal ions for an unchanging number of adsorption sites [139]. In agreement with this, Hassana and Shaban [140] reported that Fe^{3+} adsorption onto kaolinite increased with an increase in initial metal ion concentration. Sallam et al. [141] in a study to remove Cr^{6+} ions from tannery wastewater reported the highest removal ranging from 76.3% to 100% occurring with initial metal ion concentrations ranging from 10 to 50 mg/L. This illustrated that metal ion removal occurred best with relatively high initial concentrations.

At low pH, hydrogen ions are abundant in the solution, and thus they compete with metal ions for active sites on the adsorbent, thus lowering the adsorption of heavy metal ions. Research conducted by [142] to investigate the effect of pH on Hg (II) found that an increase of pH from 2 to 5 had increasing Hg adsorption. Similar studies on the removal of lead and copper by Razzaz et al. [92] found more removal at pH 6 and least at pH 2 to 4. Zhao et al. [131] studied the removal of Cu^{2+} ions using bentonite-polyacrylamide composite and reported a massive removal increase from 9% to 97% as pH was increased from 2 to 7. Cadmium removal maxed out at pH 9 in a study conducted by Kim et al. [143], achieving adsorption of 97%. Studies by Ravikumar and Udayakumar [144] also agree to this phenomenon for the removal of Cd^{2+} and Pb^{2+} achieving maximum metal ion removal at a pH of 6 for both of them, using *Moringa oleifera*/montmorillonite nanocomposite. Beyond this pH, the metal ions seemed to precipitate. In the same study, Cr^{6+} ion adsorption disagreed with this phenomenon and showed high adsorption at low pH values of 2 and 3. This was because the ions in solution existed as polyanions of $HCrO_4^-$, CrO_4^{2-}, and $Cr_2O_7^{2-}$ at low pH. Xu et al. [145] agreed with this in a similar investigation.

Concerning contact time, heavy metal ions in contact with the nano adsorbent enhance the adsorption. At the initial stage, adsorption will occur quickly because of the abundance of active sites and later slow down to a point where the adsorption is independent of the contact time. At this point, the system has reached an equilibrium between the adsorption and desorption processes [139]. A study by Jiang et al. [146] on heavy metal adsorption by kaolinite clay reported high initial heavy metal ion removal within the first 30 minutes that gradually achieved equilibrium. It was also observed that the rate of removal was ion dependent with percentage removal represented as Pb (II) > Ni (II) > Cd (II) > Cu (II) ranging from highest removal to lowest. Masheane et al. [147] used a chitosan-based nanocomposite to remove chromium and nitrate ions and reported rapid ion removal in the first 30 minutes of application. The activity was insignificant by the 60th minute which translated to a rapid saturation of active sites of adsorption on the nanocomposite material.

Temperature initially affects the viscosity of the solution, enhancing the diffusion rates of the heavy metal ions. An increased temperature can affect the adsorption process depending on whether the mechanism is exothermic or endothermic. In the case of exothermic adsorption, an increase in temperature will decrease the rate of adsorption due to the effect of heat on electrostatic interactions between the metal ions and the adsorbent in addition to desorption attributed to high ion mobility due to elevated temperatures [142]. In the case of endothermic adsorption, an increase in temperature enhances adsorption. This is attributed to increased ion mobility that results in greater access to active sites [148]. Murithi et al. [149] reported an increase in adsorption of cadmium (II) ions with an increase in temperature from 20°C to 43°C beyond which removal decreased, using the biomass of water hyacinth roots. This implied an endothermic adsorption process. Zhao et al. [131] reported Cu^{2+} adsorption increase with an increase in temperature of solution attributing it to a decrease in the ionic strength of the solution as the temperature rose.

6.2. Adsorption Isotherm Models. Isotherms describe the effect of concentration on metal ion adsorption at a constant temperature. The most common isotherm models used to describe adsorption isotherms are the Langmuir and Freundlich models [139]. Others are Temkin and Dubinin-Radushkevich, well discussed by Dada et al. [150].

Langmuir's model, depicted in the following equation [151], describes adsorption in the case of a monolayer surface with equivalence in the affinity of the adsorbate ions.

$$\frac{C_e}{q_e} = \frac{1}{Q_0 b} + \frac{C_0}{Q_0},$$ (6)

where q_e represents the amount of metal ion adsorbed (mg/g), C_e is the equilibrium concentration (mg/L), Q_0 represents the adsorption capacity (mg/g) and b is the Langmuir's constant (L/mg). The slope and intercept of the plot of (C_e/q_e) to C_e give $1/Q_0$ and $1/Q_0 b$, respectively.

In the case of heterogeneous adsorption, whereby adsorbent surface texture matters, the Freundlich model is considered. It is represented by the following equation [152]:

TABLE 3: Previous reports on heavy metal removal by clay-based nanocomposites.

Clay-based nanocomposite	Polymer used	Metal removed	Adsorption capacity (mg/g or %)	Observations	Reference
2-Aminophenol and 2-nitrophenol/iron montmorillonite	2-Aminophenol and 2-nitrophenol	Fe (III) Fe (II)	29% (adsorption area) 71% (adsorption area)	At high ranges of pH, reduction occurred in the phenolic ring.	[135]
β-Cyclodextrin/bentonite	β-cyclodextrin	Cu (II) Zn (II) Co (II)	94% 98% 92%	Metal concentration was 20 mg/L	[122]
Ion-imprinted polymer/diazonium montmorillonite	Cu (II) imprinted polymer	Cu (II)	23.3 mg/g	Adsorption capacity maxed out at pH 5.	[136]
Polyacrylamide/sodium montmorillonite nanocomposite	Polyacrylamide	Co (II) Ni (II)	98.67% 99.30	Highest removal of Ni (II) occurred at a pH of 7 and Co (II) at pH 6	[137]
Modified montmorillonite/polyethersulfone-mixed matrix membrane	Polyethersulfone	Zn (II) Ni (II)	88.9% 74.4%	Highest removal was achieved with 3% clay mixture into the polymer matrix	[138]

$$\log q_e = \log K_f + \frac{1}{n}\log C_e, \qquad (7)$$

where K_f and n represent Freundlich constants that correspond to heterogeneity and the bonding energy, respectively. These values arise from the intercept and slope of the plot of $\ln q_e$ to $\ln C_e$, respectively.

The Sip isotherm model exists to cross between the Freundlich and the Langmuir's isotherm models. It combines them through linear (8) [153]. A low concentration in this model describes adsorption in terms multilayer coverage, or Freundlich, while a high concentration describes adsorption in monolayer coverage, or Langmuir.

$$\frac{1}{q_e} = \frac{1}{Q_{max}K_s}\left(\frac{1}{C_e}\right)^{(1/n)} + \frac{1}{Q_{max}}, \qquad (8)$$

where K_s, given in L/mg, is described as the adsorption affinity and n is the heterogeneity index. These two values are derived from plots of $(1/q_e)$ against $(1/C_e)^{(1/n)}$.

The Dubinin-Radushkevich (D-R) adsorption isotherm is modeled to describe adsorption in terms of porosity and free energy. Its major purpose is to differentiate the adsorption mechanisms as either physisorption or chemisorption. This model is described as follows [154]:

$$q_e = Q_{DR}\exp\left(-K_{DR}\left[RT\ln\left(1 - \frac{1}{C_e}\right)\right]^2\right), \qquad (9)$$

$$\ln(q_e) = \ln Q_{DR} - K_{DR}\left[RT\ln\left(1 + \frac{1}{C_e}\right)\right]^2, \qquad (10)$$

where q_e in mmol/g represents the amount of metal ions adsorbed at equilibrium. Q_{DR} in mmol/g describes the maximum adsorption capacity at equilibrium. K_{DR} in mol^2/kJ^2 is usually a constant referred to as the Dubinin-Radushkevich constant. C_e in mol/dm^3 is the quantity of the metal ion adsorbed at equilibrium. (9) and (10) describe only the porosity aspects of the model and therefore are not conclusive on their own. An additional (11), therefore, relates the K_{DR} value to free energy [155].

$$E = \frac{1}{\sqrt{2\,K_{DR}}}. \qquad (11)$$

The values of E are useful for estimating the type of adsorption that occurs. When $E < 8$ Kj/mol, the adsorption is described as physisorption. When $E > 8$ kJ/mol, the adsorption process is described as chemisorption [153].

Temkim isotherm model has the implication that the heat of adsorption is describable linearly, rather than logarithmically. This model ignores the extremes of very high or low concentrations. Among other factors, consumption is also uniform in distribution of boundary energy up to certain limits described as maximum bonding energy [155]. This model is described by

$$q_e = B\ln A + B\ln C_e. \qquad (12)$$

In addition to the common parameters in isotherm models, B introduced in the Temkim model is a constant that is relatable to the heat of adsorption by the following equation:

$$B = \frac{RT}{b}, \qquad (13)$$

where b (J/mol) and A (L/g) are Temkim constants arising from slopes (B) and intercepts ($B\ln A$), respectively, of the plot of q_e versus $\ln C_e$ [155].

Sharma et al. [156] studied adsorption isotherms using both Langmuir and Freundlich model at a pH of 6 and a temperature of 25°C for a period of 2 hours. The authors reported the adsorption to be best described by the Freundlich model owing to the highest correlation coefficient values for all the studied heavy metal ions (Pb^{2+} and Cd^{2+}). Sallam et al. [141] used Langmuir, Freundlich, and Temkim isotherm models for adsorption of Cr^{6+} and reported that the adsorption was best described by the Freundlich model. This meant that the ion adsorbed onto

heterogeneous areas using different binding energies. Additional literature is summarized in Table 2.

6.3. Adsorption Kinetics.

Adsorption kinetics tries to describe the adsorption based on time and metal ion concentration. Various models have been used to describe adsorption kinetics, among which are pseudo first- and second-order, double exponential, and intra-particle diffusion [139].

Pseudo first-order is described as follows [136]:

$$\log (q_e - q_t) = \log q_e - \frac{k_1}{2.303} t. \tag{14}$$

The integrated rate of pseudo second-order equation is illustrated as follows [141]:

$$\frac{t}{q_t} = \frac{1}{k_2 q_e^2} + \frac{t}{q_e}. \tag{15}$$

In (5) and (6), q_t represents adsorption capacity, at time, t. q_e represents adsorption at equilibrium, given in mg/g. k_1 and k_2 are pseudo first-order and second-order rate constants, respectively, given in min^{-1}. T is the contact time in min. The intercept and slope of $\log (q_e - q_t)$ versus t for pseudo first-order gives the q_e and k_1 values, respectively. In the case of pseudo second-order, the intercept and slope of the plot of (t/q_t) versus t gives k_2 and q_e (equilibrium adsorption capacity), respectively.

The intra-particle diffusion model describes the adsorption of ions from the solution to the surface of the adsorbate and diffusion into the interior of the pores. It is represented in (15) [157].

$$q_t = K_{id} t^{0.5} + C, \tag{16}$$

where q_t represents the adsorption capacity at time, t. $t^{0.5}$ represents the half-life time given in seconds. K_{id} represents intra-particle diffusion rate constant in m/g·min$^{0.5}$. The boundary thickness is represented by C. The values of C and K_{id} are given by the intercept and slope of the plot of q_t versus $t^{0.5}$.

Previously reported adsorption parameters are summarized in Table 4.

Sharma et al. [156] used pseudo 1st order, pseudo 2nd order, and intra-particle diffusion to study the adsorption kinetics of mesoporous ZnO and TiO_2@ZnO monoliths and reported the adsorption kinetics best fitted the pseudo second-order kinetics. This translated to the fact that the adsorption mechanism of the metal ions was mostly chemisorption. Sallam et al. [141] used many kinetic models to study Cr^{6+} adsorption and reported that the adsorption kinetics best fit the pseudo second-order model with a very high correlation coefficient. This meant that the adsorption was most likely based on chemisorption mechanism.

6.4. Thermodynamics of Adsorption.

Thermodynamically, adsorption can be described as either endothermic or exothermic. An increase in adsorption with an increase in temperature presents an endothermic process, while a decrease in adsorption with increasing temperature describes exothermic adsorption [163].

Adsorption thermodynamics behavior can be determined using Gibb's energy, enthalpy, and entropy [164].

$$K_d = \frac{C_A}{C_B},$$

$$\Delta G^0 = -RT \ln K_d, \tag{17}$$

$$\ln K_d = \frac{\Delta S^0}{R} - \frac{\Delta H^0}{RT},$$

where K_d represents thermodynamic equilibrium constant, T is the absolute temperature in Kelvin, R universal gas constant, C_A and C_B the concentration of the adsorbate on the adsorbent and residual concentration at equilibrium, respectively [163].

A negative ΔH^0 represents an endothermic adsorption process, while a positive value represents exothermic adsorption. Negative ΔG^0 hints at spontaneous adsorption, which interprets that the adsorption is possible at any temperature. A negative ΔS^0 hints at low randomness at adsorption [163].

Sharma et al. [156] reported the adsorption of Pb^{2+} and Cd^{2+} ions on ZnO and TiO_2@ZnO monoliths to be endothermic and spontaneous in respect to a negative Gibb's energy and a positive enthalpy. They also reported positive values of entropy due change of energy between the monoliths and the metal ions adsorbed. Other reports on thermodynamic adsorption parameters are summarized in Table 5.

7. Analytical Techniques

7.1. Scanning Electron Microscopy and Transmitted Electron Microscopy.

Scanning electron microscopy (SEM) and transmission electron microscopy (TEM) are extremely essential techniques to understand the surface, morphological, and chemical interactions of materials. Both methods work differently, but the common feature between them is an electron lamp, electron apertures, and electromagnetic lenses.

SEM scans the samples in a raster fashion, detecting backscattered electrons and reflected electrons to give data about the surface of the material. It is limited to a scan area of 0~5 nm. The sample needs to be positioned at the end of the apparatus for quality scanning. TEM functions by detecting the electrons that pass through (transmit) the sample. Due to the nature of the electron, the samples need to be very thin, typically less than 150 nm. For the SEM analysis of clay-cellulose nanocomposite, clay particles are expected to be coarsely aggregated in the matrix. Mirsafaei and Kolahdoozan [167] analyzed the morphology of the poly (amide-ester-imide)/sodic montmorillonite nanocomposite using SEM and observed polymer particles inserted "crystallographically regular" in the clay structure.

TABLE 4: Previously reported adsorption parameters of clay polymer adsorbents.

Adsorbent	Metal ion	Modifying agent	Optimum parameter	Adsorption capacity (mg/g)	Isotherm	Kinetic model	References
Poly (acrylic acid)/ attapulgite nanocomposite	Pb (II)	Acrylic acid	pH = 5	38.0 mg/g	Freundlich	Pseudo 2nd order	[158]
Bentonite cellulose nanocomposite	Cu (II)	L-cysteine	Temperature = 50°C	32.37 mg/g	Langmuir	Pseudo 2nd order	[159]
Cysteine/ Montmorillonite nanocomposite	Pb (II)	Cysteine	—	0.180 mg/g	Freundlich	—	[160]
Sepiolite polymer nanocomposite	Cu (II)	Vinyltriethoxysilane	pH = 5.4	86%	—	Pseudo 2nd order	[161]
Polyetherimide/grafted bentonite membrane	Pb (II) Cd (II)	Polyetherimide	Membrane porosity = 62.7% Water uptake = 71.3%	80% (Pb ion) 76% (Cd ion)	Langmuir	Pseudo 1st order	[162]
Ion-imprinted clay/ polymer nanocomposite	Pb (II)	Visible light initiation	pH = 6.5	301 mg/g	Langmuir	Pseudo 2nd order	[136]

TABLE 5: Thermodynamic parameter of various clay polymer-based heavy metal adsorbents.

Adsorbent	Adsorbate	T (K)	ΔG^o (kJ/mol)	ΔH^o (kJ/mol)	ΔS^o (J/mol/K)	References
Polyacrylamide/bentonite hydrogel nanocomposite	Pb (II)	303	−5.81	1.42	20	[165]
		313	−6.02			
		323	−6.29			
	Cd (II)	303	−5.11	9.34	40	
		313	−5.58			
		323	−6.06			
Cellulose-montmorillonite nanocomposite	Cr (III)	298	−3.434	90.07	313.02	[119]
		308	−6.455			
		318	−9.685			
Cellulose-montmorillonite nanocomposite	Cu (II)	293	−6.796	−40.456	−116.81	[166]
		303	−4.308			
		313	−3.794			
		323	−2.356			
			−2.041			
	Cd (II)	293	−5.243	−29.639	−86.216	
		303	−2.243			
		313	−2.145			
		323	−2.794			
		333	−0.792			

SEM data are important in the analysis of surface characteristics of materials [168]. Data arising from TEM are important in detecting the internal workings of a sample inclusive of crystal structure, morphology, and stress state. TEM has been reported to achieve extremely low optical spatial resolutions of less than 50 pm [169].

Sallam et al. [141] used SEM technology to characterize a polymer-clay nanocomposite and reported smooth surfaced sticking particles that were associated with the polymerization process. The authors used XRD and FTIR techniques to describe further characteristics of the material. Khan et al. [170] used TEM to observe the structure of polyacrylamide/ bentonite hydrogel nanocomposite. The authors reported complete random exfoliation of the bentonite particles. This was so because ultrasonic synthesis was applied during the fabrication of the nanocomposite. The SEM data from the same researchers for the raw and nanosized bentonite clay

had rougher texture compared to the hydrogel nanocomposite, which showed uniform texture on the surface which did not agglomerate. Other reports on SEM and TEM analysis have been summarized in Table 6.

7.2. X-Ray Diffraction. X-ray diffraction (XRD) was developed to characterize materials by analyzing the crystalline structure of the material [175]. The principle of operation is that when a high-energy electron beam displaces an electron from the inner shell of an atom, the outer shell electron cascades to fill the gap left releasing energy in the form of x-rays. These x-rays are measurable and result in structural data of the lattice [176]. Two methods exist to excite the electrons on an atom. One method makes use of an electron beam, as is used in scanning electron microscopes. The second method makes use of x-rays, known as energy-

TABLE 6: Summary of SEM and TEM observations for clay-based nanocomposites.

Method	Material	Synthesis method	Observations	References
SEM and TEM	Polypropylene-Polypropylene-grafted-maleic anhydride-montmorillonite clay nanocomposites (PP + PP-g-MA/MMT)	Melt mix extrusion	(i) Foaming cell size decreases as cell density increases with increase in MMT content.	[171]
	Physically crosslinked polyvinyl alcohol/bentonite nanocomposite hydrogel	Freeze-thawing technique	(ii) Pore walls thicken in the nanocomposite compared to lean PVA	[172]
	Polyaniline-clay hybrid nanocomposite (PANI/Clay)	In situ polymerization	(iii) Denser regions indicating intercalation of polymer	[173]
	Post-consumer propylene/Tunisian clay nanocomposite (PCPP/Clay)	Twin-screw extrusion	(iv) Clay finely distributed in the polymer matrix,	[174]

dispersive x-rays (EXD). Whichever the source, interactions within the atoms remain the same. If the emitted rays obey Bragg's law illustrated in equation (17), the waves reflect constructively thus amplifying their signal [177]. Energy-dispersive x-ray diffraction is very sensitive to the texture of the material to be analyzed. A poorly textured sample results in noisy data, making it difficult to identify crystal lattices. The main considerations for the sample are stability in vacuumized environments and sample contamination [177]. Kumar et al. [119] used EXD to authenticate the adsorption of Cr (III) ions on the surface of the cellulose-clay nanocomposite. XRD patterns from the same study indicated the crystalline structure of the composite.

$$n\lambda = 2d \sin \theta. \tag{18}$$

In a study by Rafiei et al. [178], a poly (acrylic acid)/bentonite nanocomposite was characterized using XRD, and the interpreted diffractograms translated that polyacrylic acid (PAA) and cetyltrimethylammonium (CTA) surfactants had evenly intercalated in the mineral layers of montmorillonite of the bentonite clay. The structure of the material was therefore an intercalated nanocomposite. XRD diffractograms for bentonite clay analyzed by [165] have shown a basal peak corresponding to montmorillonite in a study to synthesize a clay-hydrogel nanocomposite for Pb^{2+} ad Cd^{2+} removal. This basal peak was reported to disappear in the diffractogram of the nanocomposite due to exfoliation of the clay structure. Other reports on XRD analysis are summarized in Table 7.

7.3. Fourier Transform Infrared Spectroscopy (FTIR). The infrared region of the electromagnetic spectrum spans between 12800 cm^{-1} and 10 cm^{-1}. It is therefore divided into three categories, namely near-infrared region (12800 ~ 4000 cm^{-1}), middle infrared region (4000~200 cm^{-1}), and far-infrared region (50~1000 cm^{-1}). Since IR spectroscopy depends on vibrational movements of molecules with dipole moments, homonuclear diatomic molecules are not detectable with this method. The technique works on the mechanism that when infrared energy is irradiated through a sample, molecules absorb the energy at various wavelengths, and some transform to excited states. The wavelengths at which the absorption occurs are detected and peaks tabulated. Molecules can have multiple absorption peaks based on the vibrational freedom in the molecules [180]. Organic

and inorganic peaks are mostly found within the 4000 ~ 400 cm^{-1} region [180]. To characterize polymer-clay nanocomposites, it is important to analyze lean clay first to detect clay peaks, corresponding to Si–O bonds. Peaks are expected to sharpen when an intercalant is added to the clay matrix [181]. Cole [181] used this method to study the degree of intercalation between propylene and montmorillonite clay particles.

In the study by Rafiei et al. [178], FTIR technique was also used in the characterization and it confirmed the XRD data that the CTA and PAA functional groups had intercalated into the clay interlayers. Unuabonah et al. [182] fabricated a PVA-modified kaolinite clay nanocomposite for the removal of Pb^{2+} and Cd^{2+} ions, and the FTIR analysis of the material shows the presence of –OH functional groups on its surface. Adsorption criteria were shown to be based on "inner-sphere surface complexation mechanism," according to FTIR data, and this increased metal ion adsorption almost three times [144]. In an FTIR characterization of polyacrylamide/bentonite hydrogel synthesized for the adsorption of Pb^{2+} and Cd^{2+}, it was reported that a C–N group peak observed prior to heavy metal adsorption shifted to a lower wave number with decreased sharpness when loaded with heavy metal ions. This illustrated an interaction between heavy metal ions and the C–N functional group in the nanocomposite [165]. Other reports in FTIR analysis are summarized in Table 8.

7.4. Thermogravimetric Analysis. Thermogravimetric analysis (TGA) is a method used to investigate the changes in mass of a material owing to thermodynamic reactions taking place in the material. The mass of the investigated material is continuously monitored as the temperature changes over time. Thereby, physical parameters, such as desorption, adsorption, absorption, and phase transitions, and chemical parameters, such as solid-gas reactions, thermal decomposition, and chemisorption, are investigated [185]. Three types of TGA exist as isothermal, quasistatic, or dynamic thermogravimetry. Isothermal, also known as static TGA, involves use of a constant temperature as change in mass is recorded inferring to time. Quasistatic TGA involves changing the temperature sequentially ensuring the sample stabilizes before the following rise. Dynamic TGA involves a linear change in temperature [186]. TGA is measured by the use of a thermogravimetric analyzer, consisting of a highly

TABLE 7: Summary of XRD observations in clay-based nanocomposites.

Method	Material	Synthesis method	Observations	References
XRD	Bimetallic-doped hybrid kaolinite nanocomposite	Solvothermal process	(i) Cu-doped compound showed an atacamite monoclinic polymorph (ii) Cu/Zn-doped composite showed a rhombohedral atacamite mineral.	[179]
	Nanocrystalline cellulose/bentonite nanocomposite (NCC-Bentonite)	Solution blending	(i) Confirmation of montmorillonite peaks in bentonite ($2\theta = 19.7°$ and $22°$) and cellulose in NCC ($2\theta = 22.3°$).	[151]
	Polypropylene-Polypropylene-grafted-maleic anhydride-montmorillonite clay nanocomposites (PP + PP-g-MA/MMT)	Melt mix extrusion	(i) The characteristic peaks of MMT at $2\theta = 19.7°$ and $22°$ decrease in intensity	[171]
	Physically crosslinked polyvinyl alcohol/bentonite nanocomposite hydrogel	Freeze-thawing technique,	(i) Absence of a peak at $2\theta = 2–10°$ indicates a possibility of exfoliation or mixed intercalated-exfoliated layers of clay in polymer matrix (ii) Characteristic peaks of semicrystalline PVA appear at $19.8°$ and $22.9°$	[172]
	Post-consumer propylene/Tunisian clay nanocomposite	Twin-screw extrusion	(i) Characteristic peaks of kaolinite identified at 7.17, 1.49, and 2.56 Å (ii) Impurities identified at 3.03 Å (calcite) and 3.33 Å (quartz) (iii) Characteristic peak of Tunisian clay at 7.12 Å retained.	[174]
	Polyacrylonitrile vinyl triethoxysilane-sepiolite nanocomposite	Chemical grafting	(i) Peak of unmodified clay observed at $2\Theta = 8.215°$ and $13.95°$ shifting to $8.87°$ and $13.45°$, respectively, on modification. Modified sepiolite peaks at $40.01°$ and $49.91°$.	[161]

TABLE 8: Summary of FTIR observations in clay-based nanocomposites.

Method	Material	Synthesis method	Observations	References
FTIR	Carboxymethyl chitosan/poly (ethylene glycol) bentonite nanocomposite (CMCh/PEG/MMT)	In situ polymerization	(i) Broad bands between 3600 and 3200 cm^{-1} due to –OH and –NH groups	[183]
	Nanocrystalline cellulose/bentonite nanocomposite (NCC-Bentonite)	Solution blending	(i) Cellulose characteristic peaks at 1045 (C–O/C–C),1357 (C–H), and 2841 (CH2) (ii) Montmorillonite characteristic peaks at 3612 (Al(Mg)–OH), 3441 (H–O–H), 1641 (-OH bending), and 1041 cm^{-1} (Si–O–Si stretch) in bentonite	[151]
	Alginate/nano-cloisite nanocomposite hydrogel	Electron beam irradiation	(i) Strong peak observed at 1071 cm^{-1} related to the overlap of C–C bonds of alginate and Si–O–Si axial plane in clay.	[184]
	Polyaniline-clay hybrid nanocomposite (PANI/Clay)	In situ polymerization	(i) PANI/Clay peaks at 1241 cm^{-1} and 1304 cm^{-1} characteristic of PANI polymer.	[173]
	Post-consumer propylene/lay nanocomposite	Twin-screw extrusion	(i) Raw clay showed quartz (impurity) characteristic peak at 420 cm^{-1}. (ii) At 1433, 711.6, and 871.6 cm^{-1}, carbonate (dolomite (Ca, Mg (CO$_3$)$_2$) or calcite (CaCO$_3$)) are observed. (iii) Smectite phase with dioctaedric character is observed at 3627 and 912.1 cm^{-1}, attributed to Al–Al–OH- stretch.	[174]
	Polyacrylonitrile vinyl triethoxysilane-sepiolite nanocomposite	Chemical grafting	(i) Characteristic sepiolite peaks at 643, 691, and 976 cm^{-1} in lean characteristic nitrile group peak appeared at 2245 cm^{-1}.erpiolite clay. (ii) New peaks at 1391, 2810, and 2970 cm^{-1}(C–H vinyl group) (iii) Characteristic nitrile group peak appeared at 2245 cm^{-1}	[161]

TABLE 9: Summary of TGA observations in clay-based nanocomposites.

Method	Material	Synthesis method	Observations	References
TGA	Polypropylene-polypropylene-grafted-maleic anhydride-montmorillonite clay nanocomposites (PP + PP-g-MA/MMT)	Melt mix extrusion	(i) Thermal stability for nanocomposite was higher than lean polymer	[171]
	Physically crosslinked polyvinyl alcohol/bentonite nanocomposite hydrogel	Freeze-thawing technique	(i) Filler content (clay) increased melting and crystallization enthalpies in the PVA.	[172]
	Polyaniline/Clay nanocomposite	In situ polymerization	(i) Material with adsorbed heavy metal exhibited lower decomposition temperature than in desorbed state. Metal ion reduced the material's thermal stability.	[173]
	Post-consumer propylene/Tunisian clay nanocomposite (PCPP/Clay)	Twin-screw extrusion	(i) Increase in clay content increased the thermal stability of the nanocomposite.	[174]
	Polyacrylonitrile vinyl triethoxysilane-sepiolite nanocomposite	Chemical grafting	(i) Thermal stability of nanocomposite reinforced by clay	[161]

sensitive precision balance and a furnace with programmable temperature control. Thermal reactions are caused often by a constant rise in temperature. The atmosphere can either include vacuum, ambient air, inert gas, corrosive gas, reducing/oxidizing gases or carburizing gases. The pressures are varied too, ranging from controlled, constant, or high pressures [187]. TGA data are usually plotted into mass or initial mass versus time or temperature. Such data form a TGA curve. In some instances, a first derivative of the curve known as the DTG is plotted to show peaks of inflections, useful in differential thermal analysis [188]. TGA is used in analysis such as paints, thermoplastics, thermosets, composites, coatings, fuels, among others [186].

In a TGA analysis of geopolymer clay nanocomposite, Maleki et al. [189] reported an initial mass loss at 80–200°C owing to water evaporation and a second one in the region 400–700°C attributed to water loss due to clay's dihydroxylation. Kalantari and Afifi [190] reported an initial 15% mass loss at 40–145°C when studying the thermal stability of chitosan/polyvinyl alcohol/talc nanocomposite. The nanocomposite was reported to be more thermally stable compared to PVA and chitosan, enabling the material to decompose at 800°C. When polymers are reinforced with clay materials, they exhibit higher thermal stability. Malayoglu [191] reported an increase in thermal stability of chitosan when reinforced with montmorillonite clay in a nanocomposite. The author attributed the observation to surfactant interaction with chitosan-clay acting as a barrier in the chitosan decay process. Abdeldaym et al. [192] reported a similar phenomenon when using a polypyrrole/natural clay nanocomposite. Plain polypyrrole decomposed at about 204°C whose decomposition was pushed higher by the addition of clay to 226°C. El-Aziz et al. [193] also reported that cellulose grafted in the presence of clay showed higher thermostability in response to the presence of clay mineral structures. Other reports in TGA analysis are summarized in Table 9.

7.5. Brunauer–Emmett–Teller Analysis. Brunauer–Emmett–Teller (BET) is used in the measurement of pore size and surface area of solid materials in adsorption of gas molecules (nitrogen gas adsorption is often used as a standard). Data arising from BET analysis give insight into the physical structure of the material, in addition to moisture retention, shelf life, dissolution rate, and catalytic activity [194]. The analysis process involves bringing the sample's temperatures to near cryogenic using liquid nitrogen. Then nitrogen gas acting as an adsorbate is fed to the solid sample in controlled measures, with relative pressure equilibrating and weight W, of nitrogen adsorbed measured after each increment. An equation is known as the BET equation (Equation 19) allows a linear plot of $1/(P_0/P - 1)$ versus (P/P_0), which limits adsorption to a region in the (P/P_0) range of 0.05–0.35. By use of the plot, the weight, W_m, of nitrogen adsorbed is determined, which represents a monolayer surface coverage. The slope of the equation and its interception give the cumulative surface area of the sample [194].

$$\frac{1}{W\left((P_0/P) - 1\right)} = \frac{1}{W_m C} + \left(\frac{C-1}{W_m C}\right)\frac{P}{P_0}, \tag{19}$$

where C is the BET constant and is related to the adsorption energy corresponding to the first layer of adsorption. The value of C indicates the magnitude of adsorbate/adsorbent interactions. This method of analysis is most preferable for materials that exhibit Type II or Type IV adsorption isotherm behaviors. These materials showcase sufficient interactions between the adsorbate and the adsorbent and therefore give reliable data [195].

In a study by Maleki et al. [189] investigating the surface area and pore volume of a magnetic geopolymer/bentonite nanocomposite, the authors reported a greater surface area in the composite compared to the plain geopolymer and a slight decrease in the pore volume of the nanocomposite. This was attributed to the loading of the magnetizing Fe_3O_4 nanoparticles. Batool et al. [196] reported similar findings for pore volume when analyzing a polyacrylonitrile/cloisite nanocomposite. Malayoglu [191] reported a decrease in BET surface area of chitosan/montmorillonite nanocomposite attributing it to compacting in clay's interlayers, of the chitosan molecules thereby blocking nitrogen passage. This research agreed with Batool et al. [196] that the average diameter of the pores of the nanocomposites involved was higher compared to the respective non-composited

TABLE 10: Summary of BET observations in clay-based nanocomposites.

Method	Material	Synthesis method	Observations	References
BET	Polyaniline-clay hybrid nanocomposite (PANI/Clay)	In situ polymerization	(i) Surface area and total pore volume increased with PANI intercalation	[173]
	Polyacrylonitrile vinyl triethoxysilane-sepiolite nanocomposite	Chemical grafting	(i) Pore volume decreased on v*inyltriethoxysilane*modification, which further decreased on grafting with polyacrylonitrile	[161]
	Montmorillonite cellulose nanocomposite	Solution blending	(i) The BET surface area and pore volume of clay reduced on cellulose intercalation, as the pore diameter had a tremendous increment	[197]
	Acid-activated montmorillonite (AA-MMT)/polyethersulfone (PES) nanocomposite membrane	Phase inversion method	(i) Increase in AA-MMT in the matrix had an increase effect on the distribution of pore sizes and volumes.	[138]
	Smectite titanium ultrafiltration membrane nanocomposite (Sm/Z UF)	Layer-by-layer technique	(i) Increase in pore size distribution observed was attributed to densification of inner and outer parts of the membrane thus increasing its porosity.	[198]

compared materials. Other reports in FTIR analysis are summarized in Table 10.

8. Areas for Future Research

Based on the work reviewed herein, following areas have been identified for future research:

(i) Mechanism of intercalation of biopolymers and clay structures.

(ii) Modification of clay-based nanocomposites to remove both organic and inorganic contaminants interchangeably.

(iii) Application of heavy metal adsorbents in real contaminated water instead of simulated specifically contaminated wastewater.

(iv) Performance comparison of low-cost adsorbents and existing adsorption technologies.

(v) Studies on large-scale applicability of clay-based adsorbents in the decontamination of water.

(vi) Comparative study of regenerative capability and sludge production and ease of disposal between the existing adsorption technologies and clay-based nanocomposites.

(vii) In-depth study of the active life cycle and sustainability of clay-based nanocomposites especially in developing countries.

9. Conclusions

In light of this review, it was concluded that:

(i) Clay-based nanocomposites mostly exhibit heterogeneous adsorption, although some nanocomposites exhibit homogeneous adsorption.

(ii) In the fabrication of clay-based nanocomposites, high swelling clays, especially smectites, are of great significance because of their increased surface area.

(iii) These nanocomposites have yet low to none industrial utilization, in as much as they portray high efficiency in heavy metal removal.

(iv) Polymer intercalation into clay increases the surface area of the clay.

(v) Clay as a filler material increases the heat retardancy of polymers in which it is incorporated.

Data Availability

The data can be accessed in the cited papers in the review article.

Conflicts of Interest

The authors declare that there are no conflicts of interest regarding the publication of this article.

Acknowledgments

References

[1] O. N. Borisova, I. G. Doronkina, and V. M. Feoktistova, "Resource-saving nanotechnologies in waste water treatment," *Nanotechnologies in Construction*, vol. 13, no. 2, pp. 124–130, 2021.

[2] F. Aquastat, "Global information system on water and agriculture: water resources," 2020, https://www.fao.org/aquastat/en/.

[3] UpKeep, "Most Interesting Statistics and Facts about Wastewater Management? Stats And Facts Watewater," 2019, https://www.upkeep.com/answers/maintenance-technicians/stats-and-facts-waste-water.

[4] World Health Organization, "1 in 3 people globally do not have access to safe drinking water," 2020, https://www.who.int/news/item/18-06-2019-1-in-3-people-globally-do-not-have-access-to-safe-drinking-water-unicef-who.

[5] G. White and M. Damon, "Finance for water is an investment in the future," 2016, https://water.org/our-impact/all-stories/finance-water-investment-future/.

[6] P. Environment Monitor, "Water Pollution- Sources of Water Pollution," 2017, http://www.environmentlaw.org.uk/rte.asp?id=90.

[7] J. A. Nathanson, "Wastewater Treatment," 2021, https://www.britannica.com/technology/wastewater-treatment.

[8] U. Epa, "Water: monitoring and assessment," *Monitoring And Assessing Water Quality—Volunteer Monitoring*, 2012, https://archive.epa.gov/water/archive/web/html/index-18.html.

[9] H. Hamdhani, D. E. Eppehimer, and M. T. Bogan, "Release of treated effluent into streams: a global review of ecological impacts with a consideration of its potential use for environmental flows," *Freshwater Biology*, vol. 65, no. 9, pp. 1657–1670, 2020.

[10] UNICEF, *Kenya's Water Crisis—Kenya's Water in 2020*, UNICEF, New York, NY, USA, 2020.

[11] J. D. Edwards, *Industrial Wastewater Treatment*, CRC Press, Boca Raton, FL, USA, 2019.

[12] M. A. Evans, "The sewage crisis in America," 2015, https://www.theatlantic.com/technology/archive/2015/09/americas-sewage-crisis-public-health/405541/.

[13] J. Peccia and P. Westerhoff, "We should expect more out of our sewage sludge," *Environmental Science and Technology*, vol. 49, no. 14, pp. 8271–8276, 2015.

[14] G. K. Kinuthia, V. Ngure, D. Beti, R. Lugalia, A. Wangila, and L. Kamau, "Levels of heavy metals in wastewater and soil samples from open drainage channels in Nairobi, Kenya: community health implication," *Scientific Reports*, vol. 10, no. 1, pp. 1–13, 2020.

[15] LennTech, "Heavy metals," 2017, https://www.lenntech.com/processes/heavy/heavy-metals/heavy-metals.htm.

[16] G. A. Engwa, P. U. Ferdinand, F. N. Nwalo, and M. N. Unachukwu, "Mechanism and Health Effects of Heavy Metal Toxicity in Humans," in *Poisoning In the Modern World—New Tricks For an Old Dog?*, O. Karcioglu and B. Arslan, Eds., 1st ed., pp. 77–95, IntechOpen, London, UK, 2019.

[17] M. Jaishankar, T. Tseten, N. Anbalagan, B. B. Mathew, and K. N. Beeregowda, "Toxicity, mechanism and health effects of some heavy metals," *Interdisciplinary Toxicology*, vol. 7, no. 2, p. 60, 2014.

[18] S. Sauvé, "Time to revisit arsenic regulations: comparing drinking water and rice," *BMC Public Health*, vol. 14, no. 1, pp. 1–5, 2014.

[19] S. J. S. Flora, "Arsenic-induced oxidative stress and its reversibility," *Free Radical Biology and Medicine*, vol. 51, no. 2, pp. 257–281, 2011.

[20] M. S. Mani, S. P. Kabekkodu, M. B. Joshi, and H. S. Dsouza, "Ecogenetics of lead toxity and its influence on risk assessment," *Human & Experimental Toxicology*, vol. 38, no. 9, pp. 1031–1059, 2019.

[21] P. B. Tchounwou, C. G. Yedjou, A. K. Patlolla, and D. J. Sutton, "Heavy metal toxicity and the environment," *EXS*, vol. 101, pp. 133–164, 2012.

[22] P. Senthil Kumar and E. Gunasundari, "Bioremediation of heavy metals," in *Energy, Environment, and Sustainability*, A. K. Agarwal, Ed., 1st ed., pp. 165–195, Springer, Berlin, Germany, 2018.

[23] Z. Fu and S. Xi, "The effects of heavy metals on human metabolism," *Toxicology Mechanisms and Methods*, vol. 30, 2020.

[24] T. S. Anirudhan and S. Rijith, "Synthesis and characterization of carboxyl terminated poly(methacrylic acid) grafted chitosan/bentonite composite and its application for the recovery of uranium(VI) from aqueous media," *Journal of Environmental Radioactivity*, vol. 106, no. 7, pp. 8–19, 2012.

[25] Health and Environment, "Components of Waste Water Barnstable County," 2018, https://www.barnstablecountyhealth.org/health-topics/wastewater/components-of-waste-water.

[26] E. D. G. J. Owusu-Ansah, A. Sampson, S. K. Amponsah, R. C. Abaidoo, and T. Hald, "Performance, compliance and reliability of Waste stabilization pond: effluent discharge quality and environmental protection agency standards in Ghana," *Research Journal of Applied Sciences, Engineering and Technology*, vol. 10, no. 11, pp. 1293–1302, 2015.

[27] M. F. Montes, "Biochemical oxygen demand," in *Encyclopedia of Earth Sciences Series*, Springer, Berlin, Germany, 2016.

[28] A. Bezsenyi, G. Sági, M. Makó, L. Wojnárovits, and E. Takács, "The effect of hydrogen peroxide on the biochemical oxygen demand (BOD) values measured during ionizing radiation treatment of wastewater," *Radiation Physics and Chemistry*, vol. 189, Article ID 109773, 2021.

[29] I. Skoczko, J. Struk-Sokołowska, and P. Ofman, "Seasonal changes in nitrogen, phosphorus, BOD and COD removal in Bystre wastewater treatment plant," *Journal of Ecological Engineering*, vol. 18, pp. 185–191, 2017.

[30] H. Nezhadheydari, R. Tavabe, A. Mirvaghefi, A. Heydari, and M. Frinsko, "Effects of different concentrations of Fe 3 O 4 @ZnO and Fe 3 O 4 @CNT magnetic nanoparticles separately and in combination on aquaculture wastewater treatment," *Environmental Technology & Innovation*, vol. 15, Article ID 100414, 2019.

[31] S. Pavithra and S. Shanthakumar, "Removal of COD, BOD and color from municipal solid waste leachate using silica and iron nano particles-A comparative study," *Global NEST Printed in Greece. All Rights Reserved Pavithra S. and Shanthakumar S*, vol. 19, pp. 122–130, 2017.

[32] M. Gharloghi, A. Yazdanbakhsh, A. Eslami, and E. Aghayani, "Efficiency of iron oxide nanoparticles in advanced treatment of secondary effluent of municipal wastewater treatment plant," *Journal of Mazandaran University of Medical Sciences*, vol. 26, no. 135, pp. 130–143, 2016.

[33] S. Allen, G. Barren, O. Bath, C. Boone, L. Breckinridge, and M. Calloway, "Total Suspended Solids And Water Quality. Kentucky Water Watch," 2012, http://www.state.ky.us/nrepc/water/ramp/rmtss.htm.

[34] M. Haeffner, M. Schwientek, S. R. Jacobs et al., "Monitoring of suspended sediments in a tropical forested landscape with citizen science," *Frontiers in Water*, vol. 1, Article ID 656770, 2021.

[35] M. U. S. G. S. Nolan, "Turbidity and Water Water Science School," 2018, https://www.usgs.gov/special-topics/water-science-school/science/turbidity-and-water.

[36] S. Heger, "An installers guide to total suspended solids. onsite installer," 2017, https://www.onsiteinstaller.com/online_exclusives/2017/09/an_installers_guide_to_total_suspended_solids.

[37] I. Fondriest Environmental, "Turbidity, total suspended solids & water clarity. fundamentals of environmental measurements," 2014, https://www.fondriest.com/environmental-measurements/parameters/water-quality/turbidity-total-suspended-solids-water-clarity/#Turbid22.

[38] T. Amerian, R. Farnood, S. Sarathy, and D. Santoro, "effects of total suspended solids, particle size, and effluent temperature on the kinetics of peracetic acid decomposition in municipal wastewater," *Water Science and Technology*, vol. 80, 2019.

[39] T. Asano, R. G. Smith, and G. Tchobanoglous, "Municipal wastewater: treatment and reclaimed water characteristics,"

in *Irrigation with Reclaimed Municipal Wastewater–A Guidance Manual,* CRC Press, Boca Raton, FL, USA, 2019.

[40] D. Mara, "Domestic wastewater treatment in developing countries," in *Domestic Wastewater Treatment in Developing Countries*, D. Duncan, Ed., RoutledgeMilton Park, UK, 2013.

[41] K. Gaurab, "Physical, chemical and biological characteristics of sewage," 2019, https://www.onlinebiologynotes.com/physical-chemical-and-biological-characteristics-of-sewage/.

[42] T. Asano, R. G. Smith, and G. Tchobanoglous, "Municipal wastewater: treatment and reclaimed water characteristics," in *Irrigation with Reclaimed Municipal Wastewater–A Guidance Manual*, G. S. Pettygrove and T. Asano, Eds., CRC Press, Boca Raton, FL, USA, pp. 2-1–2-26, 2018.

[43] B. A. Hauser, "Chemical oxygen demand," in *Practical Manual of Wastewater Chemistry*, pp. 69–72, CRC Press, Boca Raton, FL, USA, 2018.

[44] D. P. Whitehead, "Total organic carbon (TOC) analysis and measurement | ELGA LabWater," 2021, https://www.elgalabwater.com/blog/total-organic-carbon-toc.

[45] Bloganica, "Primary, secondary, and tertiary wastewater treatment: how do they work? - innovative solutions for wastewater treatment | organica water inc.organica water," 2017, https://www.organicawater.com/primary-secondary-tertiary-wastewater-treatment-work/.

[46] S. Oakley, "Preliminary treatment and primary sedimentation," in *Water and Sanitation for the 21st Century: Health and Microbiological Aspects of Excreta and Wastewater Management (Global Water Pathogen Project)*, J. R. Mihelcic and M. E. Verbyla, Eds., Carlifornia State University, Long Beach, CA, USA, 2019.

[47] M. Eddy, M. Abu-Orf, G. Bowden et al., *Wastewater Engineering: Treatment and Resource Recovery*, McGraw Hill Education, New York, NY, USA, 2014.

[48] M. Farrokhi, M. Naimi-Joubani, A. Dargahi, M. Poursadeghiyan, and H. Ali Jamali, "Investigating activated sludge microbial population efficiency in heavy metals removal from compost leachate," *Polish Journal of Environmental Studies*, vol. 27, no. 2, pp. 623–627, 2018.

[49] C. P. Gerba and I. L. Pepper, "Municipal wastewater treatment," *Environmental and Pollution Science*, pp. 393–418, 2019.

[50] J. A. Nathanson, R. Curley, S. Sinha et al., "Wastewater treatment | process, history, importance, systems, & technologies. Encyclopedia Britannica," 2021, https://www.britannica.com/technology/wastewater-treatment.

[51] S. Kusuma, "Performance evaluation of wastewater treatment plant," *International Journal of Engineering Science and Technology*, vol. 2, no. 12, pp. 7785–7796, 2010.

[52] J. H. J. M. van der Graaf, J. de Koning, A. Ravazzini, and V. Miska, "Treatment matrix for reuse of upgraded wastewater," *Water Science and Technology: Water Supply*, vol. 5, no. 1, pp. 87–94, 2005.

[53] P. Ranjit, V. Jhansi, and K. V. Reddy, "Conventional wastewater treatment processes," in *Advances in the Domain of Environmental Biotechnolog*, N. R. Maddela, L. G. Cruzatty, and S. Chakraborty, Eds., 1st ed., pp. 455–479, Springer, Berlin, Germany, 2021.

[54] L. Rodriguez-Freire, J. Gonzalez-Estrella, and G. Li, "Technologies for fractionation of wastewater and resource recovery," in *Wastewater Treatment Residues as Resources for Biorefinery Products and Biofuels*, J. A. Olivares, D. Puyol, and J. Dufour, Eds., pp. 329–354, Elsevier, Amsterdam, Netherlands, 2019.

[55] M. M. Benjamin and D. F. Lawler, *Water Quality Engineering: Physical/Chemical Treatment Processes*, John Wiley & Sons, Hoboken, NJ, USA, 2013.

[56] Y. Dahman, K. Deonanan, T. Dontsos, and A. Lammatteo, *Nanopolymers Nanotechnology and Functional Materials for Engineer*, Elsevier, Amsterdam, Netherlands, 2017.

[57] L. P. Wang and Y. J. Chen, "Sequential precipitation of iron, copper, and zinc from wastewater for metal recovery," *Journal of Environmental Engineering*, vol. 145, no. 1, Article ID 04018130, 2019.

[58] H. Li, H. Zhang, J. Long, P. Zhang, and Y. Chen, "Combined Fenton process and sulfide precipitation for removal of heavy metals from industrial wastewater: bench and pilot scale studies focusing on in-depth thallium removal," *Frontiers of Environmental Science & Engineering*, vol. 13, no. 4, 2019.

[59] A. E. Lewis, "Review of metal sulphide precipitation," *Hydrometallurgy*, vol. 104, pp. 222–234, 2010.

[60] A. N. Zainuddin, T. Azwan Raja Mamat, H. Imam Maarof, S. Wahidah Puasa, and S. Rohana Mohd Yatim, "Removal of nickel, zinc and copper from plating process industrial raw effluent via hydroxide precipitation versus sulphide precipitation," *IOP Conference Series: Materials Science and Engineering*, vol. 551, no. 1, Article ID 012122, 2019.

[61] P. N. L. Lens, R. J. W. Meulepas, R. Sampaio, M. Vallero, and G. Esposito, "Bioprocess engineering of sulfate reduction for environmental technology," in *Microbial Sulfur Metabolism*, C. Dahl and C. G. Friedrich, Eds., 1st ed., pp. 285–295, Springer, Berlin, Germany, 2008.

[62] M. Sethurajan, E. D. van Hullebusch, and Y. v. Nancharaiah, "Biotechnology in the management and resource recovery from metal bearing solid wastes: recent advances," *Journal of Environmental Management*, vol. 211, pp. 138–153, 2018.

[63] A. H. Kaksonen and J. A. Puhakka, "Sulfate reduction based bioprocesses for the treatment of acid mine drainage and the recovery of metals," *Engineering in Life Science*, vol. 7, no. 6, pp. 541–564, 2007.

[64] E. Sahinkaya, D. Uçar, and A. H. Kaksonen, "Bioprecipitation of metals and metalloids," *Sustainable Heavy Metal Remediation*, Springer, Berlin, Germany, 2017.

[65] Y. v. Nancharaiah, S. V. Mohan, and P. N. L. Lens, "Biological and bioelectrochemical recovery of critical and scarce metals," *Trends in Biotechnology*, vol. 34, no. 2, pp. 137–155, 2016.

[66] M. L. Merroun and S. Selenska-Pobell, "Bacterial interactions with uranium: an environmental perspective," *Journal of Contaminant Hydrology*, vol. 102, pp. 285–295, 2008.

[67] S. Chabalala and E. M. N. Chirwa, "Removal of uranium (VI) under aerobic and anaerobic conditions using an indigenous mine consortium," *Minerals Engineering*, vol. 23, no. 6, pp. 526–531, 2010.

[68] C. Zhou, A. Ontiveros-Valencia, L. Cornette de Saint Cyr et al., "Uranium removal and microbial community in a H2-based membrane biofilm reactor," *Water Research*, vol. 64, pp. 255–264, 2014.

[69] F. Fu and Q. Wang, "Removal of heavy metal ions from wastewaters: a review," *Journal of Environmental Management*, vol. 92, no. 3, pp. 407–418, 2011.

[70] B. Alyüz and S. Veli, "Kinetics and equilibrium studies for the removal of nickel and zinc from aqueous solutions by ion exchange resins," *Journal of Hazardous Materials*, vol. 167, pp. 482–488, 2009.

[71] S. A. Abo-Farha, A. Y. Abdel-Aal, I. A. Ashour, and S. E. Garamon, "Removal of some heavy metal cations by

synthetic resin purolite C100," *Journal of Hazardous Materials*, vol. 169, pp. 190–194, 2009.

[72] K. K. Kennedy, K. J. Maseka, M. Mbulo, K. K. Kennedy, K. J. Maseka, and M. Mbulo, "Selected adsorbents for removal of contaminants from wastewater: towards engineering clay minerals," *Open Journal of Applied Sciences*, vol. 8, no. 8, pp. 355–369, 2018.

[73] A. Mohammad-Khan and R. Ansari, "Activated charcoal: preparation, characterization and applications: a review article," *InternationAL Journal of ChemTech Research*, vol. 1, pp. 859–869, 2009.

[74] A. Bhatnagar and A. Minocha, "Conventional and non-conventional adsorbents for removal of pollutants from water," *Indian Journal of Chemical Technology*, vol. 13, pp. 203–217, 2006.

[75] T. Maruyama, "Carbon nanotubes," in *Handbook of Carbon-Based Nanomaterials*, S. Thomas, C. Sarathchandran, S. A. Ilangovan, and J. C. Moreno-Pirajan, Eds., 1st ed., pp. 299–319, Elsevier, Amsterdam, Netherlands, 2021.

[76] A. M. Holban, A. M. Grumezescu, and E. Andronescu, "Inorganic nanoarchitectonics designed for drug delivery and anti-infective surfaces," *Surface Chemistry of Nanobiomaterials: Applications of Nanobiomaterials*, pp. 301–327, 2016.

[77] H. Alijani and Z. Shariatinia, "Synthesis of high growth rate SWCNTs and their magnetite cobalt sulfide nanohybrid as super-adsorbent for mercury removal," *Chemical Engineering Research and Design*, vol. 129, pp. 132–149, 2018.

[78] H. A. Qdais and H. Moussa, "Removal of heavy metals from wastewater by membrane processes: a comparative study," *Desalination*, vol. 164, no. 2, pp. 105–110, 2004.

[79] B. S. Thaçi and S. T. Gashi, "Reverse osmosis removal of heavy metals from wastewater effluents using biowaste materials pretreatment," *Polish Journal of Environmental Studies*, vol. 28, no. 1, pp. 337–341, 2018.

[80] B. A. M. Al-Rashdi, D. J. Johnson, and N. Hilal, "Removal of heavy metal ions by nanofiltration," *Desalination*, vol. 315, pp. 2–17, 2013.

[81] G. Al-Enezi, M. F. Hamoda, and N. Fawzi, "Ion exchange extraction of heavy metals from wastewater sludges," *Journal of Environmental Science and Health - Part A: Toxic/Hazardous Substances and Environmental Engineering*, vol. 39, no. 2, pp. 455–464, 2004.

[82] J. M. Arana Juve, F. M. S. Christensen, Y. Wang, and Z. Wei, "Electrodialysis for metal removal and recovery: a review," *Chemical Engineering Journal*, vol. 435, Article ID 134857, 2022.

[83] N. A. A. Qasem, R. H. Mohammed, and D. U. Lawal, "Removal of heavy metal ions from wastewater: a comprehensive and critical review," *Npj Clean Water*, vol. 4, no. 1, pp. 1–15, 2021.

[84] R. C. Gumerman, R. L. Culp, and S. P. Hansen, "Estimating water treatment costs," 1979, http://nepis.epa.gov/Exe/ZyPDF.cgi/300009IH.PDF?Dockey=300009IH.PDF.

[85] P. Pandit, K. Singha, S. Maity, S. Maiti, and P. Kane, "Treatment of textile wastewater by agricultural waste biomasses," in *Sustainable Technologies for Textile Wastewater Treatments*, S. S. Muthu, Ed., 1st ed., pp. 137–156, Elsevier, Amsterdam, Netherlands, 2021.

[86] G. Crini, E. Lichtfouse, L. D. Wilson, and N. Morin-Crini, "Conventional and non-conventional adsorbents for wastewater treatment," *Environmental Chemistry Letters*, vol. 17, pp. 195–213, 2019.

[87] D. Park, Y. S. Yun, and J. M. Park, "The past, present, and future trends of biosorption," *Biotechnology and Bioprocess Engineering*, vol. 15, no. 1, pp. 86–102, 2010.

[88] I. Ali, "Water treatment by adsorption columns: evaluation at ground level," *Separation and Purification Reviews*, vol. 43, no. 3, pp. 175–205, 2014.

[89] A. Onur, A. Ng, W. Batchelor, and G. Garnier, "Multi-layer filters: adsorption and filtration mechanisms for improved separation," *Frontiers of Chemistry*, vol. 6, 2018.

[90] Y. Yigzaw, R. Piper, M. Tran, and A. A. Shukla, "Exploitation of the adsorptive properties of depth filters for host cell protein removal during monoclonal antibody purification," *Biotechnology Progress*, vol. 22, no. 1, pp. 288–296, 2006.

[91] A. A. Shukla and J. R. Kandula, "Harvest and recovery of monoclonal antibodies: cell removal and clarification," *Process Scale Purification of Antibodies*, vol. 21, pp. 53–78, 2008.

[92] A. Razzaz, S. Ghorban, L. Hosayni, M. Irani, and M. Aliabadi, "Chitosan nanofibers functionalized by TiO_2 nanoparticles for the removal of heavy metal ions," *Journal of the Taiwan Institute of Chemical Engineers*, vol. 58, no. 58, pp. 333–343, 2016.

[93] U. Fegade and G. Jethave, "Advances and applications," *Interface Science and Technology*, vol. 33, pp. 557–586, 2021.

[94] M. Asif, E. H. Al-Ghurabi, A. Ajbar, and N. S. Kumar, "Hydrodynamics of pulsed fluidized bed of ultrafine powder: fully collapsing fluidized bed," *Processes*, vol. 2020, 2020.

[95] G. Crini and P.-M. Badot, "Conventional and non-conventional sorbents for pollutant removal from wastewaters," in *Sorption Processes and Pollution*, Presses universitaires de Franche-Comté, Besançon, France, 2010.

[96] L. Pontoni and M. Fabbricino, "Use of chitosan and chitosan-derivatives to remove arsenic from aqueous solutionsâ€"a mini review," *Carbohydrate Research*, vol. 356, pp. 86–92, 2012.

[97] H. Hosseinzadeh and S. Ramin, "Effective removal of copper from aqueous solutions by modified magnetic chitosan/graphene oxide nanocomposites," *International Journal of Biological Macromolecules*, vol. 113, pp. 859–868, 2018.

[98] V. Gupta, P. Carrott, R. Singh, M. Chaudhary, and S. Kushwaha, "Cellulose: a review as natural, modified and activated carbon adsorbent," *Bioresource Technology*, vol. 216, 2016.

[99] S. Dridi-Dhaouadi, N. ben Douissa-Lazreg, and M. F. M'Henni, "Removal of lead and yellow 44 acid dye in single and binary component systems by raw posidonia oceanica and the cellulose extracted from the raw biomass," *Environmental Technology*, vol. 32, 2011.

[100] Z. Wu, Z. Cheng, and W. Ma, "Adsorption of Pb(II) from glucose solution on thiol-functionalized cellulosic biomass," *Bioresource Technology*, vol. 104, pp. 807–809, 2012.

[101] N. Anton, A. Uliana, M. Olga, A. Eugenia, and I. Y. Vladimir, "Physico chemical properties of montmorillonite clays and their application in clinical practice (review)," *Research Result: Pharmacology and Clinicl Pharmacology*, vol. 3, no. 2, pp. 119–128, 2017.

[102] H. Daumier, A. Savage, B. O. Sicyon, and A. Augustyn, Encyclopedia Britannica, "Clay," 2020, https://www.britannica.com/science/clay-geology.

[103] S. Barakan and V. Aghazadeh, "The advantages of clay mineral modification methods for enhancing adsorption efficiency in wastewater treatment: a review," *Environmental Science and Pollution Research*, vol. 28, 2021.

[104] M. Ghadiri, W. Chrzanowski, and R. Rohanizadeh, "Biomedical applications of cationic clay minerals," *RSC Advances*, vol. 5, no. 37, pp. 29467–29481, 2015.

[105] B. Karpiński and M. Szkodo, "Clay minerals—mineralogy and phenomenon of clay swelling in oil & gas industry," *Advances in Materials Science*, vol. 15, no. 1, pp. 37–55, 2015.

[106] Y. Khaledian, E. C. Brevik, P. Pereira, A. Cerdà, M. A. Fattah, and H. Tazikeh, "Modeling soil cation exchange capacity in multiple countries," *Catena*, vol. 158, pp. 194–200, 2017.

[107] K. G. Bhattacharyya and S. Gupta, "Adsorptive accumulation of Cd(II), Co(II), Cu(II), Pb(II) and Ni(II) ions from water onto Kaolinite: influence of acid activation," *Adsorption Science and Technology*, vol. 27, no. 1, pp. 47–68, 2009.

[108] L. de Pablo, M. L. Chávez, and M. Abatal, "Adsorption of heavy metals in acid to alkaline environments by montmorillonite and Ca-montmorillonite," *Chemical Engineering Journal*, vol. 171, no. 3, pp. 1276–1286, 2011.

[109] A. Sdiri, T. Higashi, T. Hatta, F. Jamoussi, and N. Tase, "Evaluating the adsorptive capacity of montmorillonitic and calcareous clays on the removal of several heavy metals in aqueous systems," *Chemical Engineering Journal*, vol. 172, no. 1, pp. 37–46, 2011.

[110] S. A. Al-Jlil, "Kinetic of adsorption of chromium and lead ions on bentonite clay using novel internal parallel model," *Research Journal of Environmental Toxicology*, vol. 9, no. 1, pp. 1–16, 2015.

[111] T. Zhang, W. Wang, Y. Zhao, H. Bai, T. Wen, and S. Kang, "Removal of heavy metals and dyes by clay-based adsorbents: from natural clays to 1D and 2D nano-composites," *Chemical Engineering Journal*, vol. 420, Article ID 127574, 2021.

[112] A. Awasthi, P. Jadhao, and K. Kumari, "Clay nano-adsorbent: structures, applications and mechanism for water treatment," *SN Applied Sciences*, vol. 1, no. 9, 2019.

[113] N. AlMasoud, M. Habila, Z. Alothman et al., "Nano-clay as a solid phase microextractor of copper, cadmium and lead for ultra-trace quantification by ICP-MS," *Analytical Methods*, vol. 12, no. 41, pp. 4949–4955, 2020.

[114] A. El Kassimi, Y. Achour, M. El Himri, R. Laamari, and M. El Haddad, "Removal of two cationic dyes from aqueous solutions by adsorption onto local clay: experimental and theoretical study using DFT method," *International Journal of Environmental Analytical Chemistry*, vol. 101, pp. 1–22, 2021.

[115] R. El Haouti, H. Ouachtak, A. El Guerdaoui et al., "Cationic dyes adsorption by Na-Montmorillonite Nano Clay: experimental study combined with a theoretical investigation using DFT-based descriptors and molecular dynamics simulations," *Journal of Molecular Liquids*, vol. 290, Article ID 111139, 2019.

[116] H. Masoudi, F. Ravari, and H. Mosaddeghi, "Removal of nitrate from water by modified nano-clay and comparison with nano-graphene, nano-Fe₃O₄ and nano-clay—isotherm and kinetics study," *Desalination and Water Treatment*, vol. 167, pp. 218–230, 2019.

[117] L. Rafati, M. Ehrampoush, A. Rafati, M. Mokhtari, and A. Mahvi, "Modeling of adsorption kinetic and equilibrium isotherms of naproxen onto functionalized nano-clay composite adsorbent," *Journal of Molecular Liquids*, vol. 224, pp. 832–841, 2016.

[118] K. Shapira and I. Zucker, "Emerging investigator series: molybdenum disulfide-enabled activated carbon—a multifunctional adsorbent for practical water treatment applications," *Environmental Sciences: Nano*, vol. 9, no. 2, pp. 477–488, 2022.

[119] A. S. K. Kumar, S. Kalidhasan, V. Rajesh, and N. Rajesh, "Application of cellulose-clay composite biosorbent toward the effective adsorption and removal of chromium from industrial wastewater," *Industrial & Engineering Chemistry Research*, vol. 51, no. 1, pp. 58–69, 2012.

[120] Q. Chen, R. Zhu, W. Deng et al., "From used montmorillonite to carbon monolayer–montmorillonite nanocomposites," *Applied Clay Science*, vol. 100, pp. 112–117, 2014.

[121] Y. Ma, L. Lv, Y. Guo et al., "Porous lignin based poly (acrylic acid)/organo-montmorillonite nanocomposites: swelling behaviors and rapid removal of Pb (II) ions," *Polymer*, vol. 128, pp. 12–23, 2017.

[122] A. Heydari, H. Khoshnood, H. Sheibani, and F. Doostan, "Polymerization of β-cyclodextrin in the presence of bentonite clay to produce polymer nanocomposites for removal of heavy metals from drinking water," *Polymers for Advanced Technologies*, vol. 28, no. 4, pp. 524–532, 2017.

[123] M. Irani, H. Ismail, Z. Ahmad, and M. Fan, "Synthesis of linear low-density polyethylene-g-poly (acrylic acid)-co-starch/organo-montmorillonite hydrogel composite as an adsorbent for removal of Pb (II) from aqueous solutions," *Journal of Environmental Sciences*, vol. 27, pp. 9–20, 2015.

[124] K. el Adraa, T. Georgelin, J.-F. Lambert, F. Jaber, F. Tielens, and M. Jaber, *Cysteine-montmorillonite composites for heavy metal cation complexation: a combined experimental and theoretical study*, Elsevier, 2017, https://www.google.com/search?rlz=1C1GCEB_enIN992IN992&q=Amsterdam&stick=H4sIAAAAAAAAAOPgE-LUz9U3MDJLSYpXYgcxs40LtLSyk63084vSE_MyqxJLMvPzUDhWGamJKYWliUUlqUXFi1g5HXOLgayUxNwdrIy72Jk4GAD1-FzrVgAAAA&sa=X&ved=2ahUKEwjxpbifpIr4AhXGwTgGHTjaBTAQmxMoAXoECGoQAw.

[125] C. M. Futalan, C. C. Kan, M. L. Dalida, K. J. Hsien, C. Pascua, and M. W. Wan, "Comparative and competitive adsorption of copper, lead, and nickel using chitosan immobilized on bentonite," *Carbohydrate Polymers*, vol. 83, no. 2, pp. 528–536, 2011.

[126] V. N. Tirtom, A. Dinçer, S. Becerik, T. Aydemir, and A. Çelik, "Comparative adsorption of Ni(II) and Cd(II) ions on epichlorohydrin crosslinked chitosan–clay composite beads in aqueous solution," *Chemical Engineering Journal*, vol. 197, pp. 379–386, 2012.

[127] M. Cittan, V. N. Tirtom, A. Dinçer, and A. Çelik, "Epichlorohydrin crosslinked chitosan–clay composite beads for on-line preconcentration and determination of chromium (III) by flow injection flame atomic absorption spectrometry," *Analytical Methods*, vol. 6, no. 14, pp. 5298–5303, 2014.

[128] T. S. Anirudhan and P. S. Suchithra, "Heavy metals uptake from aqueous solutions and industrial wastewaters by humic acid-immobilized polymer/bentonite composite: kinetics and equilibrium modeling," *Chemical Engineering Journal*, vol. 156, no. 1, pp. 146–156, 2010.

[129] K. El Adraa, T. Georgelin, J. F. Lambert, F. Jaber, F. Tielens, and M. Jaber, "Cysteine-montmorillonite composites for heavy metal cation complexation: a combined experimental and theoretical study," *Chemical Engineering Journal*, vol. 314, pp. 406–417, 2017.

[130] K. Kalantari, M. B. Ahmad, H. R. FardMasoumi, K. Shameli, M. Basri, and R. Khandanlou, "Rapid and high capacity adsorption of heavy metals by Fe3O4/montmorillonite nanocomposite using response surface methodology:

preparation, characterization, optimization, equilibrium isotherms, and adsorption kinetics study," *Journal of the Taiwan Institute of Chemical Engineers*, vol. 49, pp. 192–198, 2015.

[131] G. Zhao, H. Zhang, Q. Fan et al., "Sorption of copper(II) onto super-adsorbent of bentonite–polyacrylamide composites," *Journal of Hazardous Materials*, vol. 173, pp. 661–668, 2010.

[132] Á. García-Padilla, K. A. Moreno-Sader, Á. Realpe, M. Acevedo-Morantes, and J. B. P. Soares, "Evaluation of adsorption capacities of nanocomposites prepared from bean starch and montmorillonite," *Sustainable Chemistry and Pharmacy*, vol. 17, Article ID 100292, 2020.

[133] S. Yadav, V. Srivastava, S. Banerjee, F. Gode, and Y. C. Sharma, "Studies on the removal of nickel from aqueous solutions using modified riverbed sand," *Environmental Science and Pollution Research*, vol. 20, no. 1, pp. 558–567, 2013.

[134] X. Zhang and X. Wang, "Adsorption and desorption of nickel(II) ions from aqueous solution by a lignocellulose/montmorillonite nanocomposite," *PLoS One*, vol. 10, no. 2, Article ID e0117077, 2015.

[135] J. H. Hassen, "Montmorillonite nanoclay interaction with 2-aminophenol and 2-nitrophenol," *Research Journal of Pharmacy and Technology*, vol. 12, no. 6, pp. 2828–2831, 2019.

[136] R. Msaadi, G. Yilmaz, A. Allushi et al., "Highly selective copper ion imprinted clay/polymer nanocomposites prepared by visible light initiated radical photopolymerization," *Polymers*, vol. 11, 2019.

[137] K. Moreno-Sader, A. García-Padilla, A. Realpe, M. Acevedo-Morantes, and J. B. P. Soares, "Removal of heavy metal water pollutants (Co2$^+$ and Ni2$^+$) using polyacrylamide/sodium montmorillonite (PAM/Na-MMT) nanocomposites," *ACS Omega*, vol. 4, no. 6, pp. 10834–10844, 2019.

[138] M. Mahmoudian, P. G. Balkanloo, and E. Nozad, "A facile method for dye and heavy metal elimination by pH sensitive acid activated montmorillonite/polyethersulfone nanocomposite membrane," *Chinese Journal of Polymer Science*, vol. 36, no. 1, pp. 49–57, 2017.

[139] S. Wadhawan, A. Jain, J. Nayyar, and S. K. Mehta, "Role of nanomaterials as adsorbents in heavy metal ion removal from waste water: a review," *Journal of Water Process Engineering*, vol. 33, 2020.

[140] M. E. M. Hassouna, M. Shaban, and F. M. Nassif, "Removal of iron and manganese ions from ground water using kaolin sub micro powder and its modified forms," *International Journal of Bioassays*, vol. 3, no. 07, pp. 3137–3145, 2014, https://www.ijbio.com/articles/removal-of-iron-and-manganese-ions-from-groundwater-using-kaolin-sub-micropowder-and-its-modified-forms.pdf.

[141] A. E. A. Sallam, M. S. Al-Zahrani, M. I. Al-Wabel, A. S. Al-Farraj, and A. R. A. Usman, "Removal of Cr(VI) and toxic ions from aqueous solutions and tannery wastewater using polymer-clay composites," *Sustainability*, vol. 9, no. 11, 2017.

[142] R. Dubey, J. Bajpai, and A. K. Bajpai, "Chitosan-alginate nanoparticles (CANPs) as potential nanosorbent for removal of Hg (II) ions," *Environmental Nanotechnology, Monitoring & Management*, vol. 6, no. 6, pp. 32–44, 2016.

[143] E. J. Kim, C. S. Lee, Y. Y. Chang, and Y. S. Chang, "Hierarchically structured manganese oxide-coated magnetic nanocomposites for the efficient removal of heavy metal ions from aqueous systems," *ACS Applied Materials & Interfaces*, vol. 5, pp. 9628–9634, 2013.

[144] K. Ravikumar and J. Udayakumar, "Preparation and characterisation of green clay-polymer nanocomposite for heavy metals removal," *Chemistry and Ecology*, vol. 36, no. 3, pp. 270–291, 2020.

[145] Y. Xu, J. Chen, R. Chen, P. Yu, S. Guo, and X. Wang, "Adsorption and reduction of chromium(VI) from aqueous solution using polypyrrole/calcium rectorite composite adsorbent," *Water Research*, vol. 160, pp. 148–157, 2019.

[146] M. qin Jiang, X. ying Jin, X. Q. Lu, and Z. liang. Chen, "Adsorption of Pb(II), Cd(II), Ni(II) and Cu(II) onto natural kaolinite clay," *Desalination*, vol. 252, pp. 33–39, 2010.

[147] M. L. Masheane, L. N. Nthunya, S. S. Sambaza et al., "Chitosan-based nanocomposite beads for drinking water production," *IOP Conference Series: Materials Science and Engineering*, vol. 195, no. 1, Article ID 012004, 2017.

[148] N. N. Nassar, "Rapid removal and recovery of Pb(II) from wastewater by magnetic nanoadsorbents," *Journal of Hazardous Materials*, vol. 184, pp. 538–546, 2010.

[149] G. Murithi, C. O. Onindo, E. W. Wambu, and G. K. Muthakia, "Removal of cadmium (II) ions from water by adsorption using water hyacinth (*Eichhornia crassipes*) biomass," *Bioresources*, vol. 9, no. 2, pp. 3613–3631, 2014.

[150] A. O. Dada, A. P. Olalekan, and A. M. Olatunya, "Langmuir, Freundlich, Temkin and Dubinin–radushkevich Isotherms: studies of equilibrium sorption of Zn^{2+} unto phosphoric acid modified rice husk," *Journal of Applied Chemistry*, vol. 1, no. 3, pp. 38–45, 2012.

[151] J. N. Putro, S. P. Santoso, S. Ismadji, and Y. H. Ju, "Investigation of heavy metal adsorption in binary system by nanocrystalline cellulose—bentonite nanocomposite: improvement on extended Langmuir isotherm model," *Microporous and Mesoporous Materials*, vol. 246, pp. 166–177, 2017.

[152] M. Kragović, M. Stojmenović, J. Petrović et al., "Influence of alginate encapsulation on point of zero charge (pHpzc) and thermodynamic properties of the natural and Fe(III)—modified zeolite," *Procedia Manufacturing*, vol. 32, pp. 286–293, 2019.

[153] S. N. Ndung'u, T. Nyahanga, R. N. Wanjau, and E. W. Nthiga, "Adsorption evaluation of selected heavy metal ions by amino- functionalized low-cost adsorbents," *A Review*, vol. 9, no. 7, pp. 339–357, 2021.

[154] Y. Liu, G. Wang, Q. Luo, X. Li, and Z. Wang, "The thermodynamics and kinetics for the removal of copper and nickel ions by the zeolite Y synthesized from fly ash," *Materials Research Express*, vol. 6, no. 2, Article ID 025001, 2018.

[155] A. A. Inyinbor, F. A. Adekola, and G. A. Olatunji, "Kinetics, isotherms and thermodynamic modeling of liquid phase adsorption of Rhodamine B dye onto *Raphia hookeri* fruit epicarp," *Water Resources and Industry*, vol. 15, pp. 14–27, 2016.

[156] M. Sharma, J. Singh, S. Hazra, and S. Basu, "Adsorption of heavy metal ions by mesoporous ZnO and TiO2@ZnO monoliths: adsorption and kinetic studies," *Microchemical Journal*, vol. 145, pp. 105–112, 2019.

[157] E. P. de Sousa, D. T. de Araujo, V. G. Peixoto, B. F. Ferreira, E. H. de Faria, and E. F. Molina, "Effect of sodium bentonite content on structural-properties of ureasilpoly (ethylene oxide)-PEO hybrid: a perspective for water treatment," *Applied Clay Science*, vol. 191, Article ID 105605, 2020.

[158] P. Liu, L. Jiang, L. Zhu, and A. Wang, "Novel approach for attapulgite/poly(acrylic acid) (ATP/PAA) nanocomposite microgels as selective adsorbent for Pb (II) Ion," *Reactive and Functional Polymers*, vol. 74, no. 1, pp. 72–80, 2014.

[159] R. Ahmad and I. Hasan, "L-cystein modified bentonite-cellulose nanocomposite (cellu/cys-bent) for adsorption of Cu^{2+}, Pb^{2+}, and Cd^{2+} ions from aqueous solution," *Separation Science and Technology*, vol. 51, 2016.

[160] V. B. Yadav, R. Gadi, and S. Kalra, "Clay based nanocomposites for removal of heavy metals from water: a review," *Journal of Environmental Management*, vol. 232, pp. 803–817, 2019.

[161] F. Altaf, R. Batool, M. A. Ahmad, R. Raza, M. A. Khan, and G. Abbas, "Novel vinyl-modified sepiolite-based polymer nanocomposites: synthesis and characterization," *Iranian Polymer Journal (English Edition)*, vol. 27, no. 6, pp. 413–422, 2018.

[162] R. S. Hebbar, A. M. Isloor, B. Prabhu, A. M. Inamuddin Asiri, and A. F. Ismail, "Removal of metal ions and humic acids through polyetherimide membrane with grafted bentonite clay," *Scientific Reports*, vol. 8, no. 1, pp. 1–16, 2018.

[163] R. Chakraborty, A. Asthana, A. K. Singh, B. Jain, and A. B. H. Susan, "Adsorption of heavy metal ions by various low-cost adsorbents: a review," *International Journal of Environmental Analytical Chemistry*, vol. 102, pp. 342–379, 2020.

[164] G. Yeganeh, B. Ramavandi, H. Esmaeili, and S. Tamjidi, "Dataset of the aqueous solution and petrochemical wastewater treatment containing ammonia using low cost and efficient bio-adsorbents," *Data in Brief*, vol. 26, Article ID 104308, 2019.

[165] S. A. Khan, M. F. Siddiqui, and T. A. Khan, "Ultrasonic-assisted synthesis of polyacrylamide/bentonite hydrogel nanocomposite for the sequestration of lead and cadmium from aqueous phase: equilibrium, kinetics and thermodynamic studies," *Ultrasonics Sonochemistry*, vol. 60, Article ID 104761, 2020.

[166] D. Abunah, C. Onindo, D. Andala, and E. Ochoti, "Physicochemical removal of heavy metals from contaminated water using recyclable montmorillonite cellulose nanocomposite," *Journal of Materials and Environmental Sciences*, vol. 10, no. 12, pp. 1349–1361, 2019, https://www.jmaterenvironsci.com/Document/vol10/vol10_N12/JMES-2019-10-133-Abunah.pdf.

[167] R. Mirsafaei and M. Kolahdoozan, "Preparation and characterization of poly (amide-ester-imide)/Na$^+$-MMT nanocomposite via ultrasonic method," *Journal of Polymer Engineering*, vol. 37, no. 5, pp. 443–448, 2017.

[168] Z. Cherifi, B. Boukoussa, A. Zaoui, M. Belbachir, and R. Meghabar, "Structural, morphological and thermal properties of nanocomposites poly(GMA)/clay prepared by ultrasound and in-situ polymerization," *Ultrasonics Sonochemistry*, vol. 48, pp. 188–198, 2018.

[169] Thermofisher, "Electron Microscopy | TEM vs SEM | thermo Fisher scientific - ecwhermo Fisher Scientific," 2019, http://www.thermofisher.com/ng/en/home/materials-science/learning-center/applications/sem-tem-difference.html.

[170] M. A. Khan, A. A. Alqadami, S. M. Wabaidur et al., "Oil industry waste based non-magnetic and magnetic hydrochar to sequester potentially toxic post-transition metal ions from water," *Journal of Hazardous Materials*, vol. 400, pp. 1–12, Article ID 123247, 2020.

[171] T. N. Moja, N. Bunekar, S. Mojaki et al., "Polypropylene-Polypropylene-Grafted-maleic anhydride-montmorillonite clay nanocomposites for Pb (II) removal," *Journal of Inorganic and Organometallic Polymers and Materials*, vol. 1, 2018.

[172] L. M. Sanchez, P. S. Shuttleworth, C. Waiman, G. Zanini, V. A. Alvarez, and R. P. Ollier, "Physically-crosslinked polyvinyl alcohol composite hydrogels containing clays,

carbonaceous materials and magnetic nanoparticles as fillers," *Journal of Environmental Chemical Engineering*, vol. 8, no. 3, Article ID 103795, 2020.

[173] H. Soltani, A. Belmokhtar, F. Z. Zeggai, A. Benyoucef, S. Bousalem, and K. Bachari, "Copper(II) removal from aqueous solutions by PANI-clay hybrid material: fabrication, characterization, adsorption and kinetics study," *Journal of Inorganic and Organometallic Polymers and Materials*, vol. 29, no. 3, pp. 841–850, 2019.

[174] K. Zdiri, A. Elamri, M. Hamdaoui, N. Khenoussi, O. Harzallah, and J. Brendle, "Impact of Tunisian clay nanofillers on structure and properties of post-consumer polypropylene-based nanocomposites," *Journal of Thermoplastic Composite Materials*, vol. 32, no. 9, pp. 1159–1175, 2018.

[175] Y. Chen, Z. Guo, X. Wang, and C. Qiu, "Sample preparation," *Journal of Chromatography A*, vol. 1184, pp. 191–219, 2008.

[176] G. Piburn and A. R. Barron, "An introduction to energy dispersive X-ray spectroscopy," in *Physical Methods in Chemistry and Nano Science*, P. M. Raja and A. R. Barron, Eds., 2nd ed., pp. 3–139, Openstax, Houston, Tx, USA, 2012.

[177] B. Cantor, "Bragg's law," in *The Equations of Materials*, D. Henry, N. Eby, J. Goofge, and D. Mogk, Eds., 1st ed., pp. 24–44, Oxford University Press, Oxford, UK, 2020.

[178] H. R. Rafiei, M. Shirvani, and O. A. Ogunseitan, "Removal of lead from aqueous solutions by a poly (acrylic acid)/bentonite nanocomposite," *Applied Water Science*, vol. 6, no. 4, pp. 331–338, 2016.

[179] C. G. Ugwuja, O. O. Adelowo, A. Ogunlaja et al., "Visible-light-mediated photodynamic water disinfection @ bimetallic-doped hybrid clay nanocomposites [Research-article]," *ACS Applied Materials and Interfaces*, vol. 11, no. 28, pp. 25483–25494, 2019.

[180] N. Birkner, *How an Ftir Spectrometer Operates*, UC Davis ChemWiki, 2011.

[181] K. C. Cole, "Use of infrared spectroscopy to characterize clay intercalation and exfoliation in polymer nanocomposites," *Macromolecules*, vol. 41, no. 3, pp. 834–843, 2008.

[182] E. I. Unuabonah, B. I. Olu-Owolabi, K. O. Adebowale, and L. Z. Yang, "Removal of lead and cadmium ions from aqueous solution by polyvinyl alcohol-modified kaolinite clay: a novel nano-clay adsorbent," vol. 26, no. 6, 2008.

[183] R. R. Mohamed, N. A. Rizk, B. M. Abd El Hady, H. M. Abdallah, and M. W. Sabaa, "Synthesis, characterization and application of biodegradable crosslinked carboxymethyl chitosan/poly(ethylene glycol) clay nanocomposites," *Journal of Polymers and the Environment*, vol. 25, no. 3, pp. 667–682, 2017.

[184] M. Shahbazi, H. Jäger, S. J. Ahmadi, and M. Lacroix, "Electron beam crosslinking of alginate/nanoclay ink to improve functional properties of 3D printed hydrogel for removing heavy metal ions," *Carbohydrate Polymers*, vol. 240, Article ID 116211, 2020.

[185] K. R. Rajisha, B. Deepa, L. A. Pothan, and S. Thomas, "Thermomechanical and spectroscopic characterization of natural fibre composites," *Interface Engineering of Natural Fibre Composites for Maximum Performance*, pp. 241–274, 2011.

[186] M. S. H. Akash and K. Rehman, *Thermo Gravimetric Analysis. Essentials of Pharmaceutical Analysis*, Springer Nature, Berlin, Germany, 2020.

[187] N. Saadatkhah, A. Carillo Garcia, S. Ackermann et al., "Experimental methods in chemical engineering:

thermogravimetric analysis—TGA," *Canadian Journal of Chemical Engineering*, vol. 98, no. 1, pp. 34–43, 2020.

[188] T. Y. Inan, "Thermoplastic-based nanoblends: preparation and characterizations," in *Recent Developments in Polymer Macro, Micro and Nano Blends: Preparation and Characterisation*, P. M. Visakh, G. Markovic, and D. Pasquini, Eds., 1st ed., pp. 17–56, Elsevier, Amsterdam, Netherlands, 2017.

[189] A. Maleki, Z. Hajizadeh, V. Sharifi, and Z. Emdadi, "A green, porous and eco-friendly magnetic geopolymer adsorbent for heavy metals removal from aqueous solutions," *Journal of Cleaner Production*, vol. 215, pp. 1233–1245, 2019.

[190] K. Kalantari and M. Afifi, "Novel chitosan/polyvinyl alcohol/ talc composite for adsorption of heavy metals and dyes from aqueous solution," *Separation Science and Technology*, vol. 53, no. 16, pp. 2527–2535, 2018.

[191] U. Malayoglu, "Removal of heavy metals by biopolymer (chitosan)/nanoclay composites," *Seperation of science and Technology*, vol. 53, 2018.

[192] A. Abdeldaym, R. F. Khedr, and R. S. Jassas, "Investigation of structural and physical properties of polypyrrole/natural clay nanocomposite as adsorbent for Zn removal," *Sustainable Chemistry and Pharmacy*, vol. 20, Article ID 100382, 2021.

[193] A. M. E. El-Aziz, K. H. Kamal, K. A. Ali, M. S. Abdel-Aziz, and S. Kamel, "Biodegradable grafting cellulose/clay composites for metal ions removal," *International Journal of Biological Macromolecules*, vol. 118, pp. 2256–2264, 2018.

[194] NanoEarth, "BET (Brunauer–Emmett–Teller)," 2017, https://nanoearth.ictas.vt.edu/access/selector/bet.html.

[195] P. Labs, "BET specific surface area," 2011, https://www. particletechlabs.com/analytical-testing/gas-adsorption-and-porosimetry/bet-specific-surface-area.

[196] R. Batool, F. Altaf, M. U. Hameed et al., "In situ chemical synthesis and characterization of PAN/clay nanocomposite for potential removal of Pb+2 ions from aqueous media," *Journal of Polymer Research*, vol. 28, no. 8, 2021.

[197] D. Abunah, C. Onindo, D. Andala, and E. Ochoti, "Physico-chemical removal of heavy metals from contaminated water using recyclable montmorillonite cellulose nanocomposite," vol. 10, pp. 1349–1361, 2019.

[198] W. Aloulou, H. Aloulou, M. Khemakhem, J. Duplay, M. O. Daramola, and R. ben Amar, "Synthesis and characterization of clay-based ultrafiltration membranes supported on natural zeolite for removal of heavy metals from wastewater," *Environmental Technology & Innovation*, vol. 18, Article ID 100794, 2020.

Research Article

Adsorptive Behavior of Tartaric Acid Treated *Holarrhena antidysenterica* and *Citrullus colocynthis* Biowastes for Decolourization of Congo Red Dye from Aqueous Solutions

Sumaira Basharat,[1] **Rabia Rehman** (ID)**,**[1] **and Sara Basharat**[2]

[1]*Centre for Inorganic Chemistry, School of Chemistry, University of the Punjab, Lahore 54590, Pakistan*
[2]*Institute of Chemistry, University of Education, Lahore, Pakistan*

Correspondence should be addressed to Rabia Rehman; grinorganic@yahoo.com

The aim of the present work is to eradicate Congo red (CR) dye from aqueous solutions since the dye compounds are harmful to human life and the environment leading to detrimental results. For this purpose, *Holarrhena antidysenterica* (HA) and *Citrullus colocynthis* (CC) adsorbents were used for the adsorptive removal of Congo red dye from wastewaters. The unmodified adsorbents (U-HA and U-CC) were chemically modified using tartaric acid (TA). Morphological structures were examined by FTIR and SEM. Batch adsorption studies were tested at a variety of pH, time exposure, temperatures, and adsorbent dosages. Thermodynamic parameters such as Gibbs free energy ($\Delta G°$), enthalpy ($\Delta H°$), entropy changes ($\Delta S°$), and energy of activation (E_a) were also calculated. The results revealed that tartaric acid-*Citrullus colocynthis* (TA-CC) gave optimum conditions of time of contact (35 min), temperature conditions (40°C), pH (3), and dosage of adsorbent (1.6 g) for maximum dye removal. Tartaric acid-*Holarrhena antidysenterica* (TA-HA) gave equilibrium time of contact (30 min), temperature (40°C), and pH optimum (2) along with a 1.6 g dosage of adsorbent. Mechanistic understanding of adsorption isotherm provided that the Langmuir model was followed by raw and modified adsorbents. Maximum adsorption capacities Q_{max} attained were 60.61 (mg g^{-1}), 128.21 (mg g^{-1}), 87.71 (mg g^{-1}), and 131.57 (mg g^{-1}), respectively, for U-HA, TA-HA, U-CC, and TA-CC. The results of kinetic modeling displayed a high value of R^2 (0.99) along with minimal error (RMSE) for dye removal showing that the pseudo-second-order kinetic model has acceptable accuracy. Fourier transform infrared proposed the electrostatic, pi-pi interactions, and hydrogen bonding as dominant adsorption mechanisms at acidic pH, respectively. Rate-determining steps comprise both surface and intraparticle diffusions. Thermodynamics indicated that the dye adsorption of CR is spontaneous, exothermic, and favorable in nature. These agricultural wastes due to specific points such as low cost, availability, and high removal rates of adsorption are highly competent for the expulsion of anionic dye like CR from wastewaters.

1. Introduction

Water pollution is a great worry for modern civilization because of industrialization, population sprouts, and urbanization. The last decade has witnessed rapid degradation of the environment and mankind. Metals [1], drugs [2], endocrine disruptor compounds, chiral pesticides [3], paints, plastics, detergents, surfactants, and dyes are directly discharged into the wastewaters. These compounds persist for a longer time and damage ground and surface water esthetics. In humans, these compounds disrupt endocrine functions and affect the normal functionality of the eyes and skin while the sterility of the gonads is affected in male marine animals [4, 5]. Daphnids, sea shrimps, and crayfishes are poisoned [6].

Dyes when released even in minute quantities pose serious threats. They prevent sunlight penetration, retarded growth, and malfunctioning of the aquatic flora and fauna.

Several by-products are released via oxidation and hydrolysis. Their removal has attracted many researchers worldwide empowering a number of technologies for their eradication. These involve chemical procedures (ozonation, oxidation, and ion exchange) [7–9], physical processes (photolysis and magnetic nanocomposites) [10, 11], and biological methods utilizing enzymes and microorganisms [12].

These classical methods are limited to smaller scale, hazardous sludge production, elevated power consumers, costly apparatus and hardware, insufficient removal of ions, and none produce complete removal of colorants from effluents, hence opting for new insights and pathways into this research [13]. Adsorption is favored due to its low cost, simple methodology, high selectivity, environment friendliness, reduced organic solid waste production [14], simple methodology, modest instrumentation, and abundancy of adsorbents [15, 16]. Agricultural biowastes contain carboxyl, carbonyl, amines, and phenolic functional groups that bind cationic and anionic dyes [17] leading towards purified water and valuable components of production.

The world is now shifting towards the manufacturing of smart appliances, such as stimuli-responsive nanoparticles, which control polymer adsorption interactions in colloidal suspension due to electrostatic, steric, and depleting bridged structures. Dye removal was adopted by using photodegradation on nanoparticles. Nanosized photocatalysts are gaining worldwide importance due to extraordinary surface-to-volume proportion [18, 19].

Congo red, an anionic direct diazo dye, is used in paper, printing, leather, and plastic industries. It is also called 3,3′-(biphenyl-4,4′-diyldidiazene-2,1-diyl)bis (4-aminonaphthalene-1-sulfonic acid)) having molecular formula $C_{32}H_{22}N_6Na_2O_6S_2$ and molecular mass of 696.7 g mol^{-1}. Due to its complex aromatic structure (a central biphenyl group along with two symmetric napthalenic groups) [20], it is difficult to degrade from wastewaters, hence posing serious environmental hazards such as eutrophication. In humans, it causes somnolence and eye, skin, and respiratory problems [21]. Lately, CR had been removed by nanocomposite fibres [11], photocatalysis [22], microwave-assisted adsorption [23], advanced oxidation, and adsorption techniques [24].

In the present study, novel biosorbents *Holarrhena antidysenterica* and *Citrullus colocynthis* were used for the elimination of CR from wastewaters. Both of these adsorbents were subjected to tartaric acid modification to enhance the adsorption performances. Since the adsorbents used are waste materials, this experimentation provides positive significance towards solid waste management and valorisation.

The aim of this study is to utilize the aforementioned adsorbents for the sequestration of Congo red from aqueous wastewaters both in raw and tartaric acid-modified forms. The adsorbents were characterized by Fourier Transform Infrared Spectroscopy (FTIR) and scanning electron microscope. Adsorption parameters such as adsorption dosage, pH studies, temperature measurements, and contact times were studied. Thermodynamics, kinetics, and isothermal studies were investigated to elaborate an efficient and comparative research of the batch adsorption process.

2. Experimental Details

2.1. Chemicals and Instrumentation.
CR ($C_{32}H_{22}N_6Na_2O_6S_2$, molecular weight = 696.665 g/mol) was utilized as such in contrast to any modification. The adsorbents were collected from local Lahore markets (Pakistan). After washing, sunlight drying, and grinding (60 mesh), the obtained adsorbents were stored in airtight glass containers. Chemical modifications were carried out by soaking adsorbents in a 10% aqueous solution of tartaric acid (Merck). 0.1 M sodium hydroxide (NaOH) (98%, Merck) and 0.1 M hydrochloric acid (HCl) (37%, Merck) solutions were used for pH adjustments. Absorbance was observed at λ_{max} = 498 nm using UV-Visible Spectrophotometer 720 (China).

Dye solution (1000 mg/L) was prepared by dissolving 1 g of CR/1000 mL distilled water. Further solutions were made by the dilution method. Experiments were performed twice, and average values were calculated. FTIR and SEM analysis were done by Cary 630 Agilent technology (USA) and Nova NanoSem 450 (Thermo Fischer Scientific (USA)).

2.2. Batch Experiments.
Experiments were performed in batch mode. Adsorption parameters such as adsorbent dosage, temperature studies, pH, and time of contact were performed using 100 mL CR dye solutions in 250 mL conical flasks. Filtrates were checked for dye concentrations, using a UV-Vis spectrophotometer [25].

Adsorption capacity, q_t (mg·g^{-1}) or amount of CR dye adsorbed on adsorbents at time t, was calculated by following the mass-balance relationship.

$$q_t = (C_o - C_t)\frac{V}{m}, \tag{1}$$

where C_o is the initial CR concentration (mg·L^{-1}), C_t is the dye concentration at any time t, V is the volume of solution (L), and m is the amount of adsorbents used (g). The dye removal efficiency was monitored by

$$\%\text{adsorption} = C_o - \frac{C_t}{C_o} \times 100. \tag{2}$$

3. Results and Discussion

3.1. Chemical Treatment.
Chemical pretreatment of biological wastes extracts soluble organic compounds and enhances chelating properties. Different modifying agents such as mineral and organic acids (sulfuric acid, nitric acid, hydrochloric acid, tartaric acid, citric acid, and thioglycolic acid), bases (sodium carbonate, sodium hydroxide, and calcium hydroxide) [26], organic compounds (methanol, formaldehyde, epichlorohydrin, and ethylenediamine), and oxidizing agents (hydrogen peroxide) [27] were used. These entities reduce moisture levels and minimize fungal and bacterial attacks, enhancing adsorbent stability [28]. Uniform distribution of ions increases functionality, and acidic modifications rise protonation [29, 30] and ester linkages [31], exposing more binding sites. Alkali treatment promotes high micropore percentages [32, 33] and swelling and
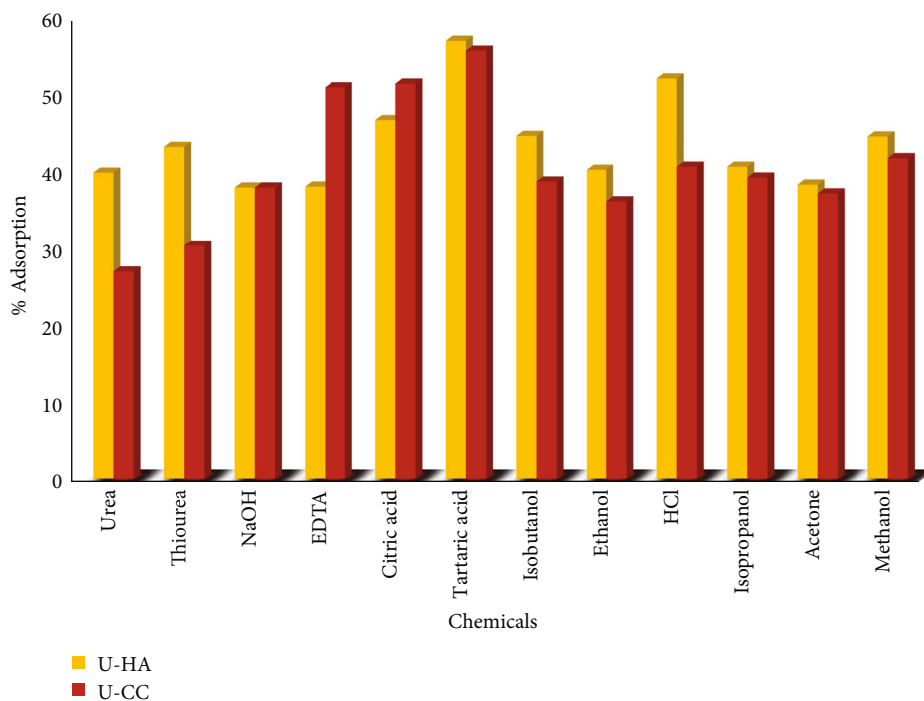
FIGURE 1: Chemical treatment of adsorbents.

disintegrating of the biomass [34, 35]. Early attainment of equilibrium is achieved [36]. 5 g U-HA and U-CC when dissolved in 25 mL of acidic, basic, and chelating solvents for 4 hours resulted in filtrates that gave the desired results when treated with CR [37]. Tartaric acid gave the most promising results as shown in Figure 1).

3.2. Characterization

3.2.1. Physiochemical Analysis. Physiochemical analysis when performed on the adsorbents gave the following results.

Moisture contents were lesser in CC than in HA. The presence of moisture decreases the pore connectivity and hampers the adsorption process. Bulk, dry densities, and porous nature of CC are nearly the same, slightly elevated than HA. A higher value of particle density, bulk density, and porosity contributes towards greater aesthetics of adsorbents [38, 39]. HA samples bore more ash content components than CC, which can interfere with the pore structure development, leading to increased hydrophilicity and catalytic effects. This causes lower adsorption, decreased mechanical strength, and restricting process during regeneration [40]. Iodine values determine the internal capacity volumes and dispersion degrees of the micropores by determining the amount of iodine adsorbed; thus, the adsorbent capability to eradicate pollutants can be determined. Surface acidity was estimated using Boehm titrations [41]. It was seen that higher acidic groups were present in CC than in HA due to reaction with tartaric acid. Boehm indicated that oxidation groups such as carboxylic acids and phenols were resultant of oxidation reactions. These were present in the lignin, cellulose, and hemicellulose components of the lignocellulosic materials. Overall, *Citrullus colocynthis* (CC) was a better

TABLE 1: Physiochemical properties of adsorbents.

Properties	HA	CC
Bulk density	0.95	0.96
Dry density (g/cm^3)	0.73	0.79
Porosity (%)	0.974	0.975
Moisture (%)	11	07
Ash (%)	23	16
Volatile matter (%)	84.24	76.42
Iodine number (mg/g)	16.92	28.99
Carboxylic groups (mmol)	1.98	1.94
Phenols (mmol)	0.94	0.96
Lactones (mmol)	0.84	1.08

adsorbent than *Holarrhena antidysenterica* (HA) towards the adsorption of CR dye. Table 1 shows the results obtained.

3.2.2. Fourier Transform Infrared Studies (FTIR). Functional groups, organic moieties, and nature of interactions between the dye and adsorbents can be estimated by using FTIR spectroscopy. Figure 2 shows FTIR band frequencies in the span of 400-4000 cm^{-1} for U-HA, TA-HA, U-CC, and TA-CC with CR dye.

U-HA reacts with CR (Figure 2(a)) to give wide stretches at 3737.6 cm^{-1} and 3653.0 cm^{-1} corresponding towards –OH groups of alcohols and phenols, and the peaks at 2922 cm^{-1}, 2918 cm^{-1}, 2853 cm^{-1}, and 2850 cm^{-1} are indicative of asymmetric and symmetric sp^3 C-H stretch [42], while weak peaks of 2371 cm^{-1} show the alkyne or nitrile group. Some peaks of 1654 cm^{-1}, 1636 cm^{-1}, and 1647 cm^{-1} demonstrate aromatic -C=O and C=C linkages of carboxylic acid
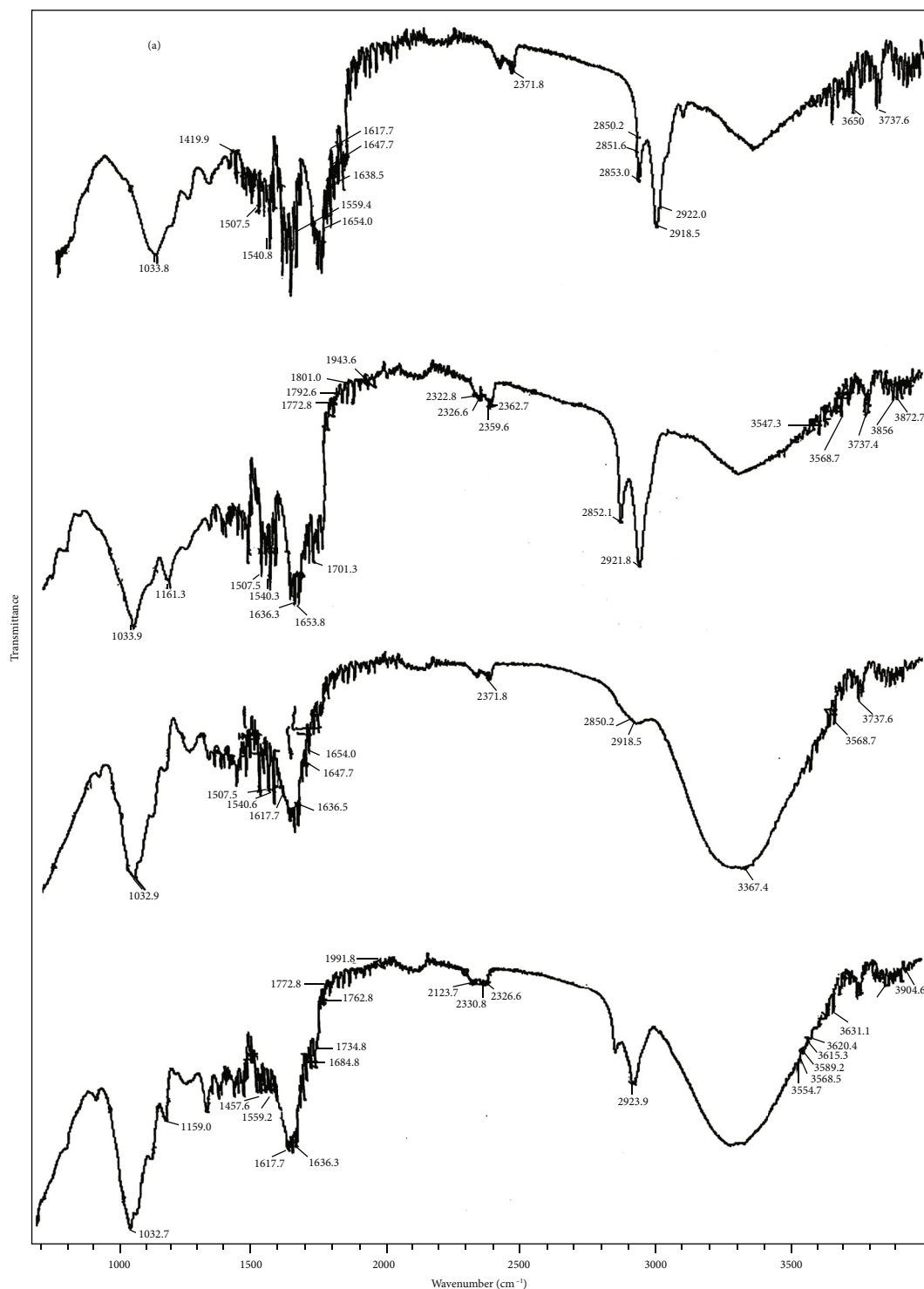
Figure 2: FTIR of raw and modified adsorbents: (a) U-HA-CR, (b) TA-HA-CR, (c) U-CC-CR, and (d) TA-CC-CR.

anions/amide linkages formed between CR and U-HA. When TA-HA was treated with CR (Figure 2(b)), a few additional peaks were observed such as $3872\,\text{cm}^{-1}$, $3856\,\text{cm}^{-1}$, $3737\,\text{cm}^{-1}$, $3568\,\text{cm}^{-1}$, and $3547\,\text{cm}^{-1}$ displaying peaks of hydroxyl of alcohols and phenols. Reduced peaks of $2921\,\text{cm}^{-1}$ and $2852\,\text{cm}^{-1}$ are evident of asymmetrical and symmetrical alkane sp^3 C-H stretch. Weak peaks of $2366\,\text{cm}^{-1}$ contribute to alkyne/nitrile moieties. Peaks of $1801\,\text{cm}^{-1}$, $1792\,\text{cm}^{-1}$, $1772\,\text{cm}^{-1}$, and $1701\,\text{cm}^{-1}$ represent C=O peaks of anhydride, carboxylic acids, and aldehydes. Strong peaks at $1653\,\text{cm}^{-1}$ and $1636\,\text{cm}^{-1}$ are evident of aromatic amides/-C=O/C=C bonds in carboxylic acid anions, indicating the reaction of CR with tartaric acid-treated adsorbent. $1540\,\text{cm}^{-1}$ and $1457\,\text{cm}^{-1}$ display C-H bending/
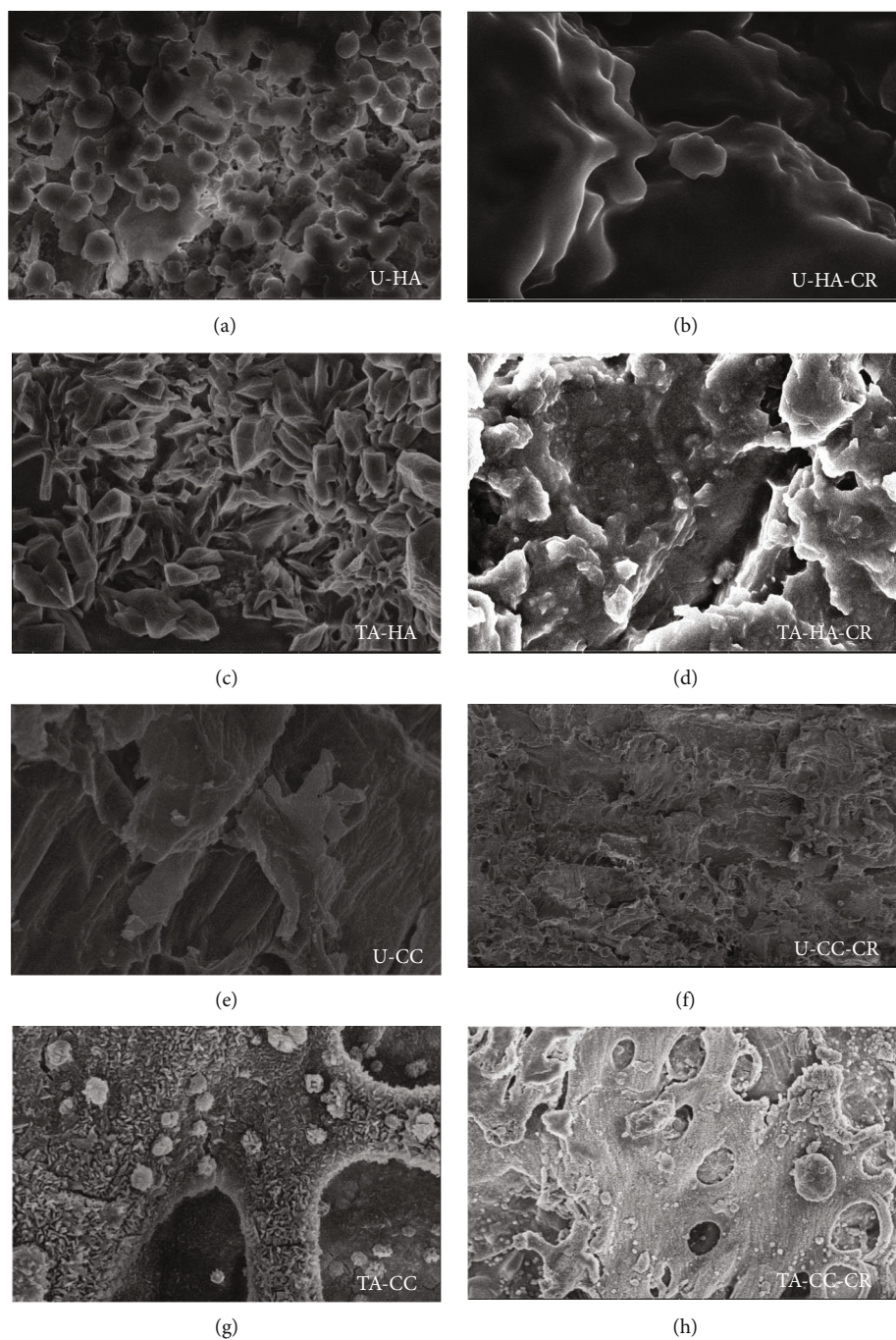
Figure 3: SEM illustrations of (a) U-HA, (b) U-HA-CR, (c) TA-HA, (d) TA-HA-CR, (e) U-CC, (f) U-CC-CR, (g) TA-CC, and (h) TA-CC-CR.

C=C/phenolic OH and –C=O of carboxylates. $1161\, cm^{-1}$ show –C-O of ester linkages formed between tartaric acid and lignocellulosic materials.

The second adsorbent U-CC (Figure 2(c)) when reacted with CR was seen to consist of -OH stretch at $3568\, cm^{-1}$ and $3737\, cm^{-1}$ while alkenyl stretch at $3367\, cm^{-1}$ and alkane C-H at $2850\, cm^{-1}$. Peaks at $1654\, cm^{-1}$, $1647\, cm^{-1}$, and $1636\, cm^{-1}$ display -C=O of amide, aromatic -C=O, and C=C of carboxylic acid anions whereas $1559\, cm^{-1}$ show C-H bending/C=C stretches. When TA-CC was treated with CR (Figure 2(d)), new peaks displaying hydroxyl groups were observed such

as $3904\, cm^{-1}$, $3841\, cm^{-1}$, $3631\, cm^{-1}$, and $3547\, cm^{-1}$. Alkyl C-H stretch was seen at $2923.9\, cm^{-1}$ while $2326\, cm^{-1}$ displayed weak nitrile groups. Weak peaks at $1772\, cm^{-1}$ represent C=O of carboxylic acids, and $1734\, cm^{-1}$ are evident of ester linkages (–COO⁻)/(–COOR) formed between cellulose and tartaric acids. $1684\, cm^{-1}$ represent amide groups of CR reaction with adsorbent while $1457\, cm^{-1}$ show C-H bend. A strong $1159\, cm^{-1}$ peak is evident of esters.

3.2.3. Scanning Electron Microscopy. SEM was used to investigate the structural properties of raw and modified forms of

(a)

(b)

(c)

(d)
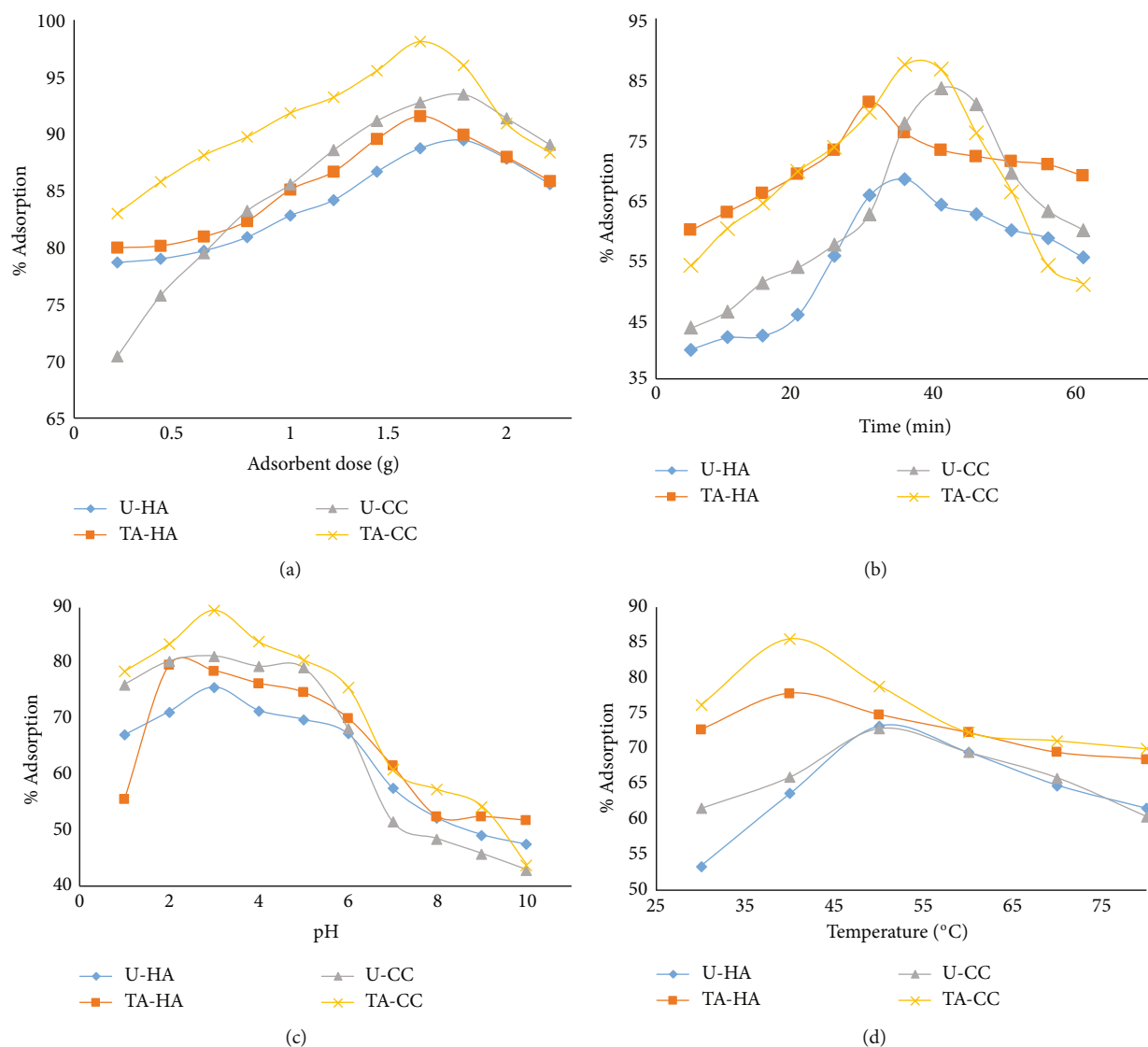
FIGURE 4: (a) Dosage of adsorbents, (b) contact times, (c) pH changes, and (d) temperature studies for CR eradiation.

adsorbents. It was seen that U-HA consists of porous, irregular, and spherical aggregates (Figure 3(a)) that convert to sharply chiseled structures upon chemical modifications (Figure 3(c)) while the U-CC consists of porous, aggregated plate-shaped structure (Figure 3(e)) that convert towards agglomerated, porous, irregular-shaped structure upon modifications (Figure 3(h)). The tissues are arranged in layers that provide additional adsorbent sites for the sequestration of the dye [43]. When CR was adsorbed, characteristic changes of the phase were observed. Irregular structures were converted to smooth pattern due to the binding of CR dye molecule over the adsorbent sites after CR adsorption (Figures 3(b), 3(d), 3(e), and 3(h))) [39].

3.3. Effect of Adsorbent Dosage. Chemical modification increased the availability of potential sites at lower concentrations; however, overlapping of sites was observed in higher amounts. U-HA removed CR dye up to 89%, and U-CC sequestered 93%, at 1.8 g, whereas TA-HA and TA-CC eradicated 91% and 98% at 1.6 g, respectively (Figure 4

(a)). After reaching maximum adsorption efficiency (91-98%), an increase in dosage does not have much dye sequestration efficiency. This is due to the gradient distribution and active site saturation between the adsorbent and dye [43, 44]. Hence, 1.8 g adsorbent dose for TA-HA and 1.6 g of TA-CC were selected for further experiments as higher concentrations did not yield significant results.

3.4. Effect of Contact Time. The effect of contact time is one of the most important parameters as adsorption mechanism and rate-determining steps are dependent upon its findings [45]. CR dye sequestration by adsorbents is determined by investigating the least time required for achieving equilibrium of dye with the adsorbent. The procedure was carried out for sixty minutes with five minutes time interval until equilibrium was achieved. Adsorption increased at initial stages [46] and decreased at later terminals, where repulsion of adsorbed-non-adsorbed species rendered its efficiency. About 68% CR dye was adsorbed at 35 minutes for U-HA that increased up to 81% at 30 minutes for TA-HA. U-CC

removed 83% of CR at 40 minutes, which rose to 87% at 35 minutes for TA-CC (Figure 4(b)).

3.5. Influence of pH on CR Adsorption.

The binding of dye molecules with the adsorbent surface is monitored by pH as it changes the degree of ionization of adsorbed species and properties of adsorbent surfaces [47, 48]. Acidic pH promotes protonation of carboxylic acids, which are present in lignocellulosic materials resulting in acidic adsorption sites. Excess of H^+ ions battles against the positive groups of basic dyes for adsorption surfaces, resulting in repulsion among the cationic groups of adsorbent and dye. A decrease in hydrogen bonding is observed and anionic dye adsorption is favored. Whereas basic pH causes deprotonation of functional moieties, more hydroxyl ions render adsorption of anionic dyes, and positive charges are reduced at solid-liquid interphase, making the adsorption surface negatively charged, attracting cationic colorants. A range of 1-10 pH was selected for the sequestration of the acidic dye. CR dye adsorption depends upon charge and surface characteristics. Point of zero charge (pHpzc) [49, 50] was found to be 5 for U-HA and 6 for U-CC, determined by the electrochemical method [51] in our previous studies [37]. At pH > pHpzc, the adsorbent is negatively charged while it is positive at pH < pHpzc. At lower pH, Congo red is dissociated into polar groups (R-SO$_3^-$) and the positive surface of adsorbent attracts the sulfonate moieties through electrostatic attractions. While at alkaline pH, higher (OH$^-$) and (COO$^-$) concentrations compete with the dye anions for potential sites, offering repulsion and decrease in adsorption capacity [52, 53]. At pH 3, U-HA removed 75% CR which increased to 79% at pH 2 for the treated form. U-CC adsorbed CR up to 81% for untreated adsorbent and 89% for modified forms at pH 3 (Figure 4(c)).

3.6. Temperature.

Rise in temperature promotes entropy changes and inflammations in dye particles. An increase in kinetic energy favors the intraparticle diffusion model. The effect of temperature (in the range of 30-80°C) on CR adsorption was studied. 73% adsorption was observed at 50°C for U-HA that rose to 75% at 40°C for modified forms. U-CC was seen to remove 72% at 50°C and 85% for treated adsorbents at 40°C (Figure 4(d)). Removal efficiency decreased after saturation point indicating the reaction to be an exothermic one. Increased mobility of larger dye ion with temperature increases adsorption.

3.7. Kinetic Studies.

Rate estimation and mechanistic understanding of adsorption procedure require the performance of kinetic studies. These studies are dependent upon physical and chemical properties of adsorbents and affect the adsorption mechanism [54, 55]. Popular models such as pseudo-first-order, pseudo-second-order [55], and Elovich models [56–58] were considered to elucidate CR adsorption mechanism on adsorbents.

Pseudo-first-order reaction displays dependency of adsorption on freely bounded surfaces. Its linear (Equation (3)) and nonlinear forms (Equation (4)) are shown as follows:

$$\ln (q_e - q_t) = \ln q_e - k_1 t, \tag{3}$$

$$q_t = q_e(1 - \exp - k_1 t), \tag{4}$$

where q_e (mgg^{-1}) and q_t (mgg^{-1}) are the amounts of CR adsorbed at equilibrium and time t, k_1 (min^{-1}) represents the rate constant for pseudo-first-order reaction. A graph between $\ln (q_e - q_t)$ against t yields a straight line, from which k_1 and regression coefficient R^2 are calculated [59].

Reaction kinetics can also be explained by using pseudo-second-order reaction. Linear (Equation (5)) and nonlinear (Equation (6)) forms are as follows:

$$\frac{t}{q_t} = \frac{1}{K_2 q_e^2} + \frac{t}{q_e}, \tag{5}$$

$$q_t = \frac{t.k_2 (q_e)^2}{1 + tk_2.q_e}. \tag{6}$$

A plot of t/q_t against t gives k_2 (g·mg^{-1} min^{-1}) which is the equilibrium rate constant. Initial rate of adsorption h (mg·g^{-1} min^{-1}) is given by Equation (7) [46]:

$$h = K_2 q_e^2. \tag{7}$$

The Elovich equation determines the adsorption on heterogeneous adsorbent surfaces. It is represented as linear (Equation (8)) and nonlinear (Equation (9)) as follows:

$$q_t = \frac{\ln (\alpha \times \beta)}{\beta} + \frac{\ln t}{\beta}, \tag{8}$$

$$q_t = q_e(1 - \exp - k_1 t), \tag{9}$$

where α (mg·min/g) and β (g/mg) are initial process rate constant and factors related to the activation energy for chemical adsorption. A plot between q_t and $\ln t$ gives a straight line from which α and β can be obtained.

Quantitative checking is performed by utilizing percent relative deviation (P) as shown in

$$P = \frac{100}{N} \sum \left\{ \frac{q_{e(\exp)} - q_{e(\text{cal})}}{q_{e(\exp)}} \right\}. \tag{10}$$

Here, $q_{e(\exp)}$ (mg·g^{-1}) is the experimental adsorption capacities, $q_{e(\text{cal})}$ (mg/g) calculated adsorption capacities, and N represents the total number of observations made during the adsorption experiment. A lower P value is indicative of higher appropriateness of the kinetic data [60].

Absorbance values were demonstrated using 25 mg/L of CR dye solutions at 298 K with a 5-minute interval for retention kinetics. The upper buoyant floating layer of CR was observed. It displayed rapid adsorption in the initial stages that gradually receded as the experiment approached equilibrium.

CR retention on adsorbents (raw and modified) was performed (Table 2). Comparison of correlation coefficient R^2 proves that Ho's model agrees with the experimental data in all states. Moreover, ($q_{e(\text{calc})}$) is in complete agreement to that of ($q_{e(\exp)}$). A smaller variance "P" is observed among

TABLE 2: Kinetic parameters for CR dye adsorption.

Kinetic models	U-HA	TA-HA	U-CC	TA-CC
Elovich				
a (g mg^{-1} min^{-1})	2.67	2.43	3.03	4.41
b (g mg^{-1})	9.62	4.26	18.05	55.56
R^2	0.9465	0.8752	0.8206	0.5199
RMSE values	0.199637	0.090748	0.286502	0.4375
Pseudo-First order Kinetics				
$q_{e(\text{experimental})}$ (mg g^{-1})	1.39	1.56	1.33	1.56
$q_{e(\text{calculated})}$ (mg g^{-1})	0.03	0.01	0.02	0.07
k_1 (1/min)	0.19	0.23	0.16	0.21
R^2	0.3724	0.7802	0.8194	0.8413
P	13.67	15.59	13.19	15.09
RMSE	0.37862719	0.43454551	0.38183609	0.45346783
Pseudo-second Order Kinetics				
$1/q$	0.7234	0.6636	0.7443	0.6408
k_2 (g/(mgmin))	0.84	6.52	1.00	2.97
q_e (mg g^{-1})	1.38	1.51	1.34	1.56
$t^{1/2}$	0.86	0.10	0.74	0.22
h (mg/g·min)	1.62	14.81	1.81	7.25
R^2	0.9978	0.9991	0.9995	0.9999
P	3.93	5.94	3.26	5.55
RMSE	0.018268723	0.018746589	0.000763183	0.002285479
Intraparticle diffusion				
k_{id} (mg/(g min$^{1/2}$))	0.0398	0.0427	0.0265	0.0276
C (mg g^{-1})	1.1041	1.279	1.1485	1.4108
R^2	0.891	0.7905	0.7958	0.8904
Film diffusion				
K_{fd} (1/min)	0.0996	0.1298	0.0576	0.0751
R^2	0.958	0.898	0.9093	0.9647

the calculated and experimental values of pseudo-second-order kinetics. An increase in initial adsorption rate "h" and a decline in $t^{1/2}$ were seen as the adsorbents shifted towards the chemically modified structures [32, 61]. Chemisorption at available adsorption sites [62] may be involved in the dye elimination utilizing covalent bonding (sharing or electron transfer) among CR and adsorbents [43, 63]. The Elovich model displayed a least fitting R^2.

3.8. Calculation of Errors. RMSE (Root Mean Square Error) (Equation (11)) was calculated in this study to estimate the deviation among the experimental and calculated observations. The model with the minimum error was the one accepted (Table 2).

$$\text{RMSE} = \sqrt{\sum \frac{\left(q_{e(\text{cal})} - q_{e(\text{exp})}\right)^2}{N}}. \quad (11)$$

Here, $q_{e(\text{exp})}$ (mg/g) defines experimental values, $q_{e(\text{cal})}$ (mg/g) calculated numbers at time t, and N displays total number of

observations. The pseudo-second-order model and Langmuir isotherms displayed the least error [64].

3.9. Mass Transfer Parameters. The intraparticle or boundary layer diffusion mechanism is responsible for CR adsorption on raw and treated adsorbents. The complete adsorption procedure consists of multiple steps such as (a) film diffusion, adsorbate heading for the massed adsorbent, (b) intraparticle/pore diffusion, penetration occurs from exterior to interior orifices, and (c) complex forming within the colorant and chemical groups in the adsorbent [65]. The intraparticle diffusion model was popularized for the understanding of the mechanism involved [66]. The Webber and Morris equation is as under

$$q_t = k_{id} t^{1/2}. \quad (12)$$

Here, q_t (mg/g) is the amount adsorbed at time t and k_{id} (mg g^{-1} min$^{-1/2}$) is the coefficient of intraparticle diffusion. This mechanism is the sole process if the origin is intersected when q_t is plotted against $t^{1/2}$. Multilinear plots show a

variety of steps involved. Initial steps involve adsorbate diffusion on the exterior of the adsorbent or the boundary layer diffusion of solute particles, next is the gradual adsorption phase where the intraparticle diffusion rate becomes limiting. At the last equilibrium stage, intraparticle diffusion slows down due to the least availability of dye particles in the solution [67]. "C" values determine the thickness of the adsorbent layer [44]. When $C = 0$, adsorption is limited and intraparticle diffusion mechanism is involved. Negative C shows an increase in the border layer while positive values are representative of rapid adsorption [68]. The values are raised for the modified forms leading towards the complexity of the adsorption procedure. Table 2 represents the entire figures of the model.

The rate of uptake is limited by the adsorbate's size, diffusion coefficient, concentration, and attraction towards the adsorbent. Degree of mixing, bulk phase, and pore-size distribution of the adsorbent also play an important role. Systems with higher concentrations of dyes, great mixing, higher particle size, and a lower adsorbent affinity towards the adsorbent favor the intraparticle diffusion mechanism [69]. The results are displayed in Figures 5(d) and 5(e).

Boyd's plots involve fractional attainment of equilibrium with time variations [70]:

$$\ln\,(1 - F) = -\left(K_{fd}t\right), \tag{13}$$

$$F = \frac{q_t}{q_e}. \tag{14}$$

When the graph plotted among B_b and t passes through the origin, the Webber-Morris mechanism is involved. However, if not crossed, the boundary layer/chemical reaction is involved. Figures 5(f) and 5(g) indicate that the mechanism is the boundary layer. Straight paths are following the curved ones with varied adsorption lengths in the initial and final stages. Hence, the boundary layer diffusion prevails in the initial stages while intraparticle in the later ones. Increased K_{fd} values along with higher correlations R^2 against intraparticle (Table 2) are in complete agreement with the proposed mechanism.

3.10. Isothermal Studies. Isothermal study determines the adsorbent's capacity, surface characteristics, and the mechanism of the adsorption process [71]. It was done by selecting 10 mg/L, 15 mg/L, 20 mg/L, 25 mg/L, 30 mg/L, 35 mg/L, and 40 mg/L concentrations of CR dye in 250 mL sealed flasks. Optimum conditions of contact time, temperature, pH, and dose of adsorbent were selected for this study. The equilibrium dye retention was investigated using the Langmuir, Freundlich, Temkin, and Dubnin Radoshkevich (D-R) isotherms.

Langmuir isotherm addresses the adsorption process as monolayered, homogeneously distributed over a fixed number of adsorption sites, involving no interaction among the adsorbed species. Homogeneity is further used for the description of binary system behavior [72].

The linear [73] and nonlinear forms [74] are given as follows:

$$\frac{1}{q_e} = \frac{1}{q_m} + \frac{1}{K_L q_m C_e}, \tag{15}$$

$$q_e = \frac{K_L q_m c_e}{1 + K_L c_e}, \tag{16}$$

where K_L (L/mg) is called the Langmuir constant; q_m (mg/g) is the maximum uptake ability of the adsorbent; C_e (mg/L) is the equilibrium CR dye adsorption. The graph between $1/C_e$ against $1/q_e$ gives the desired plot [75].

Separation factor R_L calculated from Langmuir constants holds prime importance [70]:

$$R_L = \frac{1}{1 + K_L C_o}, \tag{17}$$

where C_o (mg/g) is the initial CR concentration. The adsorption process is unfavorable if $R_L > 1$, linear if $R_L = 1$, appropriate if $0 < R_L < 1$, and irreversible if $R_L = 0$.

Freundlich isotherms is another model used for heterogeneous, multilayer adsorption systems. This isotherm favors physisorption. Linear (Equation (18)) and nonlinear forms (Equation (19)) of the Freundlich equation are shown as

$$\log q_e = \log K_f + \frac{1}{n}\,\log C_e, \tag{18}$$

$$q_e = K_f C_e^{1/n}, \tag{19}$$

where C_e (mg/L) is the CR dye equilibrium concentrations and q_e (mg/g) is the amount of CR dye adsorbed. $k_f f$ ((mg/g /(L/mg)$^{1/n}$) is the binding constant, and n (g/L) is the adsorption strength. These are determined from the slope and intercept of the straight line when $\log q_e$ is plotted against $\log C_e$. Varied adsorption systems (chemical, physical, and linear) are predicted by values of n (heterogeneity factor) [56, 72]. It depends upon the coordination number of dye, dye-adsorbate attractions, Avogadro's number, and Boltzmann constant. A value close to 0 indicates physisorption while near to 1 is imminent of chemical adsorption or cooperative adsorption.

The Temkin isotherm demonstrates linear reduction of adsorption heat in all surface structures during adsorbent-dye interactions [76]. Linear (Equation (20)) and nonlinear (Equation (21)) Temkin isotherm is given as

$$q_e = B \ln C_e + B \ln A, \tag{20}$$

$$q_t = \frac{1}{b}\,(\ln\,(a.b.t)), \tag{21}$$

where A_T (L/g) is the equilibrium binding constant and B_T (J·mol^{-1}) is the heat of adsorption. These are determined
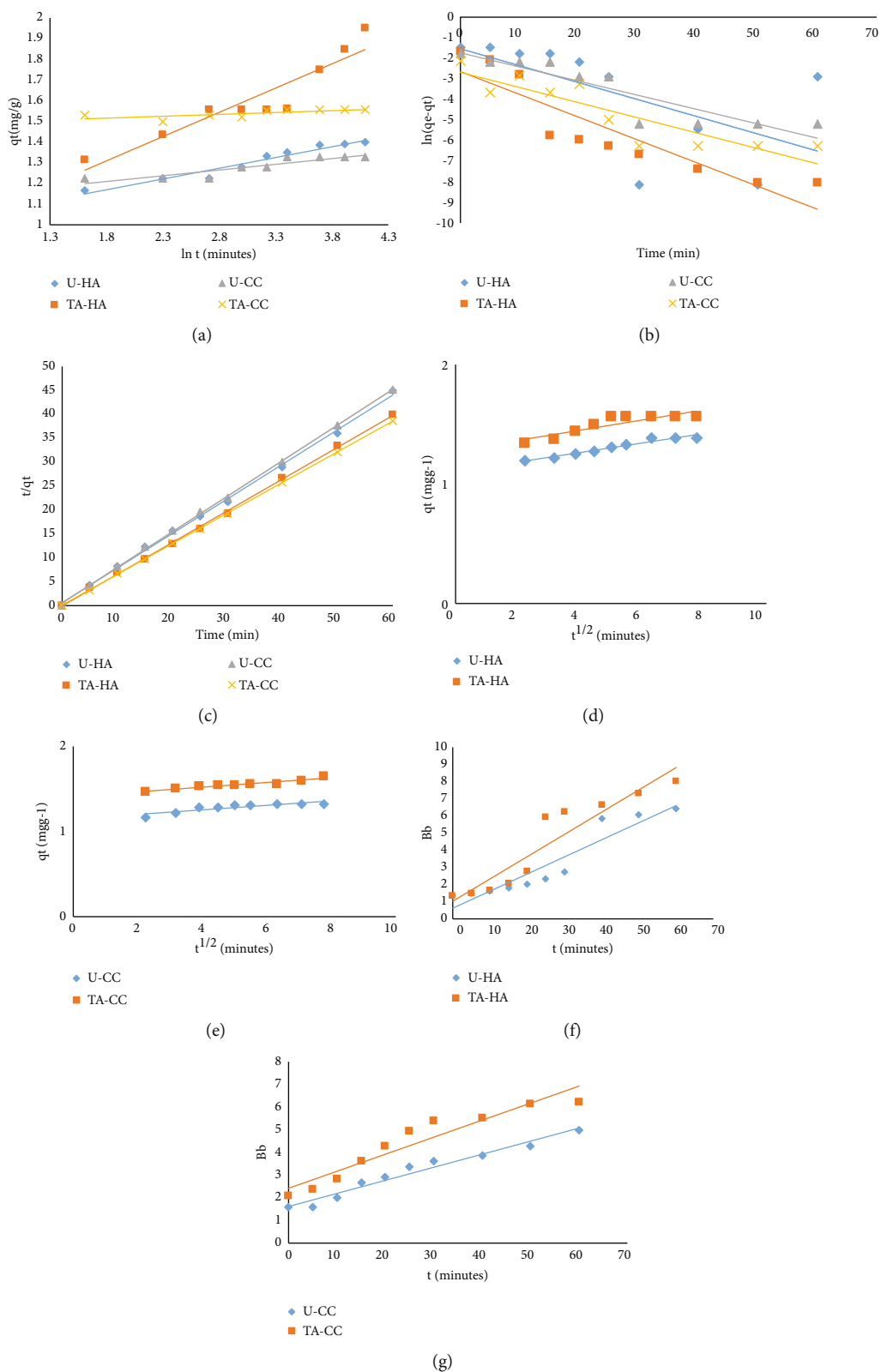
Figure 5: (a) Elovich designs, (b) Pseudo-First-Order kinetics, (c) Pseudo-Second-Order kinetics, (d) Webber-Morris plots (U-HA and TA-HA), (e) Webber-Morris plots (U-CC and TA-CC), (f) Boyd's plots (U-HA and TA-HA), and (g) Boyd's plots (U-CC and TA-CC) for CR dye.

from slope and intercept of linear plots of q_e against $\ln C_e$. B_T lower values than 8 describe weak physical adsorption but higher than 8 correspond to strong chemical adsorption [77, 78]. Moreover, a higher B_T is responsible for rapidity of the rate of adsorption at initial stages while a low A_T ratio is indicative of weak bonds among adsorbent and adsorbate.

Another adsorption isotherm is the Dubnin-Radoshkevich (D-R) isotherm, which considers adsorption on homo- and heterogeneous potential sites [79] for intermediate ranges of concentrations. Complete free energy as well as physical and chemical properties of the procedure is represented in this isotherm. Linear (Equation (22)) and nonlinear form (Equation (24)) of D-R isotherm is given as

$$\ln q_e = \ln q_m - \beta\varepsilon^2, \tag{22}$$

$$\varepsilon = RT \ln\left(1 + \frac{1}{C_e}\right), \tag{23}$$

$$q_e = q_m \exp\left(-\beta\varepsilon^2\right). \tag{24}$$

Using "β" (mol^2/J^2), mean free energy "E" (Equation (25)) is calculated:

$$E = \frac{1}{\sqrt{2\beta}}. \tag{25}$$

The adsorption process depends upon E values, where <8 kJmol^{-1} represents physical adsorption, intermediate range 8-16 kJmol^{-1} shows ion-exchange phenomenon, and >16 kJmol^{-1} shows chemical adsorption process. Plots of $\ln q_e$ and $\mathcal{E}^2$ provide linear plots of D-R isotherms [70].

Equilibrium isotherms are used for describing surface characterization and equilibrium behavior between dye and adsorbent (Table 3 and Figure 6). As seen from the table, correlation coefficient R^2 for Langmuir isotherm is in close proximity to one and higher than correlation coefficients of all other isothermic models. Hence, the Langmuir model is more in acceptance towards the experimental data. Q_m for U-CC and its modified forms is higher than U-HA and its treated forms, indicating better CR dye quenching. Hence, adsorption of CR on raw and modified adsorbents is single-layered, homogeneous, and chemically adsorbed process with no side reactions occurring among the molecules [80]. R_L values were lower than one implying a favorable adsorption [71]. Moreover, b values were in favor of CR adsorption on raw and modified adsorbents.

The correlation coefficient of Freundlich, which is lesser, does not favor the physisorption mechanism. Temkin and D-R isotherm lower R^2 values also render fitting of these models towards the experimental values. A higher ratio of potential sites and better chelating abilities of CR are responsible for this trend.

3.11. Thermodynamic Studies. To study the effect of temperature on CR adsorption, temperature-controlled studies were done in the 283 K-323 K range. Equations (26)–(28)

TABLE 3: Isothermal parameters for CR dye adsorption.

Isotherm models	U-HA	TA-HA	U-CC	TA-CC
Langmuir				
Q_m (mg/g)	60.61	128.21	87.71	131.57
R_L (L mg^{-1})	0.47-0.25	0.12-0.05	0.29-0.13	0.15-0.06
b (L g^{-1})	0.03	0.23	0.07	0.25
R^2	0.9801	0.9812	0.9921	0.9918
RMSE	10.851	3.005	9.4962	1.605805728
Freundlich				
n	0.691	1.53	0.75	1.43
K_f (mg/g)	1.25	25.28	6.32	29.26
R^2	0.9667	0.9672	0.9897	0.9838
RMSE	11.048	3.745	9.924	2.561
Temkin				
B (J mol^{-1})	0.07	0.09	0.07	0.07
A (L g^{-1})	0.25	2.30	0.73	2.03
R^2	0.918186	0.9525	0.9517	0.98
RMSE	14.095	52.701	17.092	25.997
D-R				
Q_m (mg/g)	56.4864	65.157	56.7582	79.3366
B_D (mol^2/KJ^2)	6×10^{-6}	3×10^{-7}	3×10^{-6}	1×10^{-7}
E_D (KJ/mol)	0.28	0.41	0.40	0.71
R^2	0.9219	0.9482	0.9282	0.9346
RMSE	3.0368	10.272	10.0011	17.948

were employed for the calculations and represented in (Table 4) along with (Figure 7).

$$\ln K_d = \frac{-\Delta H^\circ}{RT} + \frac{\Delta S^\circ}{R}, \tag{26}$$

$$\Delta G^\circ = -RT \ln K_d, \tag{27}$$

$$K_d = \frac{Q_e}{C_e}, \tag{28}$$

where K_d is the equilibrium constant. ΔG°, ΔH°, and ΔS° are Gibbs free energy, enthalpy, and entropy, respectively. ΔH° and ΔS° are determined from Van't Hoff plots. A favorable adsorption process is the one that shows negative (ΔG°) and increased K_d with the advancement of temperature [81]. ($0 > \Delta H^\circ$) shows the exothermic nature of the CR adsorption, and ($0 < \Delta S^\circ$) shows increased randomness or entropy of the process. Activation energy is determined by the Arrhenius equation:

$$\ln k = \frac{\ln A - E_a}{RT}, \tag{29}$$

where A is the frequency factor. Overall, the reaction comes out to be a physical one.
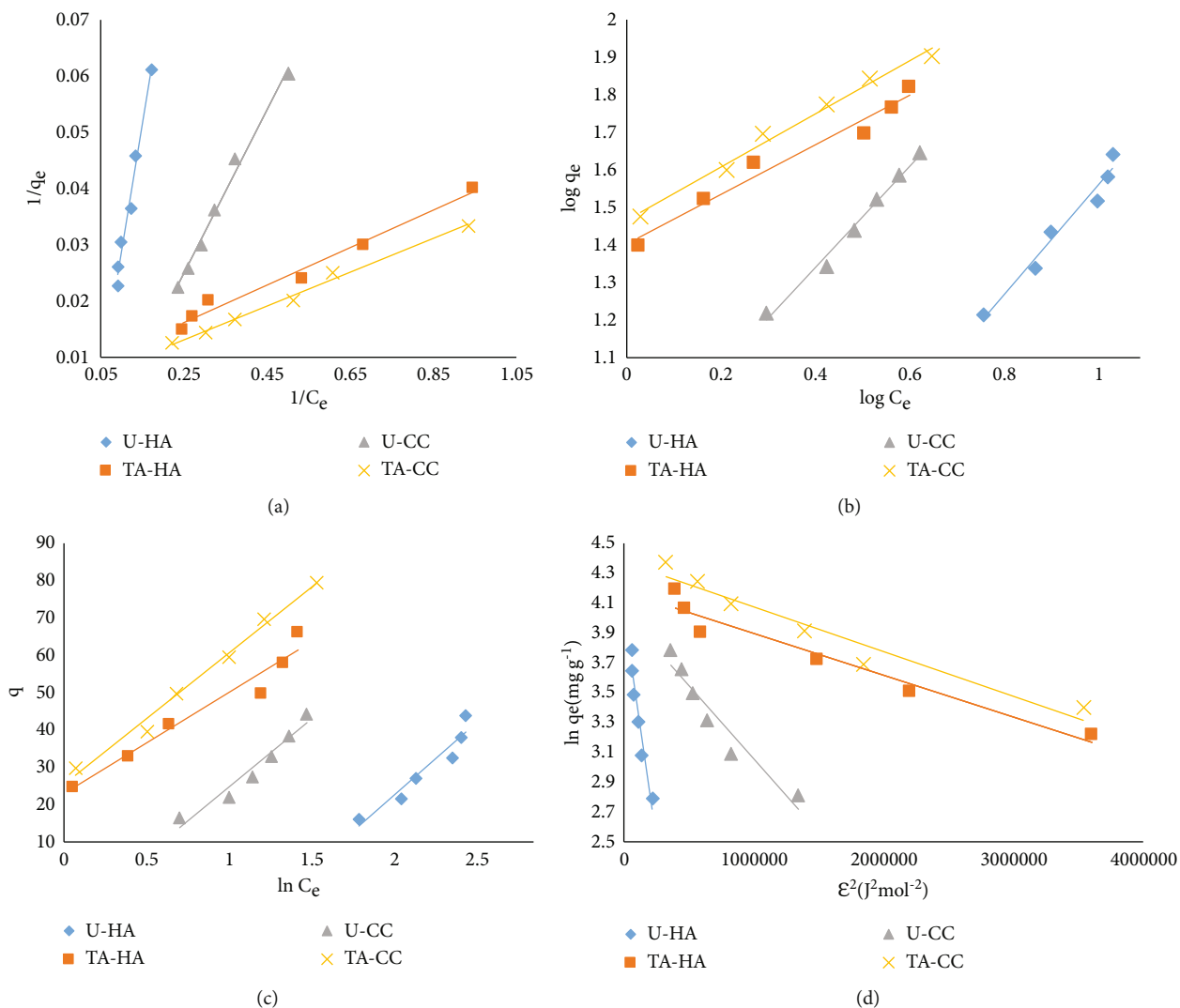
FIGURE 6: (a) Langmuir (b) Freundlich, (c) Temkin, and (d) D-R isothermal studies for CR dye.

3.12. Adsorption Mechanism. Different functional moieties such as (−COOH), (−SO), (−NH$_2$), and (−OH) are present in the adsorbents that are responsible for the binding of the dye. A basic pH converts these groups into anionic forms (COO$^-$) and (OH$^-$) and is unable to adsorb negatively charged dye particles because of interionic repulsion among similar charged entities. Excessive OH$^-$ ions that compete for potential sites hinder the adsorption of anionic dyes at higher pH. For CR, the isoelectronic point is 3.0 and it occurs in negatively charged forms in the pH range of 5.0-10.0. Point of zero charge pH$_{pzc}$ was demonstrated that the adsorbent surface was positive below 6 (U-HA) and 5 (U-CC) and negative above it. Carboxylate ions have pKa 3.0-5.0, below which it dissociates into positively charged species. In an acidic solution, CR dissociates into polar groups (SO$_3^-$) and adsorbs on positively charged adsorbent [44], inducing electrostatic interactions between the surface and dye [82]. Hydrogen bonding occurs between oxygen (carbonyl and carboxyl) and nitrogen-containing functional groups of CR and adsorbents [82].

The FTIR spectra when observed displayed variations in wavenumbers and peak intensities of the raw and modified dye adsorptions. For example, the peaks of hydroxyl stretching 3737.6 cm^{-1}, 3653.0 cm^{-1}, and 3568.7 cm^{-1} in IR of U-HA adsorbents when reacted with CR (Figure 2(a)) shifted towards 3872 cm^{-1}, 3855 cm^{-1}, and 3752 cm^{-1} for TA-HA with CR (Figure 2(b)). The second adsorbent U-CC when treated with CR was seen to consist of -OH stretch at 3568 cm^{-1} and 3737 cm^{-1} (Figure 2(c)), when TA-CC was treated with CR new peaks displaying hydroxyl groups were observed such as 3904 cm^{-1}, 3841 cm^{-1}, 3631 cm^{-1}, and 3547 cm^{-1} (Figure 2(d)).

Also, peaks corresponding to -C=O groups show a slight shift in wavenumbers, demonstrating the involvement of surface oxygen functionalities in dye removal. Strong electrostatic and chemical binding is the dominant phenomenon in removing CR from an aqueous phase.

The peaks at 2922 cm^{-1}, 2853 cm^{-1}, and 2850 cm^{-1} corresponding towards asymmetric and symmetric sp^3 C-H stretch in U-HA adsorbent (Figure 2(a)) show reduced peaks

TABLE 4: Thermodynamic parameters for CR dye adsorption.

Adsorbents	T (K)	$\Delta G°$ (kJmol^{-1})	K_D	$\Delta H°$ (kJmol^{-1})	$\Delta S°$ (Jmol^{-1} K^{-1})	E_a (kJmol^{-1})
U-HA	283	-1.3445	1.770619			
	293	-1.74341	2.045326			
	303	-2.07376	2.277439	-48.9993044	180.941278	21.276294
	313	-2.4044	2.518822			
	323	-4.9317	6.651246			
TA-HA	283	-2.14711	2.49026			
	293	-2.56614	2.866906			
	303	-3.3066	3.714912	-56.44781139	214.45573	24.5105564
	313	-4.67482	6.026144			
	323	-5.81927	8.728507			
U-CC	283	-1.41599	1.82523			
	293	-1.82091	2.111433			
	303	-2.15721	2.354134	-25.48959516	101.2978	11.068
	313	-2.7413	2.866906			
	323	-3.16494	3.249012			
TA-CC	283	-2.28265	2.637902			
	293	-2.44928	2.732639			
	303	-2.96897	3.249012	-44.08980004	171.2372	19.1445079
	313	-3.79373	4.295567			
	323	-5.43528	7.565737			
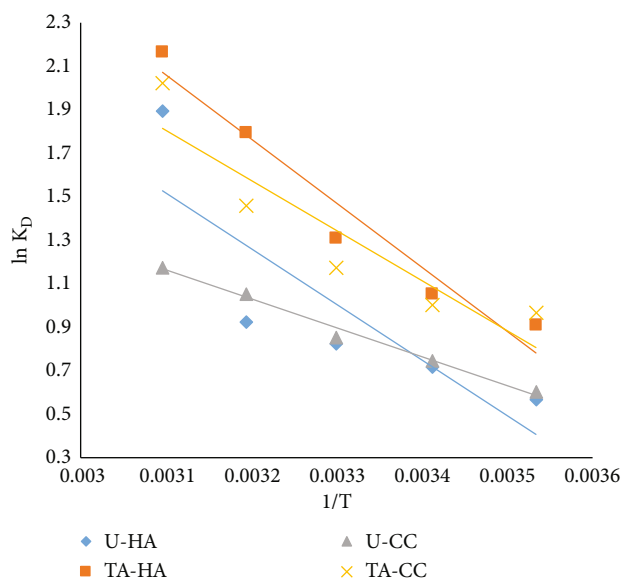
FIGURE 7: Thermodynamic studies for CR dye.

of 2921 cm^{-1} and 2852 cm^{-1} in modified forms (Figure 2(b)). In the second adsorbent U-CC, alkane C-H at 2850 cm^{-1} (Figure 2(c)) shifted to alkyl C-H stretch at 2923.9 cm^{-1} (Figure 2(d)). This is evident of C-H groups as potential sites contributing to the removal of CR from the water phase via pi-pi interactions. The isothermal studies showed a greater correlation of the Langmuir isotherm than other models leading towards chemisorption.

Strong hydrophobic interactions are the result of size and hydrophilicity of CR dye. Physisorption involving surface adsorption and hydrophobic and pi-pi interactions are observed with the adsorbent surfaces. In addition to these, strong electrostatic interactions along with the chemical binding of the oxygen functionalities are engaged in CR removal from the active sites.

Thus, the adsorption mechanism (Figure 8) is a complex physicochemical procedure [83] involving electrostatic interactions, chemical binding with surface functionalities, and hydrogen bondings. Similar mechanisms were proved by Lafi et al. using coffee waste-activated carbon [52] and Al-Zoubi et al. with jojoba residues [83].

3.13. Comparison with Other Adsorbents. Traditionally used biosorbents pose significant problems towards the adsorption procedure such as slow adsorption kinetics and lesser adsorption capacities. The purification of wastewaters should be efficient and able to neutralize effluents and return purified water and valuable components of production [2, 84]. As mentioned in the following (Table 5), CR was removed from the modified adsorbents in an efficient manner and the adsorbents followed all the aforementioned properties of a good adsorbent. The adsorbents are efficient, inexpensive, and readily available. High adsorption capacities are achieved, and modifying them with more advanced smart materials will enhance them more. Further research is still needed to adopt new pathways for studying their properties and expediency of their functionalization.
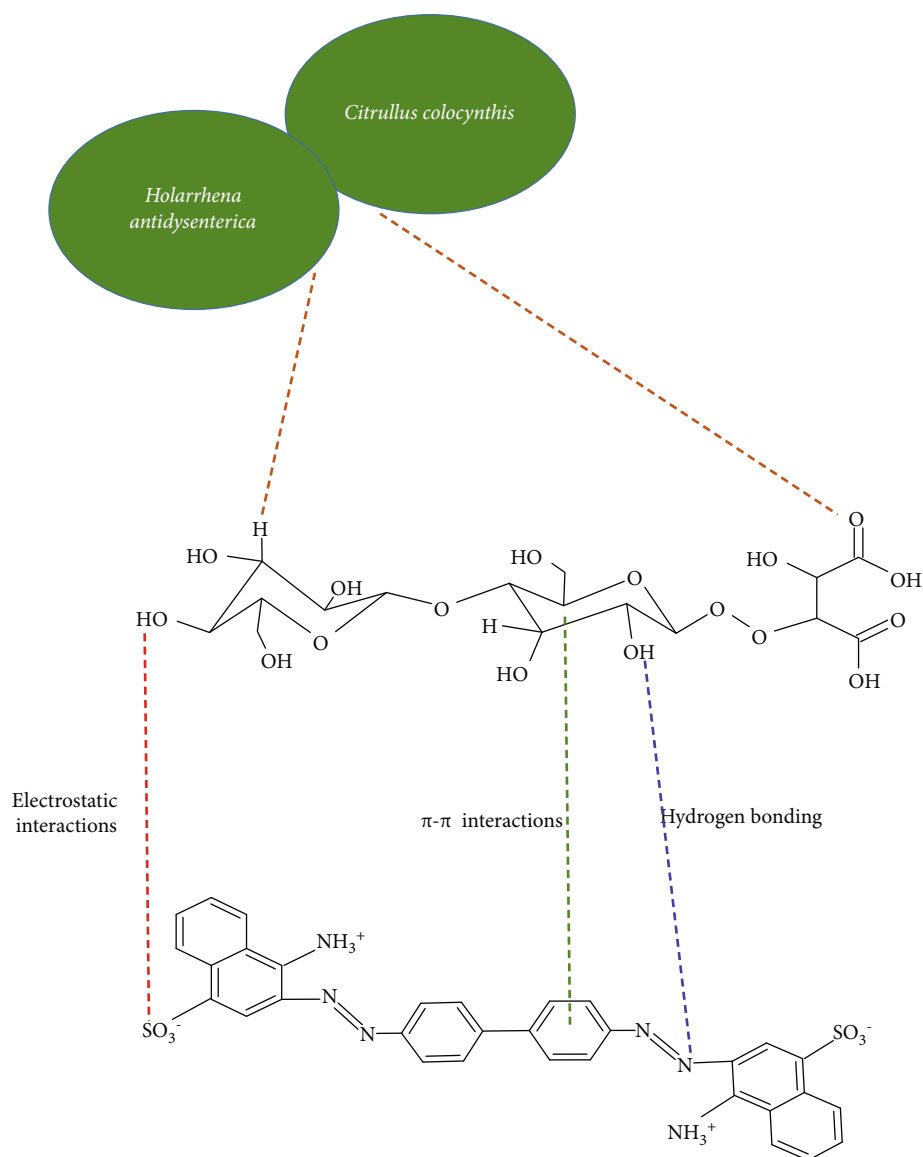
Mechanism of CR Dye adsorption

FIGURE 8: Proposed mechanism of CR dye adsorption.

3.14. Regeneration Study. Regeneration was performed in three consecutive cycles, which yielded about 80%, 88%, 84%, and 90% dye removal for U-HA, TA-HA, U-CC, and TA-CC, respectively.

3.15. Novelty of the Procedure. Within the scope of the authors' exhaustive search, *Holarrhena antidysenterica* and *Citrullus colocynthis* are unreported for the adsorption of Congo red dye contributing towards the novelty of the current research. The ability of modified adsorbents for the efficient and low-cost removal of Congo red dye contaminant from wastewaters has been evaluated, and mechanistic study of adsorption was fully comprehended.

3.16. Research Limitations/Implications. Usage of these adsorbents for metal sequestration, organic pollutant elimi-

TABLE 5: Estimation of Q_{max} between previous and experimented adsorbents.

Adsorbents	Q_{max} (mg g^{-1})	Reference
Wheat straw	71.2	[72]
Trametes versicolor	51.81	[85]
Jojoba seeds	58.82	[83]
Green coffee residues	20.04	[86]
Pinus pinaster bark	3.92	[87]
U-HA	60.61	This study
TA-HA	128.21	This study
U-CC	87.71	This study
TA-CC	131.57	This study

nation, activated carbon manufacturing, and nanoadsorbent functioning in advanced wastewater treatments is the further and future investigation underway.

4. Conclusions

Thus, it is concluded that adsorbents U-HA and U-CC are cheap and environmentally friendly possessing high dye removal properties. Their possession of higher oxygen-containing functionalities after the treatment with tartaric acid makes them the most promising candidates. FTIR and SEM studies confirm the presence of -COOH and -OH groups that bind CR with hydrophobic, pi-pi, chemical, and electrostatic interactions. Exterior surfaces pose ample binding surfaces for dye binding followed by the transfer of dye within the interior as evident from Boyd's and Webber-Morris plots. The Langmuir model gave Q_{max} 128 ($mg\,g^{-1}$) for TA-HA and 131 ($mg\,g^{-1}$) for TA-CC with dye removal. Both treated and untreated adsorbents were in correspondence towards the pseudo-second-order kinetic model. Thermodynamics proved the procedure exothermic and spontaneous along with increasing randomness in the system.

Data Availability

All data related to this work is presented in the results section along with references.

Conflicts of Interest

Regarding the publication of this article, we have no potential conflict of interest.

Acknowledgments

References

[1] I. Ali, T. A. Khan, and I. Hussain, "Treatment and remediation methods for arsenic removal from the ground water," *International journal of environmental engineering*, vol. 3, no. 1, pp. 48–71, 2011.

[2] I. Ali, T. Kon'kova, V. Kasianov et al., "Preparation and characterization of nano-structured modified montmorillonite for dioxidine antibacterial drug removal in water," *Journal of Molecular Liquids*, vol. 331, article 115770, 2021.

[3] A. A. Basheer, "Chemical chiral pollution: impact on the society and science and need of the regulations in the 21stcentury," *Chirality*, vol. 30, no. 4, pp. 402–406, 2018.

[4] Z. A. ALOthman, A. Y. Badjah, and I. Ali, "Facile synthesis and characterization of multi walled carbon nanotubes for fast and effective removal of 4-tert-octylphenol endocrine disruptor in water," *Journal of Molecular Liquids*, vol. 275, pp. 41–48, 2019.

[5] F. Saputra, C.-H. Yen, C.-Y. Hsieh et al., "Toxicity effects of the environmental hormone 4-tert-octylphenol in zebrafish (Danio rerio)," *International Journal of Marine Science*, vol. 6, 2016.

[6] A. A. Basheer and I. Ali, "Stereoselective uptake and degradation of (±)-o, p-DDD pesticide stereomers in water-sediment system," *Chirality*, vol. 30, no. 9, pp. 1088–1095, 2018.

[7] G. Sharma, V. K. Gupta, S. Agarwal, A. Kumar, S. Thakur, and D. Pathania, "Fabrication and characterization of nanoparticles: ion exchange behavior and photocatalytic activity against malachite green," *Journal of Molecular Liquids*, vol. 219, pp. 1137–1143, 2016.

[8] R. Shokoohi, M. Salari, R. Safari, H. Zolghadr Nasab, and S. Shanehsaz, "Modelling and optimisation of catalytic ozonation process assisted by ZrO_2-pumice/H_2O_2in the degradation of rhodamine B dye from aqueous environment," *International Journal of Environmental Analytical Chemistry*, vol. 101, no. 15, pp. 2629–2653, 2021.

[9] R. H. Thabet, M. K. Fouad, I. Ali, S. A. El Sherbiney, and M. A. Tony, "Magnetite-based nanoparticles as an efficient hybrid heterogeneous adsorption/oxidation process for reactive textile dye removal from wastewater matrix," *International Journal of Environmental Analytical Chemistry*, pp. 1–23, 2021.

[10] R. Tayebee, E. Esmaeili, B. Maleki, A. Khoshniat, M. Chahkandi, and N. Mollania, "Photodegradation of methylene blue and some emerging pharmaceutical micropollutants with an aqueous suspension of WZnO-NH_2@$H_3PW_{12}O_{40}$ nanocomposite," *Journal of Molecular Liquids*, vol. 317, article 113928, 2020.

[11] H. Yang, J. Zhang, Y. Liu et al., "Rapid removal of anionic dye from water by poly (ionic liquid)-modified magnetic nanoparticles," *Journal of Molecular Liquids*, vol. 284, pp. 383–392, 2019.

[12] M. Fatima, R. Farooq, R. W. Lindström, and M. Saeed, "A review on biocatalytic decomposition of azo dyes and electrons recovery," *Journal of Molecular Liquids*, vol. 246, pp. 275–281, 2017.

[13] C. R. Marcelo, G. A. Puiatti, M. A. Nascimento, A. F. Oliveira, and R. P. Lopes, "Degradation of the reactive blue 4 dye in aqueous solution using zero-valent copper nanoparticles," *Journal of Nanomaterials*, vol. 2018, Article ID 4642038, 9 pages, 2018.

[14] I. Ali, S. Afshinb, Y. Poureshgh et al., "Green preparation of activated carbon from pomegranate peel coated with zero-valent iron nanoparticles (nZVI) and isotherm and kinetic studies of amoxicillin removal in water," *Environmental Science and Pollution Research*, vol. 27, no. 29, pp. 36732–36743, 2020.

[15] I. Burakova, A. Burakov, A. Tkachev et al., "Kinetics of the adsorption of scandium and cerium ions in sulfuric acid solutions on a nanomodified activated carbon," *Journal of Molecular Liquids*, vol. 253, pp. 277–283, 2018.

[16] A. Yazidi, L. Sellaoui, G. L. Dotto, A. Bonilla-Petriciolet, A. C. Fröhlich, and A. B. Lamine, "Monolayer and multilayer adsorption of pharmaceuticals on activated carbon: application of advanced statistical physics models," *Journal of Molecular Liquids*, vol. 283, pp. 276–286, 2019.

[17] A. Stavrinou, C. Aggelopoulos, and C. Tsakiroglou, "Exploring the adsorption mechanisms of cationic and anionic dyes onto agricultural waste peels of banana, cucumber and potato: adsorption kinetics and equilibrium isotherms as a tool," *Journal of Environmental Chemical Engineering*, vol. 6, no. 6, pp. 6958–6970, 2018.

[18] I. Ali, O. M. Alharbi, Z. A. ALOthman, A. Alwarthan, and A. M. al-Mohaimeed, "Preparation of a carboxymethylcellulose-iron composite for uptake of

atorvastatin in water," *International Journal of Biological Macromolecules*, vol. 132, pp. 244–253, 2019.

[19] I. Ali, O. M. Alharbi, Z. A. Alothman, and A. Y. Badjah, "Kinetics, thermodynamics, and modeling of amido black dye photodegradation in water using Co/TiO$_2$ nanoparticles," *Photochemistry and Photobiology*, vol. 94, no. 5, pp. 935–941, 2018.

[20] P. Rath, S. Behera, B. Priyadarshini et al., "Influence of Mg doping on ZnO NPs for enhanced adsorption activity of Congo red dye," *Applied Surface Science*, vol. 491, pp. 256–266, 2019.

[21] B. Priyadarshini, T. Patra, and T. R. Sahoo, "An efficient and comparative adsorption of Congo red and trypan blue dyes on MgO nanoparticles: kinetics, thermodynamics and isotherm studies," *Journal of Magnesium and Alloys*, vol. 9, no. 2, pp. 478–488, 2021.

[22] Z. Wu, X. Yuan, H. Zhong et al., "Highly efficient adsorption of Congo red in single and binary water with cationic dyes by reduced graphene oxide decorated NH2-MIL-68 (Al)," *Journal of Molecular Liquids*, vol. 247, pp. 215–229, 2017.

[23] K. Elwakeel, A. Elgarahy, G. Elshoubaky, and S. Mohammad, "Microwave assist sorption of crystal violet and Congo red dyes onto amphoteric sorbent based on upcycled sepia shells," *Journal of Environmental Health Science and Engineering*, vol. 18, no. 1, pp. 35–50, 2020.

[24] M. R. Abukhadra, A. Adlii, and B. M. Bakry, "Green fabrication of bentonite/ oxide composite (BE/) of enhanced adsorption and advanced oxidation removal of Congo red dye and Cr (VI) from water," *International Journal of Biological Macromolecules*, vol. 126, pp. 402–413, 2019.

[25] A. A. Alqadami, M. Naushad, M. A. Abdalla et al., "Efficient removal of toxic metal ions from wastewater using a recyclable nanocomposite: a study of adsorption parameters and interaction mechanism," *Journal of Cleaner Production*, vol. 156, pp. 426–436, 2017.

[26] F. K. Liew, S. Hamdan, M. Rahman et al., "Synthesis and characterization of cellulose from green bamboo by chemical treatment with mechanical process," *Journal of Chemistry*, vol. 2015, Article ID 212158, 6 pages, 2015.

[27] G. Enaime, A. Baçaoui, A. Yaacoubi, and M. Lübken, "Biochar for wastewater treatment—conversion technologies and applications," *Applied Sciences*, vol. 10, no. 10, p. 3492, 2020.

[28] Y. Chen, Y. Zhu, Z. Wang et al., "Application studies of activated carbon derived from rice husks produced by chemical-thermal process—a review," *Advances in Colloid and Interface Science*, vol. 163, no. 1, pp. 39–52, 2011.

[29] S. S. Pillai, M. D. Mullassery, N. B. Fernandez, N. Girija, P. Geetha, and M. Koshy, "Biosorption of Cr(VI) from aqueous solution by chemically modified potato starch: equilibrium and kinetic studies," *Ecotoxicology and Environmental Safety*, vol. 92, pp. 199–205, 2013.

[30] A. Ş. Yargıç, R. Y. Şahin, N. Özbay, and E. Önal, "Assessment of toxic copper (II) biosorption from aqueous solution by chemically-treated tomato waste," *Journal of Cleaner Production*, vol. 88, pp. 152–159, 2015.

[31] L. W. Low, T. T. Teng, N. Morad, and B. Azahari, "Studies on the adsorption of methylene blue dye from aqueous solution onto low-cost tartaric acid treated bagasse," *APCBEE Procedia*, vol. 1, pp. 103–109, 2012.

[32] B. C. S. Ferreira, F. S. Teodoro, A. B. Mageste, L. F. Gil, R. P. de Freitas, and L. V. A. Gurgel, "Application of a new carboxylate-functionalized sugarcane bagasse for adsorptive removal of crystal violet from aqueous solution: kinetic, equilibrium and thermodynamic studies," *Industrial Crops and Products*, vol. 65, pp. 521–534, 2015.

[33] N. Mojoudi, N. Mirghaffari, M. Soleimani, H. Shariatmadari, C. Belver, and J. Bedia, "Phenol adsorption on high microporous activated carbons prepared from oily sludge: equilibrium, kinetic and thermodynamic studies," *Scientific Reports*, vol. 9, no. 1, pp. 1–12, 2019.

[34] A. Daochalermwong, N. Chanka, K. Songsrirote, P. Dittanet, C. Niamnuy, and A. Seubsai, "Removal of heavy metal ions using modified celluloses prepared from pineapple leaf fiber," *ACS Omega*, vol. 5, no. 10, pp. 5285–5296, 2020.

[35] A. Mittal, R. Katahira, M. E. Himmel, and D. K. Johnson, "Effects of alkaline or liquid-ammonia treatment on crystalline cellulose: changes in crystalline structure and effects on enzymatic digestibility," *Biotechnology for Biofuels*, vol. 4, no. 1, pp. 1–16, 2011.

[36] T. Mahmud, "Biosorption of Auramine O and Drimarene dyes from aqueous solutions using seed powder of *Diospyros lotus*," *International Journal of Environment and Sustainability*, vol. 6, no. 3, 2018.

[37] S. Basharat, R. Rehman, T. Mahmud, S. Basharat, and L. Mitu, "Tartaric acid-modified *Holarrhena antidysenterica* and *Citrullus colocynthis* biowaste for efficient eradication of crystal violet dye from water," *Journal of Chemistry*, vol. 2020, Article ID 8862167, 18 pages, 2020.

[38] D. Chowdhuri, R. Nakul, G. P. Jeppu, and P. Vairavel, "Process optimization, isotherm, kinetics, and thermodynamics studies for removal of remazol brilliant blue-R dye from contaminated water using adsorption on guava leaf powder," *Desalination and Water Treatment*, vol. 185, pp. 318–343, 2020.

[39] P. Vairavel, N. Rampal, and G. Jeppu, "Adsorption of toxic Congo red dye from aqueous solution using untreated coffee husks: kinetics, equilibrium, thermodynamics and desorption study," *International Journal of Environmental Analytical Chemistry*, pp. 1–20, 2021.

[40] A. N. Alene, G. Y. Abate, and A. T. Habte, "Bioadsorption of basic blue dye from aqueous solution onto raw and modified waste ash as economical alternative bioadsorbent," *Journal of Chemistry*, vol. 2020, Article ID 8746035, 11 pages, 2020.

[41] H. P. Boehm, "Surface oxides on carbon and their analysis: a critical assessment," *Carbon*, vol. 40, no. 2, pp. 145–149, 2002.

[42] M. Moradi, M. Hosseini Sabzevari, F. Marahel, and A. Shameli, "Removal of reactive green KE-4BD and Congo red dyes in textile effluent by natural clinoptilolite particles on a biosorbent as a cheap and efficient adsorbent: experimental design and optimisation," *International Journal of Environmental Analytical Chemistry*, pp. 1–19, 2021.

[43] R. Nodehi, H. Shayesteh, and A. R. Kelishami, "Enhanced adsorption of Congo red using cationic surfactant functionalized zeolite particles," *Microchemical Journal*, vol. 153, article 104281, 2020.

[44] R. M. Kulkarni, R. Vaidya, S. Srinivas, S. Anand, and B. Narayana, "Application of water hyacinth root powder for Congo red dye removal in batch and continuous packed bed operation," *Nanotechnology for Environmental Engineering*, vol. 6, no. 2, pp. 1–11, 2021.

[45] M. Naushad, G. Sharma, A. Kumar et al., "Efficient removal of toxic phosphate anions from aqueous environment using pectin based quaternary amino anion exchanger," *International Journal of Biological Macromolecules*, vol. 106, pp. 1–10, 2018.

[46] A. M. Abbas, F. H. Abdulrazzak, and T. Himdan, "Kinetic study of adsorption of azo dye from aqueous solutions by zeolite and modified synthetic zeolite," *Journal of Materials and Environmental Science*, vol. 9, no. 9, pp. 2652–2659, 2018.

[47] I. Ali, O. M. Alharbi, Z. A. ALOthman, A. M. al-Mohaimeed, and A. Alwarthan, "Modeling of fenuron pesticide adsorption on CNTs for mechanistic insight and removal in water," *Environmental Research*, vol. 170, pp. 389–397, 2019.

[48] M. Foroughi-Dahr, H. Abolghasemi, M. Esmaili, A. Shojamoradi, and H. Fatoorehchi, "Adsorption characteristics of Congo red from aqueous solution onto tea waste," *Chemical Engineering Communications*, vol. 202, no. 2, pp. 181–193, 2015.

[49] A. Chham, E. Khouya, M. Oumam et al., "The use of insoluble mater of Moroccan oil shale for removal of dyes from aqueous solution," *Chemistry International*, vol. 4, no. 1, pp. 67–77, 2018.

[50] A. Gouza, K. Fanidi, S. Saoiabi, A. Laghzizil, and A. Saoiabi, "Effect of heat treatment on the surface properties of selected bituminous shale for cationic dye sorption," *Desalination and Water Treatment*, vol. 66, pp. 274–280, 2017.

[51] M. El Haddad, R. Slimani, R. Mamouni, S. ElAntri, and S. Lazar, "Removal of two textile dyes from aqueous solutions onto calcined bones," *Journal of the Association of Arab Universities for Basic and Applied Sciences*, vol. 14, no. 1, pp. 51–59, 2013.

[52] R. Lafi, I. Montasser, and A. Hafiane, "Adsorption of Congo red dye from aqueous solutions by prepared activated carbon with oxygen-containing functional groups and its regeneration," *Adsorption Science & Technology*, vol. 37, no. 1-2, pp. 160–181, 2019.

[53] Z. L. Yaneva and N. V. Georgieva, "Insights into Congo red adsorption on agro-industrial materials-spectral, equilibrium, kinetic, thermodynamic, dynamic and desorption studies. A Review," *International Review of Chemical Engineering*, vol. 4, no. 2, pp. 127–146, 2012.

[54] H. Shayesteh, A. Rahbar-Kelishami, and R. Norouzbeigi, "Evaluation of natural and cationic surfactant modified pumice for Congo red removal in batch mode: kinetic, equilibrium, and thermodynamic studies," *Journal of Molecular Liquids*, vol. 221, pp. 1–11, 2016.

[55] S. W. Won, K. Vijayaraghavan, J. Mao, S. Kim, and Y.-S. Yun, "Reinforcement of carboxyl groups in the surface of *Corynebacterium glutamicum* biomass for effective removal of basic dyes," *Bioresource Technology*, vol. 100, no. 24, pp. 6301–6306, 2009.

[56] S. Coruh, S. Elevli, and G. Doğan, "Optimization study of adsorption of crystal violet and Congo red onto sepiolite and clinoptilolite," *Global NEST Journal*, vol. 19, 2019.

[57] S. J. Santosa, "Adsorption of Congo Red Dye on HDTMA Surfactant-Modified Zeolite A Synthesized from Fly Ash," in *Defect and Diffusion Forum*, Trans Tech Publications Ltd, 2018.

[58] J. Song, W. Zou, Y. Bian, F. Su, and R. Han, "Adsorption characteristics of methylene blue by peanut husk in batch and column modes," *Desalination*, vol. 265, no. 1-3, pp. 119–125, 2011.

[59] N. El Messaoudi, M. El Khomri, Z. G. Chegini et al., "Dye removal from aqueous solution using nanocomposite synthesized from oxalic acid-modified agricultural solid waste and $ZnFe_2O_4$ nanoparticles," *Nanotechnology for Environmental Engineering*, vol. 7, no. 1, pp. 1–15, 2021.

[60] C. Cheung, J. Porter, and G. McKay, "Sorption kinetic analysis for the removal of cadmium ions from effluents using bone char," *Water Research*, vol. 35, no. 3, pp. 605–612, 2001.

[61] V. Verma and A. Mishra, "Kinetic and isotherm modeling of adsorption of dyes onto rice husk carbon," *Global NEST Journal*, vol. 12, no. 2, pp. 190–196, 2019.

[62] M. A. Islam, A. Benhouria, M. Asif, and B. Hameed, "Methylene blue adsorption on factory-rejected tea activated carbon prepared by conjunction of hydrothermal carbonization and sodium hydroxide activation processes," *Journal of the Taiwan Institute of Chemical Engineers*, vol. 52, pp. 57–64, 2015.

[63] K. Y. Chong, C. H. Chia, S. Zakaria, and M. S. Sajab, "Vaterite calcium carbonate for the adsorption of Congo red from aqueous solutions," *Journal of Environmental Chemical Engineering*, vol. 2, no. 4, pp. 2156–2161, 2014.

[64] C. A. Igwegbe, O. D. Onukwuli, K. K. Onyechi, and S. Ahmadi, "Equilibrium and kinetics analysis on vat yellow 4 uptake from aqueous environment by modified rubber seed shells: nonlinear modelling," *Journal of Materials and Environmental Science*, vol. 11, no. 9, pp. 1424–1444, 2020.

[65] K. Tan and B. Hameed, "Insight into the adsorption kinetics models for the removal of contaminants from aqueous solutions," *Journal of the Taiwan Institute of Chemical Engineers*, vol. 74, pp. 25–48, 2017.

[66] W. J. Weber and J. C. Morris, "Kinetics of adsorption on carbon from solution," *Journal of the Sanitary Engineering Division*, vol. 89, no. 2, pp. 31–59, 1963.

[67] A. Kumar, S. Kumar, and S. Kumar, "Adsorption of resorcinol and catechol on granular activated carbon: equilibrium and kinetics," *Carbon*, vol. 41, no. 15, pp. 3015–3025, 2003.

[68] A. Chaib, N. Boukhalfa, and A. Boudjemaa, "Congo red removal using Fesdis soil: kinetic, equilibrium and thermodynamic studies," *International Journal of Environmental Analytical Chemistry*, pp. 1–21, 2021.

[69] M. B. Amran and M. A. Zulfikar, "Removal of Congo red dye by adsorption onto phyrophyllite," *International Journal of Environmental Studies*, vol. 67, no. 6, pp. 911–921, 2010.

[70] R. Abdul, M. Tariq, A. Muhammad, R. Rabia, and B. Sumaira, "Usage of fruit-fibers of *Luffa cylindrica* for the sorptive removal of direct blue 15 dye from water," *Desalination and Water Treatment*, vol. 120, pp. 350–360, 2018.

[71] R. Fiaz, M. Hafeez, and R. Mahmood, "Removal of brilliant green (BG) from aqueous solution by using low cost biomass *Salix alba* leaves (SAL): thermodynamic and kinetic studies," *Journal of Water Reuse and Desalination*, vol. 10, no. 1, pp. 70–81, 2020.

[72] R. Zhang, J. Zhang, X. Zhang, C. Dou, and R. Han, "Adsorption of Congo red from aqueous solutions using cationic surfactant modified wheat straw in batch mode: kinetic and equilibrium study," *Journal of the Taiwan Institute of Chemical Engineers*, vol. 45, no. 5, pp. 2578–2583, 2014.

[73] I. Langmuir, "The adsorption of gases on plane surfaces of glass, mica and platinum," *Journal of the American Chemical Society*, vol. 40, no. 9, pp. 1361–1403, 1918.

[74] A. Benmessaoud, D. Nibou, E. H. Mekatel, and S. Amokrane, "A comparative study of the linear and non-linear methods for determination of the optimum equilibrium isotherm for adsorption of Pb^{2+} ions onto Algerian treated clay," *Iranian Journal of Chemistry and Chemical Engineering (IJCCE)*, vol. 39, no. 4, pp. 153–171, 2020.

[75] C. Yahiaoui, M. Kameche, C. Innocent, and A. Khenifi, "Conception of yeast microbial desalination cell: applications to dye wastewater treatment and lead removal," *Chemical Engineering Communications*, vol. 208, no. 3, pp. 364–375, 2021.

[76] I. Ali, A. E. Burakov, A. V. Melezhik et al., "Removal of copper (II) and zinc (II) ions in water on a newly synthesized polyhydroquinone/graphene nanocomposite material: kinetics, thermodynamics and mechanism," *Chemistry Select*, vol. 4, no. 43, pp. 12708–12718, 2019.

[77] M. A. E. Barakat, R. Kumar, M. K. Seliem et al., "Exfoliated clay decorated with magnetic iron nanoparticles for crystal violet adsorption: modeling and physicochemical interpretation," *Nanomaterials*, vol. 10, no. 8, p. 1454, 2020.

[78] M. H. Jnr and A. I. Spiff, "Equilibrium sorption study of Al^{3+}, Co^{2+} and Ag^+ in aqueous solutions by fluted pumpkin (*Telfairia occidentalis* HOOK f) waste biomass," *Acta Chimica Slovenica*, vol. 52, pp. 174–181, 2005.

[79] O. Celebi, Ç. Üzüm, T. Shahwan, and H. N. Erten, "A radiotracer study of the adsorption behavior of aqueous Ba^{2+} ions on nanoparticles of zero-valent iron," *Journal of Hazardous Materials*, vol. 148, no. 3, pp. 761–767, 2007.

[80] J. O. Eniola, R. Kumar, A. A. Al-Rashdi, M. O. Ansari, and M. A. Barakat, "Fabrication of novel Al $(OH)_3$/CuMnAl-layered double hydroxide for detoxification of organic contaminants from aqueous solution," *ACS Omega*, vol. 4, no. 19, pp. 18268–18278, 2019.

[81] J. O. Ighalo and A. G. Adeniyi, "Adsorption of pollutants by plant bark derived adsorbents: an empirical review," *Journal of Water Process Engineering*, vol. 35, article 101228, 2020.

[82] G. Sriram, U. Uthappa, D. Losic, M. Kigga, H.-Y. Jung, and M. D. Kurkuri, "Mg–Al-layered double hydroxide (LDH) modified diatoms for highly efficient removal of Congo red from aqueous solution," *Applied Sciences*, vol. 10, no. 7, p. 2285, 2020.

[83] H. Al-Zoubi, M. Zubair, M. S. Manzar et al., "Comparative adsorption of anionic dyes (eriochrome black t and Congo red) onto jojoba residues: isotherm, kinetics and thermodynamic studies," *Arabian Journal for Science and Engineering*, vol. 45, no. 9, pp. 7275–7287, 2020.

[84] I. Ali, A. V. Babkin, I. V. Burakova et al., "Fast removal of samarium ions in water on highly efficient nanocomposite based graphene oxide modified with polyhydroquinone: isotherms, kinetics, thermodynamics and desorption," *Journal of Molecular Liquids*, vol. 329, article 115584, 2021.

[85] A. Binupriya, M. Sathishkumar, K. Swaminathan, C. Kuz, and S. Yun, "Comparative studies on removal of Congo red by native and modified mycelial pellets of *Trametes versicolor* in various reactor modes," *Bioresource Technology*, vol. 99, no. 5, pp. 1080–1088, 2008.

[86] M. S. Manzar, M. Zubair, N. A. Khan et al., "Adsorption behaviour of green coffee residues for decolourization of hazardous Congo red and eriochrome black T dyes from aqueous solutions," *International Journal of Environmental Analytical Chemistry*, pp. 1–17, 2020.

[87] K. Litefti, M. S. Freire, M. Stitou, and J. González-Álvarez, "Adsorption of an anionic dye (Congo red) from aqueous solutions by pine bark," *Scientific Reports*, vol. 9, no. 1, pp. 1–11, 2019.

Research Article

Comparative Evaluation of the Adsorption Performance of Citric Acid-Treated Peels of *Trapa natans* and *Citrullus lanatus* for Cationic Dyes Degradation from Water

Muhammad Sadiq Hussain, Rabia Rehman [ID], and Muhammad Imran

Centre for Inorganic Chemistry, School of Chemistry, University of the Punjab, Quaid-e-Azam Campus, Lahore-54590, Pakistan

Correspondence should be addressed to Rabia Rehman; grinorganic@yahoo.com

Various chemicals were explored in chemical combinations with two selected agrowastes in order to optimize, enhance, and improve their biosorption potential for the optimal and effective eradication of noxious, carcinogenic, and malignant cationic and basic dyes from wastewater. In this project, environmentally safe, economic, inexpensive, and widely available peels of *Trapa natans* (TP) and *Citrullus lanatus* (CP) were collected, dried, and pretreated with citric acid, revealing promising results. FT-IR and SEM characterizations of chemically changed biosorbents (C-TP and C-CP) have evidenced the presence of more secondary adsorption sites on their surfaces. These acid-modified biosorbents were employed to eliminate the hazardous and toxic basic dyes such as Rhodamine B (RAD) and Brilliant Green Dye (BLG) in batch mode processing. The Langmuir model was best fitted to equilibrium experimental data as compared to Freundlich and Temkin isothermal mathematical models with Q_{max} of 15.63 and 27.55 mg/g for RAD using C-TP and C-CP, respectively, whereas, for BLG on C-TP and C-CP, it was 128 and 189 mg/g, respectively. Therefore, the mechanism is related to chelation and ion exchange modes between adsorbate molecules and adsorbent surfaces, leading to homogeneous and monolayer adsorption and following pseudo-2nd-order kinetics in the best way. Thermodynamic parameters such as ΔG^0, ΔS^0, ΔH^0, and ΔE^0 are determined statistically for the adsorption performance of both novel chemically mutant biosorbents, which reflect that biosorption mechanisms are exothermic as well as spontaneous.

1. Introduction

The most severe and alarming ecological worldwide threat is water pollution, which deteriorates the water quality. Textile, fabrics, and printing industrial processing units discharged about 10–15% coloring matters into water bodies, which persist for an extended time span due to nonbiodegradable ability [1]. Dyes consumption in textile industrial units is more than 10000 tons per annum on global level, whereas, according to an estimate after dyeing process, their wastewater comprises dyes effluents about 1000 tons per annum which has a significant role in contaminating water resources [2, 3]. Unprocessed or partially treated dyestuffs containing industrial water have serious adverse effects on natural ecosystem and severely damage the water resources ultimately and cause the complicated health problems in

mankind and increase in mortality rate per annum [4]. The dyes mostly persist in water for extended period of time and even in traces are easily visible and can be identified in water [5]. Organic dyes such as azo dyes on introduction in human body can cause tumors and bladder cancer, due to destruction of DNA molecules [6]. Previous investigations revealed that drinking water containing dyes effluents like Rhodamine B (RAD) and Brilliant Green Dye (BLG) has highly toxic, carcinogenic, hazardous, and severe mutagenic effects on human bodies [7] and leads to acute poisoning, gastrointestinal problems, liver dysfunction, breath shortness, infections in respiratory tract, and skin dermatitis [7]. Therefore, it is the requirement of time to get rid of such toxic, hazardous, lethal, mortal, and incurable effluents from water streams to save the precious lives of infants and people. Different techniques including physical and chemical

methods such as electrochemical oxidation, precipitation, ozonolysis, coagulation-flocculation, and ion exchange have been employed to eradicate the dyestuffs from water but most of them are complicated and highly sensitive to environmental factors, prolong operational time, are costly, and generate hazardous byproducts [8, 9]. In this investigation, biosorption, the most emerging technique, is employed to remove hazardous and toxic dyes from water. This technique is widely explored because raw materials (agrowaste) are usually eco-friendly, cheap, easy to use, and easily available for removing any type of contaminants from water. In previous investigations, agrowastes like *Dalbergia sissoo*-activated carbon [10], raw pomegranate peels [11], raw timber wood sawdust [12], nitric acid-treated pine cone [13], banana peels [14], and jackfruit peels [15] had given efficient adsorptive removal outcomes for RAD, while for the adsorptive eradication of BLG areca nut husk [16], *Sesamum indicum* tree waste [17], almond shells [16], date pits-activated carbon [3], tree wood of guava-activated carbon [18], and rice husk [19] were utilized as biosorbents. It was observed from reported data that chemically processed biosorbents had shown good and promising results as compared to the raw and untreated forms. In the consideration of previously reported results of biosorption of dyes, two cheap, eco-friendly, abundant, and easily accessible agrowastes, TP and CP, have been selected for the expulsion of toxic and hazardous RAD and BLG from wastewater. The main objective of this investigation is to alter the surface morphology of the lignocellulosic biomass by providing additional active adsorption binding sites for the associations with the dye molecules from wastewater. After treatment with the most suitable modifying agent, the adsorbents will become more efficient and quicker to eradicate the dyestuffs from the water. In this study, the selected biosorbents will be chemically modified by using different chemicals (solvents and chelating agents) to assess their adsorption performance and efficiency for the removal of selected dyes under suitable operating conditions.

2. Materials and Method

2.1. Chemicals and Glass Apparatus.
In this study, pure chemicals and reagents were acquired from well-known and high reputed companies Merck and Fluka, which were BLG-λ_{max} of 625 nm, RAD-λ_{max} of 554 nm, urea, thiourea, EDTA, hydrochloric acid, sulfuric acid, nitric acid, sodium hydroxide, sodium carbonate, sodium chloride, potassium iodide, iodine, indicators, (R-OH) methyl, ethyl, and Isopropyl alcohols, propanone, organic acids chelating agents like lactic acid, citric acid, and tartaric acid, while glassware were made of Pyrex, were washed with deionized distilled water, and were sterilized for 30 min. at 80°C in electrical oven.

2.2. Methodology for the Preparation of Raw Biosorbents.
The biosorbents selected for this investigation are eco-friendly, nontoxic, and easily accessible locally. The peels of both biosorbents, *Trapa natans* (TP) and *Citrullus lanatus*

(CP), were acquired from Lahore and nearby areas and, thereafter, washed with running water to remove entrapped dust and other waste matters. The peels of both adsorbents were trimmed with a sharp knife into suitable sizes for experiments and then carefully washed with distilled water. Later, the peels were dried in sunlight for ten days and placed in an oven at about 70°C for 72 hours to remove the entrapped moisture in the first phase. After literature survey, the peels were ground and sieved to a 70-mesh size, resulting in fine powder [20]. These powdered peels were again dried in an oven for 24 hours to remove further entrapped moisture in the second phase and were placed in plastic jars labelled as TP and CP for use in adsorption experimental investigations. Flow sheet diagram for the preparation of raw biosorbents is elaborated in Figure 1.

2.3. Characterization of Biosorbents.
TP and CP were analyzed through different techniques like Boehm titration for identification of acidic/basic moieties, pH, % age of moisture and ash contents, elemental and volatile matters determinations, estimation of porosity/bulk density, and iodine titration as listed in Table 1 [21].

2.4. Chemical Treatment of Biosorbents.
The surface morphologies of both biosorbents (TP and CP) were chemically amended by using different modifying agents such as different kinds of alcohols (methyl, ethyl, and isopropyl alcohols), acetone, mineral acid like HCl, caustic soda (NaOH), numerous chelating agents like EDTA, urea, thiourea, and organic acids (citric acid, lactic acid, and tartaric acid). The chemistry of treatment of biosorbents with different chemicals was categorized in two phases.

Phase I: chemical processing with different solvents:

100 g of each biosorbent was placed in 250 mL of each solvent in Erlenmeyer flasks sealed with Al-foil for 6–10 hours at 30°C on an orbital shaker at 150 rpm. Extra and excessive soaking in solvent-based modifying agents was avoided to protect the raw adsorbents from deterioration and decay, especially in the cases of alkali and acids. The content in each flask was filtered and washed with distilled and deionized water carefully to remove entrapped solvent molecules. Afterward, the chemically modified biosorbents were dried for 24 hours at 80°C in an electric oven and then stored in plastic jars for further experimental work.

Phase II: chemical processing with different chelating agents:

To increase the additional active adsorption binding sites on the interfaces of both raw biosorbents (TP and CP), solid phase chemical modification was carried out by using different chelating agents. For this purpose, 54 g of each powdered biosorbent, TP and CP, was thoroughly mixed with 6 g of each chelating agent in different China dishes separately. Each China dish was wrapped in aluminum foil and microwave-irradiated for 8–10 minutes [22]. The chemically treated
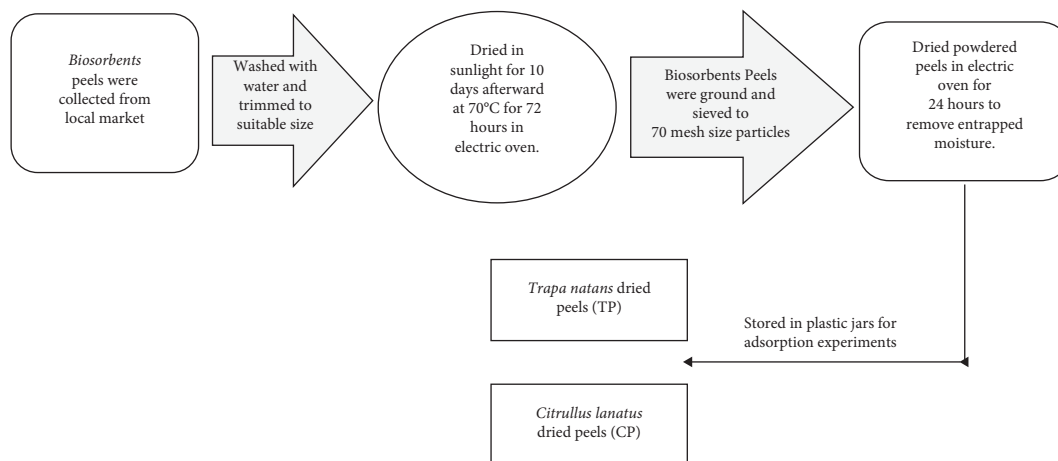
FIGURE 1: Schematic diagrams for the preparation of raw adsorbents.

TABLE 1: Physicochemical characterization of both biosorbents.

Evaluation of parameters	TP values	CP values
pH	5.6	5.9
Particle density (g.cm^{-3})	0.588	0.479
Bulk density (g.cm^{-3})	0.5	0.96
Percentage of ash content	6.8	2.4
Percentage of moisture content	7.7	8.3
Percentage of porosity	0.78	0.2
Percentage of volatile organic components	89.7	5.6
Iodine number (mg.g^{-1})	15.5	2.1
Phenolic moieties (millimoles)	0.0841	0.0038
Lactones (millimoles)	0.0592	0.0056
Carboxylic acids (millimoles)	0.0391	2.442
Surface basic sites (millimoles)	0.0048	2.011

FIGURE 2: Chemical structure of Rhodamine B.

adsorbents were carefully stored in plastic jars for further experimentation. These chemically modified adsorbents were tested under optimized operational conditions for the adsorption removal of RAD and BLG from water bodies in a batch mode investigation.

2.5. Experimental Investigations on Biosorption.

The maximum adsorptive removal of both basic dyes (RAD and BLG) was promising with the citric acid-treated novel adsorbents during the batch mode experiments. The native TP after chemical treatment and amendment was labeled as C-TP, whereas native CP was labeled as C-CP for further studies. During the experimental approach, for each experiment, 25 ppm of each of the RAD and BLG solutions was prepared and 25 mL of each solution was taken in 100 mL conical flasks to optimize the operational factors for adsorption studies. The chemical structures of two basic (cationic) model dyes selected for their elimination from wastewater are shown in Figures 2 [23] and 3 [24], respectively.

2.5.1. Optimization of Operational Parameters.

During the biosorption experimental comparative studies, various operational parameters, such as biosorbent dosage range (0.2–2.0 g with difference 0.1 g), pH range (1–10), temperature range (10–80°C), and contact time range (5–60 minutes), as well as shaking speed range (25–200 rpm with gap of 25 rpm), were optimized to get better results. Mathematical modeling for isothermal and kinetic equilibria investigations was also determined to analyze and manipulate the reliability of the adsorption results. The % age adsorption of both dyes by using modified adsorbents was determined from the relation given in the following equation [25]:

$$\%\text{Adsorption} = \left(\frac{C_o - C_e}{C_o}\right) \times 100. \tag{1}$$

The amounts (mg/g) of adsorbed dyes were determined from the following equation [26]:

$$Q = \left[\frac{(C_o - C_e)V}{W}\right]. \tag{2}$$

In the above relations, for each adsorbent, Q is amount of dyes (mg/g), C_o represents initial concentration (ppm), C_e is concentration (ppm) in equilibrium of both RAD and BLG, V is volume in L, and W is mass in grams.
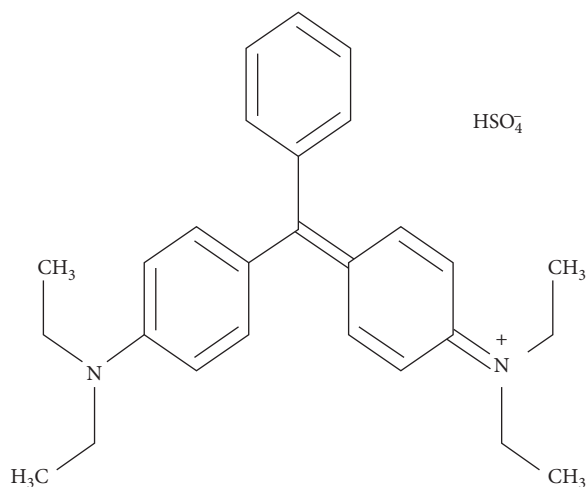
FIGURE 3: Chemical structure of Brilliant Green Dye.

3. Results and Discussion

The biosorbents were chemically modified with numerous modifying agents as mentioned in Section 2.4. After the performance of many repeatedly experiments, the most suitable modifying agent was selected for the amendment of surface morphology of TP and CP. The characterization of adsorbents was carried out through FT-IR and SEM. The validity and reliability of equilibrium data were evaluated by Langmuir, Freundlich, Temkin, and kinetics modeling.

3.1. Chemical Modification of Biosorbents. The raw biosorbents TP and CP were chemically treated with different chemicals, including various organic solvents, acids, alkalis, and chelating agents, as mentioned in experimental Section 2.4. The adsorption performance of chemically processed biosorbents with different chemicals was assessed for the removal of RAD and BLG from the water system. It was observed after repeated experiments that citric acid-treated TP and CP performed better and showed maximum adsorptive removal of RAD and BLG, as elaborated in Figure 4. It was evidenced from FT-IR and SEM analysis that citric acid has been esterified with the OH groups on the surfaces of biosorbents and has provided extra and additional adsorption sites to associate with dye molecules from aqueous solutions. Therefore, enhanced active binding sites on modified biosorbents surfaces have contributed to efficient and quick adsorption equilibria at the interface of adsorbate-adsorbents.

The maximum adsorptions of RAD on citric acid-modified adsorbents C-TP and C-CP at optimum conditions were found to be 91% and 96%, respectively, whereas for BLG on C-TP and C-CP they were 88% and 92%, respectively, which were promising as compared to other utilized chemicals. Solid phase chemical modification treatment of raw biosorbents (TP and CP) with citric acid under microwave irradiation was performed as mentioned in Section 2.4.

3.2. Spectroscopic Analysis

3.2.1. FT-IR Analysis of Chemically Processed Adsorbents. 0.8 g of each C-TP and C-CP had been placed separately in four conical flasks containing 25 mL solutions of RAD and BLG with 25 ppm conc. for 20 minutes at 125 rpm and 30°C. After adsorption, each sample was filtered and the residue was dried for FT-IR evaluation. Figure 5 represents a comparative study of *Trapa natans* peels, native form (TP), and after chemical treatment with citric acid (C-TP). The region between 3900 and 3600 cm^{-1} indicated the surface modification under the influence of esterification between free OH moieties of alcohols on TP and modifying agent citric acid. A broad band at 3300 cm^{-1} showed the COOH moieties on TP which was obviously changed after treatment and, similarly, a high amendment between 1395 and 1440 cm^{-1} in C-TP as compared to TP is a good signal for additional COOH groups which had played promising role during adsorption.

The region between 1330 and 1415 cm^{-1} reflected the OH bending for alcohols. Thus, the modified spectra of TP had more and additional carboxylic acid groups for the efficient and quicker adsorption of selected dyes. Figure 6 expresses a comparative study of *Citrullus lanatus* peels, native form (CP), and after chemical processing with citric acid (C-CP). The region between 3850 and 3650 cm^{-1} on C-TP showed the surface chemical alteration due to reaction between free OH groups on TP and modifying agent citric acid.

A reduced broad band at 3500–3200 cm^{-1} on C-TP as compared to CP showed intermolecular bonded forces of citric acid with free OH moieties. A changed frequency at the region between 3000 and 2700 cm^{-1} on C-CP represented the COOH moieties, while wavenumber (1778–1745) indicated the COOH and esterified groups of citric acid molecules in C-TP. The new peaks in the range of 1435–1400 cm^{-1} in C-TP as compared to TP associated with OH bending groups of carboxylic acids, which had played good role during adsorption of dyes. The region of 1260–1100 cm^{-1} reflected ester linkage. Therefore, the amended morphology of TP after chemical treatment shown in C-TP in Figure 6 had provided numerous (COOH) groups for the better and quicker adsorption equilibria in aqueous solutions of RAD and BLG.

3.2.2. FT-IR Analysis after Adsorption of Dyes. Figure 7 depicts the FT-IR spectra of model dyes RAD and BLG following adsorption on citric acid-treated adsorbents C-TP and C-CP.

Figures 7(a) and 7(b) show the FT-IR spectra following the adsorption of the first model dye, RAD, on C-TP and C-CP, respectively. The change in wavenumber in the case of C-TP after adsorption of RAD at 3875, 3730, and 3610 cm^{-1} in Figure 7(a) and for C-CP at frequencies of 3902, 3855.5, and 3737 cm^{-1} in Figure 7(b) reflects the adsorption under the influence of strong intermolecular hydrogen bonding caused by the involvement of the O-H group of -COOH moieties with the dye molecules, while peaks between 3390 and 3200 cm^{-1} in Figure 7(a) and between 3330 and
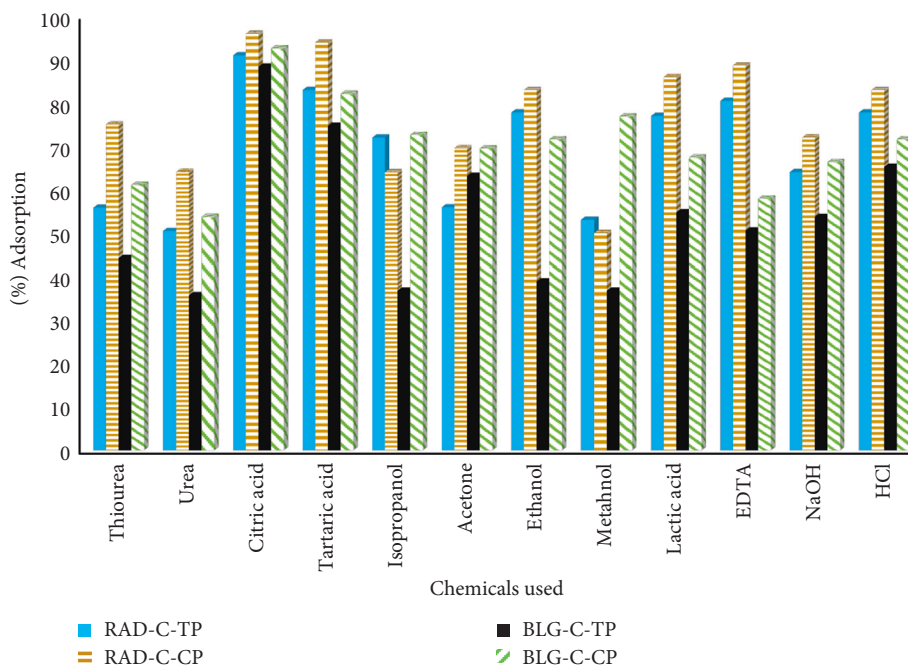
FIGURE 4: A comparative study of adsorption of dyestuffs after chemical modification with different modifying agents.
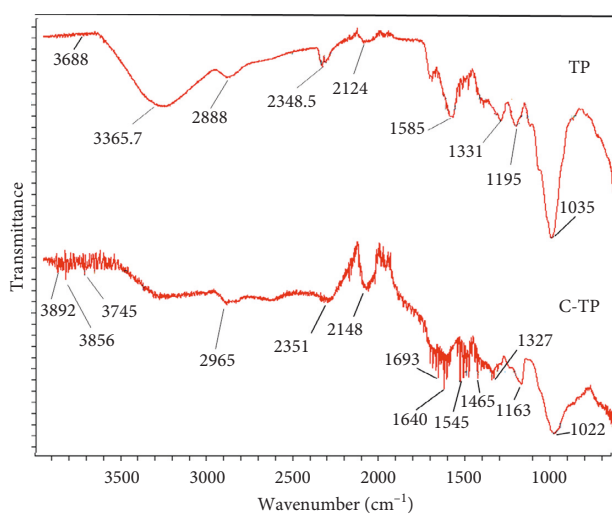

FIGURE 5: A comparative FT-IR analysis of native (TP) and citric acid-modified (C-TP) *Trapa natans* peels.

$3250\,cm^{-1}$ in Figure 7(b) indicate interactions with RAD caused by the -OH group of carboxylic acid on acid-modified adsorbents C-TP and C-CP, respectively. Figures 7(c) and 7(d) show the FT-IR spectra following the adsorption of the second model dye, BLG, on C-TP and C-CP, respectively. In both cases, the change in wavenumber at 3900, 3845, and $3740\,cm^{-1}$ in Figure 7(c) and at 3900, 3820, and $3700\,cm^{-1}$ in Figure 7(d) indicate significant intermolecular interactions between BLG and the citric acid-modified adsorbents C-TP and C-CP. The wavenumber at $1800–1570\,cm^{-1}$ in 7(c) and $1760–1520\,cm^{-1}$ in 7(d) associated with the adsorption of BLG. It was noticed from previously reported data that functional groups containing oxygen promote the adsorption of cationic dyes [27–29]. The

prominent peaks in Figure 7(c) at $1437\,cm^{-1}$ and in Figure 7(d) at $1440\,cm^{-1}$ illustrate (OH) bending groups for COOH moieties on modified adsorbents C-TP and C-CP, respectively.

3.2.3. SEM Analysis of Modified Adsorbents. The unprocessed TP in Figure 8(a) has packed tubular shapes gaps and voids, while its chemically amended form using citric acid C-TP in Figure 8(b) has irregular tubular, granular, and honeycomb-like arrangements with increased surface area. This revealed that the morphology of native TP had been modified which favored and provided enhanced additional binding linkages, surface area, and adsorption sites for adsorptive elimination of selected dyes from water. The structural morphology of raw CP is depicted in Figure 8(c), with gaps, tiny imprinted depressions in between the many spherical bodies, and dense circular clusters. Figure 8(d) shows a chemically modified citric acid-treated form of CP. It is converted into fleece lined, flossy, granular, frizzy, and frothy bodies with numerous binding sites for efficient, quicker, and good adsorptive removal of RAD and BLG from aqueous solution. Figure 8(d) shows an aggregate of clusters of citric acid molecules on the interface of C-CP. The modified surface morphology of both C-TP and C-CP with numerous available active adsorption sites promotes adsorption phenomenon as compared to their unprocessed forms which is reported in different investigations and shown in Table 2.

3.3. Optimization of Operational Conditions. Parameters settings for experiments like T (°C), biosorbent dosage, retention time, stirring rate, and pH of solution were used to determine the best conditions for adsorptive eradication of
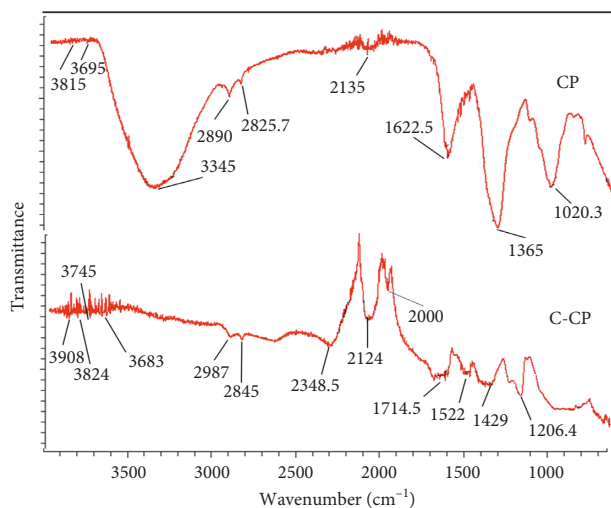
Figure 6: A comparative FT-IR analysis of native (CP) and citric acid-modified (C-CP) *Citrullus lanatus* peels.

RAD and BLG by using citric acid-modified adsorbents C-TP and C-CP, respectively.

3.3.1. Modified Adsorbent Dosage Effect on Adsorption.
The adsorbent dose of C-TP and C-CP ranged from 0.2 to 2.0 g, with a difference of 0.1 g being utilized under different operational conditions.

According to FT-IR interpretation, citric acid-modified adsorbents C-TP and C-CP with additional COOH groups have more active binding affinity on their interfaces for association with cationic dye molecules RAD^+ and BLG^+. For this study, 25 ppm solutions with a volume of 25 mL were taken separately in four sets of Erlenmeyer flasks, and each set contained ten flasks for smooth experimental studies. The experimental operational conditions for the study of adsorption dose investigation were employed as follows: temperature of 30°C, 125 rpm agitation speed, initial pH = 5, and final pH for RAD on C-TP and C-CP = 4, whereas for BLG on C-TP it was 4.5 and for BLG on C-CP it was 4. Figure 9 depicts the experimental results graphically. For 0.8 g of C-TP, the maximum RAD adsorptive removal from aqueous solution was 91.5 percent, and, for 0.8 g of C-CP, it was 96.8 percent. Similarly, the maximum adsorptive elimination of the second model dye, BLG, was determined to be 96.84 percent on 0.8 g of C-TP and 98.94 percent on 0.8 g of C-CP. Figure 9 also illustrates that, at low concentrations, the adsorption of each model dye, RAD and BLG, increases due to a greater number of available binding adsorption sites on the acid-treated biosorbents, but as concentration increases, the equilibrium between adsorbates and adsorbents interfaces is quickly established, resulting in decreased adsorption [45]. The optimal adsorbent dose of 0.8 g was determined for further experimental studies.

3.3.2. Contact Time Influence on Adsorption.
As shown in Figure 10, the performance of the adsorption process is related to the contact time interval and the number of available binding sites on the interfaces of biosorbents C-TP
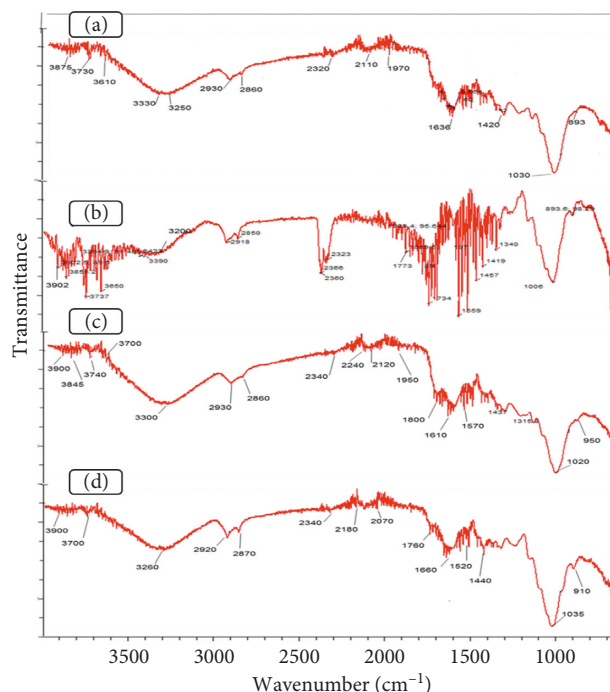
Figure 7: FT-IR spectra after adsorption of RAD and BLG. (a) RAD-C-TP. (b) RAD-C-CP. (c) BLG-C-TP. (d) BLG-C-CP.

and C-CP. Initially, with the increase in contact time interval, the adsorption of RAD and BLG enhanced till the optimal time interval was achieved and afterward decreased by unit mass due to the establishment of equilibrium and many vacant adsorption binding sites left on the surfaces of C-TP and C-CP. A contact time duration of 60 minutes with a difference of 5 minutes was selected for this study by using 25 mL of each of RAD and BLG solutions with a concentration of 25 ppm. The optimal time interval for maximum adsorption removal of RAD on C-TP was 91.51% at 25 minutes, while for BLG on C-TP it was 93.68% at 25 minutes, whereas the adsorptive eradication from aqueous solution of RAD on C-CP was 96.99% at 20 minutes, while for BLG on C-CP it was 97.89% at 20 minutes as illustrated in Figure 10. By comparing the results of citric acid-modified biosorbents with the previously reported data as tabulated in Table 2, the efficiency of the adsorption performance of C-TP and C-CP is promising due to the accessibility of RAD and BLG toward extra adsorption active sites and intra-particle diffusion [46]. Moreover, after the optimal time interval and with the passing of time period, the over-abundance of the RAD and BLG cations on the surfaces of C-TP and C-CP induces reduction and a cessation of the efficiency of the adsorption performance [28]. Therefore, the optimal contact time interval of 20 minutes was determined for further experimental work.

3.3.3. Influence of Agitation on Adsorption.
It is another significant factor that controls the adsorption behavior because it results in the formation of a light coating of adsorbates (RAD and BLG) on adsorbents from solutions. The formation of a distinctive and different outermost
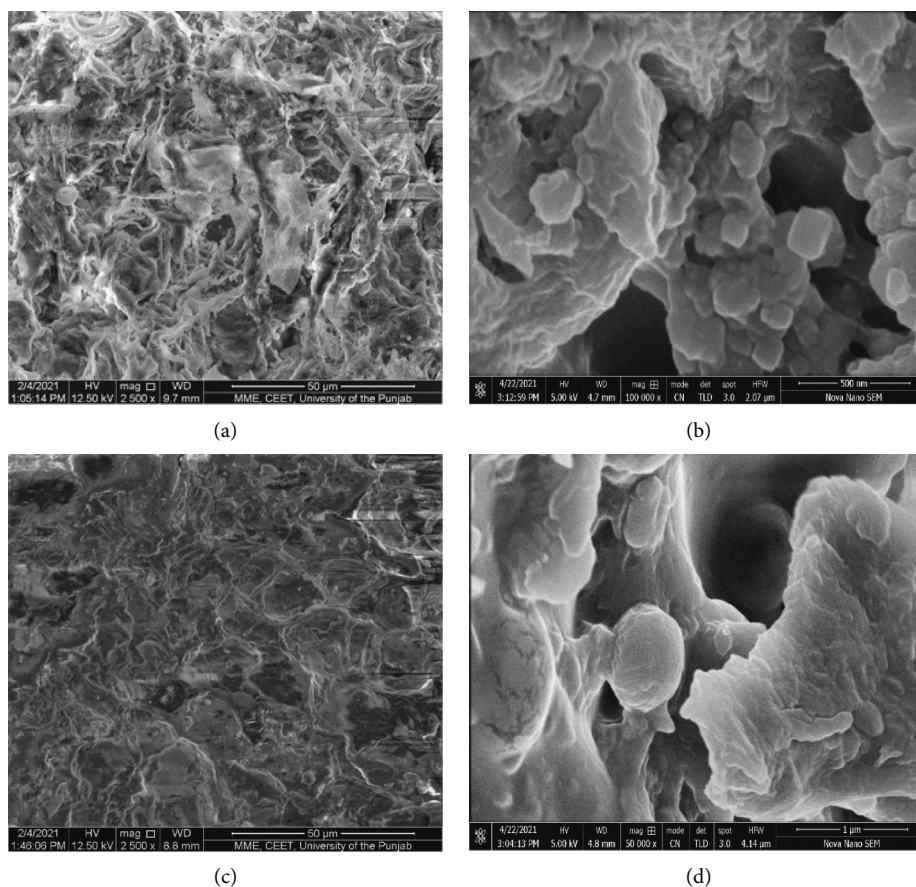
(a)

(b)

(c)

(d)

FIGURE 8: A comparative SEM evaluation. (a) TP, (b) C-TP, (c) CP, and (d) C-CP.

boundary of cationic dye molecules on modified adsorbents boosts and promotes adsorption performance [47]. Therefore, agitation rate influenced the adhering of RAD and BLG on citric acid-modified C-TP and C-CP. This factor was studied in the range of 25 to 200 rpm speed with just difference of 25 rpm. Experiments in batch mode were carried out under other appropriate operating parameters such as contact time of 20 minutes, temperature of 30°C, 0.8 g adsorbent dose, initial pH of 5, and the conc. of each dye solution of 25 ppm with a 25 mL volume.

As a consequence, maximal decontamination of RAD on C-TP and C-CP was 91 and 92.6% at 125 rpm agitation speed, whereas maximum adsorptive reduction of BLG on C-TP was 97% at 125 RPM and that on C-CP was 96% at 100 RPM, as graphically shown in Figure 11. During the experiment, high RPM speed was observed to be connected to a decrease in the adsorption process owing to the creation of excessive uniform circular motion velocity of independent RAD and BLG molecules from water [48], which can also be seen in Figure 11.

3.3.4. Influence of Temperature Variations on Adsorption. The adsorption mechanism can be exothermic or endothermic, and it is strongly linked to temperature fluctuations, which can be seen in Figure 12.

Temperature changes influence the kinetic energy of dye molecules, which ultimately change the thermodynamic parameters. According to the literature, adsorption is generally temperature-dependent, so higher temperatures decrease the rate of the adsorption process [48]. The impact of temperature varying from 10 to 80°C with just a 10°C gap was examined for optimization of the aforementioned parameters during this study by using a 25 mL volume of each RAD and BLG separately, with a concentration of 25 ppm under optimized conditions. The highest adsorption percentage expulsion of RAD on C-TP was 89% at 40°C and on C-CP it was 94% at 30°C, while the maximal percentage removal of BLG on C-TP and C-CP was 90.5% and 97%, respectively, at 30°C. The adsorption of dyes rises at certain high temperature levels, as mentioned in Figure 12, because the adsorbent framework is degraded and disrupted by the high temperature. As a consequence, in such cases, the adsorbents expand, bulge, and elongate. Consequently, dyes (RAD and BLG) penetrate deeper into the deteriorated structure of the adsorbents [49]. Hence, the rate of adsorption accelerates. As a consequence, in some cases, adsorption increases at high temperature variations, such as RAD adsorption on C-TP rising from 50 to 60°C (78 to 83%), RAD adsorption on C-CP continuing to increase from 60 to 70°C (67 to 72%), and BLG adsorption on C-TP increasing

TABLE 2: A comparison of the adsorption capacity with some previously published works.

Biosorbents	Adsorption capacity (mg/g)	References
Detoxification of Rhodamine B dye		
Rhizophora mucronata, carbon nanotubes composite	6.784	[30]
Gracilaria edulis	8.96	[31]
Kappaphycus alvarezii	9.84	[31]
Gracilaria salicornia	11.03	[31]
Crude coconut fibers	13	[32]
HCOOH-modified coconut fibers	22	[32]
Artocarpus heterophyllus seed	26.4	[33]
Hexadecyltrimethylammonium bromide-treated *Volvariella volvacea*	33.51	[34]
Acrylic acid-processed walnut shell	48.87	[35]
Inactivated *Aspergillus oryzae*	98.59	[36]
Elaeis guineensis shell	108	[37]
Trapa natans peels modified with citric acid	15.63	Current research work
Citrullus lanatus peels modified with citric acid	27.55	Current research work
Detoxification of Brilliant Green Dye		
Peanut shells	19.92	[38]
Raw peels of *Trapa natans*	50.51	[39]
Rock melon skin	118	[40]
Snail shell-rice husk	129.8	[41]
White rice husk ash	85.56	[42]
Cellulose (raw)	90.5	[43]
H_3PO_4-treated cellulose	150	[43]
Banana peels	22.44	[44]
Trapa natans peels modified with citric acid	128	Current research work
Citrullus lanatus peels modified with citric acid	189	Current research work
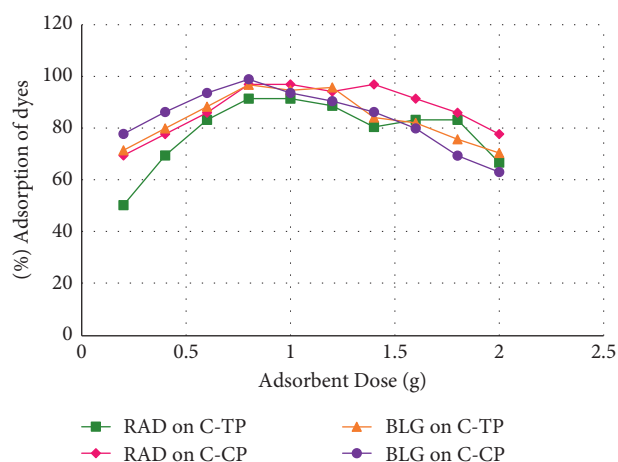
FIGURE 9: Effect of modified adsorbents dosage. Initial pH = 5, final pH for RAD on C-TP and C-CP = 4, BLG on C-TP = 4.5, and BLG on C-CP = 4.

FIGURE 10: Contact time influence on adsorption. Initial pH = 5, final pH for RAD on C-TP and C-CP = 4, BLG on C-TP = 4.5, and BLG on C-CP = 4.

from 60 to 70°C (75 to 77%). As a result, the optimal temperature of 30°C was determined for future experiments.

3.3.5. Influence of pH on Adsorption. The pH of the dye adsorption on lignocellulose substrates was adjusted using 0.1 M NaOH or 0.1 M HCl solutions during the experimental work [50]. The pH_{PZC} of both biosorbents TP and CP is significant for evaluating their adsorption potentials for both model dyes RAD and BLG and was experimentally determined to be 5.8 and 5.6 for TP and CP, respectively [24].

Figure 13 illustrates the influence of pH on the adsorption of model dyes RAD and BLG on citric acid-amended C-TP and C-CP in a pH range from 1 to 10. For this investigation, 25 ppm solutions with a volume of 25 mL were taken separately in four sets of Erlenmeyer flasks, and each set contained ten flasks for smooth experimental studies, while 0.8 g of each modified C-TP and C-CP was added to each pair of conical flasks containing 25 mL of RAD and BLG solutions with a
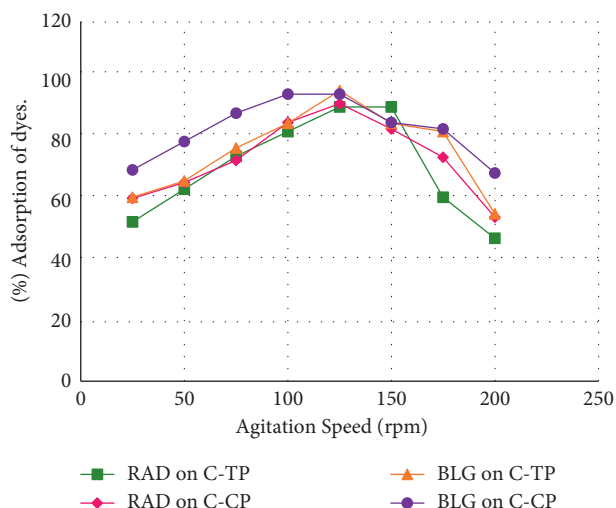
FIGURE 11: Effect of agitation speed on adsorption. Initial pH = 5, final pH for RAD on C-TP = 4, RAD on C-CP = 4.5, BLG on C-TP = 4.5, and BLG on C-CP = 4.
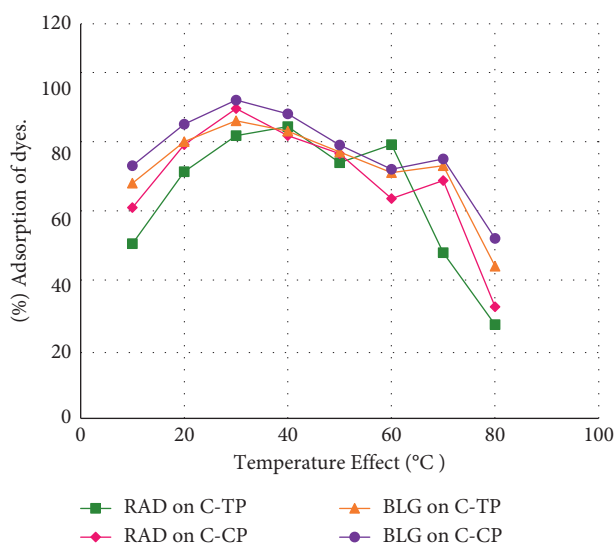

FIGURE 12: Influence of a change in temperature on biosorption. Initial pH = 5, final pH for RAD on C-TP and C-CP = 4, BLG on C-TP = 4.5, and BLG on C-CP = 4.

concentration of 25 ppm. The maximum adsorption elimination of RAD on C-TP was 96.99% at pH = 6, while RAD on C-CP was 91.51% at pH = 5, whereas maximum removal of BLG on C-TP was 93.68% and on C-CP it was 96.84% at pH 5, respectively. Figure 13 also illustrates that the decrease in adsorption performance of RAD and BLG was associated with an increase in pH, which influenced the development of equilibria with the adsorption binding active sites [COO⁻] on the surfaces of biosorbents C-TP and C-CP and attractive associations of [RAD⁺] and [BLG⁺] cations with free [OH-] ions in the aqueous solutions [51], resulting in hindering their accessibility to negatively charged adsorption sites on the interfaces of biosorbents [52].
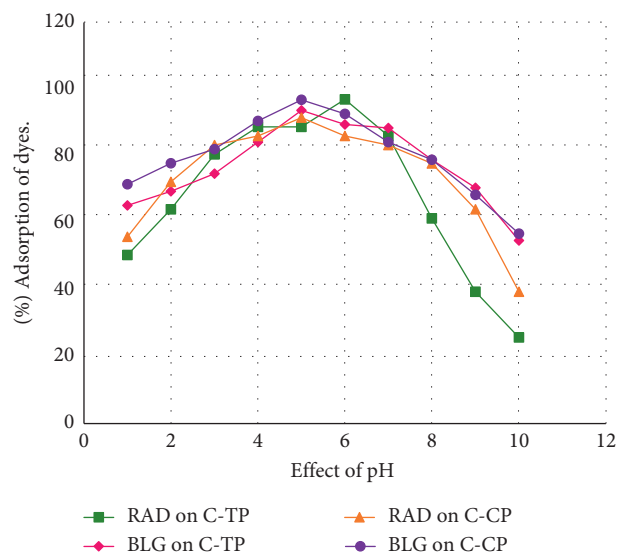
FIGURE 13: Influence of pH on adsorption mechanism.

Figure 13 also demonstrates that a decrease in pH causes the protonation of the negatively binding sites of biosorbents due to excessive H^+ ions in the solution, which compete with the RAD^+ and BLG^+ cationic dye molecules, resulting in hindered adsorption at the interfaces of biosorbents [53]. Therefore, by considering the above results, an optimal pH value of 5 was determined for further studies.

3.4. Isothermal and Kinetic Modelling of Biosorption Processes

3.4.1. Approach to Equilibrium Isothermal Models. For the validity and reliability of the experiments conducted for the adsorption of RAD and BLG on citric acid-modified biosorbents (C-TP and C-CP), three equilibrium isothermal models by Langmuir, Freundlich, and Temkin were correlated and implemented by using linear equations (3), (6), and (7), respectively. The biosorption investigation was carried out with the following optimized parameters: The contact time interval was 20 minutes, the adsorbent dose utilized was 0.8 g of each of C-TP and C-CP, the temperature was 30°C, the agitation speed was 125 rpm, the initial pH of solutions used was 5, and the initial volume and concentrations of each dye solution (RAD and BLG) were 100 mL and 25 ppm.

(1) Langmuir Isotherm. Equation (3) displays a linear regression formulation of the Langmuir isotherm model [54], and Figure 14 elaborates on effective graphical factors.

$$\frac{1}{Q_e} = \left(\frac{1}{b.Q_{max}}\right)\frac{1}{C_e} + \left(\frac{1}{Q_{max}}\right). \tag{3}$$

Here, quantity (ppm) of RAD and BLG adsorbed is indicated as "Q_e," while residual quantity is expressed as C_e, and the adsorption capability "Q_{max}" is the maximum adsorption capacity in $mg.g^{-1}$, while "b" is the adsorption capacity (L/g) [55].
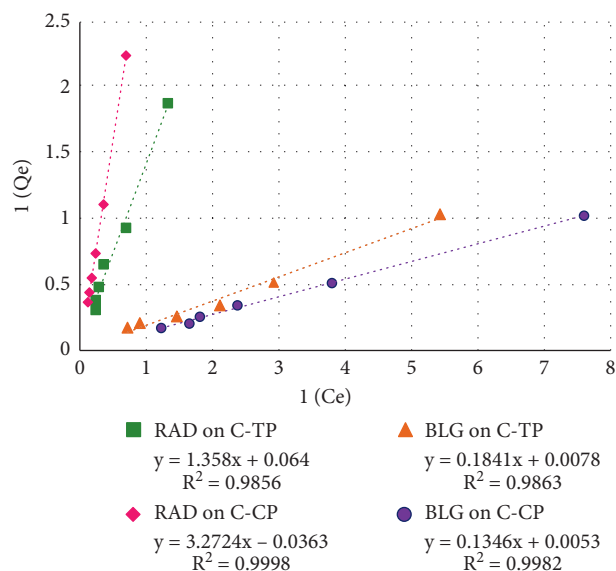
FIGURE 14: A comparison of the Langmuir isothermal model for the adsorptive dye removal efficiency of acid-treated biosorbents. Initial pH = 5, final pH for RAD on C-TP and C-CP = 4, BLG on C-TP = 4.5, and BLG on C-CP = 4.

The correlation coefficient (R^2) for the adsorption of RAD on C-TP was 0.985, while on C-CP it was 0.999, whereas for the adsorption of BLG on C-TP it was 0.986 and on C-CP it was 0.999. The values of "R^2" are close to unity in all cases, revealing that the Langmuir model is the best fit for the adsorption performance of C-TP and C-CP in this study. The maximum adsorption capacity (Q_{max}) for adsorption of RAD on C-TP was 15.6 and on C-CP it was 27.5 mg/g, whereas for BLG on C-TP it was 128 and on C-CP it was 189 mg/g, as tabulated in Table 3. The separation factor (R_L) was calculated by using the following equation:

$$R_L = \left[\frac{1}{1 + bC_o}\right]. \tag{4}$$

Its value between "0 and 1" reflects a good rate of adsorption. The separation factor (R_L) for the adsorption of RAD on C-TP was 0.414 and on C-CP it was 0.750, whereas for the adsorption of BLG on C-TP it was 0.440 and on C-CP it was 0.458. These values, being less than "1," indicate the good rate of adsorption and reflect the good and effective application of the Langmuir model for biosorption. Furthermore, the least values of RMSE for the adsorption of RAD on C-TP and C-CP were 2.76 and 2.03, respectively, while for BLG on C-TP and C-CP they were 4.1 and 5.2, respectively, indicating favorable adsorption for all cases. Moreover, "Q_{max}" values signify the monolayer homogeneity adsorption of dyes on C-TP and C-CP at a specific number of identical adsorption binding sites distributed on the interface boundaries of both biosorbents.

(2) Freundlich Isothermal Model. Freundlich isothermal model is employed to evaluate the surface heterogeneity of acid-modified adsorbents (C-TP and C-CP), as well as their activity for adsorption performance toward RAD and BLG

in aqueous solutions. It is concerned with the comparative distribution of energy in both physisorption and chemisorption. Equation (5) represents a linear trend of this isothermal system [54].

$$\ln q_e = \left(\ln K_F + \frac{1}{n}\ln C_e\right). \tag{5}$$

Here, "K_F" ($mg^{1-1/n}$ $L^{1/n}$ g^{-1}) is the binding factor and "n" represents the adsorption frequency. A graphic comparison of the Freundlich model [ln Q_e versus ln C_e] is depicted schematically in Figure 15, which illustrates straight lines for both citric acid-modified biosorbents (C-TP and C-CP).

As the graphical representation shown in Figure 15, for each model dye, exhibiting a slope (1/n) less than 1 with correlation coefficient value for RAD on C-TP and C-CP was 0.94 and 0.91, respectively, whereas, for BLG on C-TP and C-CP was 0.77 and 0.92, respectively, which measured the interface diversity or uptake capacities of C-TP and C-CP. The correlation coefficients (R^2) for the adsorptive removal of RAD on C-TP and C-CP were 0.96 and 0.93, respectively, whereas for BLG on C-TP and C-CP they were 0.98 and 0.94, respectively. The correlation coefficients, as tabulated in Table 3, reveal that the Langmuir model is more precise and perfect for this investigation than the Freundlich model.

(3) Temkin Isothermal Studies. Based on the fundamental assumption, Temkin modeling predicts an approximately equivalent dispersion of binding affinities on C-TP and C-CP. As a result, thermal diffusivity gradually decreases as the saturation of binding sites on the surface of adsorbents by RAD and BLG molecules increases. Linear representation of the Temkin isotherm is shown in the following equation:

$$q_e = \left(B_T \ln K_T + B_T \ln C_e\right). \tag{6}$$

The Temkin isotherm constant $B_T = R_T/b_T$ ($kjmol^{-1}$) designates the energy released during adsorption, whereas the equilibrium binding constant "K_T" ($L.g^{-1}$) reflects the maximal binding energy.

These constants were determined during the experimental research by linear regression of the graph plotted between "C_e and $\ln C_e$" by using equation (6) for the adsorption of RAD and BLG on C-TP and C-CP, as shown graphically in Figure 16. The Temkin isotherm parameters are presented in Table 3, in which the heat of adsorption (B_T) for RAD on C-TP and that on C-TP were 1.1512 $Jmol^{-1}$ and 1.315 $Jmol^{-1}$, respectively, while for BLG on C-TP and on C-CP they were 1.28 $Jmol^{-1}$ and 1.5 $Jmol^{-1}$, respectively. These B_T results are less than 8, confirming weak and physical adsorbate-adsorbent interactions and demonstrating physisorption rather than chemisorption.

The correlation coefficients (R^2) as tabulated in Table 3 for adsorption of RAD on C-TP and C-CP were 0.83 and 0.93, respectively, whereas, for adsorption of BLG on C-TP and C-CP they were 0.95 and 0.84, respectively. These values of R^2 for Temkin were less as compared to the Langmuir or Freundlich isothermal systems, suggesting that this model is unsatisfactorily fitted to this adsorption system. Equilibrium

TABLE 3: A comparison of isothermal parameters for the adsorptive elimination of RAD and BLG on citric acid-treated adsorbents C-TP and C-CP.

Parameters	RAD- C-TP	RAD-C-CP	BLG-C-TP	BLG-C-CP
Langmuir isothermal adsorption model				
R^2	0.986	0.985	0.99	0.998
Q_{max} (mg/g)	15.625	27.55	128	189
R_L (L/mg)	0.41428	0.75031	0.4403	0.4585
b (L/mg)	0.047	0.011	0.04368	0.03938
Root mean sq. error	2.76	2.03	4.101	5.256
Freundlich isothermal adsorption model				
R^2	0.96	0.936	0.98	0.94
$1/n$	0.94	0.91	0.77	0.92
n (1/m)	1.0675	1.0964	1.304	1.084
K_F (mg/g)	1.4395	2.5656	2.9450	4.1133
Root mean sq. error	3.14	2.43	4.496	5.493
Temkin isothermal adsorption model				
R^2	0.831	0.939	0.95	0.84
B_T (J.mol^{-1})	1.1512	1.3154	1.28	1.5
K_T (L.g^{-1})	1.8228	1.0050	9.85	10.0
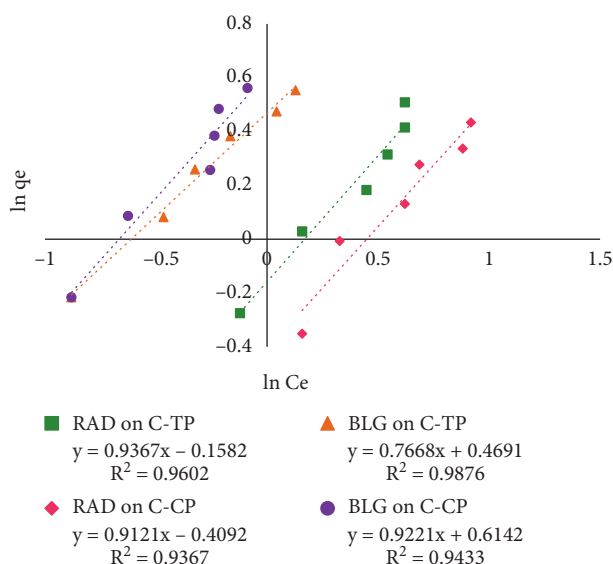
FIGURE 15: Evaluation of the Freundlich model regarding adsorptive dye removal efficiency of acid-treated biosorbents. Initial pH = 5, final pH for RAD on C-TP and C-CP = 4, BLG on C-TP = 4.5, and BLG on C-CP = 4.

binding constants "K_T" (L.g^{-1}) for adsorption of RAD on C-TP and C-CP were 1.822 and 1.00, respectively, while for BLG on C-TP and C-CP they were 9.85 and 10.0, respectively. The higher the magnitude of "K_T," the greater the number of accessible functional groups (like COOH, OH) on the surface of adsorbents [56]. The root mean square errors of C-TP and C-CP for adsorption of both RAD and BLG were determined by using equation (7) [57] and they are listed in Table 3.

$$\text{RMSE} = \sqrt{\sum\left[\frac{\left(Q_{e(cal)} - Q_{e(\exp)}\right)^2}{N}\right]}. \tag{7}$$

The smaller root mean square values suggest that the experimental findings for the adsorptive elimination of RAD and BLG on citric acid-treated adsorbents (C-TP and C-CP) were favorable.

3.4.2. Batch Adsorption Kinetic Analyses. Pseudo-first-order and pseudo-second-order kinetics have been used to investigate the adsorption of each dye (RAD and BLG) on chemically altered adsorbent materials (C-TP and C-CP) [58].

(1) Pseudo-First-Order Kinetics. Equation (8) displays the general formulation of Lagergren's expression for this kinetic [59].

$$\ln\left[Q_{eq} - Q_t\right] = \left[\left(\ln Q_{eq}\right) - \left(k_1 t\right)\right], \tag{8}$$

where "Q_{eq}" (mg/g) is indeed the quantity of RAD and BLG taken at equilibrium and "K_1" is the experimental data rate constant for pseudo-first-order kinetics (g/mg^{-1}min^{-1})) and "Q_t" (mg/g) is the adsorption capacity in "mg" of every dye RAD and BLG at time t (min^{-1}) on 1 g of each C-TP and C-CP, respectively [60]. A plot "$\ln[Q_{eq} - Q_t]$ versus (t)" drawn illustrates adsorptive expulsion of both RAD and BLG on citric acid-modified biosorbents C-TP and C-CP, respectively, depicted in Figure 17. The corresponding characteristic parameters are shown in Table 4. The correlation coefficients R^2 for adsorption of RAD on C-TP and C-CP were 0.53 and 0.71, respectively, while for adsorption of BLG on C-TP and C-CP they were 0.63 and 0.59, respectively. These smaller values of R^2 for both dyes on each modified adsorbent reveal that Lagergren's expression for the pseudo-first-order mechanism presented in relation (8) is not properly applicable to the overall adsorption process. Furthermore, high values of RMSE for adsorption of RAD on C-TP and C-CP were 4.557 and 5.604, while for adsorption of BLG on C-TP and C-CP they were 6.15 and 10.272, also
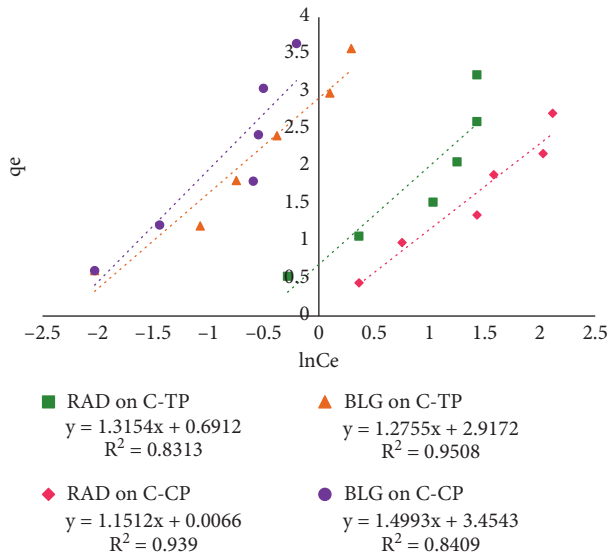
FIGURE 16: A comparison of the Temkin isothermal model for the adsorptive dye removal efficiency of acid-treated biosorbents. Initial pH = 5, final pH for RAD on C-TP and C-CP = 4, BLG on C-TP = 4.5, and BLG on C-CP = 4.
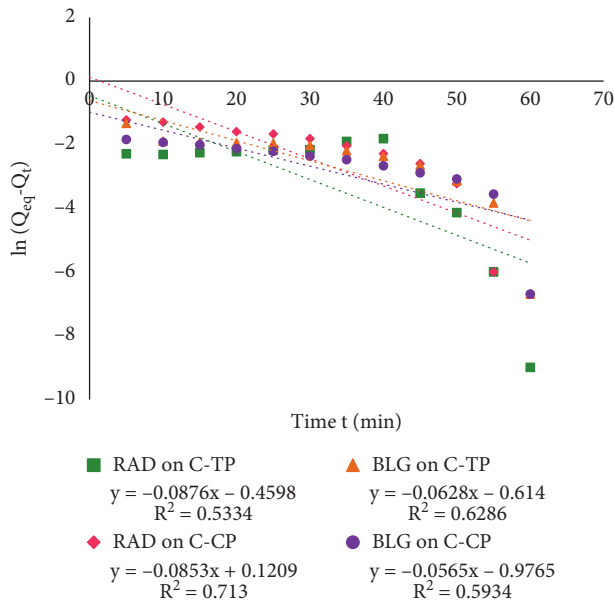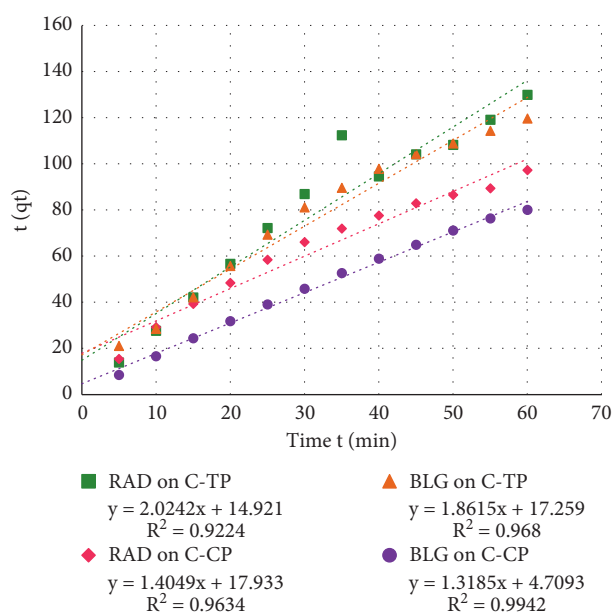

FIGURE 17: A comparative evaluation of the pseudo-first-order kinetics for the adsorptive dye removal performance of acid-treated biosorbents. Initial pH = 5, final pH for RAD on C-TP and C-CP = 4, BLG on C-TP = 4.5, and BLG on C-CP = 4. (b) Pseudo-second-order kinetics.

indicating that this kinetic model is not suitable and does not fit this adsorption system.

The rate equation (9) for pseudo-second-order mechanism was presented by HO and McKay and is given as follows [61]:

$$\frac{t}{Q_t} = \left[\left(\frac{1}{K_2 \cdot Q_{eq}^2} \right) + \left(\frac{t}{Q_{eq}} \right) \right]. \tag{9}$$

In the above equation, Q_{eq} (mg/g) denotes the optimum adsorption capability, whereas Q_t signifies the adsorption efficiency in time t (min^{-1}). An experimental data rate factor (g/mg^{-1}min^{-1}) is termed as K_2 [62].

The correlational evaluation for graph plotted linearly among (Q_t vs t), depicted graphically displayed in Figure 18. This data is used to determine the rate constants and adsorption capability from the slope by using equation (9). The significant parameters have been determined and are listed in Table 4. The correlation coefficients (R^2) for the adsorption of RAD on C-TP and C-CP were 0.92 and 0.96, respectively, while for the adsorption of BLG on C-TP and C-CP they were 0.96 and 0.99, respectively, near to unity, indicating that the pseudo-second-order kinetic model seems to be more fit than the pseudo-first-order kinetic model. The RMSE values of pseudo-second-order kinetics for the adsorption of RAD on C-TP and C-CP were 3.328 and 3.418, respectively, while for the adsorption of BLG on C-TP and C-CP they were 4.5 and 6.63, as mentioned in Table 4. These values are smaller rather pseudo second order kinetic. This also reflects the suitability and fitness of the pseudo-second-order model for this adsorption system.

(2) Determination of Percent Relative Deviation (P). The percent relative deviation has been used to determine the validity of kinetics models for the adsorption of RAD and BLG on both C-TP and C-CP. Equation (10) was employed to determine it, and the conclusions are summed up in Table 4. The least values of percent relative deviation for the adsorption of RAD on C-TP and C-CP were −0.551 and −1.186, while for BLG on C-TP and C-CP they were −0.553 and −0.103, respectively, reflecting that second-order kinetics support the acceptability and suitability in better way as compared to the first-order kinetics [63].

$$\%\text{Relative Deviation}(P) = \frac{100}{N} \sum \left[\frac{\left(Q_{e(\text{exp})} - Q_{e(\text{cal})} \right)}{Q_{e(\text{exp})}} \right], \tag{10}$$

where N represents the number of observations, Q_e (exp.) (mg/g) denotes the experimental value of adsorption binding capacity, and Q_e (cal.) (mg/g) represents the calculated value of adsorption binding capabilities.

(3) Thermodynamic Investigation. Temperature change will have an impact on the adsorption mechanism, leading to variations in the kinetic energies of RAD and BLG molecules. Because of the entire porous interface of used cellulosic biomass, this factor accelerates the amount of dispersion of RAD and BLG. Table 5 highlights that the effectiveness and rate of adsorption of RAD and BLG on innovative C-TP and C-CP are determined by operational thermodynamic parameters, such as Gibbs free energy, enthalpy changes, and entropy changes. The increase $(-\Delta G^o)$

TABLE 4: A comparison of parameters for kinetics studies.

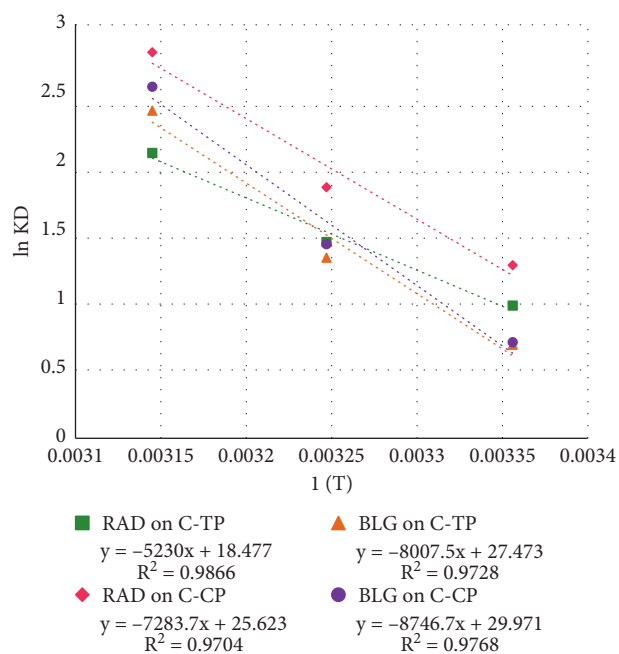|		Kinetic equilibrium models for adsorption		
Parameters	RAD-C-TP	RAD-C-CP	BLG-C-TP	BLG-C-CP
Evaluation of pseudo-first-order kinetics				
R^2	0.53	0.71	0.63	0.59
Q_e (exp.-mg/g)	0.46	0.62	0.50	0.75
Q_e (cal.-mg/g)	0.63	1.13	0.54	0.38
K_1 (g/mg^{-1}min^{-1})	0.00146	−0.00142	−0.00105	−0.00094
Root mean sq. error	4.557	5.604	6.157	10.272
% relative deviation	−2.837	−6.359	2.05	3.82
Evaluation of pseudo-second-order kinetics				
R^2	0.922	0.963	0.963	0.994
K_2 (g/mg^{-1}min^{-1}))	0.275	0.11	0.201	0.369
Q_e (exp.mg/g)	0.46	0.62	0.50	0.75
Q_e (cal.mg/g)	0.494	0.712	0.54	0.76
Root mean sq. error	3.328	3.418	4.502	6.637
% relative deviation	−0.551	−1.186	−0.553	−0.103

FIGURE 18: A comparison of the pseudo-second-order kinetics for the adsorptive dye removal performance of acid-treated biosorbents. Initial pH = 5, final pH for RAD on C-TP and C-CP = 4, BLG on C-TP = 4.5, and BLG on C-CP = 4.

of both unique citric acid-treated adsorbents reflects a rapid, exothermic, and spontaneous adsorption mechanism. These calculations were estimated from the following equation:

$$\Delta G^o = [RT (\ln K_D)], \qquad (11)$$

where "R" is the universal gas constant, "T" is temperature in Kelvin, and K_D (distribution coefficient) is determined using the following equation:

$$K_D = \frac{(C_o - C_e)}{C_e}. \qquad (12)$$

Enthalpy change values varying from 2.1 to 20.9 kJmol^{-1} suggest physisorption, whereas values ranging from 80 to 200 kJmol^{-1} reflect strong interactions leading to chemisorption. Adsorption of each RAD and BLG on C-TP and C-CP was observed chemically in nature and summarized in Table 5. The fact that the citric acid-altered adsorbents have greater enthalpy change values, determined from equation (13), promotes adsorption over their untreated forms.

The distortedness at the solid-liquid boundaries during the adsorption can also be determined by the change in entropy ($\Delta S°$) and was calculated as follows:

$$\ln K_D = \left[\frac{\Delta S°}{R} - \frac{\Delta H°}{RT} \right]. \qquad (13)$$

Its high positive values favor a considerable pace of adsorption [64]. A linear graph was drawn across "$\ln K_D$ versus $1/T$," depicted in Figure 19.

The slope and intercept were used to determine the values of $\Delta H°$ and $\Delta S°$ for the adsorptive elimination of dyes (RAD and BLG) on C-TP and C-CP. Equation (14), which is a rearranged form of equation (13), can be used to determine $\Delta H°$ and $\Delta S°$.

$$\Delta G° = [\Delta H° - T\Delta S°]. \qquad (14)$$

The energy of activation (E_a) for the adsorptive elimination of each RAD and BLG on C-TP and C-CP was calculated using the Arrhenius equation.

$$\ln K = \left[\ln A - \left(\frac{E_a}{RT} \right) \right]. \qquad (15)$$

Physical adsorption, E_a, ranges from 5 to 40 kJ/mole, whereas chemical adsorption ranges from 40 to 800 kJ/mole. In this investigation, the data given in Table 5 reveals the physisorption process.

3.5. Mechanism of Adsorption. As evidenced by FT-IR and SEM analysis, chemically modified adsorbents C-TP and C-CP with chelator (citric acid) were suggested to include various additional moieties, including carboxylic acids and hydroxyl, carbonyls, and primary amines across their

Table 5: Thermodynamic comparative evaluation of the adsorptive elimination of RAD and BLG by citric acid-treated adsorbents (C-TP and C-CP).

Thermodynamic parameters analysis					
Temperature	K_D	ΔG^0 (kJmol^{-1})	ΔH^0 (kJmol^{-1})	ΔS^0 (Jmol^{-1}K^{-1})	E_a (kJmol^{-1})
RAD on C-TP					
298 K	2.614	−2.4	−44	154	44
308 K	4.141	−3.7			
318 K	7.902	−5.5			
RAD on C-CP					
298 K	3.506	−3.1	−61	213	61
308 K	6.157	−4.7			
318 K	16.38	−7.4			
BLG on C-TP					
298 K	1.969	−1.7	−67	228	67
308 K	3.703	−3.4			
318 K	10.728	−6.3			
BLG on C-CP					
298 K	2.006	−1.7	−73	249	73
308 K	4.08	−3.6			
318 K	12.768	−6.7			

Figure 19: A comparison of the thermodynamics parameters for the adsorptive dye removal performance of acid-treated biosorbents. Initial pH = 5, final pH for RAD on C-TP and C-CP = 4, BLG on C-TP = 4.5, and BLG on C-CP = 4.

interfacing regions to interact with RAD and BLG, and they were also discussed and explored in Sections 2.4 and 3.1. A schematic and proposed interaction mechanisms created by C-TP and C-CP with dye molecules (RAD and BLG) can be seen in Figure 20. The weak Van der Waals interactions, such as hydrogen bonding [65], surface complexion [66], chelation [67], ion exchange [68], and electrostatic forces [69], cause chemical bonding between dye molecules (RAD and BLG) on chemically amended-adsorbent surfaces.

According to reported data, chemical modification by using organic acids like citric acid, tartaric acid, or oxalic acids on solid base adsorbents alters and improves their surface morphology, orientation, and topography by providing additional functional groups like COOH and OH, resulting in improved adsorption capacity and affinity of novel C-TP and C-CP lignocellulosic biomass. It was noted that the adsorption phenomenon was highly dependent on pH of the dye solutions. The rate of adsorption was increased and directly related to the ionization of carboxylic acid, with the result of producing negatively charged adsorption sites at the interface of C-TP and C-CP. The deprotonation of carboxylic acids was associated with the rise in pH. The resulting ion exchange mechanism of H$^+$ with cations of RAD$^+$ and BLG$^+$ was carried out as shown in Figure 20 [47, 70].

In addition to this, hydrogen bonding linkages in between "OH" moieties on lignocellulosic biomass of C-TP and C-CP and a lone pair on nitrogen of amino groups of both RAD and BLG were created, which partially contributed to enhancing the rate of adsorption [47].

Furthermore, electrostatic forces were also established between cations of dye molecules and negatively active binding sites on the surfaces of both modified adsorbents [70]. Under the influence of such associations [51, 71], mentioned below in Figure 21, the adsorption of hazardous and toxic dyes has become more efficient and quicker during this experimental approach.

3.6. Conclusion. In this investigation, the peels of *Trapa natans* and *Citrullus lanatus* were pretreated chemically with tricarboxylic acid (citric acid) to provide modified and effective novel forms for the adsorptive removal of harmful, noxious, and carcinogenic basic and cationic dyes like Rhodamine B and Brilliant Green from the aqueous system. FT-IR and SEM analysis have provided evidence for
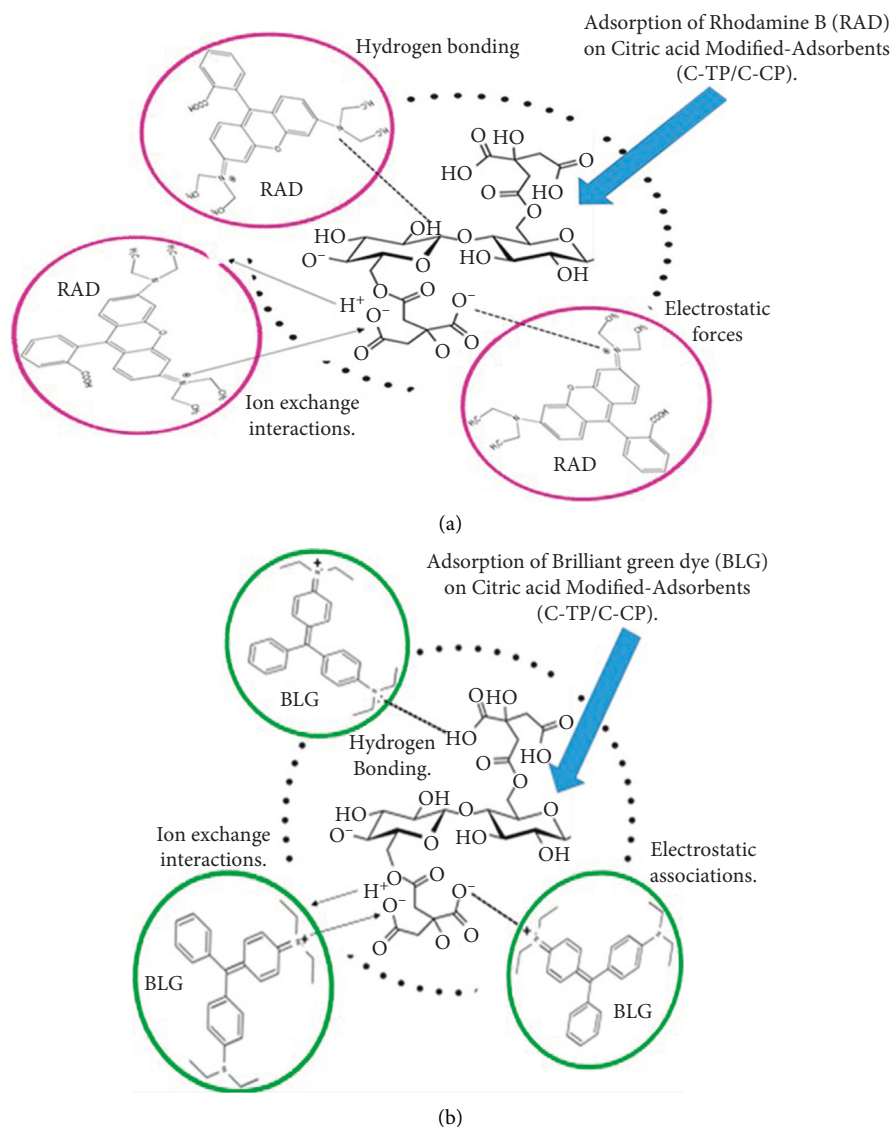
(a)

(b)

FIGURE 20: Schematic diagram for the adsorption mechanism. (a) RAD on C-TP and C-CP. (b) BLG on C-TP and C-CP.

alteration of surface amendment under the influence of the extra and additional oxygen-containing groups like COOH and OH, which are directly associated with enhancing the adsorption efficiency. Langmuir isotherm has shown that the maximum adsorption capacity (Q_{max}) for RAD on C-TP was 15.6 and that on C-CP was 27.5 mg/g, while for BLG on C-TP it was 128 and on C-CP it was 189 mg/g. Furthermore, correlation coefficient (R^2) for the adsorption of RAD on C-TP was 0.985, while on C-CP it was 0.999, whereas for the adsorption of BLG on C-TP it was 0.986 and on C-CP it was 0.999. Therefore, "R^2" is close to unity in all cases, revealing that the Langmuir model is the best fit for the adsorption performance of C-TP and C-CP in this study rather than the Freundlich and Temkin isotherms. High Langmuir isotherm regression coefficients, on the other hand, indicate that the adsorption mechanism is monolayer, with homogeneous chemisorption on equivalent active binding sites that are abundant on the surfaces of acid-treated biosorbents (C-TP

and C-CP). The heats of adsorption (B_T) for RAD on C-TP and on C-TP were 1.1512 Jmol^{-1} and 1.315 Jmol^{-1}, respectively, whereas B_T for BLG on C-TP and on C-CP was 1.28 Jmol^{-1} and 1.5 Jmol^{-1}, respectively, indicating weak and physical adsorbate-adsorbent interactions and demonstrating physisorption rather than chemisorption. The correlation coefficients (R^2) for the adsorption of RAD on C-TP and C-CP were 0.92 and 0.96, respectively, while for the adsorption of BLG on C-TP and C-CP they were 0.96 and 0.99, respectively, near to unity, indicating that the pseudo-second-order kinetic model seems to be more fit than the pseudo-first-order kinetic model. High negative ΔG^0 predicts that the adsorption mechanism is exothermic as well as spontaneous. The adsorption efficiency of the citric acid-treated peels of *Trapa natans* and *Citrullus lanatus* was also assessed by comparing them with the adsorption ability of previously reported biosorbents, as illustrated in Table 2, and it was concluded that these novel adsorbents have a
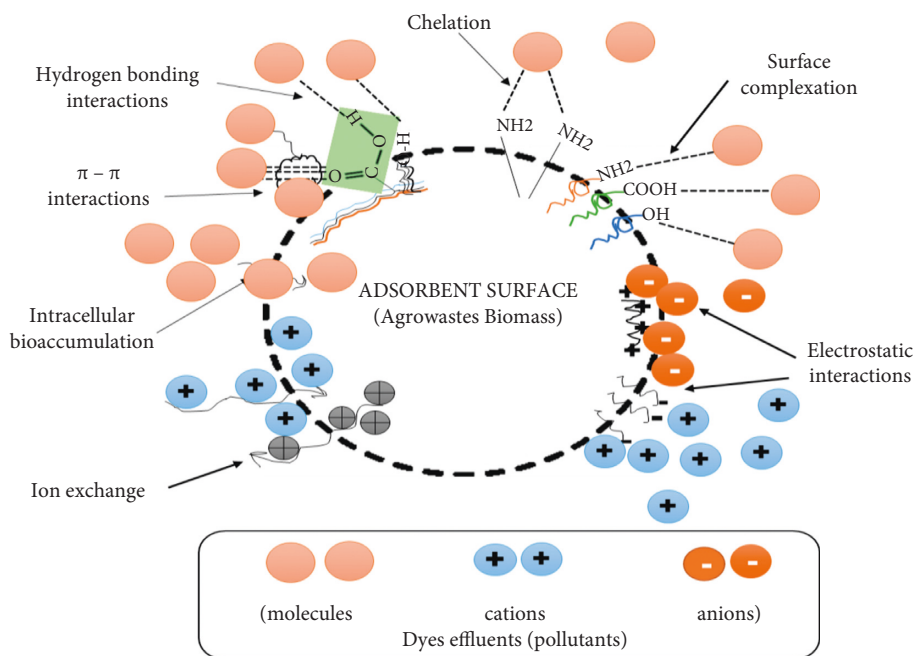
FIGURE 21: Proposed adsorption interactions between adsorbate and adsorbents are depicted schematically.

much higher ability to eliminate and evacuate basic and cationic dyes like Rhodamine B and Brilliant Green from wastewater [72].

Abbreviations

TP: Raw *Trapa natans* peels
CP: Raw *Citrullus lanatus* peels
C-TP: Citric acid-treated *Trapa natans* peels
C-CP: Citric acid-treated *Citrullus lanatus* peels
RAD: Rhodamine B dye
BLG: Brilliant Green Dye
FT-IR: Fourier-transform infrared spectroscopy
SEM: Scanning electron microscopy
pH_{PZC}: Point of zero charge
RMSE: Root mean square errors.
P: Percent relative deviation

Data Availability

All data related to this work are presented in Results and Discussion section along with references.

Conflicts of Interest

Regarding the publication of this article, the authors have no potential conflicts of interest.

Acknowledgments

References

[1] S. Gita, A. Hussan, and T. Choudhury, "Impact of textile dyes waste on aquatic environments and its treatment," *Environment and Ecology*, vol. 35, no. 3C, pp. 2349–2353, 2017.

[2] J. Mittal, V. Thakur, and A. Mittal, "Batch removal of hazardous azo dye Bismark Brown R using waste material hen feather," *Ecological Engineering*, vol. 60, pp. 249–253, 2013.

[3] R. A. E.-G. Mansour, M. G. Simeda, and A. A. Zaatout, "Removal of brilliant green dye from synthetic wastewater under batch mode using chemically activated date pit carbon," *RSC Advances*, vol. 11, no. 14, pp. 7851–7861, 2021.

[4] R. Kant, "Textile dyeing industry an environmental hazard," *Natural Science*, vol. 4, no. 1, pp. 22–26, 2012.

[5] R. Rehman, S. J. Muhammad, and M. Arshad, "Brilliant green and acid orange 74 dyes removal from water by *Pinus roxburghii* leaves in naturally benign way: an application of green chemistry," *Journal of Chemistry*, vol. 2019, Article ID 3573704, 10 pages, 2019.

[6] R. D. Saini, "Textile organic dyes: polluting effects and elimination methods from textile waste water," *International Journal of Chemical Engineering Research*, vol. 9, no. 1, pp. 121–136, 2017.

[7] S. Haq, A. W. Raja, S. U. Rehman et al., "Phytogenic synthesis and characterization of NiO-ZnO nanocomposite for the photodegradation of brilliant green and 4-nitrophenol," *Journal of Chemistry*, vol. 2021, Article ID 3475036, 10 pages, 2021.

[8] B. Cojocariu, A. M. Mocanu, G. Nacu, and L. Bulgariu, "Possible utilization of PET waste as adsorbent for Orange G dye removal from aqueous media," *Desalination and Water Treatment*, vol. 104, pp. 338–345, 2018.

[9] L. Bulgariu, L. B. Escudero, O. S. Bello et al., "The utilization of leaf-based adsorbents for dyes removal: a review," *Journal of Molecular Liquids*, vol. 276, pp. 728–747, 2019.

[10] D. Shrestha, "Efficiency of wood-dust of *Dalbergia sisoo* as low-cost adsorbent for rhodamine-B dye removal," *Nanomaterials*, vol. 11, no. 9, Article ID 2217, 2021.

[11] R. Ghibate, O. Senhaji, and R. Taouil, "Kinetic and thermodynamic approaches on Rhodamine B adsorption onto pomegranate peel," *Case Studies in Chemical and Environmental Engineering*, vol. 3, Article ID 100078, 2021.

[12] T. Utheyakumaran, *Removal of Rhodamine B Dye in Aqueous Solution Using Raw Timber Wood Sawdust as Adsorbent*, Universiti Malaysia Kelantan, Kota Bharu, Malaysia, 2020.

[13] M. Gören, "Removal of rhodamine B from aqueous solution by using pine cone activated with HNO_3," *Journal of International Environmental Application & Science*, vol. 16, no. 3, pp. 123–132, 2021.

[14] S. Singh, N. Parveen, and H. Gupta, "Adsorptive decontamination of rhodamine-B from water using banana peel powder: a biosorbent," *Environmental Technology & Innovation*, vol. 12, pp. 189–195, 2018.

[15] B. S. Inbaraj and N. Sulochana, "Use of jackfruit peel carbon (JPC) for adsorption of rhodamine-B, a basic dye from aqueous solution," *Indian Journal of Chemical Technology*, vol. 13, pp. 17–23, 2006.

[16] K. Sukla Baidya and U. Kumar, "Adsorption of brilliant green dye from aqueous solution onto chemically modified areca nut husk," *South African Journal of Chemical Engineering*, vol. 35, pp. 33–43, 2021.

[17] N. Buvaneswari, "Removal of brilliant green dye by the adsorption on *Sesamum indicum* tree waste from aqueous solution and its recovery," *Journal of Engineering Sciences*, vol. 11, no. 3, 2020.

[18] R. A. Mansour, A. El Shahawy, A. Attia, and M. S. Beheary, "Brilliant green dye biosorption using activated carbon derived from guava tree wood," *International Journal of Chemical Engineering*, vol. 2020, Article ID 8053828, 12 pages, 2020.

[19] S. Sawasdee, H. Jankerd, and P. Watcharabundit, "Adsorption of dyestuff in household-scale dyeing onto rice husk," *Energy Procedia*, vol. 138, pp. 1159–1164, 2017.

[20] R. C. Pundlik, S. D. Chowdhury, R. R. Dash, and P. Bhunia, "Life-cycle assessment of agricultural waste-based and biomass-based adsorbents," *Biomass, Biofuels, Biochemicals*, pp. 669–695, Elsevier Science, Amsterdam, Netherlands, 2021.

[21] S. Latif, R. Rehman, M. Imran, S. Iqbal, A. Kanwal, and L. Mitu, "Removal of acidic dyes from aqueous media using *Citrullus lanatus* peels: an agrowaste-based adsorbent for environmental safety," *Journal of Chemistry*, vol. 2019, Article ID 6704953, 9 pages, 2019.

[22] O. H. Heba, S. Ali, and N. Abdullah, "Chelate coupling with pineapple leaves as a modified bio-sorbent for lead ions (II) removal," *International journal of Environmental Science and Technology*, vol. 16, no. 11, pp. 7293–7304, 2019.

[23] Y. Zhao, H. Yang, J. Sun, Y. Zhang, and S. Xia, "Enhanced adsorption of Rhodamine B on modified oil-based drill cutting ash: characterization, adsorption kinetics, and adsorption isotherm," *ACS Omega*, vol. 6, no. 26, pp. 17086–17094, 2021.

[24] M. S. Hussain, R. Rehman, and M. Imran, "Isothermal and kinetic investigation of exploring the potential of citric acid-treated Trapa natans and *Citrullus lanatus* peels for biosorptive removal of brilliant green dye from water," *Journal of Chemistry*, vol. 2021, Article ID 6051116, 23 pages, 2021.

[25] R. Rehman, J. Anwar, T. Mahmud, and M. Salman, "Removal of murexide (dye) from aqueous media using rice husk as an adsorbent," *Journal of the Chemical Society of Pakistan*, vol. 33, no. 4, p. 598, 2011.

[26] V. Vaishnav, S. Chandra, and K. Daga, "Adsorption studies of Zn (II) ions from wastewater using calotropis procera as an adsorbent," *Research Journal of Recent Sciences*, vol. 1, pp. 160–165, 2012.

[27] Y. Hua, J. Xiao, Q. Zhang, C. Cui, and C. Wang, "Facile synthesis of surface-functionalized magnetic nanocomposites for effectively selective adsorption of cationic dyes," *Nanoscale Research Letters*, vol. 13, no. 1, p. 99, 2018.

[28] N. I. Taib, N. A. Rosli, N. I. Saharrudin, N. M. Rozi, N. A. A. Kasdiehram, and N. N. T. Abu Nazri, "Kinetic, equilibrium, and thermodynamic studies of untreated watermelon peels for removal of copper (II) from aqueous solution," *Desalination and Water Treatment*, vol. 227, pp. 289–299, 2021.

[29] P. Saravanan, J. Josephraj, B. Pushpa Thillainayagam, and G. Ravindiran, "Evaluation of the adsorptive removal of cationic dyes by greening biochar derived from agricultural bio-waste of rice husk," *Biomass Conversion and Biorefinery*, pp. 1–14, 2021.

[30] F. Ngugi, "Adsorption of rhodamine b from aqueous solution using mangroves (*Rhizophora mucronata*) carbon nanotubes nanocomposites," *International Journal of Multidisciplinary Research and Development*.

[31] A. Selvakumar and S. Rangabhashiyam, "Biosorption of Rhodamine B onto novel biosorbents from *Kappaphycus alvarezii*, *Gracilaria salicornia* and *Gracilaria edulis*," *Environmental Pollution*, vol. 255, Article ID 113291, 2019.

[32] R. J. Nascimento, K. R. A. Pereira, and F. Avelino, "Parametric and modeling studies of Rhodamine-B adsorption using coconut coir-based materials as eco-friendly adsorbents," *Journal of Environmental Chemical Engineering*, vol. 9, no. 5, Article ID 105943, 2021.

[33] M. R. R. Kooh, M. K. Dahri, and L. B. Lim, "Jackfruit seed as a sustainable adsorbent for the removal of Rhodamine B dye," *Journal of Environment & Biotechnology Research*, vol. 4, no. 1, pp. 7–16, 2016.

[34] Q. Li, X. Tang, Y. Sun et al., "Removal of Rhodamine B from wastewater by modified Volvariella volvacea: batch and column study," *RSC Advances*, vol. 5, no. 32, pp. 25337–25347, 2015.

[35] X. Guo, Z. Liu, Z. Tong, N. Jiang, and W. Chen, "Adsorption of rhodamine B from an aqueous solution by acrylic-acid-modified walnut shells: characterization, kinetics, and thermodynamics," *Environmental Technology*, pp. 1–25, 2021.

[36] F. H. M. Souza, V. F. C. Leme, G. O. B. Costa, K. C. Castro, T. R. Giraldi, and G. S. S. Andrade, "Biosorption of rhodamine B using a low-cost biosorbent prepared from inactivated Aspergillus oryzae cells: kinetic, equilibrium and thermodynamic studies," *Water, Air, & Soil Pollution*, vol. 231, no. 5, pp. 242–313, 2020.

[37] L. L. Zhi and M. A. A. Zaini, "Rhodamine B dyes adsorption on palm kernel shell based activated carbons," *Malaysian Journal of Fundamental and Applied Sciences*, vol. 15, pp. 743–747, 2019.

[38] A. Aadil, S. Murtaza, K. Shahid, M. Munir, R. Ayub, and S. Akber, "Comparative study of adsorptive removal of Congo red and brilliant green dyes from water using peanut shell," *Middle-East Journal of Scientific Research*, vol. 11, no. 6, pp. 828–832, 2012.

[39] R. Rehman, B. Salariya, and L. Mitu, "Batch scale adsorptive removal of brilliant green dye using *Trapa natans* peels in cost

effective manner," *Revue Chimique*, vol. 67, pp. 1333–1337, 2016.

[40] A. A. Romzi, M. R. R. Kooh, L. B. L. Lim, N. Priyantha, and C. M. Chan, "Environmentally friendly adsorbent derived from rock melon skin for effective removal of toxic brilliant green dye: linear versus non-linear analyses," *International Journal of Environmental Analytical Chemistry*, pp. 1–20, 2021.

[41] L. T. Popoola, T. A. Aderibigbe, A. S. Yusuff, and M. M. Munir, "Brilliant green dye adsorption onto composite snail shell–rice husk: adsorption isotherm, kinetic, mechanistic, and thermodynamics analysis," *Environmental Quality Management*, vol. 28, no. 2, pp. 63–78, 2018.

[42] M. P. Tavlieva, S. D. Genieva, V. G. Georgieva, and L. T. Vlaev, "Kinetic study of brilliant green adsorption from aqueous solution onto white rice husk ash," *Journal of Colloid and Interface Science*, vol. 409, pp. 112–122, 2013.

[43] F. de Castro Silva, M. M. F. da Silva, L. C. B. Lima, J. A. Osajima, and E. C. da Silva Filho, "Modifying cellulose with metaphosphoric acid and its efficiency in removing brilliant green dye," *International Journal of Biological Macromolecules*, vol. 114, pp. 470–478, 2018.

[44] Z. N. Abudi, F. Lattieff, T. Fahem, and M. Nsaif Abbas, "Isotherm and kinetic study of the adsorption of different dyes from aqueous solution using banana peel by two different methods," *Global Journal of Bio-Science and Biotechnology*, vol. 7, no. 2, pp. 220–229, 2018.

[45] A. Sharafzad, S. Tamjidi, and H. Esmaeili, "Calcined lotus leaf as a low-cost and highly efficient biosorbent for removal of methyl violet dye from aqueous media," *International Journal of Environmental Analytical Chemistry*, vol. 101, no. 15, pp. 2761–2784, 2021.

[46] A. Nasrullah, H. Khan, A. S. Khan et al., "Potential biosorbent derived from *Calligonum polygonoides* for removal of methylene blue dye from aqueous solution," *The Scientific World Journal*, vol. 2015, Article ID 562693, 11 pages, 2015.

[47] K. Roa, E. Oyarce, A. Boulett et al., "Lignocellulose-based materials and their application in the removal of dyes from water: a review," *Sustainable Materials and Technologies*, vol. 29, Article ID e00320, 2021.

[48] M. Mohapi, J. S. Sefadi, M. J. Mochane, S. I. Magagula, and K. Lebelo, "Effect of LDHs and other clays on polymer composite in adsorptive removal of contaminants: a review," *Crystals*, vol. 10, no. 11, p. 957, 2020.

[49] E. P. Fernandes, T. S. Silva, C. M. Carvalho et al., "Efficient adsorption of dyes by γ-alumina synthesized from aluminum wastes: kinetics, isotherms, thermodynamics and toxicity assessment," *Journal of Environmental Chemical Engineering*, vol. 9, no. 5, Article ID 106198, 2021.

[50] G. A. Tochetto, T. C. da Silva, J. Bampi, C. da Luz, G. D. Leal Pasquali, and A. Dervanoski, "Highly efficient biosorbent produced from *Syagrus romanzoffiana* to be applied in water treatment," 2021.

[51] H. Khalili, A. Ebrahimian Pirbazari, F. Esmaeili Khalil Saraei, and S. H. Mousavi, "Simultaneous removal of basic dyes from binary systems by modified orange peel and modeling the process by an intelligent tool," *Preprints*, Article ID 2021060224, 2021.

[52] F. Largo, R. Haounati, S. Akhouairi et al., "Adsorptive removal of both cationic and anionic dyes by using sepiolite clay mineral as adsorbent: experimental and molecular dynamic simulation studies," *Journal of Molecular Liquids*, vol. 318, Article ID 114247, 2020.

[53] M. Rabipour, Z. Sekhavat Pour, R. Sahraei, M. Ghaemy, M. Erfani Jazi, and T. E. Mlsna, "pH-sensitive nanocomposite hydrogels based on poly (vinyl alcohol) macromonomer and graphene oxide for removal of cationic dyes from aqueous solutions," *Journal of Polymers and the Environment*, vol. 28, no. 2, pp. 584–597, 2020.

[54] Ü. Geçgel, G. Özcan, and G. Ç. Gürpınar, "Removal of methylene blue from aqueous solution by activated carbon prepared from pea shells (*Pisum sativum*)," *Journal of Chemistry*, vol. 2013, Article ID 614083, 9 pages, 2013.

[55] T. W. Weber and R. K. Chakravorti, "Pore and solid diffusion models for fixed-bed adsorbers," *AIChE Journal*, vol. 20, no. 2, pp. 228–238, 1974.

[56] S. Sulaiman, R. S. Azis, I. Ismail et al., "Adsorptive removal of copper (II) ions from aqueous solution using a magnetite nano-adsorbent from mill scale waste: synthesis, characterization, adsorption and kinetic modelling studies," *Nanoscale Research Letters*, vol. 16, no. 1, pp. 168–217, 2021.

[57] M. Salman, R. Rehman, U. Farooq, A. Tahir, and L. Mitu, "Biosorptive removal of cadmium (II) and copper (II) using microwave-assisted thiourea-modified *Sorghum bicolor* agrowaste," *Journal of Chemistry*, vol. 2020, Article ID 8269643, 11 pages, 2020.

[58] G. Henini, Y. Laidani, S. Hanini, A. Fekaouni, and K. Djellouli Della, "Equilibrium, thermodynamic and kinetic modeling for the adsorption of textile dye (Bemacid blue) onto activated carbon synthesized from olive cores," *Scientific Study & Research. Chemistry & Chemical Engineering, Biotechnology, Food Industry*, vol. 22, no. 3, pp. 271–288, 2021.

[59] Y.-S. Ho and G. McKay, "Pseudo-second order model for sorption processes," *Process Biochemistry*, vol. 34, no. 5, pp. 451–465, 1999.

[60] A. A. Oyekanmi, A. Ahmad, K. Hossain, and M. Rafatullah, "Adsorption of rhodamine B dye from aqueous solution onto acid treated banana peel: response surface methodology, kinetics and isotherm studies," *PLoS One*, vol. 14, no. 5, Article ID e0216878, 2019.

[61] Y. S. Ho, J. C. Ng, and G. McKay, "Kinetics of pollutant sorption by biosorbents," *Separation and Purification Methods*, vol. 29, no. 2, pp. 189–232, 2000.

[62] A. Ermolenko, A. Shevelev, M. Vikulova et al., "Wastewater treatment from lead and strontium by potassium polytitanates: kinetic analysis and adsorption mechanism," *Processes*, vol. 8, no. 2, p. 217, 2020.

[63] H. P. AkankshaKalra, "Adsorption of dyes from water on to bamboo-based activated carbon-error analysis method for accurate isotherm parameter determination," *Journal of Water Science and Engineering*, vol. 1, no. 1, pp. 1–11, 2019.

[64] N. K. Mondal and S. Kar, "Potentiality of banana peel for removal of Congo red dye from aqueous solution: isotherm, kinetics and thermodynamics studies," *Applied Water Science*, vol. 8, no. 6, pp. 157–212, 2018.

[65] L. R. Martins, L. Catone Soares, L. V. Alves Gurgel, and L. F. Gil, "Use of a new zwitterionic cellulose derivative for removal of crystal violet and orange II from aqueous solutions," *Journal of Hazardous Materials*, vol. 424, Article ID 127401, 2022.

[66] A. C. Sadiq, A. Olasupo, W. S. W. Ngah, N. Y. Rahim, and F. B. M. Suah, "A decade development in the application of chitosan-based materials for dye adsorption: a short review," *International Journal of Biological Macromolecules*, vol. 191, pp. 1151–1163, 2021.

[67] Y. Liu, C. Jin, Z. Yang, G. Wu, G. Liu, and Z. Kong, "Recent advances in lignin-based porous materials for pollutants

removal from wastewater," *International Journal of Biological Macromolecules*, vol. 187, pp. 880–891, 2021.

[68] A. G. Pereira, F. H. Rodrigues, A. T. Paulino, A. F. Martins, and A. R. Fajardo, "Recent advances on composite hydrogels designed for the remediation of dye-contaminated water and wastewater: a review," *Journal of Cleaner Production*, vol. 284, Article ID 124703, 2021.

[69] H. Ren, Z. F. Cao, Y. Y. Chen, X. Y. Jiang, and J. G. Yu, "Graphene oxide-Bicine composite as a novel adsorbent for removal of various contaminants from aqueous solutions," *Journal of Environmental Chemical Engineering*, vol. 9, no. 6, Article ID 106769, 2021.

[70] B. Lapo, J. J. Bou, J. Hoyo et al., "A potential lignocellulosic biomass based on banana waste for critical rare earths recovery from aqueous solutions," *Environmental Pollution*, vol. 264, Article ID 114409, 2020.

[71] A. Abdolali, W. Guo, H. Ngo, S. Chen, N. Nguyen, and K. Tung, "Typical lignocellulosic wastes and by-products for biosorption process in water and wastewater treatment: a critical review," *Bioresource Technology*, vol. 160, pp. 57–66, 2014.

[72] S. M. Badr and S. Isra'a, "Using agricultural waste as biosorbent for hazardous brilliant green dye removal from aqueous solutions," *Journal of Engineering Science & Technology*, vol. 16, no. 4, pp. 3435–3454, 2021.

Research Article

Adsorption Characteristics of Chitosan-Modified Bamboo Biochar in Cd(II) Contaminated Water

Anxiang Huang ⦿**, Wenlian Bai, Shoulu Yang, Zhongwei Wang, Nengying Wu, Yanxiong Zhang** ⦿**, Ning Ji, and Dan Li**

Guizhou Academy of Forestry, Guiyang 550005, China

Correspondence should be addressed to Yanxiong Zhang; yanxiongzhang421@163.com

The purpose of this study was to fabricate a low-cost and eco-friendly adsorbent using bamboo biochar (BB), a kind of charcoal composed of high Brunauer–Emmett–Teller surface area and variety of functional groups, and chitosan as substrates for remediation of Cd(II) in Cd(II) contaminated water and characterized the functional group characteristics, surface morphology, and Cd(II) adsorption effect using the Fourier transform infrared (FT-IR), scanning electron microscope (SEM), and energy-dispersive X-ray spectrometer (EDS). Results showed that chitosan-modified bamboo biochar (CBB) provided more active adsorption sites (such as –NH$_2$, –COOH, –OH, and C=O) on the surface to enhance the Cd(II) removal efficiency in Cd(II) contaminated wastewater. Meanwhile, the optimal pH, contact time, and dose of CBB on the Cd(II) removal efficiency are 7, 120 min, and 600 mg, respectively. In addition, the adsorption isotherm results revealed that the possible adsorption mechanisms might include surface adsorption, electrostatic adsorption, and ion exchanges. Furthermore, the maximum adsorption capacity (Q_m) values predicted from the Langmuir model were 37.74 and 93.46 mg/g for BB and CBB, respectively, also indicating a potential application of CBB in practical wastewater. Desorption and regeneration of CBB were attained simultaneously and the results showed that even after five cycles of adsorption-elution, the adsorption and desorption of CBB exhibited a slight decline and still reached at 71.70% and 65.92%. Results from this study would provide a reference to functionalized CBB for Cd(II) adsorption in contaminated water.

1. Introduction

Water pollution is one of the most severe problems on our planet. It is a novel challenge to manage water resources sustainably under climate change and population growth in the 21st century [1, 2]. Because of the high toxicity and persistence of cadmium (Cd(II)) in natural water and farmland, it has become an increasing concern over the past decades [3]. In Japan, the main cause of the *itai-itai* disease was Cd(II) accumulation in the aquatic environment [4]. Meanwhile, according to the World Health Organization (WHO), as one of the most toxic heavy metals, Cd(II) could lead to Cd(II) accumulation to cause harmful effects on the human body and causes carcinogenicity and liver damage [3]. Hence, Cd(II) must be removed from the contaminated water and soil before they were disposed to the environment

[5, 6]. During the past decades, many techniques, including ion exchange [7], membrane filtration [6], flocculation/coagulation [8], chemical precipitation [9], photocatalysis [10], phytoremediation [11], and adsorption [12], are performed to remove heavy metals from the contaminated water and soil. Especially, various physical and chemical techniques have been employed to lower the Cd(II) concentration to meet environmental standards, including chemical precipitation, ultrafiltration, membrane separation, electrochemical deposition, and adsorption [13]. However, these techniques have great limitations for heavy metals removal due to their higher cost of energy and sludge production.

Biochar is produced from sustainably sourced biomass and is used for nonoxidative applications in agriculture [14, 15]. If biochar is used as a fuel to burn and the carbon is

oxidized into CO_2, hence it is actually classified as charcoal. Activated carbon is produced from any carbon source, such as fossil, waste, and renewable, and engineered to be used as sorbents to remove contaminants from both gases and liquids [16, 17]. Thus, it is defined as a material for contaminant sorption without exigencies in regard to the sustainability of its production nor to the fate of the carbon after its use. The bio-based adsorption is a promising method for heavy metals removal because it has good potential application prospects with an abundance of functional groups. Recently, the recycling of agricultural wastes as renewable adsorbents has received more and more attention. As an eco-friendly material, biochar has been widely used to remediate heavy metals and organic pollutants in soil and water contaminants [18–20]. Bamboo biochar (BB), a kind of charcoal composed of high Brunauer–Emmett–Teller (BET) surface area and a variety of functional groups (e.g., $-NH_2$, $-COOH$, and $-OH$) that have gained more and more attention, is an eco-friendly, readily available, low-cost, and renewable biochar [18–20]. However, the BB adsorption performance for heavy metal removal is not so good since the surface functional groups are still insufficient. Therefore, to enhance the heavy metals removal performance of BB, in recent years, many attempts, for example, citric-acid modification, amino modification, polyethylenimine modification, and some other methods, have been performed to surface modification with more functional groups [21–24]. Chitosan, an abundant natural polysaccharide in the world, is a plentiful, inexpensive, and nontoxic product of the shellfish processing industry. In recent years, chitosan has been used as alternative sorbents in many industrial and environmental applications because their amine functional groups have a strong bonding ability to various heavy metals [25–28].

Herein, the objectives of this research were to (1) fabricate chitosan-modified bamboo biochar (CBB); (2) characterize the surface morphology, element abundance, and functional groups of CBB; (3) determine the Cd(II) adsorption effect of CBB in contaminated water; and (4) speculate the possible adsorption mechanisms of CBB in Cd(II) contaminated water.

2. Materials and Methods

2.1. Materials.
The offcuts of bamboo (*Phyllostachys heterocycla* (Carr.) Mitford *cv. Pubescens*), collected from the bamboo forest (N26°29′49″ and E106°44′10″) in the Guizhou Academy of Forestry, Guizhou Province, China. The chemicals were purchased from Aladdin-reagent Co., Ltd. (Shanghai, China).

2.2. Preparation of BB and CBB.
The BB and CBB samples were prepared by following the procedures reported previously with some modifications [29, 30]. The offcuts of bamboo were washed with deionized water for three times to remove the dirt contained in the samples. The washed samples were air-dried, chopped into a particle size below

$1.0 \times 1.0 \times 1.0$ cm, and then oven-dried at $100 \pm 5°C$ for 8 h before use. After that, the bamboo particles were pyrolyzed at 900°C for 4 h under N_2 flow (100 mL/min) using a vacuum annealing furnace. After pyrolysis, the samples were ground via a ball grinder and passed through a standard 200 mesh sieve to obtain a particle size of about 75.0 μm. The samples were rinsed several times with deionized water and then oven-dried at 80°C for 24 h to obtain BB products for further use. After that, 0.4 g of chitosan mixed with 2.0 g BB were added into 30 mL of water. The mixtures were stirred well with sonication for 2 d at 30°C and 75% relative humidity (RH) and then separated by vacuum filtration and dried at $100 \pm 5°C$ to give rise to the CBB.

2.3. Characterization of BB and CBB.
The particle size distribution and specific surface area of BB and CBB were measured using a laser Bettersize 2600 particle analyzer (Bettersize Instruments Ltd., Dandong, China). The Fourier transform infrared (FT-IR) spectra of BB and CBB were obtained using a Thermo Nicolet 380 FT-IR spectrometer (Waltham, MA, USA). The surface morphology and elements of BB and CBB were scanned using a Quanta 250 Scanning Electron Microscope (SEM; FEI, Oregon, USA) equipped with a Bruker Quantax X-Flash 5030 energy dispersive X-ray spectrometer (EDS; Bruker, Berlin, Germany). The zeta potential values of BB and CBB were measured by a zeta potential analyzer (Malvern Instruments Ltd., Malvern, UK).

2.4. Batch-Adsorption Experiments.
Batch-adsorption experiments were performed to evaluate the maximum Cd(II) adsorption efficiency of BB and CBB in 30 mL Cd(II) contaminated water with a concentration of 10 μg/mL. Briefly, different BB or CBB amounts (100, 200, 400, 600, 800, and 1000 mg) with pH 7 and contact time of 2 h, different contact times (5, 10, 30, 60, 120, 180, and 240 min) with pH 7 and BB or CBB amount of 600 mg, and initial pH (3, 4, 5, 6, 7, and 8) with a contact time of 2 h and BB or CBB amount of 600 mg on the Cd(II) adsorption efficiency in Cd(II) contaminated water were studied systemically. Briefly, the mixtures were shaken in a rotary shaker at 20°C and 120 rpm. After adsorption, the suspension was filtered with a 0.2 μm syringe filter, the Cd(II) concentration in the filtrate was determined by an iCE 3500 flame atomic absorption spectrometer (FAAS; Thermo Fisher, MA, USA) and an inductively coupled plasma mass spectrometry (ICP-MS; Thermo Scientific, MA, USA). For experimental accuracy, each trial was repeated three times.

The adsorption rate R (%) and adsorption amount Q (mg/g) of Cd(II) in Cd(II) contaminated water by BB or CBB were calculated using equations (1) and (2), where C_0 (mg/L) and C_e (mg/L) represent the Cd(II) concentrations at the initial and adsorption equilibrium state, respectively, V (mL) represents the volume of the aqueous solution, and m (g) is the amount of BB or CBB.

$$R(\%) = \frac{C_0 - C_e}{C_0} \times 100\%, \tag{1}$$

$$Q(\%) = \frac{C_0 - C_e}{m} \times V. \tag{2}$$

2.5. Model for Equilibrium Study of Adsorption.

The adsorption kinetics of Cd(II) was studied in Cd(II) contaminated water using the Langmuir and Freundlich isotherm models (3) and (4), where C_e (mg/L) is the equilibrium concentration, Q_m (mg/g) denotes the maximum adsorption capacity, Q_e (mg/g) represents the Cd(II) adsorbed amount at the equilibrium concentration, K_L (mg/g) and K_F (mg/g) are Langmuir and Freundlich isotherm constants, respectively, and $1/n$ relates to the adsorption capacity [31–34].

$$Q_e = \frac{Q_m K_L C_e}{1 + K_L C_e}, \tag{3}$$

$$Q_e = K_F C_e^{1/n}. \tag{4}$$

2.6. Desorption and Regeneration.

To investigate the possibility of repeated use of the adsorbent CBB, in this study, the generation experiment was also conducted through five consecutive adsorption-desorption processes with the essential pH, contact time, and dose. Meanwhile, for the desorption experiment after Cd(II) adsorption, the CBB was transferred to a flask containing 40 mL of 0.2 M HCl desorbing agent. The mixture was shaken at 200 rpm using a rotary shaker for 3 h. After elution, the CBB was rinsed three times with deionized water to remove any traces of acid and suspended again in Cd(II) solution for the next adsorption cycle. The adsorption-desorption cycle was repeated five times using the same CBB. The desorption rates of CBB were evaluated as

$$\text{desorption rate}(\%) = \frac{\text{released Cd (II) concentration}}{\text{initially sorbed Cd (II) concentration}} \times 100. \tag{5}$$

2.7. Statistical Analysis.

Statistical analysis was conducted by ANOVA with software SPSS 17.0 (SPSS Inc, Chicago, USA).

3. Results and Discussion

3.1. Preparation of BB and CBB.

This study successfully fabricated a new kind of CBB using BB and chitosan as substrates for Cd(II) remediation in Cd(II) contaminated water. Some previous studies reported by Zhou et al. [29] and Zhang et al. [30] had also explored the use of chitosan to modify the BB surface to fabricate chitosan-modified biochars (CMB) and chitosan-modified magnetic biochar (CMMB) to enhance their affinity to heavy metals (Cr(IV), Pb(II), Cu(II), and Cd(II)) in water. It is interesting to note that the preparation technology to fabricate CBB reported in our present study is relatively simple and environmentally friendly without using NaOH, $Fe_2(SO_4)_3$, and

$FeSO_4 \cdot 7H_2O$. Therefore, as far as we know, it is the first report to fabricate CBB using the above method reported in our present study.

3.2. Characterization of BB and CBB.

As shown in Table 1, after the modification, CBB has no significant impact on the specific surface area and particle size distribution of BB. However, contrary to our findings, many biochar with organic matter have been shown to register very low surface areas [35].

Figures 1(a)–1(c) show that the BB surface exhibits notable smoothness and has a rich pore structure and numerous small particles, which may be formed after the degradation of some bamboo tissue during high-temperature pyrolysis, whereas Figures 1(d)–1(f) show that the CBB is slightly rather rough due to the irregular stacking of the bamboo charcoal particles. Meanwhile, EDS showed that the abundances of C, K, N, and O elements, which were the essential components of active functional groups, such as $-NH_2$, $-COOH$, $C=O$, and $-OH$ were found to be uniformly distributed along the surface of BB and CBB. In comparison, the abundances of C, K, N, and O were more densely distributed at CBB than BB, suggesting that CBB has abundant active ligand sites and has a positive contribution to the Cd(II) adsorption.

3.3. Zeta Analysis.

The effect of pH on the zeta potential charge of BB and CBB surface is determined. As shown in Figure 2(a), the zeta potentials of BB and CBB decreased with the increase of the pH value, probably because of the deposition of more OH^- on the adsorbent surface [36]. Zeta potentials of BB were in the range of +18.90 to –22.10 mV as the initial pH of the suspensions increased from 3 to 8, whereas the zeta potentials of CBB increased (+35.80 to –5.26 mV) in the designed pH range from 3 to 8. The point of zero charge pH (pH_{pzc}) of BB is 5.2, whereas the pH_{pzc} of CBB increased to 7.6 after being modified by chitosan, suggesting that chitosan loaded on the BB surface increased the positive charge. Meanwhile, Figure 2(b) shows that, after Cd(II) adsorption, the zeta potentials of BB and CBB had an apparent increase at the pH of 7, illustrating that amino functionalization of chitosan had been adsorbed on the surface of CBB and the adsorption mechanism of CBB was based on electrostatic attraction [37, 38].

3.4. Infrared Spectroscopy Study.

The surface functional groups information of BB and CBB before and after Cd(II) adsorption are presented in Figure 3. Figure 3 shows that the broad FT-IR band at 3420 cm^{-1} was attributed to the stretching vibrations of $-OH$ and $-NH-$ groups [39]. The bands at 2960 and 1750 cm^{-1} were associated with the stretching vibration of $-CH-$ and $C=O$, respectively [40, 41]. The band at 1430 cm^{-1} was assigned to the in-of-plane bending vibration for $-COO^-$ and $-OH$ of $-COOH$ [42]. The band at 1160 cm^{-1} was ascribed to the stretching vibration of $C-O$ of various groups [43, 44]. The band at 1070 cm^{-1} indicated the occurrence of the $C-O$ group [45]. Figure 3 also shows that, compared to BB, the contents of the main

TABLE 1: The specific surface area and particle size distribution of BB and CBB.

Parameters	BB	CBB
Specific surface area (m^2/kg)	84.99	85.05
Volume mean diameter (μm)	83.45	82.61
Area mean diameter (μm)	26.15	26.13
Quantity mean diameter (μm)	0.907	0.912
D90 (μm)	186.8	187.0
D50 (μm)	63.05	62.37
D10 (μm)	13.25	12.81
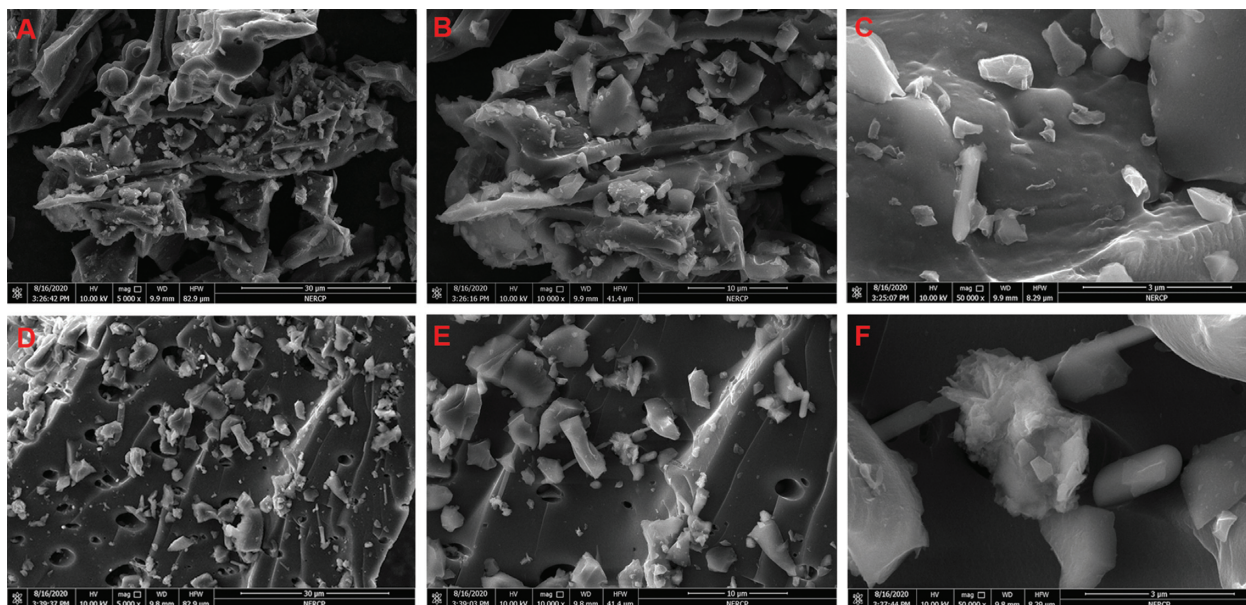
FIGURE 1: SEM images of BB (a–c) and CBB (d–f).

(a)   (b)
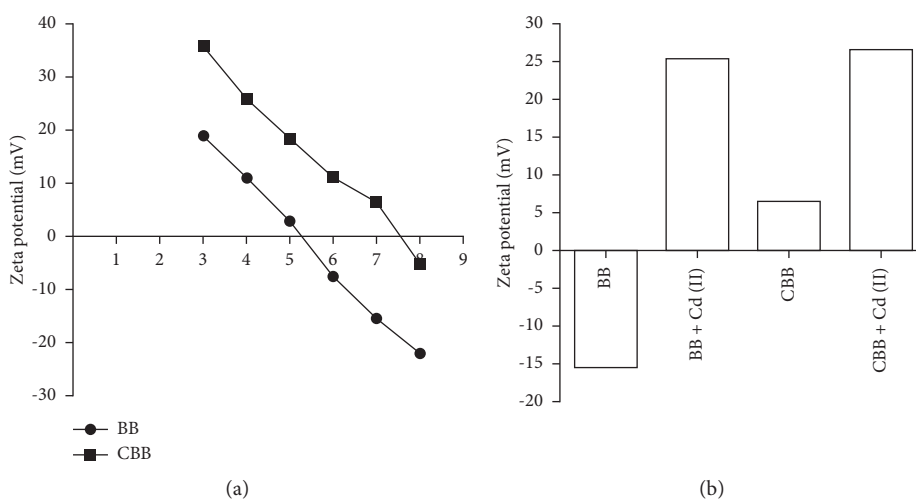
FIGURE 2: The zeta potential for BB and CBB in Cd(II) contaminated water at different pH values (a) and before and after Cd(II) adsorption at pH = 7 (b).

oxygen-containing functional groups, such as C–O, –COOH, C=O, and –OH, significantly increased during the preparation of CBB. Surfaces with abundant oxygen-containing functional groups could change the surface zeta potentials to strengthen the metal ions adsorbent in contaminated water [46].

3.5. Effect of pH, Contact Time, and Dose on the Cd(II) Adsorption.

pH, an important parameter for affecting heavy metals adsorption, could affect the surface potential, counter ions concentration on the functional groups, and ionization degree of adsorbents [47–50]. To examine the effect of pH on the Cd(II) adsorption, the pH values were varied from 3 to 8.
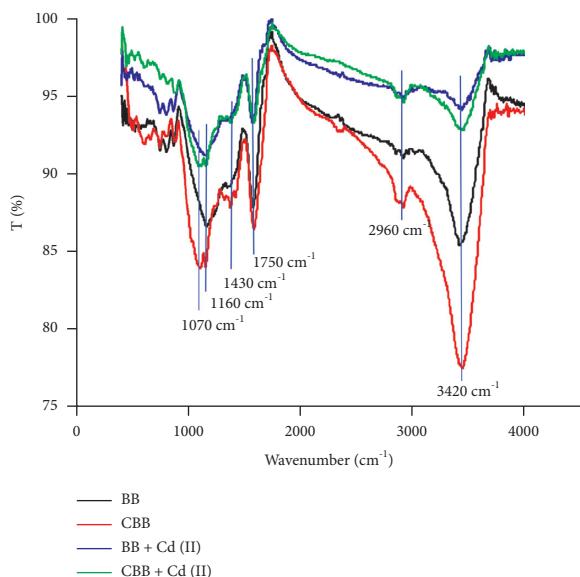
FIGURE 3: The FT-IR spectra of BB and CBB before and after Cd(II) adsorption.

As shown in Figure 4(a), the adsorption rates of BB and CBB in Cd(II) contaminated water depend on the pH values and show similar trends. The adsorption rates of CBB increased from 66.78% to 90.66%, respectively, over the pH values range from 3 to 7, while the adsorption of Cd(II) tends to be stable when pH is greater than 7. Therefore, the optimal pH of CBB on the Cd(II) removal efficiency is 7. This is consistent with the results reported for heavy metal removal from industrial wastewater using chitosan-modified oil palm shell charcoal which was in the pH values range of 6.8–7.1 [47]. Therefore, our results demonstrated that pH is one of the most essential parameters in the Cd(II) adsorption process and might change the function groups, mainly oxygen-containing groups, of CBB [51].

Contact time is one of the critical parameters for the contaminated water treatment system [52, 53]. To examine the effect of contact time on the Cd(II) removal efficiency, the contact time were varied from 5 to 240 min. As shown in Figure 4(b), the Cd(II) adsorption rates of CBB in Cd(II) contaminated water are higher than those of BB and increase with an increase in contact time before adsorption equilibrium is reached. It can be seen that the adsorption rates of CBB increase from 81.54% to 90.24% when the contact time increase from 5 to 120 min. Therefore, the optimum contact time for CBB is found to be 120 min, compared to that of BB which is 180 min. Hence, CBB requires a shorter contact time to reach adsorption equilibrium, demonstrating that the greater availability of various functional groups on the surface of chitosan could significantly improve the binding capacity and the adsorption of Cd(II) from wastewater [54–56].

The effect of different doses of BB and CBB on the Cd(II) adsorption was studied by varying the amount of adsorbents from 100 to 1000 mg, while keeping the pH value and contact time constant. Figure 4(c) shows that the Cd(II) removal efficiency of the BB and CBB adsorbents generally improves with the increasing adsorbent dose. This is expected that the higher dose of adsorbents added in Cd(II) contaminated water, the greater removal availability of adsorbents for Cd(II) removal, and then shows no further increase in Cd(II) adsorption after a certain amount of BB and CBB adsorbents were added [57, 58]. Meanwhile, the results, as shown in Figure 4(c), also indicate that the Cd(II) adsorption rates of CBB in Cd(II) contaminated water are higher than those of BB as well as increase with an increase in dose before equilibrium is reached. It can be seen that the adsorption rates of CBB increased from 73.33% to 90.66% when the doses of CBB were increased from 100 to 600 mg. Therefore, the optimum dose for CBB adsorbents is 600 mg, compared to that of BB which is 800 mg.

3.6. Adsorption Isotherms. To further investigate the adsorption mechanism of BB and CBB, the adsorption equilibrium isotherms of Cd(II) in Cd(II) wastewater were determined at 20°C with optimal conditions. Figure 5(a) shows the effect of contact time on the theoretical Cd(II) adsorption capacity by BB and CBB, and the adsorption curves of BB and CBB increased steeply within the first 180 min, indicating that the abundant adsorption sites on the BB and CBB surface were rapidly occupied by Cd(II) via surface absorption. Figure 5(b) shows the effect of C_e on the Cd(II) adsorption capacity by BB and CBB. When $C_e < 45$ mg/L, the Cd(II) adsorption capacity of the BB and CBB adsorbents was found to increase remarkably, which could be ascribed to the sufficient active sites on the BB and CBB surface. Meanwhile, as the C_e values continue to increase, the available active adsorption sites on the surface of the BB and CBB adsorbents tend to saturate, therefore resulting in a dynamic adsorption equilibrium for the Cd(II) adsorption capacity. Similar results were reported by Yan et al. [58]. The Langmuir and Freundlich fitting curves of BB and CBB are plotted in Figures 5(c) and 5(d) and the related parameters are presented in Table 2. Figures 5(c) and 5(d) as well as Table 2 show that the Langmuir and Freundlich models exhibit the best fit for BB and CBB with both the highest correlation coefficients exceeding 0.95, indicating that the BB and CBB surface are homogeneous [59]. Generally, $1/n$ represents the heterogeneity factor of the site energy on the functional groups, and the smaller $1/n$ is, the better the adsorption capacity is, such as $0 < 1/n < 1$ indicates favorable adsorption [60, 61]. This study shows that the $1/n$ values of BB and CBB are 0.24 and 0.21, respectively, indicating a favorable Cd(II) adsorption by the two adsorbents. The K_F obtained from the Freundlich model as well as K_L obtained from the Langmuir model could be the critical indicators of heavy metals adsorption [58]. Table 2 shows that the K_F and K_L values followed the order: BB > CBB, suggesting that CBB had an adsorption affinity toward Cd(II). Furthermore, the maximum adsorption capacity (Q_m) values predicted from the Langmuir model were 37.74 and 93.46 mg/g for BB and CBB, respectively. In recent years, many modified biochars were also prepared [61–65] and the comparison of the Q_m values of Cd(II) was listed in Table 3. Table 3 shows that the Q_m value of Cd(II) is higher than most of the reported modified biochars, indicating a potential application of CBB in practical wastewater.
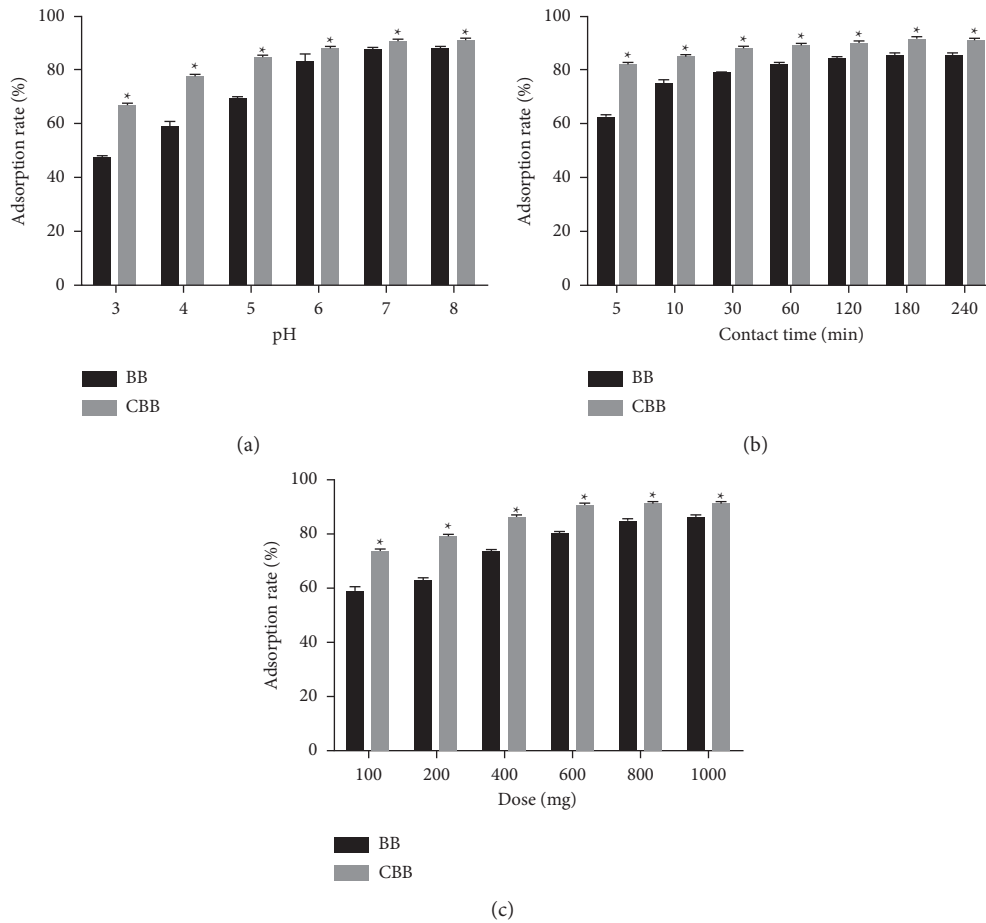
(a)

(b)

(c)

FIGURE 4: Effect of pH (a), contact time (b), and dose (c) on the adsorption rates of BB and CBB in Cd(II) contaminated water. Error bars mean the standard deviation. *indicates a significant difference ($p < 0.05$) between the adsorption rates of BB and CBB at different pH, contact times, and doses.
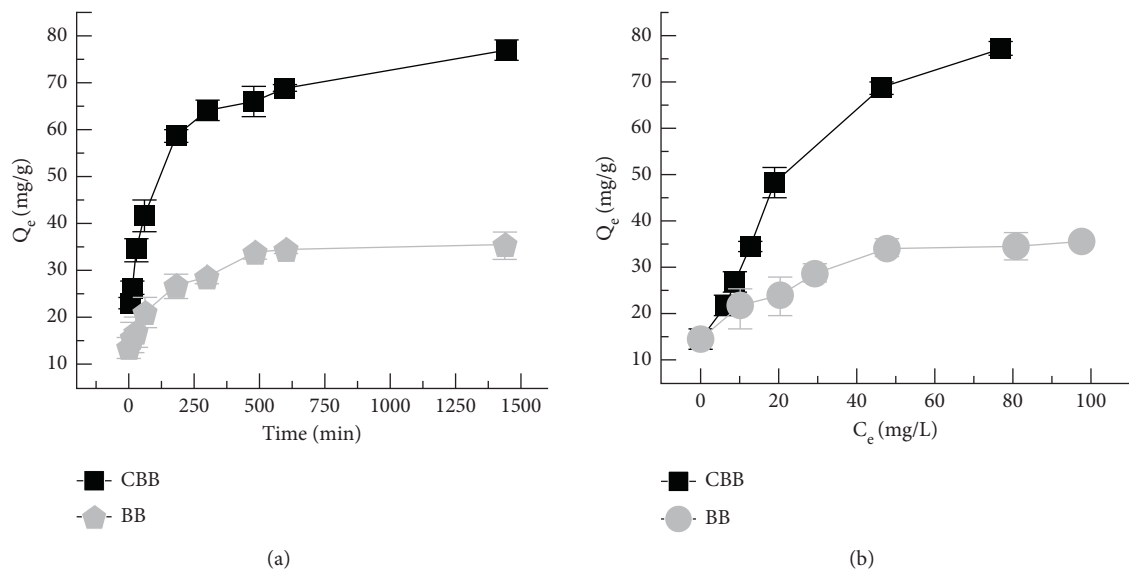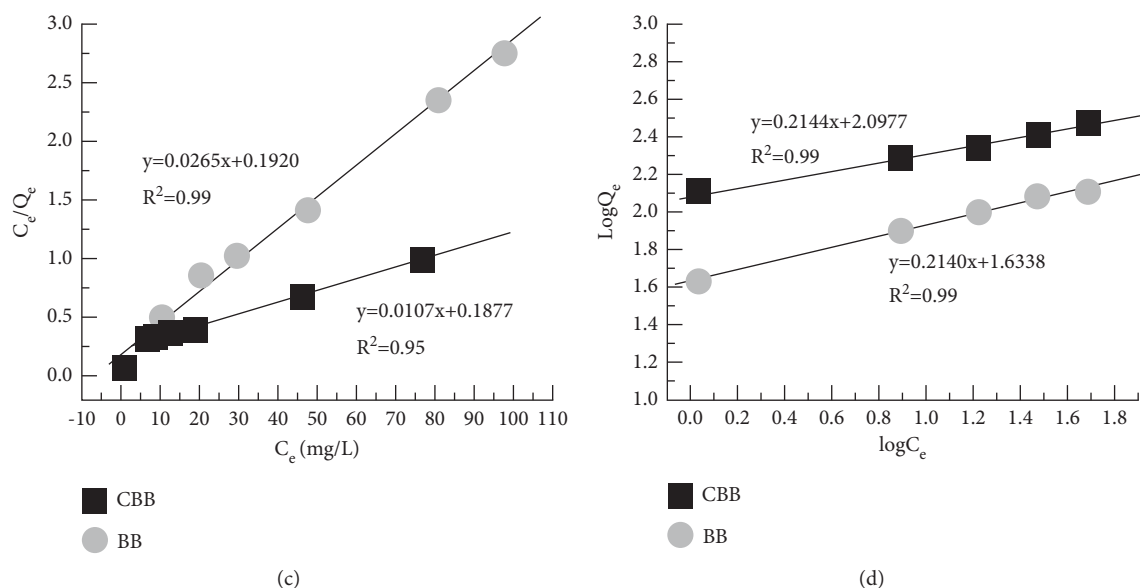

(a)

(b)

FIGURE 5: Continued.

(c)

(d)

FIGURE 5: (a) Effect of contact time on equilibrium adsorbate concentration of the Cd(II) adsorption by CBB and BB; (b) effect of equilibrium adsorbate concentration on Cd(II) adsorption by CBB and BB; (c) Langmuir fitting curves; (d) Freundlich fitting curves. Error bars mean the standard deviation.

TABLE 2: Langmuir and Freundlich isotherm parameters for the adsorption of Cd(II).

Adsorbents	Langmuir			Freundlich		
	Q_m (mg/g)	K_L	R^2	K_F	$1/n$	R^2
BB	37.74	0.14	0.99	2.63	0.24	0.99
CBB	93.46	0.06	0.95	2.10	0.21	0.99

TABLE 3: Comparison of the Q_m values of Cd(II) of different modified biochars.

Absorbent	Q_m (mg/g)	Reference
CBB	93.46	This study
Chitosan-modified biochar	71.5	[29]
Phosphate-modified activated bamboo biochar	202.66	[61]
Fe-Mn binary oxide-biochar	72.9927	[62]
Ball-milled bone biochar	165.77	[63]
Sulfonated biochar	85.76	[64]
Magnesium oxide biochar-chitosan composite	68.223	[65]

FIGURE 6: Five consecutive adsorption-desorption cycles of CBB for Cd(II) adsorption. Error bars mean the standard deviation. *indicates a significant difference at $p < 0.05$ compared with cycle 1.

3.7. Desorption and Reusability. The recyclability of adsorbent is one of the important performance indexes to evaluate the applicability of adsorbent in treating actual wastewater [66]. The adsorption and desorption rates of Cd(II) in five adsorption-desorption cycles were shown in Figure 6. It was found that after five cycles, the adsorption and desorption of CBB exhibited a slight decline and still reached at 71.70% and 65.92%, respectively. The good reproducibility indicated that CBB could be used as a desirable, economic, and recyclable adsorbent in practical wastewater.
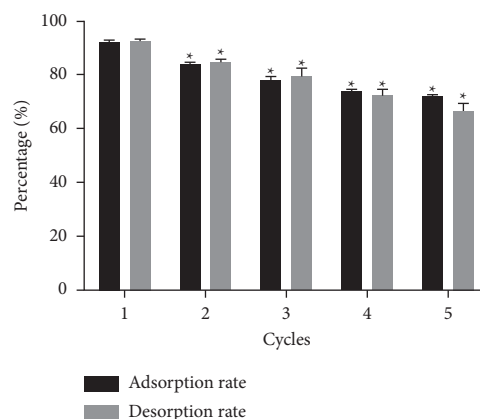
3.8. Possible Adsorption Mechanism. Based on the above analysis and isotherm results, a possible mechanism for the adsorption of Cd(II) by CBB has been proposed and depicted in Figure 7. As shown in Figure 7, we speculate that the possible adsorption mechanisms include surface adsorption, electrostatic adsorption, and ion exchanges. More specifically, the surface of CBB has abundant pores and active functional groups ($-NH_2$, $-COOH$, $-OH$, and $C=O$), which could significantly improve the surface adsorption capacity. Meanwhile, abundant $-OH$ and $-COOH$ active functional groups on the surface of CBB could change the surface zeta potentials by loss of H^+ to form charged functional groups, thus strengthening the electrostatic adsorption of the adsorbent in Cd(II) contaminated water. In addition, after carbonization at high temperature, the abundant K of CBB are transformed into
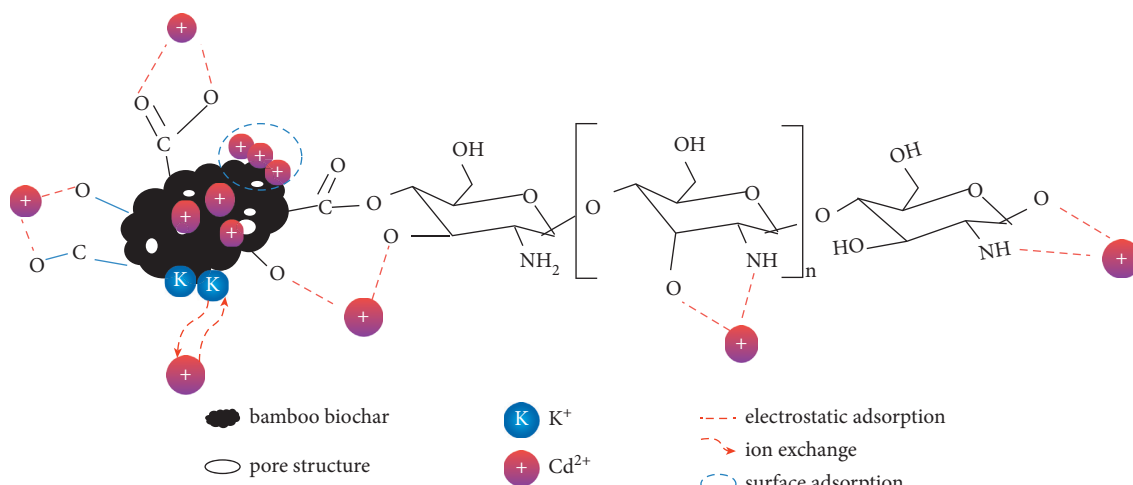
Figure 7: Diagram showing the possible adsorption mechanism of CBB on Cd(II) adsorption.

free K^+, which continuously exchange with Cd(II) in an aqueous solution, thus promoting the process of Cd(II) ion exchange.

4. Conclusions

In summary, a new eco-friendly and low-cost adsorbent for Cd(II) was prepared by the modification of BB with chitosan via a simple method. Results showed that the modification could significantly improve the surface properties and adsorption performance for Cd(II) adsorption. As well, the adsorption isotherm results show that the possible adsorption mechanisms include surface adsorption, electrostatic adsorption, and ion exchanges. Thus, the CBB can be considered as a feasible, promising, and high value-added approach for Cd(II) contaminated water recycling.

Data Availability

All data included in this study are available upon request by contacting the corresponding author.

Conflicts of Interest

The authors declare that there are no conflicts of interest.

Acknowledgments

References

[1] I. Anastopoulos, I. Pashalidis, A. Hosseini-Bandegharaei et al., "Agricultural biomass/waste as adsorbents for toxic metal decontamination of aqueous solutions," *Journal of Molecular Liquids*, vol. 295, Article ID 111684, 2019.

[2] L. P. Lingamdinne, J.-K. Yang, Y.-Y. Chang, J. R. Koduru, and J. R. Koduru, "Low-cost magnetized *Lonicera japonica* flower biomass for the sorption removal of heavy metals," *Hydrometallurgy*, vol. 165, pp. 81–89, 2016.

[3] Q. Zhou, B. Liao, L. Lin, W. Qiu, and Z. Song, "Adsorption of Cu(II) and Cd(II) from aqueous solutions by ferromanganese binary oxide-biochar composites," *The Science of the Total Environment*, vol. 615, pp. 115–122, 2018.

[4] P. Chowdhury, S. Athapaththu, A. Elkamel, and A. K. Ray, "Visible-solar-light-driven photo-reduction and removal of cadmium ion with Eosin Y-sensitized TiO_2 in aqueous solution of triethanolamine," *Separation and Purification Technology*, vol. 174, pp. 109–115, 2017.

[5] K. Rao, M. Mohapatra, S. Anand, and P. Venkateswarlu, "Review on cadmium removal from aqueous solutions," *International Journal of Engineering Science and Technology*, vol. 2, pp. 81–103, 2010.

[6] M. R. H. M. Haris, N. A. Wahab, C. W. Reng, B. Azahari, and K. Sathasivam, "The sorption of cadmium (II) ions on mercerized rice husk and activated carbon," *Turkish Journal of Chemistry*, vol. 35, pp. 939–950, 2011.

[7] M. Naushad, A. Mittal, M. Rathore, and V. Gupta, "Ion-exchange kinetic studies for Cd(II), Co(II), Cu(II), and Pb(II) metal ions over a composite cation exchanger," *Desalination and Water Treatment*, vol. 54, no. 10, pp. 2883–2890, 2015.

[8] Z. You, C. Zhuang, Y. Sun, S. Zhang, and H. Zheng, "Efficient removal of TiO_2 nanoparticles by enhanced flocculation-coagulation," *Industrial & Engineering Chemistry Research*, vol. 58, no. 31, pp. 14528–14537, 2019.

[9] A. A. H. Faisal, S. F. A. Al-Wakel, H. A. Assi, L. A. Naji, and M. Naushad, "Waterworks sludge-filter sand permeable reactive barrier for removal of toxic lead ions from contaminated groundwater," *Journal of Water Process Engineering*, vol. 33, Article ID 101112, 2020.

[10] G. Sharma and M. Naushad, "Adsorptive removal of noxious cadmium ions from aqueous medium using activated carbon/zirconium oxide composite: isotherm and kinetic modelling," *Journal of Molecular Liquids*, vol. 310, Article ID 113025, 2020.

[11] S. Muthusaravanan, N. Sivarajasekar, J. S. Vivek et al., "Phytoremediation of heavy metals: mechanisms, methods and enhancements," *Environmental Chemistry Letters*, vol. 16, no. 4, pp. 1339–1359, 2018.

[12] M. Naushad, Z. A. Alothman, M. R. Awual, M. M. Alam, and G. E. Eldesoky, "Adsorption kinetics, isotherms, and thermodynamic studies for the adsorption of Pb^{2+} and Hg^{2+} metal ions from aqueous medium using Ti(IV) iodovanadate cation exchanger," *Ionics*, vol. 21, no. 8, pp. 2237–2245, 2015.

[13] S. Zhang, M. Cui, J. Chen et al., "Modification of synthetic zeolite X by thiourea and its adsorption for Cd (II)," *Materials Letters*, vol. 236, pp. 233–235, 2019.

[14] J. Lehmann and S. Joseph, *Biochar for Environmental Management: An Introduction in Biochar for Environmental Management: Science, Technology and Implementation*, Routledge, Oxford, UK, 2015.

[15] European Biochar Certificate (EBC), *European Biochar Foundation—European Biochar Certificate—Guidelines for a Sustainable Production of Biochar; Version 6.3E of August 14, 2017*, European Biochar Certificate (EBC), Arbaz, Switzerland, 2017.

[16] H. Marsh and F. R. Reinoso, *Activated Carbon*, Elsevier, Amsterdam, Netherlands, 2006.

[17] M. Smisek and S. Cerny, "Activated carbon," in *Topics in Organic and General Chemistry*, Elsevier Co., New York, NY, USA, 1970.

[18] J. B. Zhou, *Study on the Mechanism of Action and Environmental Application of Bamboo Charcoal*, Nanjing Forestry University, PHD thesis, Nanjing, China, 2005.

[19] J.-H. Park, J.-S. Cho, Y. S. Ok et al., "Comparison of single and competitive metal adsorption by pepper stem biochar," *Archives of Agronomy and Soil Science*, vol. 62, no. 5, pp. 617–632, 2016.

[20] K. Lu, X. Yang, G. Gielen et al., "Effect of bamboo and rice straw biochars on the mobility and redistribution of heavy metals (Cd, Cu, Pb and Zn) in contaminated soil," *Journal of Environmental Management*, vol. 186, pp. 285–292, 2017.

[21] J. Rivera-Utrilla, M. Sánchez-Polo, V. Gómez-Serrano, P. M. Álvarez, M. C. M. Alvim-Ferraz, and J. M. Dias, "Activated carbon modifications to enhance its water treatment applications. An overview," *Journal of Hazardous Materials*, vol. 187, no. 1–3, pp. 1–23, 2011.

[22] J. P. Chen, S. Wu, and K.-H. Chong, "Surface modification of a granular activated carbon by citric acid for enhancement of copper adsorption," *Carbon*, vol. 41, no. 10, pp. 1979–1986, 2003.

[23] G.-X. Yang and H. Jiang, "Amino modification of biochar for enhanced adsorption of copper ions from synthetic wastewater," *Water Research*, vol. 48, pp. 396–405, 2014.

[24] Y. Ma, W.-J. Liu, N. Zhang, Y.-S. Li, H. Jiang, and G.-P. Sheng, "Polyethylenimine modified biochar adsorbent for hexavalent chromium removal from the aqueous solution," *Bioresource Technology*, vol. 169, pp. 403–408, 2014.

[25] R. N. Tharanathan and F. S. Kittur, "Chitin-the undisputed biomolecule of great potential," *Critical Reviews in Food Science and Nutrition*, vol. 43, no. 1, pp. 61–87, 2003.

[26] C. Gerente, V. K. C. Lee, P. L. Cloirec, and G. McKay, "Application of chitosan for the removal of metals from wastewaters by adsorption-mechanisms and models review," *Critical Reviews in Environmental Science and Technology*, vol. 37, no. 1, pp. 41–127, 2007.

[27] L. Pontoni and M. Fabbricino, "Use of chitosan and chitosan-derivatives to remove arsenic from aqueous solutions—a mini review," *Carbohydrate Research*, vol. 356, pp. 86–92, 2012.

[28] A. Bhatnagar and M. Sillanpää, "Applications of chitin- and chitosan-derivatives for the detoxification of water and wastewater—a short review," *Advances in Colloid and Interface Science*, vol. 152, no. 1-2, pp. 26–38, 2009.

[29] Y. Zhou, B. Gao, A. R. Zimmerman, J. Fang, Y. Sun, and X. Cao, "Sorption of heavy metals on chitosan-modified biochars and its biological effects," *Chemical Engineering Journal*, vol. 231, pp. 512–518, 2013.

[30] H. Zhang, R. Xiao, R. Li, A. Ali, A. Chen, and Z. Zhang, "Enhanced aqueous Cr(VI) removal using chitosan-modified magnetic biochars derived from bamboo residues," *Chemosphere*, vol. 261, p. 127694, 2020.

[31] Y. Rashtbari, S. Hazrati, A. Azari, S. Afshin, M. Fazlzadeh, and M. Vosoughi, "A novel, eco-friendly and green synthesis of PPAC-ZnO and PPAC-nZVI nanocomposite using pomegranate peel: cephalexin adsorption experiments, mechanisms, isotherms and kinetics," *Advanced Powder Technology*, vol. 31, no. 4, pp. 1612–1623, 2020.

[32] A. Hamzezadeh, Y. Rashtbari, S. Afshin, M. Morovati, and M. Vosoughi, "Application of low-cost material for adsorption of dye from aqueous solution," *International Journal of Environmental Analytical Chemistry*, vol. 102, no. 1, 2020.

[33] S. Afshin, Y. Rashtbari, M. Shirmardi, M. Vosoughi, and A. Hamzehzadeh, "Adsorption of basic Violet 16 dye from aqueous solution onto mucilaginous seeds of *Salvia sclarea*: kinetics and isotherms studies," *Desalination and Water Treatment*, vol. 161, pp. 365–375, 2019.

[34] S. Afshin, Y. Rashtbari, M. Vosough et al., "Application of Box-Behnken design for optimizing parameters of hexavalent chromium removal from aqueous solutions using Fe_3O_4 loaded on activated carbon prepared from alga: kinetics and equilibrium study," *Journal of Water Process Engineering*, vol. 42, Article ID 102113, 2021.

[35] G. N. Kasozi, A. R. Zimmerman, P. Nkedi-Kizza, and B. Gao, "Catechol and humic acid sorption onto a range of laboratory-produced black carbons (biochars)," *Environmental Science and Technology*, vol. 44, no. 16, pp. 6189–6195, 2010.

[36] C. Lu and F. Su, "Adsorption of natural organic matter by carbon nanotubes," *Separation and Purification Technology*, vol. 58, no. 1, pp. 113–121, 2007.

[37] J. Pan, Y. Li, K. Chen, Y. Zhang, and H. Zhang, "Enhanced physical and antimicrobial properties of alginate/chitosan composite aerogels based on electrostatic interactions and noncovalent crosslinking," *Carbohydrate Polymers*, vol. 266, Article ID 118102, 2021.

[38] I. S. Lopes, M. Michelon, L. G. R. Duarte, P. Prediger, R. L. Cunha, and C. S. F. Picone, "Effect of chitosan structure modification and complexation to whey protein isolate on oil/water interface stabilization," *Chemical Engineering Science*, vol. 230, Article ID 116124, 2021.

[39] S. Wu, M. Lu, and S. Wang, "Antiageing activities of water-soluble chitosan from Clanis bilineata larvae," *International Journal of Biological Macromolecules*, vol. 102, pp. 376–379, 2017.

[40] S. Ali, M. Rizwan, M. B. Shakoor, A. Jilani, and R. Anjum, "High sorption efficiency for As(III) and As(V) from aqueous solutions using novel almond shell biochar," *Chemosphere*, vol. 243, Article ID 125330, 2020.

[41] P. S. Saravana, T. C. Ho, S.-J. Chae et al., "Deep eutectic solvent-based extraction and fabrication of chitin films from crustacean waste," *Carbohydrate Polymers*, vol. 195, pp. 622–630, 2018.

[42] C. Vasile, G. G. Bumbu, R. Petronela Dumitriu, and G. Staikos, "Comparative study of the behavior of carboxymethyl cellulose-g-poly(N-isopropylacrylamide) copolymers and their equivalent physical blends," *European Polymer Journal*, vol. 40, no. 6, pp. 1209–1215, 2004.

[43] Y.-H. Lin and P.-H. Su, "Behavior of aluminum adsorption in different compost-derived humic acids," *Clean-Soil, Air, Water*, vol. 38, no. 10, pp. 916–920, 2010.

[44] M.-E. Lee, J. H. Park, and J. W. Chung, "Comparison of the lead and copper adsorption capacities of plant source materials and their biochars," *Journal of Environmental Management*, vol. 236, pp. 118–124, 2019.

[45] Y. Shigemasa, H. Matsuura, H. Sashiwa, and H. Saimoto, "Evaluation of different absorbance ratios from infrared spectroscopy for analyzing the degree of deacetylation in chitin," *International Journal of Biological Macromolecules*, vol. 18, no. 3, pp. 237–242, 1996.

[46] S. M. Nomanbhay and K. Palanisamy, "Removal of heavy metal from industrial wastewater using chitosan coated oil palm shell charcoal," *Electronic Journal of Biotechnology*, vol. 8, pp. 43–53, 2005.

[47] Y. Guo, R. Wang, P. Wang, L. Rao, and C. Wang, "Developing a novel layered boron nitride-carbon nitride composite with high efficiency and selectivity to remove protonated dyes from water," *ACS Sustainable Chemistry & Engineering*, vol. 7, no. 6, pp. 5727–5741, 2019.

[48] Y. Guo, R. Wang, C. Yan, P. Wang, L. Rao, and C. Wang, "Developing boron nitride-pyromellitic dianhydride composite for removal of aromatic pollutants from wastewater via adsorption and photodegradation," *Chemosphere*, vol. 229, pp. 112–124, 2019.

[49] P. Wang, C. Wu, Y. Guo, and C. Wang, "Experimental and theoretical studies on methylene blue and methyl orange sorption by wheat straw-derived biochar with a large surface area," *Physical Chemistry Chemical Physics*, vol. 18, no. 43, pp. 30196–30203, 2016.

[50] X. Tan, Y. Liu, G. Zeng et al., "Application of biochar for the removal of pollutants from aqueous solutions," *Chemosphere*, vol. 125, pp. 70–85, 2015.

[51] K. Kadirvelu, C. Karthika, N. Vennilamani, and S. Pattabhi, "Activated carbon from industrial solid waste as an adsorbent for the removal of Rhodamine-B from aqueous solution: kinetic and equilibrium studies," *Chemosphere*, vol. 60, no. 8, pp. 1009–1017, 2005.

[52] W. Li, L. Zhang, J. Peng, N. Li, S. Zhang, and S. Guo, "Tobacco stems as a low cost adsorbent for the removal of Pb(II) from wastewater: equilibrium and kinetic studies," *Industrial Crops and Products*, vol. 28, no. 3, pp. 294–302, 2008.

[53] N. T. Abdel-Ghani, M. Hefny, and G. A. F. El-Chaghaby, "Removal of lead from aqueous solution using low cost abundantly available adsorbents," *International journal of Environmental Science and Technology*, vol. 4, no. 1, pp. 67–73, 2007.

[54] S. Shahraki, H. S. Delarami, F. Khosravi, and R. Nejat, "Improving the adsorption potential of chitosan for heavy metal ions using aromatic ring-rich derivatives," *Journal of Colloid and Interface Science*, vol. 576, pp. 79–89, 2020.

[55] B. Li, J. Gong, J. Fang, Z. Zheng, and W. Fan, "Cysteine chemical modification for surface regulation of biochar and its application for polymetallic adsorption from aqueous solutions," *Environmental Science and Pollution Research*, vol. 28, no. 1, pp. 1061–1071, 2021.

[56] F. C. Christopher, S. Anbalagan, P. S. Kumar, S. R. Pannerselvam, and V. K. Vaidyanathan, "Surface adsorption of poisonous Pb(II) ions from water using chitosan functionalised magnetic nanoparticles," *IET Nanobiotechnology*, vol. 11, no. 4, pp. 433–442, 2017.

[57] Z. Wan, D. Chen, H. Pei et al., "Batch study for Pb^{2+} removal by polyvinyl alcohol-biochar macroporous hydrogel bead," *Environmental Technology*, vol. 42, no. 4, pp. 648–658, 2021.

[58] Y. Yan, L. Zhang, Y. Wang et al., "Clanis bilineata larvae skin-derived biochars for immobilization of lead: sorption isotherm and molecular mechanism," *The Science of the Total Environment*, vol. 704, Article ID 135251, 2020.

[59] Y. Yao, B. Gao, M. Inyang et al., "Removal of phosphate from aqueous solution by biochar derived from anaerobically digested sugar beet tailings," *Journal of Hazardous Materials*, vol. 190, no. 1–3, pp. 501–507, 2011.

[60] H. J. Cho, K. Baek, J.-K. Jeon, S. H. Park, D. J. Suh, and Y.-K. Park, "Removal characteristics of copper by marine macro-algae-derived chars," *Chemical Engineering Journal*, vol. 217, pp. 205–211, 2013.

[61] S. Zhang, H. Zhang, J. Cai, X. Zhang, J. Zhang, and J. Shao, "Evaluation and prediction of Cadmium removal from aqueous solution by phosphate-modified activated bamboo biochar," *Energy and Fuels*, vol. 32, no. 4, pp. 4469–4477, 2018.

[62] G. Yin, X. Song, L. Tao et al., "Novel Fe-Mn binary oxide-biochar as an adsorbent for removing Cd(II) from aqueous solutions," *Chemical Engineering Journal*, vol. 389, Article ID 124465, 2020.

[63] J. Xiao, R. Hu, and G. Chen, "Micro-nano-engineered nitrogenous bone biochar developed with a ball-milling technique for high-efficiency removal of aquatic Cd(II), Cu(II) and Pb(II)," *Journal of Hazardous Materials*, vol. 387, Article ID 121980, 2020.

[64] W. Yu, J. Hu, Y. Yu et al., "Facile preparation of sulfonated biochar for highly efficient removal of toxic Pb(II) and Cd(II) from wastewater," *The Science of the Total Environment*, vol. 750, Article ID 141545, 2021.

[65] J. Xiang, Q. Lin, X. Yao, and G. Yin, "Removal of Cd from aqueous solution by chitosan coated MgO-biochar and its in-situ remediation of Cd-contaminated soil," *Environmental Research*, vol. 195, Article ID 110650, 2021.

[66] F. Zhang, B. Wang, P. Jie, J. Zhu, and F. Cheng, "Preparation of chitosan/lignosulfonate for effectively removing Pb(II) in water," *Polymer*, vol. 228, Article ID 123878, 2021.

Research Article

Synthesis and Characterization of ZnO-Nanocomposites by Utilizing Aloe Vera Leaf Gel and Extract of *Terminalia arjuna* Nuts and Exploring Their Antibacterial Potency

Amara Dar,[1] **Rabia Rehman** (ID)**,**[2] **Warda Zaheer,**[1] **Umer Shafique** (ID)**,**[3] **and Jamil Anwar**[1,4]

[1]*Centre for Analytical Chemistry, School of Chemistry, University of the Punjab, Lahore, Punjab, Pakistan*
[2]*Centre for Inorganic Chemistry, School of Chemistry, University of the Punjab, Quaid-e-Azam Campus, Lahore 54590, Pakistan*
[3]*Chemistry Department, Government College University, Lahore, Punjab, Pakistan*
[4]*Chemistry Department, University of Management & Technology, Lahore, Punjab, Pakistan*

Correspondence should be addressed to Rabia Rehman; grinorganic@yahoo.com

Nanotechnology has found vast applications in everyday life. Use of plant extract in the synthesis of nanocomposites produces relatively less toxic and environment-friendly materials. The present study deals with the synthesis of zinc oxide nanocomposite using gel from leaves of *Aloe vera* (black *Aloe vera* (BAV) and white *Aloe vera* (WAV)) and extract from powder of nuts of *Terminalia arjuna*. Synthesized nanocomposites were then characterized by using SEM, FTIR, and UV-Vis techniques. Disc diffusion method was opted to inquire the antimicrobial ability of nanocomposites against different bacterial strains such as *Escherichia coli* (−) and *Burkholderia stabilis* (+). ZnO-BAV possessed good antimicrobial potential against both selected strains as proved from zone of inhibitions. However, ZnO-WAV and ZnO-N showed potential against E. *coli* and no response for *B. stabilis*.

1. Introduction

The study and utilization of material at atomic, molecular, and macromolecular scale is an uprising subdiscipline in different fields of science. During nanocomposite synthesis, particle size reduction of metals is a very attractive field for the researchers as it opens different opportunities to produce novel products [1]. There is a remarkable interest in the synthesis of nanoparticles as they exhibit tremendous properties such as rapid disintegration, shorter dissolution time, and organic, inorganic, and organometallic components and can be used for synthesizing nanoparticles.

Electrochemical and physiochemical nature of nanoparticles defines various areas of their applications, such as optics, photonics, chemisensitive sensing, medicine, pharmaceutics, data storage devices, ceramics, and water purification by catalysis and adsorption [1, 2]. Synthesis of nanoparticles is generally performed by following two different approaches termed as top-down and bottom-up. In the former method, the macroparticles are reduced to nanosized particles, but they are of nonuniform shape, whereas in the later approach, nanoparticles of definite size, shape, and structure are produced. Green synthesis defines the route to produce nanoparticles using less and relatively safer reagents in order to protect the environment [3, 4]. Enzymes and biological materials can be utilized as the capping and reducing agents [3]. Nanoparticles can be synthesized by using micro-organisms such as fungi instead of plant extract, and these microorganisms' help to reduce the metals effectively [5].

During recent years, plant-mediated synthesis of metal nanocomposites has gained noticeable popularity [6]. One significant reason is that the plant-mediated synthesis of nanoparticles is relatively faster than microorganism-based synthesis of nanoparticles [7].

It has been already reported that various techniques can be employed for the synthesis of ZnO nanopowders as thermal decomposition of organic precursor,

electrodeposition, microwave-assisted techniques, spray pyrolysis, hydrothermal methods, precipitation methods, sol gel method, and use of microemulsions [8–17].

A large variety of plant materials has been used for the synthesis of metal nanocomposites, and their potential antimicrobial effects have also been reported in literature [18, 19]. In present studies, zinc nanoparticles are synthesized with the help of *Aloe vera* gel and *Terminalia arjuna* nuts.

Zinc is a strong reducing agent with a moderately reactive property [20]. ZnO nanoparticles have promising potential as an antimicrobial agent. It was observed that ZnO maintains its antibacterial tendency even after composite formation. Its antimicrobial properties include damaging the micro-organism cell by discharge of ions [21]. ZnO composites have also been used as nanofertilizer [22].

Aloe vera is a succulent plant species from the genus *Aloe*. It has cacti-like leafy structure and mostly found in African and Asian regions. It is used as general tonic for immune system, and its juice can potentially be used to treat various diseases [23, 24]. It is effective in treating lung cancer, diabetes, rheumatic arthritis, ulcers, skin burns, and indigestion; it is used as an anti-inflammatory agent and has cosmological importance [25–29].

Terminalia arjuna belongs to genus *Terminalia*. This plant is usually located around riverbanks or near the derelict riverbank in South Asia [30–32]. The main chemical constituents of *Terminalia* nuts include triterpenoids, tannins, saponins, gallic acid, flavonoids, phytosterols, and ellagic acid [33]. Different studies showed that *Terminalia arjuna* plant exhibits antioxidant potential, hypotensive, anti-inflammatory, antiatherogenic, antimutagenic, anticarcinogenic, and gastroproductive effects. Extracts of this plant has proved it useful against coronary heart diseases.

2. Materials and Methods

2.1. Materials.
All the chemicals are used in the present study: carbon tetrachloride, silver nitrate, zinc acetate, sodium hydroxide, and chromic acid were obtained from Sigma Aldrich. Furthermore, double distilled water was used for preparing all the solutions.

2.2. Collection of Plant Material.
In this study, two plants having medicinal significance were selected, i.e., *Aloe vera* and *Terminalia arjuna*. Two varieties of dried *Aloe vera* gel (commercially available marked as black *Aloe vera* (BAV) and white *Aloe vera* (WAV)) were purchased from the local market. The dried plant material was ground to fine powder and sieved through 20 ASTM and kept in a jar for further use.

Almost dried nuts of *Terminalia arjuna* were directly collected from the trees grown at Quaid-e-Azam Campus, University of the Punjab, Lahore. The nuts were washed, dried, and grounded using a ball mill and sieved through 20 ASTM. The powder was dried at 70°C and kept in an air-tight jar for further use.

2.3. Plant Extract Preparation.
For the preparation of the plant extract, 5 g of dried plant material was taken separately in distilled water (100 mL). They were stirred at 100 rpm on a hot plate for 15 minutes at 70°C. This solution was filtered after cooling and used for the preparation of ZnO nanoparticles. Extract of both plant materials was prepared following the same procedure.

2.4. Synthesis of ZnO Nanocomposites.
To synthesize the ZnO nanomaterial with medicinal plant extracts, initially zinc acetate (2.9 g) was dissolved in 50 mL of water. This solution thus obtained was stirred using a magnetic stirrer for 1 hour at room temperature in a conical flask. Then, 20 mL of 10% sodium hydroxide solution was slowly added, and the contents were mixed thoroughly. Now, the flask is covered after adding 50 mL of plant extract and left it for 1 hour. Then, it was placed on an orbital shaker at 100 rpm for 3 hours. Then, the contents were allowed to stand for another 30 minutes. The yellow-coloured ZnO nanocomposites, settled down at bottom, were separated either by centrifuging or by decanting off the supernatant liquid carefully. The ZnO composites were dried in an oven at 80°C for 2 hours. The scheme used is given in Figure 1.

2.5. Characterization of ZnO Nanocomposites.
Composite nanoparticles of zinc were characterized by using FTIR, UV, and SEM techniques.

To study the presence of various functional groups, FTIR analysis (Perkin Elmer) was carried out in the range of 4000–400 cm^{-1} for plant extract and then compared with the plant-based ZnO nanocomposites.

For conducting the UV analysis, Labomed 3500-UVD was used to find λ_{max} of the synthesized material. They absorb the characteristic wavelengths with a little variation due to the organic molecules from plant materials acting as capping and reducing agents.

To study the surface morphology of any material, SEM analysis was conducted. To verify the formation of nanocomposites, the comparison of SEM of dried plant material and synthesized nanocomposite was studied. It reveals the change in the structural morphology that occurs during the formation of nanocomposites.

3. Results and Discussion

3.1. FTIR Analysis of ZnO-BAV.
FTIR spectra of BAV-Zn indicated various bands. Weak signals at 3633 cm^{-1} are owing to the presence of N-H amines. Strong stretching vibration owing to the formation of N-H amides is found at 1533 cm^{-1}. The spectra of ZnO-BAV, ZnO-WAV, and ZnO-N are displayed in Figures 2–4.

3.2. FTIR Analysis of ZnO-N.
The presence of secondary amines was displayed due to N-H amines at 3343 cm^{-1}. Strong stretching vibrational signals at 1511 cm^{-1} is owing to the formation of the N-H amide bond. Strong stretching vibration at 1362 cm^{-1} is because of alpha methyl bending.
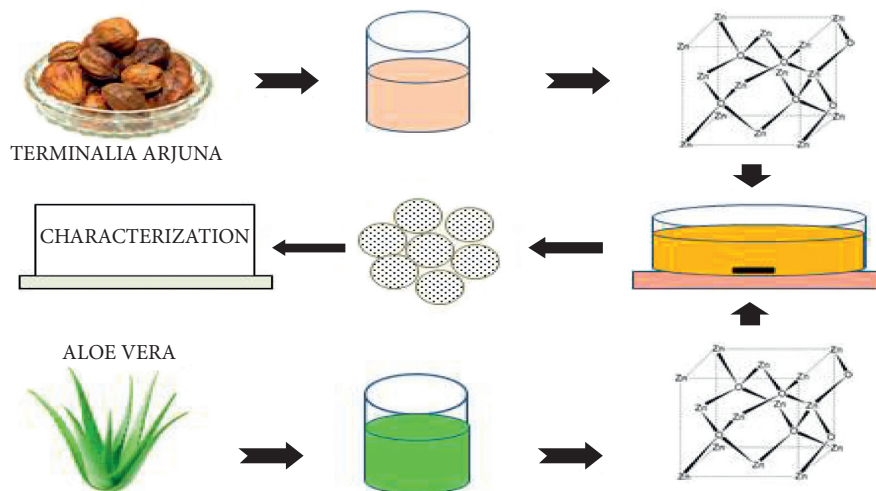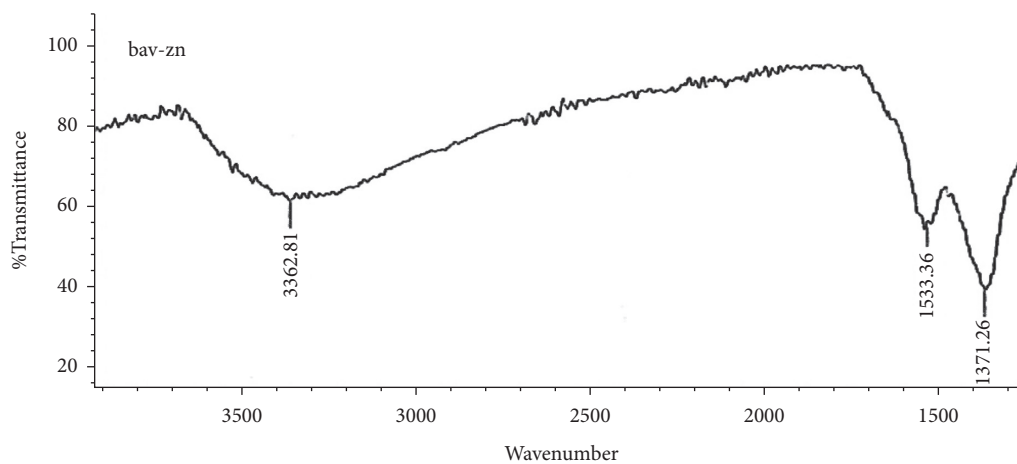
FIGURE 1: Scheme of synthesis of ZnO nanocomposites.
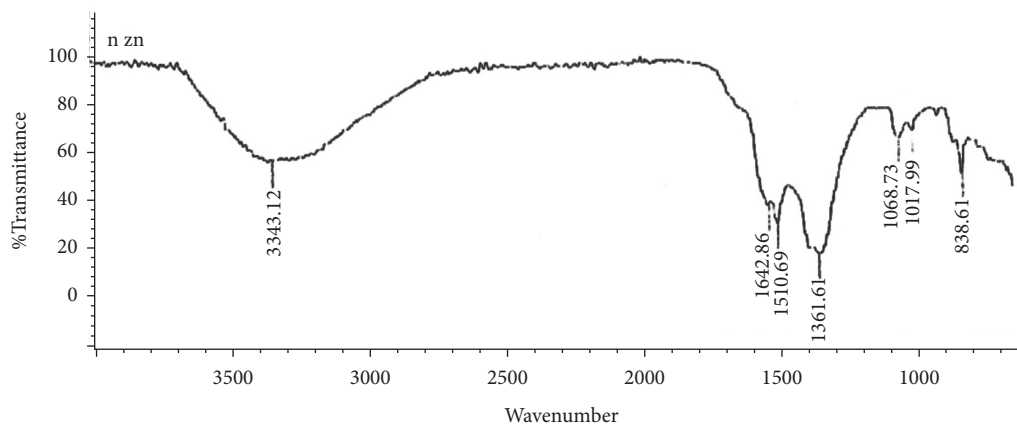

FIGURE 2: FTIR spectrogram of ZnO-BAV nanocomposites.

FIGURE 3: FTIR spectrogram of ZnO-N nanocomposites.

Peak at $1069 \, \text{cm}^{-1}$ indicated strong stretching due to oxygen-carbon bond. Band at $838 \, \text{cm}^{-1}$ shows strong stretching vibrations caused by the C-H bond. The work of Dobrucka also validates our work who found the bands are at 3243, 2168, 1383, 1599, 1076, 780, and $515 \, \text{cm}^{-1}$. Peaks near $515 \, \text{cm}^{-1}$ can be owing to the stretching vibration of ZnO.
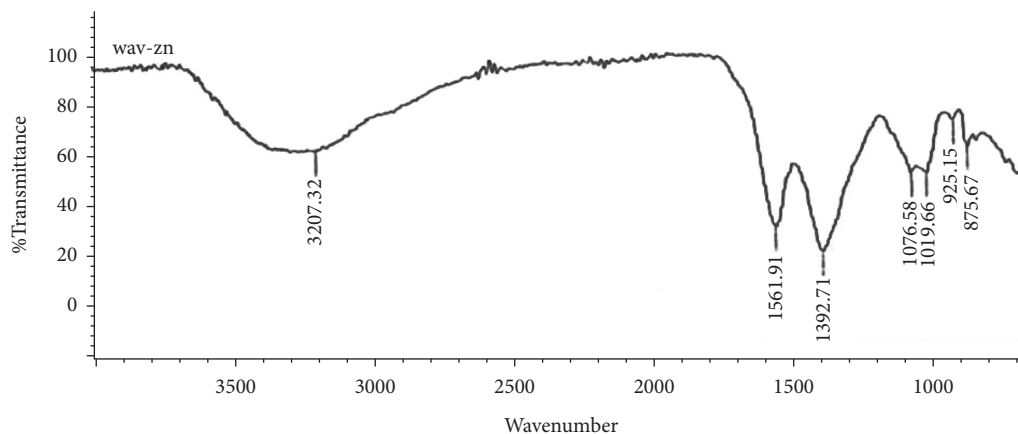
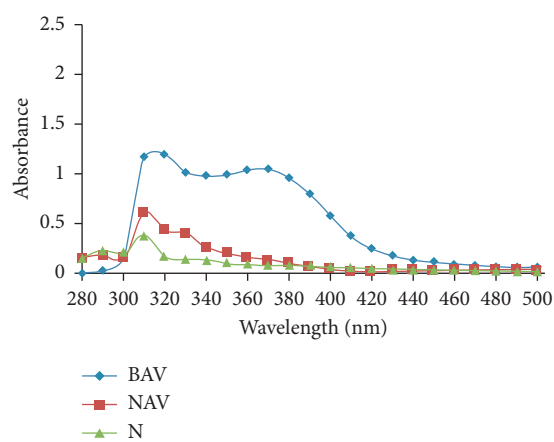Figure 4: FTIR spectrogram of ZnO-WAV nanocomposites.

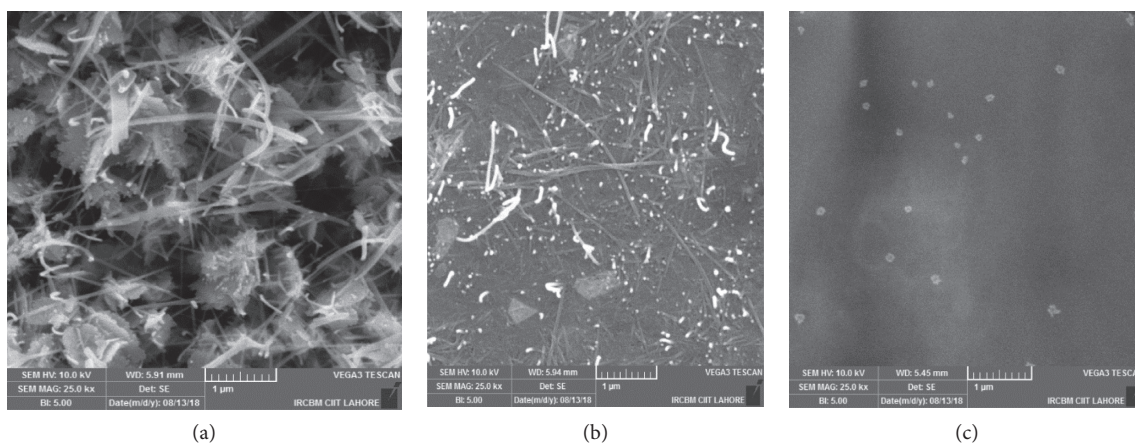Figure 5: UV-Vis spectrogram of ZnO nanocomposites synthesized by BAV, WAV, and nuts.

Figure 6: SEM images of (a) ZnO-BAV, (b) ZnO-N, and (c) ZnO-WAV nanocomposites.

Other bands at 3245 and 1599 cm^{-1} are indicating the -OH group. The peaks at 1383 and 1076 cm^{-1} may be ascribed to -C-O- and -C-O-C-stretching vibes [34].

3.3. FTIR Analysis of ZnO-WAV.

In the spectrogram of ZnO-WAV, the band at 3207 cm^{-1} demonstrated the presence of amines, whereas the band at 1393 cm^{-1} is owing
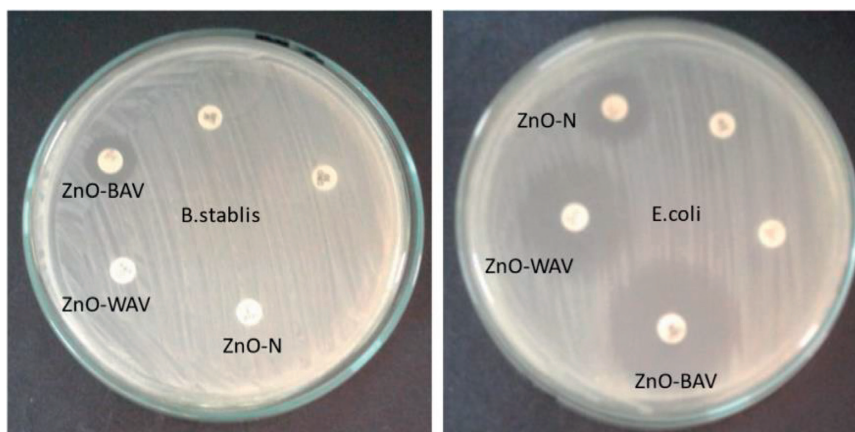
FIGURE 7: Images showing the application of synthesized nanocomposites of ZnO by using BAV, WAV, and N for antibacterial activity against *E. coli* and *B. stabilis*.

TABLE 1: Zone of inhibition produced by different ZnO nanocomposites.

Nanocomposites	Zone of inhibitions for zinc nanocomposites	
	Escherichia coli	*Burkholderia stabilis*
ZnO-BAV	0.24 ± 0.02	0.11 ± 0.01
ZnO-WAV	0.20 ± 0.02	—
ZnO-N	0.11 ± 0.02	—

to C-O-H bonding. The stretching of two O-C bonds is exhibited by the band at $1020 \, \text{cm}^{-1}$. The analysis of Jamdagni also strengthens our spectral results, who gained FTIR peeks at 3340.6, 3258.2, 2127.8, 1641.1, 1456.7, 1362.5, 1040, 1026.8, 746.25, and $620.65 \, \text{cm}^{-1}$ for ZnO nanocomposites [34].

3.4. UV-Vis Analysis. UV-Vis spectrographs were taken in the range of 280–500 nm for ZnO nanocomposites using suitable solvents. UV absorption spectra for ZnO nanocomposites with BAV, WAV, and nuts are shown in Figure 5. It is revealed that λ_{max} is shown at 320 and 310 nm, respectively. Nearly, the same results were reported in the previous work [34].

3.5. SEM Imaging. SEM images of ZnO-nanocomposites have been performed on FEI Nova 450 NanoSEM. The shape of each Figure (Figures 6(a), 6(b), 6(c)) obtained by SEM images are fibrous-wired structure, scattered particle, and octahedral, respectively. The different surface morphology of ZnO nanocomposite revealed that ZnO-BAV showed fibrous-wired structure (~27 to 71 nm particle size), ZnO-N showed scattered particle formation (~32 to 83 nm particle size), and ZnO-WAV showed octahedral zinc composite (~29 to 75 nm particle size) as shown in Figure 6.

3.6. Antimicrobial Activity. Antimicrobial potential of synthesized ZnO-nanocomposites was investigated against two bacterial strains, i.e., *Burkholderia stabilis* and *Escherichia coli.* After preparing Petri plates using agar medium

and uniformly distributing the bacterial strains over the agar surface, the disc diffusion method was applied. DMSO was used to make the solutions. The zone of inhibition in case of zinc oxide nanocomposites, as shown in Figure 7, revealed active antimicrobial potency against the selected strains of bacteria. Zone of inhibitions for ZnO nanocomposites are compared in Table 1.

4. Conclusion

Nanocomposites of zinc oxide were synthesized by using the plant extract of *Aloe vera* and *Terminalia* plants. These nanoparticles are synthesized under ecofriendly conditions with less toxic chemical production. Nanoparticles are then characterized by using different analytical techniques such as FTIR, UV-VIS, and SEM. In FTIR studies, the synthesized nanoparticles showed absorbance and bending at expected specific wavenumbers due to various functional groups which confirmed the synthesis of nanocomposites. In the UV-Vis, spectrum the synthesized products showed the maximum absorption at specific wavelength assigned for ZnO that confirms the formation of the product of interest. From SEM images, the nanoparticle's structure was further confirmed, and it shows the morphology of the nanoparticles. Then, the antibacterial potential was checked against two bacterial strains *Burkholderia stabilis* and *Escherichia coli*, and both types of nanocomposites indicated efficient antibacterial potency.

References

[1] A. B. Moghaddam, T. Nazari, J. Badraghi, and M. Kazemzad, "Synthesis of ZnO nanoparticles and electrodeposition of polypyrrole/ZnO nanocomposite film," *Intrenational Journal of Electrochemical Science*, vol. 4, no. 2, pp. 247–257, 2009.

[2] A. Tripathi, N. Chandrasekaran, A. M. Raichur, and A. Mukherjee, "Antibacterial applications of silver nanoparticles synthesized by aqueous extract of *Azadirachta indica* (Neem) leaves," *Journal of Biomedical Nanotechnology*, vol. 5, no. 1, pp. 93–98, 2009.

[3] B. K. Vogler and E. Ernst, "Aloe vera: a systematic review of its clinical effectiveness," *British Journal of General Practice*, vol. 49, no. 447, pp. 823–828, 1999.

[4] B. Vázquez, G. Avila, D. Segura, and B. Escalante, "Antiinflammatory activity of extracts from aloe vera gel," *Journal of Ethnopharmacology*, vol. 55, no. 1, pp. 69–75, 1996.

[5] C. Ramteke, T. Chakrabarti, B. K. Sarangi, and R. A. Pandey, "Synthesis of silver nanoparticles from the aqueous extract of leaves of *Ocimum sanctum* for enhanced antibacterial activity," *Journal of Chemistry*, vol. 2013, Article ID 278925, 7 pages, 2013.

[6] D. Ramkumar and S. S. C. Rao, "Efficacy and safety of traditional medical therapies for chronic constipation: systematic review," *The American Journal of Gastroenterology*, vol. 100, no. 4, pp. 936–971, 2005.

[7] F. Capasso, F. Borrelli, R. Capasso et al., "Aloe and its therapeutic use," *Phytotherapy Research: An International Journal Devoted to Pharmacological and Toxicological Evaluation of Natural Product Derivatives*, vol. 12, no. S1, pp. S124–S127, 1997.

[8] F. Rataboul, C. Nayral, M. J. Casanove, A. Maisonnat, and B. Chaudret, "Synthesis and characterization of monodisperse zinc and zinc oxide nanoparticles from the organometallic precursor [Zn (C_6H_{11})$_2$]," *Journal of Organometallic Chemistry*, vol. 643-644, pp. 307–312, 2002.

[9] G. A. Ozin, "Nanochemistry: synthesis in diminishing dimensions," *Advanced Materials*, vol. 4, no. 10, pp. 612–649, 1992.

[10] J. L. Gardea-Torresdey, E. Gomez, J. Peralta-Videa et al., "Formation and growth of Au nanoparticles inside live alfalfa plants," *Nano Letters*, vol. 2, no. 4, pp. 397–401, 2002.

[11] H. J. Zhai, W. H. Wu, F. Lu, H. S. Wang, and C. Wang, "Effects of ammonia and cetyltrimethylammonium bromide (CTB) on morphologies of ZnO nano- and micromaterials under solvothermal process," *Materials Chemistry and Physics*, vol. 112, no. 3, pp. 1024–1028, 2008.

[12] J. F. Jennifer, "Aloe for AIDS," *Medical Anthropology*, vol. 11, pp. 498–504, 1997.

[13] J. J. Wu and S. C. Liu, "Low-temperature growth of well-aligned ZnO nanorods by chemical vapor deposition," *Advanced Materials*, vol. 14, no. 3, pp. 215–218, 2002.

[14] J. P. Yadav, S. Kumar, L. Budhwar, A. Yadav, and M. Yadav, "Characterization and antibacterial activity of synthesized silver and iron nanoparticles using aloe vera," *Journal of Nanomedicine and Nanotechnology*, vol. 7, no. 384, p. 2, 2016.

[15] J. R. Morones, J. L. Elechiguerra, A. Camacho et al., "The bactericidal effect of silver nanoparticles," *Nanotechnology*, vol. 16, no. 10, pp. 2346–2353, 2005.

[16] K. N. Thakkar, S. S. Mhatre, and R. Y. Parikh, "Biological synthesis of metallic nanoparticles," *Nanomedicine: Nanotechnology, Biology and Medicine*, vol. 6, no. 2, pp. 257–262, 2010.

[17] K. Okuyama and W. W. Lenggoro, "Preparation of nanoparticles via spray route," *Chemical Engineering Science*, vol. 58, no. 3-6, pp. 537–547, 2003.

[18] M. Bitenc, M. Marinšek, and Z. Crnjak orel, "Preparation and characterization of zinc hydroxide carbonate and porous zinc oxide particles," *Journal of the European Ceramic Society*, vol. 28, no. 15, pp. 2915–2921, 2008.

[19] P. Mohanpuria, N. K. Rana, and S. K. Yadav, "Biosynthesis of nanoparticles: technological concepts and future applications," *Journal of Nanoparticle Research*, vol. 10, no. 3, pp. 507–517, 2008.

[20] M. Rai, A. Yadav, and A. Gade, "CRC 675-Current trends in phytosynthesis of metal nanoparticles," *Critical Reviews in Biotechnology*, vol. 28, no. 4, pp. 277–284, 2008.

[21] M. Singhal, V. Chhabra, P. Kang, and D. O. Shah, "Synthesis of ZnO nanoparticles for varistor application using Zn-substituted aerosol OT microemulsion," *Materials Research Bulletin*, vol. 32, no. 2, pp. 239–247, 1997.

[22] P. Chithra, G. B. Sajithlal, and G. Chandrakasan, "Influence of aloe vera on the healing of dermal wounds in diabetic rats," *Journal of Ethnopharmacology*, vol. 59, no. 3, pp. 195–201, 1998.

[23] P. Jamdagni, P. Khatri, and J. S. Rana, "Green synthesis of zinc oxide nanoparticles using flower extract of *Nyctanthes arbortristis* and their antifungal activity," *Journal of King Saud University Science*, vol. 30, no. 2, pp. 168–175, 2018.

[24] P. J. P. Espitia, N. D. F. F. Soares, J. S. D. R. Coimbra, N. J. de Andrade, R. S. Cruz, and E. A. A. Medeiros, "Zinc oxide nanoparticles: synthesis, antimicrobial activity and food packaging applications," *Food and Bioprocess Technology*, vol. 5, no. 5, pp. 1447–1464, 2012.

[25] P. Sukumaran and E. K. Poulose, "Silver nanoparticles: mechanism of antimicrobial action, synthesis, medical applications, and toxicity effects," *International Nano Letters*, vol. 2, no. 1, pp. 1–10, 2012.

[26] R. Dobrucka and J. Długaszewska, "Biosynthesis and antibacterial activity of ZnO nanoparticles using *Trifolium pratense* flower extract," *Saudi Journal of Biological Sciences*, vol. 23, no. 4, pp. 517–523, 2016.

[27] S. Dwivedi and M. P. Agarwal, "Antianginal and cardioprotective effects of *Terminalia arjuna*, an indigenous drug, in coronary artery disease," *The Journal of the Association of Physicians of India*, vol. 42, no. 4, pp. 287–289, 1994.

[28] S. Dwivedi, "*Terminalia arjuna* wight & Arn.-a useful drug for cardiovascular disorders," *Journal of Ethnopharmacology*, vol. 114, no. 2, pp. 114–129, 2007.

[29] S. Rajasekaran, K. Sivagnanam, K. Ravi, and S. Subramanian, "Hypoglycemic effect of aloe vera gel on streptozotocin-induced diabetes in experimental rats," *Journal of Medicinal Food*, vol. 7, no. 1, pp. 61–66, 2004.

[30] S. Senapati, A. Ahmad, M. Sastry, R. Kumar, and R. Kumar, "Extracellular biosynthesis of bimetallic Au-Ag alloy nanoparticles," *Small*, vol. 1, no. 5, pp. 517–520, 2005.

[31] S. Sabir, M. Arshad, and S. K. Chaudhari, "Zinc oxide nanoparticles for revolutionizing agriculture: synthesis and applications," *The Scientific World Journal*, vol. 2014, Article ID 925494, 8 pages, 2014.

[32] T. Klaus, R. Joerger, E. Olsson, and C. G. Granqvist, "Silver-based crystalline nanoparticles, microbially fabricated," *Proceedings of the National Academy of Sciences*, vol. 96, no. 24, pp. 13611–13614, 1999.

[33] X. L. Hu, Y. J. Zhu, and S. W. Wang, "Sonochemical and microwave –assisted synthesis of linked single-crystalline

ZnO rods," *Materials Chemistry and Physics*, vol. 88, no. 2-3, pp. 421–426, 2004.

[34] Y. L. Wei and P. Chang, "Characteristics of nano zinc oxide synthesized under ultrasonic condition," *Journal of Physics and Chemistry of Solids*, vol. 69, no. 2-3, pp. 688–692, 2008.